The Henryk Niewodniczański
INSTITUTE OF NUCLEAR PHYSICS
Polish Academy of Sciences
ul. Radzikowskiego 152, 31-342 Kraków, Poland

www.ifj.edu.pl/publ/hab/

Kraków, January 17, 2013

Measurements of final states with τ leptons in proton-proton collisions using the ATLAS detector at the LHC

Anna Kaczmarska

Habilitation Thesis

This work was supported in part by the Polish Ministry of Higher Education
under grant no. NN202127937.

Wydrukowano nakładem Instytutu Fizyki Jądrowej
Polskiej Akademii Nauk
Kraków, 2013
Recenzent: Prof. dr hab. Barbara Wosiek
ISBN 978-83-934248-8-7

Physics is like sex: sure, it may give some practical results, but that's not why we do it.
- Richard Feynman -

Abstract

This monograph describes first analyses of processes with τ leptons in final state that have been performed with proton-proton collision data at the centre-of-mass energy of $\sqrt{s} = 7$ TeV collected with the ATLAS detector at the LHC. Described studies are based on early data, recorded in 2010 and corresponding to an integrated luminosity of 35 pb^{-1}. Presented Higgs boson(s) searches, requiring higher statistics samples, are based on more data, corresponding to an integrated luminosity of 1.06 fb^{-1} and collected in 2010 and the first half of 2011.

The reconstruction algorithms and identification methods for hadronically decaying τ leptons in the ATLAS experiment are described in detail. Validation of those algorithms in data as well as the first attempts to estimate the rate of the mis-identification of Quantum Chromodynamics jets or electrons as τ candidates are also presented. A dedicated Chapter is devoted to the first measurements of $Z \to \tau\tau$ and $W \to \tau\nu$ production cross sections. The use of the latter process for determination of the hadronic τ decay identification efficiency is also reported.

The early analyses of Higgs boson(s) searches with τ leptons in final states, presented in this document, cover studies of both the Standard Model and Minimal Supersymmetric Standard Model neutral Higgs boson(s) decaying into the $H \to \tau\tau$ final state as well as Minimal Supersymmetric Standard Model charged Higgs boson decays, $H^+ \to \tau\nu$. No significant excess over the expected background is observed in any of these studies. Nevertheless, even though performed on limited statistics, they provided improved exclusion limits as compared to those obtained by previous experiments.

Streszczenie

Niniejsza rozprawa habilitacyjna opisuje pierwsze analizy procesów z leptonami τ w stanach końcowych przeprowadzone na danych zebranych przez detektor ATLAS na akceleratorze LHC. Użyte dane zostały zgromadzone przy zderzeniach proton-proton z energią w środku masy $\sqrt{s} = 7$ TeV. Opisane wyniki uzyskano w większości z wykorzystaniem pierwszych danych zebranych w roku 2010, odpowiadających wycałkowanej świetlności 35 pb^{-1}. Wyjątek stanowią rezultaty poszukiwań bozonu(ów) Higgsa, gdyż wymagały one większej liczby zarejestrowanych przypadków. Zostały więc one oparte o dane odpowiadające wycałkowanej swietlności 1.06 fb^{-1}, zebrane zarówno w roku 2010 jak i w pierwszej połowie roku 2011.

Praca zawiera szczegółowy opis algorytmów użytych do rekonstrukcji i identyfikacji hadronowych rozpadów leptonów τ. Przedstawione zostały także testy tych algorytmów na zebranych danych doświadczalnych, oraz pierwsze próby wyznaczenia częstości mylnej identyfikacji dżetów Chromodynamiki Kwantowej (QCD) lub elektronów jako kandydatów na leptony τ. Osobny rozdział poświęcony został pierwszym pomiarom przekrojów czynnych procesów $Z \to \tau\tau$ i $W \to \tau\nu$ w eksperymencie ATLAS oraz użyciu przypadków $W \to \tau\nu$ do oszacowania efektywności identyfikacji hadronowych rozpadów τ.

W ostatnich rozdziałach podsumowano pierwsze analizy mające na celu poszukiwanie bozonu(ów) Higgsa w rozpadach z leptonami τ w stanach końcowych. Opisano zarówno poszukiwania prowadzone w ramach Modelu Standardowego jak i jego Minimalnego Supersymetrycznego rozszerzenia. W żadnej z opisanych analiz nie znaleziono znaczącego sygnału ponad tło. Niemniej, analizy te, nawet przeprowadzone na małej statystyce dostępnych wówczas przypadków, zawęziły limity wykluczeń wyznaczone przez wcześniejsze eksperymenty.

Acknowledgments

This monograph is the result of many years of work and effort, and I could not have completed it without the support of many people. Let me devote this page to all who helped me.

To Elżbieta Richter-Wąs, without whose motivation and encouragement I would not have written this monograph. She provided the vision and advise necessary for me to understand how interesting the τ lepton physics field is. I am thankful to her for always having time for discussions, for sharing her impressive knowledge and experience and for her criticism always honest and constructive. I will always owe her a debt of gratitude for all she has done for me.

To Piotr Malecki, without whom I would not have been in the ATLAS experiment and who taught me that a true experimentalist should not be scared of challenges and should be able to learn everything, even from scratch (but with a manual).

To Barbara Wosiek, for continuous support of my research and in particular, of preparing this monograph.

To the Tau Working Group of the ATLAS experiment, and its former and present conveners, for creating the stimulating and pleasant atmosphere to work on our beloved leptons. Special thanks go to Stan Lai who was always full of laughter, joy, and support for me and to Zofia Czyczula for long discussions about physics and life.

To the $Z \to \tau\tau$ Working Group and in particular to Susanne Kuehn, Elias Coniavitis and Matthew Beckingham for spending countless and sometimes late hours working to understand and solve problems related to the first $Z \to \tau\tau$ process observation and its cross section measurement.

To Paris LPNHE group where I had a privilege to spend a lot of my time thanks to Polish-French IN2P3 collaboration and invitations from University Paris 7. In particular to Frederic Derue for numerous interesting discussions and showing me how a beautiful country France is.

To my home institute ATLAS group for vibrant coffee discussions and for friendly and motivating place to work. I will never forget all the experiences I have shared with you guys. I am very happy that, in many cases, our friendship have extended well beyond working hours.

To Paweł Brückman, with whom I have the pleasure to stay in the same office, for sharing with me joys and sorrows in the challenging life of a Polish physicist. Thank you for uplifting my soul every time I felt down.

To the ATLAS Collaboration for allowing me to participate in preparation of our experiment and then to share the excitement of commissioning the ATLAS detector and analysing the first LHC data.

To Mariusz for being the most understanding husband in the world. Thank you for supporting me in everything that I do. Finally, to my little son Iwo, for being my spark of optimism when I had hard time. I love you both a lot.

Statement on author's contribution

The physics of τ leptons as well as reconstruction and identification of their hadronic decays have been my major interest since 2006.

In years 2006-2010, I was creating, developing, maintaining and validating algorithms in the `tauRec` package, the official tool of the ATLAS Collaboration for reconstruction and identification of hadronically decaying τ leptons. I introduced the track-based algorithm to complement the existing simple, calorimeter-based one. I was leading the development of both algorithms and finally, their full merge into a single, robust and effective package. It was used by the collaboration for all the studies with τ leptons in final states in the first ATLAS data. Prior to the data taking period I was an author of several ATLAS internal notes documenting development and validation of the `tauRec` package [1, 2, 3, 4, 5, 6, 7].

In years 2008-2009 when the ATLAS detector, already commissioned in its underground cavern, collected several hundred million cosmic ray events I was participating in tests of the reconstruction and identification of fake τ candidates in those data [8, 9]. I was continuing similar studies with the early data coming from proton-proton collisions, first at the centre-of-mass energy of 900 GeV [10] and then 7 TeV [11, 12]. Thus I contributed to all stages of obtaining results presented in Chapter 4 of the presented monograph, not only to the final outcome but also to the long process of the creation, development and validation of the algorithms needed to obtain it.

In parallel to the development and validation of the reconstruction and identification of hadronically decaying τ leptons I studied the $Z \to \tau\tau$ process. As the first stage I prepared and optimised the cut flow of the analysis in order to obtain the clear signal over the background. These studies were first performed using Monte Carlo samples [13, 14]. After collision data taking had started, this analysis led to the first observation of $Z \to \tau\tau$ decays in the ATLAS experiment [15] and then to the cross section measurement of this process [16]. I was playing a central role in those studies as a convener of the $Z \to \tau\tau$ analysis group and co-editor of the observation conference note and the cross section measurement paper. Thus my contribution both to the final $Z \to \tau\tau$ studies described in Chapter 5 as well as their preparation is a major one.

I was not directly involved in the $W \to \tau\nu$ studies described in Chapter 5 but I contributed to them by discussions, help and passing experience from my group to the parallel $W \to \tau\nu$ group doing their analysis after the $Z \to \tau\tau$ cross section had been measured.

I was not involved in the Standard Model and Minimal Supersymmetric Standard Model Higgs boson(s) searches analyses described in Chapter 6 and Chapter 7 for completeness of the presented monograph. Nevertheless, it should be stressed that those studies would not be possible without the `tauRec` package developed by myself in preceding years. Currently, I have started to work on searches for heavy charged Higgs bosons with τ lepton final states.

Following the rules of the ATLAS Collaboration, only official, public results and plots are included in the presented monograph, but references to internal notes are given.

Contents

We were not yet prepared to claim that we had found a new charged lepton, but we were ready to claim that we had found something new. To accentuate our uncertainty I denoted the new particle by U for unknown in some of our 1975-1977 papers. The name τ came later. This name was suggested by Rapidis, who was then a graduate student and had worked with me in the early 1970s on the $e-\mu$ problem. The letter τ is from the Greek $\tau\rho\iota\tau\nu$ for "third" -the third charged lepton.

Martin Perl, The Discovery of the Tau Lepton, in "The Rise of the Standard Model", Cambridge Univ. Press 1997.

1 Introduction

The history of the τ lepton began 39 years ago when Kobayashi and Maskawa [17] proposed a mechanism for the CP violation which involved the hypothesis of a third generation of quarks and leptons. At that time there was no experimental evidence and need for another generation. In early seventies, physicists tried to understand differences between the muon and the electron. They believed that, perhaps, if other higher mass versions of these particles exist, then through studying them a new understanding of the origin of lepton differences might emerge. The first search was performed by two experiments at the ADONE storage ring [18], but its energy was below the threshold for τ pair production. The next was the Mark I experiment on the SPEAR storage ring at SLAC which began to take data in 1973. One year later the first anomalous $e-\mu$ events, with exactly two oppositely charged particle tracks, consistent with being an electron and a muon, were observed. However, because of additional checks and scepticism surrounding the discovery, the first claim of evidence for a new heavy lepton was published only in late 1975 [19]. The existence of the τ was considered firmly established by the end of 1978 [20, 21].

Since that time, properties of the τ lepton have been extensively studied. Its mass, lifetime, decay modes and polarisation, have been precisely measured in several experiments using e^+e^- collisions, namely the LEP experiments [22], BaBar [23], Belle [24], BESII [25], CLEO [26] and KEDR [27].

A new era for τ leptons came with hadron colliders, Tevatron [28] and Large Hadron Collider (LHC) [29]. For those experiments, τ decays themselves are not of primary interest, but rather they are used to measure properties of τ production processes. τ leptons, and particularly their hadronic decays, play an important role in measurements of properties of electroweak bosons and top quarks. They are also crucial for discovery physics, like searches for Higgs boson(s) [30, 31, 32, 33, 34, 35], Supersymmetry (SUSY) [36, 37, 38, 39, 40, 41, 42, 43, 44], or other unexpected phenomena.

τ leptons are heavy particles with a measurable life-time, undergoing only electroweak interactions. They couple to SUSY particles via Yukawa coupling free from Quantum Chromodynamics (QCD) effects. The production and decay vertices of τ leptons in typical LHC collisions are well separated in space, providing a potential for measurements of the polarisation, spin correlations and parity of resonances decaying to τ leptons. The excellent knowledge of their decay modes from low energy experiments make them an ideal signature for observations of New Physics.

Despite the strong physics motivation for exploring data with τ leptons in the final state, reconstruction at hadron colliders remains a very difficult task in terms of distinguishing interesting events from backgrounds dominated by the overwhelming QCD multijet production. Another related challenge is to provide an efficient triggering for events with hadronic τ decays, while keeping trigger rates at levels manageable by the trigger system.

The LHC started operation in November 2009 and since 30 March 2010 proton-proton (pp) collisions at the centre-of-mass energy of $\sqrt{s} = 7$ TeV have been taking place. In this monograph, the first analyses involving τ

leptons, using data recorded by the ATLAS detector [45] during 2010 and corresponding to an integrated luminosity of 35 pb^{-1}, are presented. Only exception are the Higgs boson(s) searches, based on more data (from 2010 and the first half of 2011) corresponding to an integrated luminosity of 1.06 fb^{-1}. Both $t\bar{t}$ and New Physics processes studied with τ leptons in final state are omitted in the monograph as they require higher statistics of data.

The document is organised as follows.

Chapter 2 gives a short description of τ lepton properties and decays. A review of processes with τ leptons in final states follows after.

Chapter 3 briefly introduces the ATLAS detector, its subsystems and techniques for particle identification. As Monte Carlo samples are used in described analyses, their production chain is also presented. For the first data studies, similar preselection of events, based on detector performance is usually applied. It is described roughly at the end of this Chapter.

In Chapter 4, the algorithms for the τ lepton reconstruction and identification are presented. Their performance in terms of identification efficiencies and mis-identification rates is also described.

Chapter 5 focuses on Standard Model processes with τ leptons: $W \to \tau\nu$ and $Z \to \tau\tau$ decays. The first measurements of their cross sections in ATLAS experiment are described. Finally, an application of those studies for the measurement of the τ identification efficiency in data using $W \to \tau\nu$ events is presented

The Higgs boson(s) searches with τ leptons in final state are presented in Chapter 6 for the Standard Model and in Chapter 7 for the Minimal Supersymmetric Standard Model.

In Appendix A, the $\tau^+\tau^-$ mass reconstruction techniques used in the presented analyses, are described.

Conventions

The ℓ refers to either an electron or a muon. The l symbol refers to an electron or a muon or a τ lepton.
In the following, τ^+, τ^- are indicated simply as τ, unless otherwise stated. The same applies to other particles.
The hadronically decaying τ lepton is denoted as τ_{had}, while leptonically decaying as τ_{lep}.
Charged Higgs bosons are denoted as H^+, with the charge-conjugate H^- always implied.
The natural units are used where proton carries a positive unit of charge and the speed of light c= 1.

Is the tau simply a standard model lepton, or will the physics of the tau lead us outside of the standard model?

Martin Perl

. . . . . they are ill discoverers that think there is no land when they can see nothing but sea.

Francis Bacon

2 Physics with τ leptons

The τ lepton together with the τ neutrino forms the third generation of the Standard Model (SM) leptons. Its properties have been studied in detail in past decades. Now, with the LHC start, a new window opens for physics with the τ particle. Because of its properties, it is an interesting probe for many processes beyond the Standard Model. In this Chapter, the main properties of the τ lepton and its role in the ATLAS physics program are presented.

2.1 Properties of the τ lepton

The τ lepton is the first discovered member of the third quark-lepton family. For its discovery in 1975 at the SLAC [19] Martin Perl was awarded the 1995 Nobel Prize in physics. The measured rest mass of the τ lepton is 1776.82 ± 0.16 MeV [46]. This is almost 3500 times heavier than the equivalent particle of the first generation, the electron. The τ lepton is unstable, it has a mean lifetime of $(290.6 \pm 1.0) \times 10^{-15}$ s, corresponding to a decay length of 87.11 μm [46].

The τ lepton is the only lepton heavy enough to decay leptonically and hadronically. The coupling of the τ^- current [1] to the W^- boson of the weak interaction, shown in Figure 2.1, produces a weakly interacting τ neutrino. The virtual W^- created in this reaction then couples to an additional pair of leptons, $e^-\bar{\nu_e}$ or $\mu^-\bar{\nu_\mu}$, or quarks, $\bar{u}d$ or $\bar{u}s$. All other quark pairings, such as $\bar{c}d$, $\bar{c}s$, are too massive to be produced. Therefore, to lowest order all decays of τ leptons are included in these four processes:

$$\tau^- \to \nu_\tau \bar{\nu_e} e^- \tag{2.1}$$

$$\tau^- \to \nu_\tau \bar{\nu_\mu} \mu^- \tag{2.2}$$

$$\tau^- \to \nu_\tau \bar{u}d \to \nu_\tau \text{ hadrons} \tag{2.3}$$

$$\tau^- \to \nu_\tau \bar{u}s \to \nu_\tau \text{ hadrons}. \tag{2.4}$$

Quarks which couple to W^- may be from the same generation, as in the $\bar{u}d$ case, or from different generations, as in the $\bar{u}s$ case. The relative strengths of these couplings are given by the elements of the Cabibbo-Kobayashi-Maskawa (CKM) matrix [46]. Couplings to quarks within the same generation are highly favoured over couplings across generations. Consequently, the $\bar{u}s$ decays of the τ have much smaller branching fractions than the analogous $\bar{u}d$ decays.

A list of decays of the τ lepton is given in Table 2.1, along with experimental values for their branching ratios (BR) [46]. These decays are grouped according to the four possible pairs of particles produced at the W^- vertex. In

[1] In this Chapter processes with τ^- are shown as an example. Charge-conjugate particles and decays are implied.

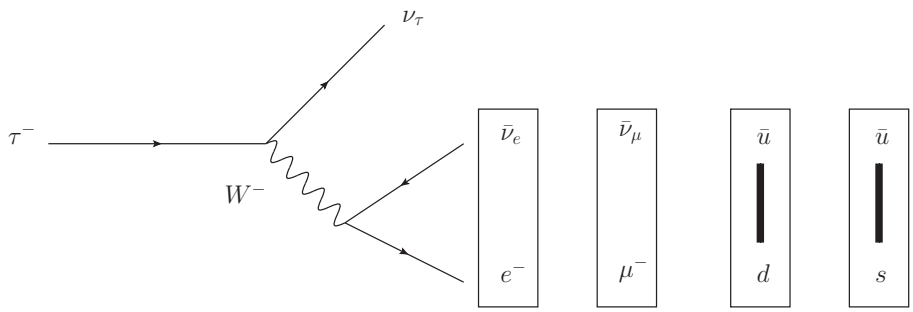

Figure 2.1: Particle doublets at the W^- vertex in τ^- lepton decays.

Table 2.1: τ^- decays and branching ratios. Decays are classified according to the particles at the W^- vertex and the number of K and π in the final state. Experimental values are current world averages [46].

τ lepton decays			Branching ratio (%)
W^- vertex	channel	final state	
$\bar{\nu}_e e^-$		e^-	17.85 ± 0.05
$\bar{\nu}_\mu \mu^-$		μ^-	17.36 ± 0.05
$\bar{u}d$	π^-	π^-	10.91 ± 0.07
	ρ^-	$\pi^-\pi^0$	25.51 ± 0.09
	a_1^-	$\pi^-\pi^+\pi^-$	9.32 ± 0.07
	a_1^-	$\pi^-\pi^0\pi^0$	9.29 ± 0.11
		$\pi^-\pi^+\pi^-\pi^0$	4.61 ± 0.06
		$\pi^-\pi^0\pi^0\pi^0$	1.04 ± 0.07
		$\pi^-\pi^+\pi^-\pi^+\pi^-$	0.0839 ± 0.0035
		$\pi^-\pi^+\pi^-\pi^0\pi^0$	0.495 ± 0.032
		$\pi^-\pi^0\pi^0\pi^0\pi^0$	0.15 ± 0.04
		K^-K^0	0.159 ± 0.016
		$K^-K^+\pi^-$	0.140 ± 0.005
		$K^-K^0\pi^0$	0.159 ± 0.020
		$\pi^-K^0\bar{K}^0$	0.17 ± 0.04
$\bar{u}s$	K^-	K^-	0.696 ± 0.023
	K^{*-}	$K^-\pi^0$	0.429 ± 0.015
	K^{*-}	K^-K^0	0.84 ± 0.04
	K_1^-	$K^-\pi^+\pi^-$	0.287 ± 0.016
	K_1^-	$K^-\pi^0\pi^0$	0.065 ± 0.023
	K_1^-	$\pi^-K^0\pi^0$	0.40 ± 0.04
		$K^-K^+K^-$	$(1.58 \pm 0.15) \times 10^{-3}$
		$K^-K^0\bar{K}^0$	

leptonic decays, there is only one decay mode for each of the possible lepton pairs. In hadronic decays, the $\bar{u}d$ or $\bar{u}s$ quarks undergo strong interactions in which additional $\bar{u}u$, $d\bar{d}$, or $\bar{s}s$ quark pairs may be created. The net result of this process is the production of some number of mesons, predominantly π and K, both charged and neutral.

In 35.2% of the time τ lepton decays leptonically and in 64.8% of the time into one or more hadrons. Considering only hadronically decaying τ leptons, decays with only one charged particle (so called *1-prong*) occur in

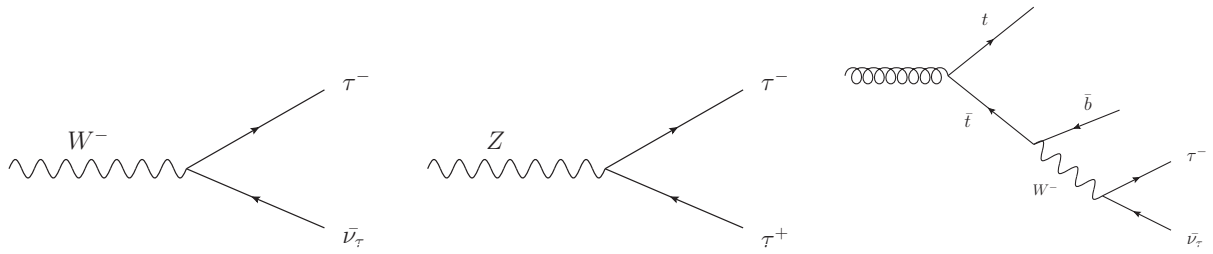

(a) (b) (c)

Figure 2.2: Important Standard Model processes with τ leptons in the final state: W and Z boson production and top quark decays.

about 72% of the time and with three charged particles (so called *3-prong*) in about 23% of the time. The 5-prong decay has only a fraction of about 0.1%. The hadronic final states are dominated by $\pi^\pm$ and π^0 mesons, but there is also a small fraction of decays containing $K^\pm$ and K^0 mesons. As can be seen in Table 2.1, these are dominated by resonance production.

Leptonic decay modes are well described theoretically. Measurements of leptonic branching ratios of τ decays and of the lifetime enable precise tests of lepton universality, the fundamental assumption of the Standard Model.

Due to the short-enough lifetime of τ leptons and their parity-violating decays, τ leptons are the only leptons whose spin information is preserved in kinematics of its decay products recorded by the detector. Especially the hadronic decay to one charged pion and neutrino final state is sensitive to the spin orientation of the parent τ lepton.

2.2 Standard Model processes with τ final states

The measurement of SM processes was the crucial step in the ATLAS physics program. τ leptons play an important role in such studies. Decays of Standard Model gauge bosons to τ leptons, $W \to \tau\nu$ and $Z \to \tau\tau$, are essential to calibrate τ energy and measure τ lepton detection performance. They are important in the search for New Physics phenomena as they are dominant background processes in such searches. Thus, their production cross sections need to be measured precisely. Studies of $W \to \tau\nu$ and $Z \to \tau\tau$ processes at the LHC centre-of-mass energies are also interesting in their own right, complementing the measurements of the production of the Z boson through its electron and muon decay modes.

The main source of τ leptons at the LHC is $W \to \tau\nu$ decay (Figure 2.2(a)) with a cross section times branching ratio of $\sigma \times \mathrm{BR} = 10.46 \pm 0.52$ nb [47, 48, 49] at the centre-of-mass energy $\sqrt{s} = 7$ TeV. Having one τ lepton and a neutrino in the final state, this process requires a good τ identification and missing energy reconstruction due to the escaping neutrino. This decay channel can be used to measure the leptonic branching ratio of the W boson and the cross section of W production. In addition, $W \to \tau\nu$ decays can be used to validate the reconstruction and identification techniques for τ leptons and the measurement of the missing transverse energy, which are both fundamental physics objects in a wide spectrum of measurements at the LHC.

The $Z \to \tau\tau$ decay (Figure 2.2(b)) has a cross section of an order of magnitude lower than $W \to \tau\nu$, but it has two τ leptons in the final state, with an invariant mass near the Z pole. It provides more robust prospects for analysis. It is called the *golden channel* for the detection of τ leptons, since one τ can be used to identify the event, while the other can probe the performance. This channel can be used to understand the efficiency of τ identification and τ trigger as well as reconstruction methods for visible [2] and invariant masses of both τ leptons. In addition, because the visible mass distribution of the τ_{lep}-τ_{had} final state is sensitive to the energy scale of the reconstructed τ candidates, a measurement of the τ lepton energy scale can be made with this sample. Additionally, the $\tau\tau$ invariant mass is sensitive to $E_{\mathrm{T}}^{\mathrm{miss}}$, hence $E_{\mathrm{T}}^{\mathrm{miss}}$ reconstruction properties can be studied with this sample and a measurement of the $E_{\mathrm{T}}^{\mathrm{miss}}$ scale can be made. The measurement of the $Z \to \tau\tau$ cross section can provide also a test

[2] The invariant mass of visible τ decay products.

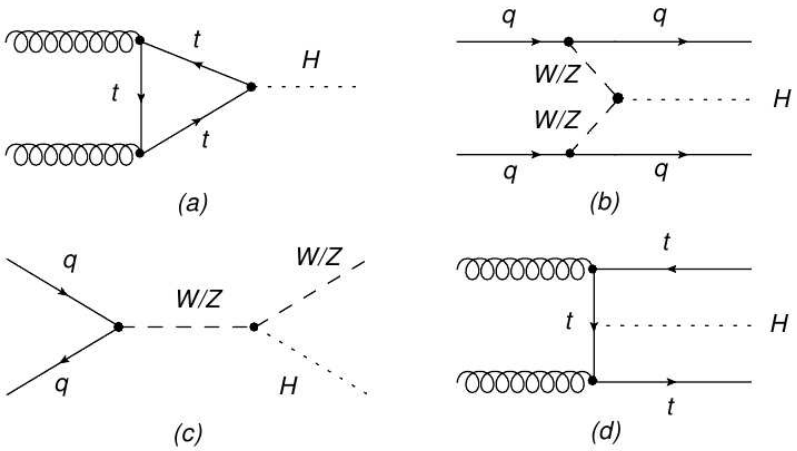

Figure 2.3: Relevant Standard Model Higgs boson production processes in leading order. (a) gluon fusion, (b) vector boson fusion, (c) W/Z associated and (d) $t\bar{t}$ associated production.

of universality, when compared to the $Z \to ee$ and $Z \to \mu\mu$ counterparts. Finally τ polarisation in $W \to \tau\nu$ and $Z \to \tau\tau$ decays can be measured. This has not been done previously at hadron colliders.

At the LHC, top quark pairs ($t\bar{t}$) are produced in abundance due to the high centre-of-mass energy. In that case one or both W bosons from top quark decays can decay further to τ leptons (Fig. 2.2(c)). This process has more jets in the event, coming from hadronic W boson decays and b-quarks and gives a different environment compared to $W \to \tau\nu$ and $Z \to \tau\tau$. It leads also to a more complex and difficult reconstruction. This final state can provide an important alternative measurement of the top quark pair production cross section. It can be also further used as an input in searches of the possible charged Higgs production via top quark decays.

2.3 Standard Model Higgs boson searches with τ final states

Discovering the mechanism responsible for electroweak symmetry breaking and the origin of mass for elementary particles is one of the fundamental tasks of the LHC. In the Standard Model, this mechanism requires existence of one scalar particle, the Higgs boson. Direct experimental searches provided only limits on its mass. Indirect limits on the Higgs boson mass of $m_H < 185$ GeV at 95% confidence level were set using global fits to electroweak precision data [50]. The experiments at LEP placed the limit at $m_H > 114.4$ GeV [51] and the Tevatron, excluded the range of 156-177 GeV [52]. During completion of this monograph, both ATLAS and CMS collaborations claimed observation of a new boson with mass ~(125-126) GeV [53, 54]. More details and consequences of this observation for the Higgs boson searches with τ lepton final states are given in Summary of Chapter 6.

At the LHC the dominant Higgs production mechanism is the fusion of two gluons via a heavy-quark loop, as shown in Figure 2.3 (a). Detection of the Higgs boson produced via gluon fusion, however, is challenging, because there are large background contributions from QCD multijet production which are hard to suppress if no other striking signal signatures are present. Only Higgs boson decays to two or more leptons (such as in $H \to ZZ$ or $H \to WW$) or the Higgs decay to two photons will provide sufficient discrimination against backgrounds.

The second largest contribution comes from the fusion of vector bosons radiated from the initial state quarks (VBF) as shown in Figure 2.3 (b). This process leaves a special signature in the detector. The quarks hadronise to jets which will be detected in the forward region of the detector (close to the beam pipe). There is no colour connection between the two quarks, hence between the two forward jets, and so little hadronic activity is expected in the signal process. This typical VBF signature is used to suppress QCD multijet background.

The third contribution comes from associated production WH, ZH as shown in Figure 2.3 (c). In this process, the Higgs boson is radiated off a weak vector boson (Higgsstrahlung). This process is important in the intermediate mass range $m_H < 2m_Z$, but its cross section falls rapidly with an increasing value of m_H.

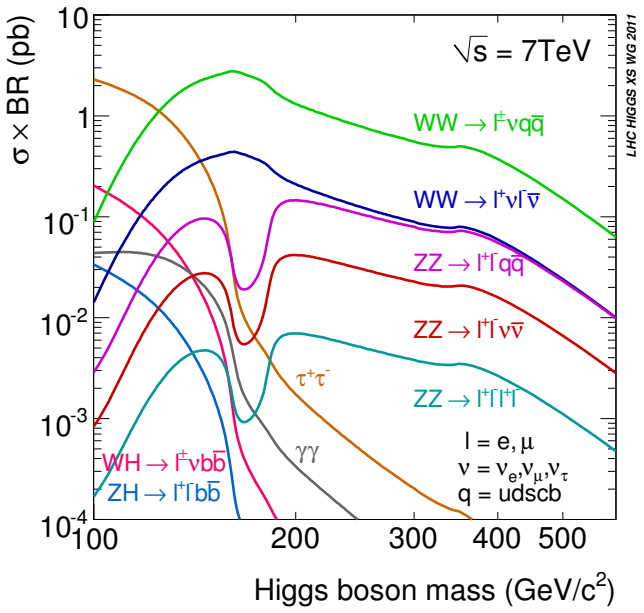

Figure 2.4: The SM Higgs boson production cross sections multiplied by decay branching ratios in pp collisions at $\sqrt{s} = 7$ TeV as a function of Higgs boson mass [55].

The smallest contribution comes from associated production $t\bar{t}H$ presented in Figure 2.3 (d). It is less important because the cross section is about five times smaller than the one for WH or ZH for $m_H < 200$ GeV.

The branching ratios and cross sections of the Higgs boson production and decay channels are fixed by theory as soon as the Higgs boson mass is known. The presented Higgs boson decay branching ratios take into account the recently calculated higher-order QCD and electroweak (EW) corrections in each Higgs boson decay mode [55]. The total SM Higgs boson signal production cross section multiplied by the branching ratio for the final states analysed currently by the LHC experiments is shown in Figure 2.4. As can be seen, decay of the Higgs into a pair of τ leptons is an important channel for $m_H < 140$ GeV. It suffers from high background mainly from $Z \to \tau\tau$ decays but the sensitivity can be enhanced by requiring that the Higgs boson is produced in association with jets. The Higgs boson can be produced in association with jets, at the next-to-leading order (NLO) in the gluon fusion process and at the leading order in the vector boson fusion process. The presence of jets allows topological selections which enhance the signal-to-background ratio. In this configuration, the Higgs boson can acquire a boost in the transverse plane, enhancing the missing transverse energy in the event (due to the undetected neutrinos from τ decays) which allows for a better discrimination of the signal against some of the background processes [56, 57, 58, 59]. Also, the measurement of the $H \to \tau\tau$ decay rate is a test of the SM prediction for the τ Yukawa coupling. This decay mode also offers a unique opportunity to study CP violation in the Higgs sector. Higgs CP properties can be studied in hadronic decays of τ leptons.

2.4 MSSM Higgs bosons searches with τ final states

The Minimal Supersymmetric Standard Model (MSSM) [60, 61, 62, 63, 64] is the minimal extension to the Standard Model that realises supersymmetry. It is minimal in the sense that it contains the smallest number of new particle states and new interactions consistent with phenomenology.

Two complex Higgs doublets are required in the MSSM - one to generate masses for "up-type" particles, and the other to generate masses for "down-type" particles. Each Higgs field has a vacuum expectation value, and the ratio of these is denoted as $\tan\beta$ (in SM $\tan\beta = 1$). Of the eight degrees of freedom provided by the two doublets, three are absorbed by the longitudinal degrees of freedom of EW bosons. Five physical Higgs bosons

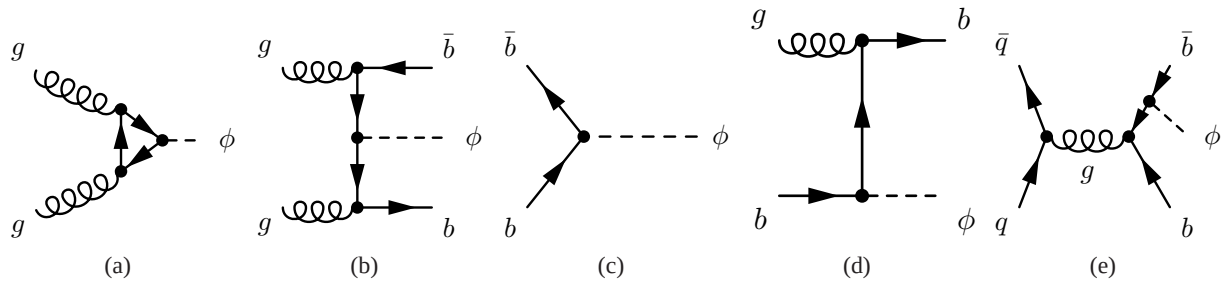

Figure 2.5: Feynman diagrams contributing to the MSSM Higgs boson production. Diagram a) is called 'direct production', diagrams b) to e) contribute to the b quark associated production. In the above diagrams ϕ represents either of the neutral Higgs bosons in the MSSM, h, H, or A.

remain: $H^{\pm}$, h (neutral lighter scalar), H (neutral heavier scalar) and A (neutral pseudoscalar). The h and H neutral Higgs bosons are CP-even, while the A-boson is CP-odd. At the tree level, the Higgs sector of the MSSM can be completely described in terms of mass of the neutral pseudoscalar, m_A, and tanβ. For the $H^{\pm}$ studies, those are usually chosen to be the charged Higgs boson mass and tanβ. Higher order corrections introduce dependence on another 105 SUSY parameters. Making some general assumptions can reduce this somewhat, as it would be unfeasible to consider all possible scenarios. Instead, various benchmark models have been defined [65]. The model used in analyses described in this monograph is the *maximal mixing* scenario, m_h^{max}. The m_h^{max} scenario is designed to give the largest possible mass of the lightest neutral Higgs boson (h), in order to provide the best agreement with the limits from LEP experiments [51]. In this scenario the upper bound on the mass of the light Higgs boson h is expected to be around 135 GeV. While the light neutral Higgs boson may be difficult to distinguish from its Standard Model counterpart, the other heavier Higgs bosons are a distinctive signal of physics beyond the Standard Model. In the m_h^{max} scenario the h and A boson states are almost degenerate in mass for $m_A \leq 130$ GeV, the H and the A are approximately degenerate in mass if $m_A \geq 130$ GeV. The remaining mass difference depends on tanβ and becomes smaller with increasing tanβ. At $m_A \sim 130$ GeV, in the intense coupling region, all three neutral Higgs bosons come close in mass and their separation would be very difficult.

Production of neutral Higgs bosons and their decays are different from those in the Standard Model. While decays into ZZ or WW are dominant in the Standard Model for Higgs boson masses above $m_H > 2m_W$, for high values of tanβ these decay modes are either suppressed in case of the h and H or even absent in the case of the A bosons. At lower values of tanβ, the production of neutral Higgs bosons proceeds dominantly via gluon-fusion as presented in Figure 2.5(a). Its rates are significantly larger than for the Standard Model and for the range of higher tanβ it is still dominant for low m_A. As tanβ increases, production in association with b-jets (Figure 2.5(b)-2.5(e)) gains importance, and (0-2) b-jets can be observed in the final state. For very large values of m_A (depending on tanβ) the cross section of the lightest CP even boson h becomes larger than the cross section for H and A. This is also called the decoupling region. In fact, if a small value of tanβ is realised in nature, the h will be the only visible MSSM Higgs over a large range of m_A. It will then be indistinguishable from the SM Higgs boson.

The coupling of the Higgs bosons to third generation fermions is strongly enhanced for large regions of the MSSM parameter space. The dominant decay mode is to $b\bar{b}$ pairs, accounting for approximately 90% of all decays (high tanβ region). As with SM Higgs searches, large QCD backgrounds associated with this final state make the analysis difficult, despite the enhanced production cross section (with respect to a SM Higgs). Approximately 10% of all MSSM Higgs boson decays are to $\tau\tau$ pairs. In the SM the $H \to \tau\tau$ mode is only relevant for a light Higgs boson masses but in the MSSM this channel is relevant in the whole allowed mass region up to 1 TeV. Previous results excluding some regions of parameters space come from LEP [66] and Tevatron [67, 68].

The search strategies for charged Higgs bosons depend on the charged Higgs boson mass, which dictates both the production and the available decay modes. Below the top quark mass, the main production mode is through top quark decays, $t \to H^+ b$. The dominant source of top quarks at the LHC is through $t\bar{t}$ production. The cross section for charged Higgs boson production from top quark decays in single-top events is much smaller. For tan$\beta > 3$,

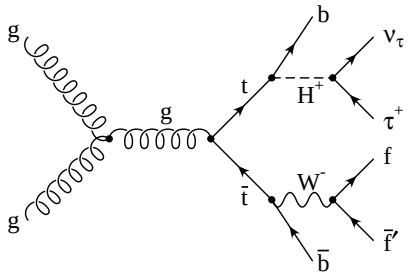

Figure 2.6: Example for a leading-order Feynman diagram for the production of a charged Higgs boson through gluon fusion in $t\bar{t}$ decays.

charged Higgs bosons decay mainly via $H^+ \to \tau\nu$ [55]. Figure 2.6 presents a leading-order Feynman diagram for the production of a charged Higgs boson through the gluon fusion in $t\bar{t}$ decays.

Above the top quark threshold, the production mainly takes place through gb fusion ($g\bar{b} \to \bar{t}H^+$). For such high charged Higgs boson masses, the decay into a top and a b quark dominates, $H^+ \to t\bar{b}$, but $H^+ \to \tau\nu$ can still be sizable and offers a much cleaner signature.

Direct searches at LEP [69] give a lower limit of $m_{H^+} \sim 90$ GeV for BR($H^+ \to \tau\nu$)=1. At the Tevatron, no evidence for charged Higgs boson production has been found. Hence, the Tevatron experiments placed upper limits on BR($t \to H^+b$) assuming BR($H^+ \to \tau\nu$) = 1 in the 15-20% range [70, 71].

2.5 Searching for New Physics with τ final states

τ leptons often appear in final states of various supersymmetric scenarios. According to the electroweak symmetry breaking, a left and right handed sfermion mixing appears in the SUSY breaking, which results in a mixture of left and right handed components in the mass eigenstates. In certain SUSY models, large mixing between left and right sfermions, the partners of the left-handed and right-handed SM fermions, implies that the lightest sfermions belong to the third generation. This leads to a large production rate of τ leptons from decays of $\tilde{\tau}$ sleptons and gauginos, the partners of the SM gauge bosons, in SUSY cascade decays. For example, in the context of Gauge Mediated SUSY Breaking (GMSB) [72, 73, 74, 75, 76, 77] scenario, the lighter of the two $\tilde{\tau}$ sleptons is the next-to-lightest supersymmetric particle (NLSP) for a large part of the parameter space, and the very light gravitino, $\tilde{G}$, is the LSP. Hence $\tilde{\tau}$ sleptons decay to a τ lepton and a gravitino.

Previous experiments at LEP [78, 79, 80] have placed constraints on $\tilde{\tau}$ and $\tilde{e}$ masses and on more generic GMSB signatures. Among these, the limits from the OPAL experiment [78] were the most stringent, excluding $\tilde{\tau}$ NLSPs with masses below 87.4 GeV. The D0 Collaboration performed a search for squark production in events with hadronically decaying τ leptons, jets, and missing transverse momentum [81], and the CMS Collaboration performed searches for New Physics in same-sign di-τ events [82] and multi-lepton events [83] including τ pairs, but the GMSB model was not specifically considered in any of these results.

While writing this monograph, the ATLAS collaboration published recent results on searches for SUSY in events with large missing transverse momentum, jets, and at least one hadronically decaying τ lepton, with zero or one additional electron or muon [84]. The studies have been performed using 4.7 fb^{-1} of pp collision data at $\sqrt{s}$ = 7 TeV. No excess above the SM background expectation is observed and a 95% confidence level (CL) limit for new phenomena is set. In the framework of GMSB model, exclusion limits on the GMSB breaking scale λ are set at 47 TeV, independently of tanβ. These limits provide the most stringent tests to date of GMSB SUSY breaking models in a large part of the parameter space considered.

Looking for τ pairs in final states is also valuable for a search for high mass resonances. Heavy gauge bosons (Z', W') are predicted in various models [85, 86, 87, 88, 89, 90]. In particular, models with extended weak or hypercharge gauge groups, predict that such bosons preferentially couple to the third generation fermions. Direct searches for the τ pair final state have been performed previously by the CDF [91] and CMS [92] collaborations. The latter sets the most stringent 95% CL limits and excludes Z' masses below 468 GeV using 36 pb^{-1} integrated

luminosity. Precision electroweak measurements at LEP [93] indirectly exclude Z' masses below 1090 GeV.

Recently, new results on the search for high-mass resonances decaying into τ leptons pairs in the ATLAS experiment were published [94]. Z' bosons of the Sequential Standard Model [95] with masses less than 1.3 TeV are excluded at 95% CL.

An experiment is a question which science poses to Nature
and a measurement is the recording of Nature's answer.

Max Planck

3

The ATLAS detector at the Large Hadron Collider

The Large Hadron Collider (LHC) at CERN [1] is actually the largest and highest energy particle accelerator in the world. It provides collisions of particles allowing to recreate, on a microscale, the state that existed a fraction of nanosecond after the Big Bang. Under these extreme conditions, never reached before in a laboratory, new particles may be produced and measured in the detectors providing signs of New Physics. The ATLAS experiment is one of the four main experiments at the LHC. This Chapter describes briefly details of the ATLAS detector, luminosity measurement as well as particle reconstruction and identification crucial for the analyses with τ leptons in final states. Also the data quality and preselection of events for early data analyses are presented.

3.1 The Large Hadron Collider

The LHC is the largest and most energetic particle collider in the world. It is a hadron collider which produces proton-proton collisions most of the time. Besides proton-proton collisions, lead ions are collided during a short period of the year, using the same accelerator infrastructure.

The proton beams were successfully circulated at the LHC for the first time in September 2008. Due to a serious electrical fault between two magnets resulting in a large helium leak into the tunnel, the operations were interrupted shortly after its opening and restarted in November 2009 at the injection energy of 450 GeV per beam. The first collision at the centre-of-mass energy of $\sqrt{s} = 7$ TeV took place at the end of March 2010 with luminosity 2×10^{27} cm^{-2} s^{-1}. In 2011 the luminosity reached 3.65×10^{33} cm^{-2} s^{-1}. An integrated luminosity of 45 pb^{-1} has been delivered by autumn 2010 and of 5.25 fb^{-1} until autumn 2011 as shown in Figure 3.1.

In 2012 the LHC has been running with a higher collision energy of 4 TeV per beam in order to enhance the machine's discovery potential and open up further possibilities in the searches for New Physics. At the end of 2012, the LHC will shut down for maintenance for up to two years and then will attempt to reach the design energy of 14 TeV.

To investigate particle collisions at the LHC, several detectors were built: ATLAS and CMS [96] as detectors for multi-purpose physics analyses, ALICE [97] for heavy ion collisions, LHCb [98] to investigate CP-violation and properties of the bottom quark and LHCf [99] and TOTEM [100] to study particle productions, elastic scatterings and total cross sections of pp collisions.

[1] Conseil Européen pour la Recherche Nucléaire, European Organization for Nuclear Research.

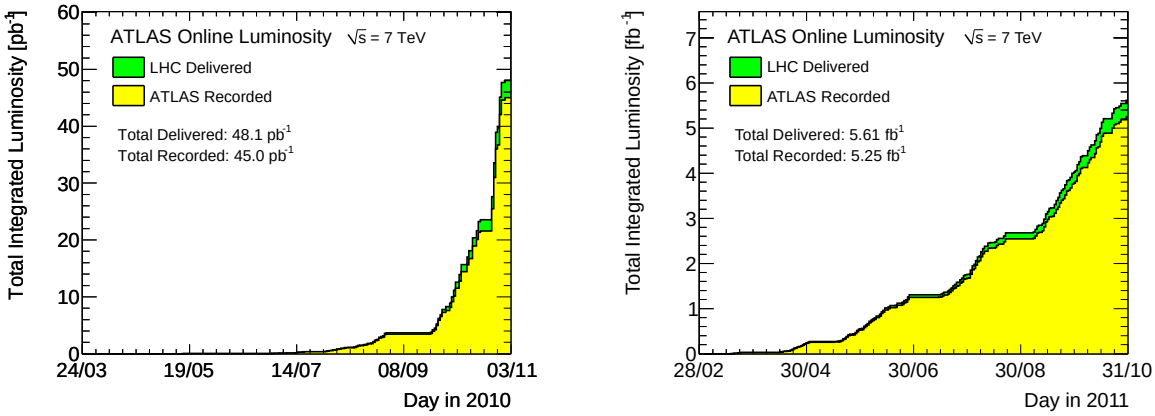

(a) (b)

Figure 3.1: Cumulative luminosity versus day delivered to (green), and recorded by ATLAS (yellow) during stable beams and for pp collisions at 7 TeV centre-of-mass energy in 2010 (a) and 2011 (b) [101].

3.2 The ATLAS detector

ATLAS (A Toroidal Lhc ApparatuS) is one of the two multi-purpose detectors operating at the LHC, designed to identify the broadest range of particles and measure their properties. It is 44 m long, with a diameter of 25 m, and it weighs 7000 tonnes. The goal of ATLAS is to cover the largest possible range of physics, such as searches for new heavy bosons (in particular the Higgs boson), supersymmetric particles or any other phenomena indicating New Physics at energies up to a few TeV. Masses of new particles are, in general, unconstrained by theory and their branching fractions into different final states depend on their masses. The detector has to be, therefore, sensitive to a large number of possible decay channels. It needs to be capable of measuring four-momentum and position of particles with high resolution and provide an excellent particle identification. Due to the very high interaction rate, the detectors require fast and radiation-hard electronics.

Since the QCD multijet production dominates by many orders of magnitude over the production of new particles, ATLAS has to identify efficiently experimental features characteristic to the rare processes. Also, a highly efficient trigger system is needed to allow for the detection of processes even with very small cross sections providing strong background rejection at the high event rate of the LHC. A typical signature of many New Physics processes is the presence of non-interacting particles, such as the Standard Model (SM) [102, 103, 104] neutrinos or supersymmetric neutralinos. Their observation is possible through detection of the momentum imbalance in the transverse plane often referred to as the missing transverse energy, $E_{\mathrm{T}}^{\mathrm{miss}}$. For the reconstruction of $E_{\mathrm{T}}^{\mathrm{miss}}$ it is important that the ATLAS calorimeter system has a coverage as close to 4π as possible. Many New Physics events, such as Higgs boson production and decay, are characterised by the presence of b quarks in the final state. The ATLAS detector was therefore designed to allow for a precise reconstruction of secondary vertices which are of great importance in identification of b-jets.

To accomplish its tasks, ATLAS consists of several layers of sub-detectors – from the interaction point outwards, the Inner Detector tracking system, the electromagnetic and hadronic calorimeters, and the muon system. The ATLAS detector is forward-backward symmetric around the interaction point. It is composed of a central barrel part and two end-caps. A scheme of the detector and of its sub-systems is shown in Figure 3.2.

Coordinate system The nominal interaction point is defined as the origin of the coordinate system, while the counterclockwise beam direction defines the z-axis and the x-y plane is transverse to the beam direction. The positive x-axis is defined as pointing from the interaction point to the centre of the LHC ring and the positive y-axis is defined as pointing upwards. The azimuthal angle ϕ is measured around the beam axis and the polar angle θ is the angle from the beam axis. The pseudorapidity is defined as $\eta = -\ln\tan(\theta/2)$. The transverse momentum p_{T},

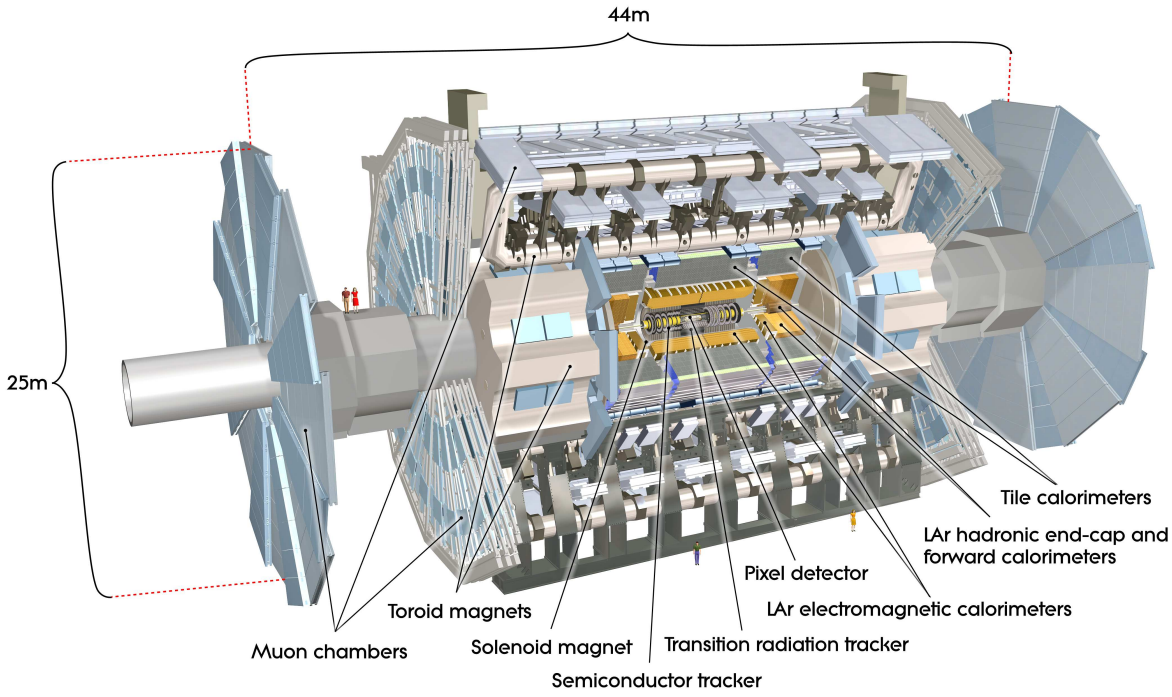

Figure 3.2: The ATLAS detector [45].

the transverse energy E_{T}, and the transverse missing energy $E_{\mathrm{T}}^{\mathrm{miss}}$ are defined in the x-y plane. The distance ΔR in the $\eta - \phi$ space is defined as $\Delta R = \sqrt{(\Delta\eta)^2 + (\Delta\phi)^2}$.

3.2.1 Inner Detector

The Inner Detector (ID) provides high-precision tracking information for charged particles allowing for reconstruction of tracks and vertices in the event. This information consists of very efficient and accurate position measurements of particles along their trajectories thus allowing the momentum and charge sign determination and consequently contributing to their identification. The ID is exposed to a high density particle flux because of its position closest to the beam line and the interaction point. Thus, a high granularity and a fast readout system is required.

The Inner Detector is immersed in a 2 T magnetic field generated by the central solenoid. It consists of three sub-systems, the pixel detector, the SemiConductor Tracker (SCT) and the Transition Radiation Tracker (TRT). The first two subsystems cover a region of $|\eta| < 2.5$ in pseudorapidity, while the TRT reaches up to pseudorapidity $|\eta| = 2.0$. An outline of the ID is shown in Figure 3.3. A track in the ID central region typically produces 11 hits in the pixel and SCT detectors and 36 hits in the TRT detector.

The innermost component of the ID is a silicon pixel detector with a high degree of segmentation. This is necessary to cope with the high track density and to reconstruct primary and secondary vertices. The use of silicon pixel allows also to measure the z coordinate of tracks with sufficient precision to discriminate between tracks from the primary interaction and tracks from additional pile-up interactions. The pixels are arranged in three layers with the design requirement to achieve a resolution of 10 μm in the Rϕ direction and 115 μm in the beam direction. The innermost layer, called B-layer, provides the critical vertexing information used to reconstruct the displaced vertices of short-lived particles.

The next part of the tracking system is the SCT. The reduced charged particle density and radiation level in that region allow for the use of silicon strips which have a coarser overall granularity while still providing an excellent measurement accuracy in the Rϕ direction. The use of silicon strips rather than pixels allowed to cover a

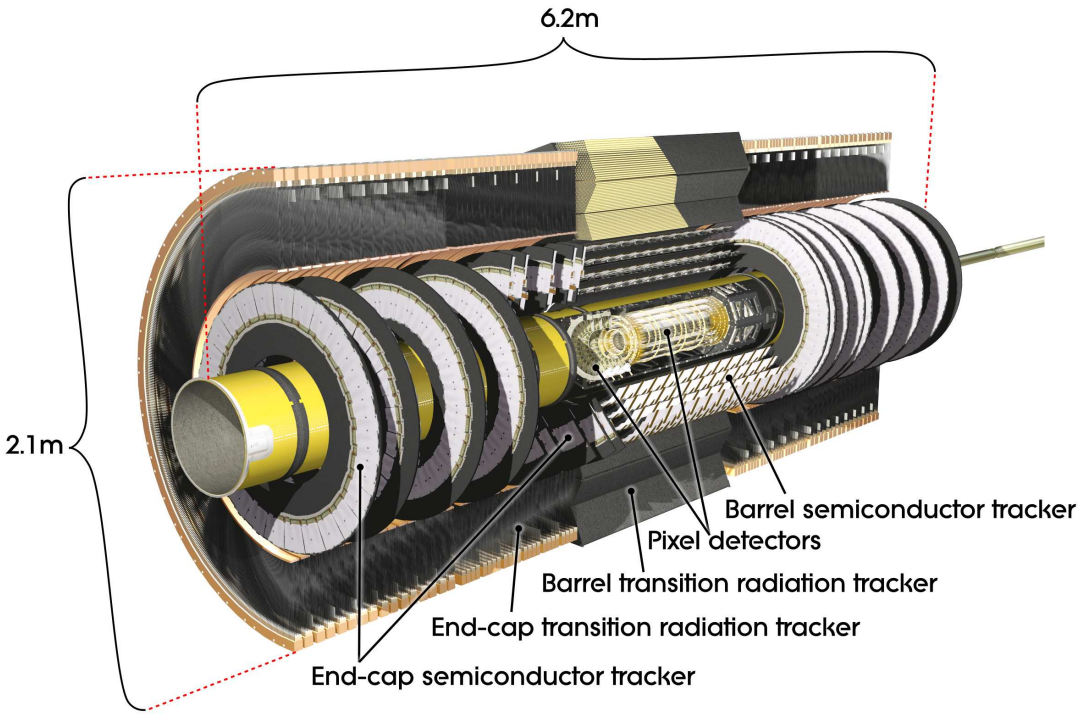

Figure 3.3: Overview of the ATLAS Inner Detector [45].

large area at a reasonable cost. In the barrel, the strip detectors are arranged in four layers at different radii. Each layer is composed of two stereo layers oriented at an angle of 40 mrad relative to each other, which provides a 3-dimensional position measurement. The system contributes to momentum, impact parameter and vertex position measurements, as well as provides good pattern recognition thanks to high granularity. The spatial resolution is 17 μm in Rϕ and 580 μm along the beam direction.

At larger radii the surface area of the detector becomes larger, which would lead to high costs for a silicon detector. Therefore, a Transition Radiation Tracker is installed there. It consists of 4 mm diameter drift tubes (straws). In the barrel part the straws are arranged parallel to the beam axis, while in the end-caps a radial arrangement is used. The TRT contributes only with information from the Rϕ plane with resolution of 130 μm per straw. The TRT provides a quasi-continuous tracking with over 30 space-point measurements per track. This leads to an improvement of the momentum resolution at small pseudorapidities, $|\eta| < 2.0$.

The TRT is not only designed for tracking measurements, but also for simple particle identification. The transition radiation, which occurs when a charged particle with a high velocity crosses a boundary between two media with different dielectric constants, is also used to discriminate between electrons and pions. There are two independent thresholds to distinguish between tracking hits and transition radiation (TR) hits. The tracking hits pass the lower threshold while the TR hits pass the higher one.

3.2.2 Calorimeters

The calorimeter system consists of several components designed to meet the requirements of measuring electrons, photons and jets with high efficiency as well as excellent spatial and energy resolutions. Figure 3.4 gives an overview of the ATLAS calorimeter system.

All ATLAS calorimeters are sampling calorimeters providing full solid angle coverage up to $|\eta| < 4.9$. The granularity of the calorimeters varies from a fine grained structure at the region which overlaps with the ID, and a coarser structure at the rest. Due to high homogeneity and a wide range of acceptance, the calorimeters allow to reconstruct the missing transverse energy. The smallest units of the calorimeters with a proper signal readout are

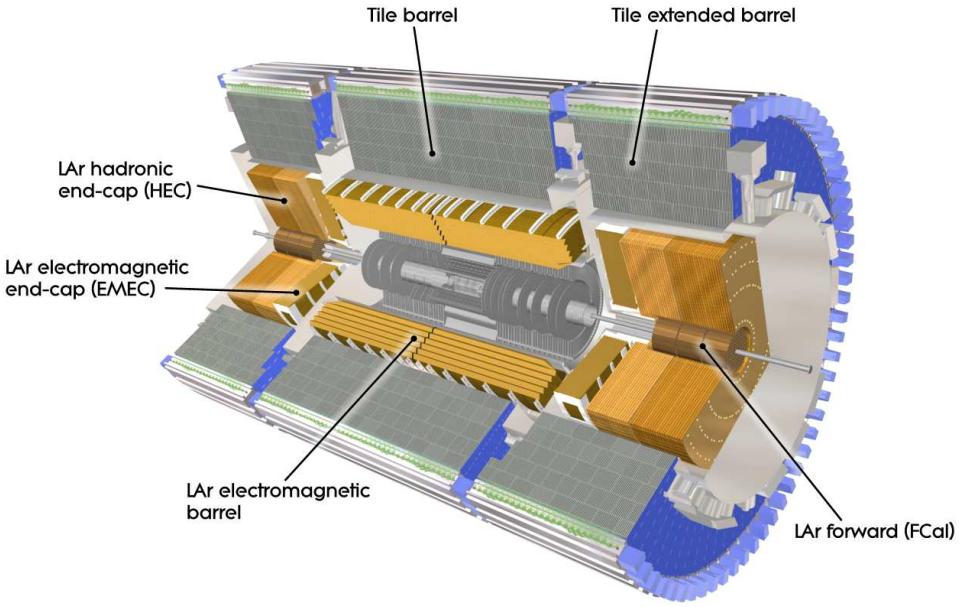

Figure 3.4: Overview of the ATLAS calorimeter system [45].

called cells.

Electromagnetic Calorimeter The innermost layer is the electromagnetic (EM) calorimeter consisting of a barrel part reaching up to $|\eta| < 1.475$ and two end-caps (EMEC) up to $|\eta| < 3.2$. These calorimeters use liquid argon (LAr) as active medium as it offers stable response over time and good radiation hardness. The use of LAr forces the operation at low temperatures, and therefore the calorimeter is immersed inside a cryostat. The absorber material are lead plates in accordion shape which allows for fast signal and uniform response. The EM calorimeter is longitudinally divided into three segments as shown in Figure 3.5. The first layer is highly segmented in η with strip-shaped read-out cells. It provides spatial resolution high enough to disentangle two nearby photon showers from $\pi^0 \to \gamma\gamma$ decays. In the η direction, eight strips of the first layer correspond to one read-out cell in the second layer. The second layer is segmented into squared cells extending the segmentation in the ϕ direction. Here the main part of the electromagnetic shower is measured. The third layer collects the tail of the deposited energy and has a coarser segmentation in η. The electromagnetic calorimeter is completed with the presampler, a 11 mm thick LAr calorimeter, which is mounted in front of the first layer. This detector provides first energy sampling in order to estimate the energy loss by electrons and photons in the material in front of the calorimeter. The transition region between the barrel and the end-cap EM calorimeters, $1.37 < |\eta| < 1.52$, is expected to have poorer performance because of more passive material in the front of the calorimeters. The total thickness in terms of radiation lengths, X_0, in the barrel is at least 24 and at least 26 in the end-caps.

The electromagnetic calorimeter is complemented by two forward electromagnetic calorimeters in the region up to $|\eta| < 4.9$ using copper as an absorber.

Hadronic Calorimeter The EM calorimeters are surrounded by hadronic calorimeters measuring strongly interacting particles forming jets. The hadronic calorimeters consist of a barrel Tile Calorimeter ($|\eta| < 1.0$), two extended barrel Tile Calorimeters ($0.8 < |\eta| < 1.7$), two hadronic end-cap calorimeters ($1.5 < |\eta| < 3.2$) and the forward hadron calorimeters ($3.2 < |\eta| < 4.8$).

The Tile Calorimeter (TileCal) is the high precision hadronic calorimeter with the absorber made of steel, and scintillating tiles used as the active material. The TileCal including all the previous systems and support structures, corresponds at $\eta = 0$ to 9.7 interaction lengths, λ_{int}.

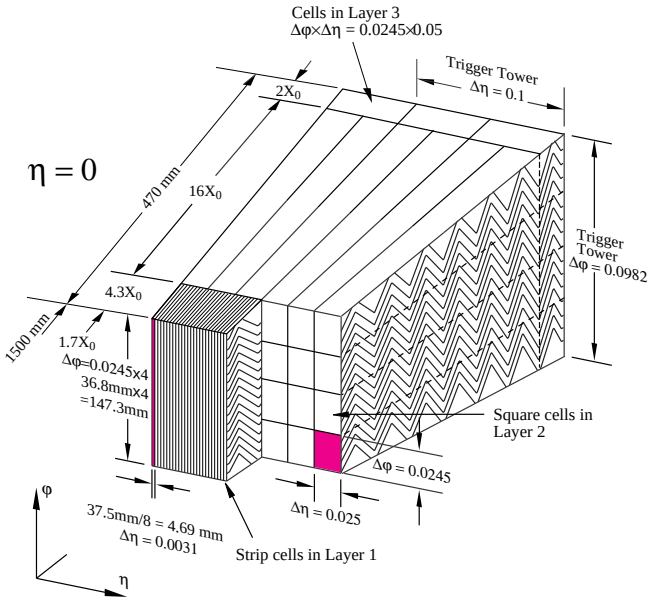

Figure 3.5: Drawing of a barrel module of the EM calorimeter, with the accordion shaped absorber plates and electrodes, consisting of three longitudinal segments with different cell sizes in η and ϕ [45].

The end-cap calorimeters consists of the Hadronic End-Cap Calorimeter (HEC) and a high-density Forward Calorimeter (FCal). Due to the high radiation density in the end-cap and forward region a radiation-hard material is used. The HEC calorimeters use liquid argon as active material. Copper is used as an absorber in the HEC and in the first part of the FCal, while tungsten in the second and third part of FCal.

A total of at least 10 interaction lengths is provided by the EM and hadronic calorimeters together. It allows for a good energy resolution of highly energetic jets and minimises punch-through of particles to the muon spectrometer. The large η coverage of the calorimeters ensures a good missing transverse energy measurement, which is important for many physics studies, such as those involving τ leptons and supersymmetric particles.

3.2.3 Muon spectrometer

The muon spectrometer is the outermost detector system designed for the high precision measurement and identification of muons with transverse momenta above 3 GeV which is the mean energy loss of muons in the calorimeters. It covers pseudorapidity range of $|\eta| < 2.7$. The muon spectrometer has its own magnetic field, allowing measurements of the muon momentum independently of the ID. It is provided by a superconducting air-core toroid magnet system which minimises multiple-scattering of the muons. The muon spectrometer uses four different chamber systems: Monitored Drift Tubes (MDT) and Cathode Strip Chambers (CSC) designed for measurements of track coordinates, Resistive Plate Chambers (RPC) and Thin Gap Chambers (TGC) having fast drift times and used for triggering. A view of the muon spectrometer is shown in Figure 3.6.

The MDT and the CSC detectors are both designed to provide precise measurement of the muon track segments and thus the sagitta. The MDT are aluminium tubes of 30 mm diameter, (70 - 630) cm length and filled with an Ar(93%)CO2 (7%) gas mixture with gold-plated tungsten-rhenium anode wires in the tube centres. The average spatial resolution of a drift tube is 80 μm. The track position resolution of the MDT chambers is 35 μm. The CSC are used as precision muon tracking chambers in the innermost layer of the very forward region ($2.0 < |\eta| < 2.7$). They are multi-wire proportional chambers with strip-segmented cathodes having a shorter response time than the MDT chambers to cope with the high background rates in this detector region. The average spatial resolution of a CSC chamber in the bending plane is 60 μm.

The RPC and TGC detectors form the muon trigger system. The trigger requires a good resolution not only in space but also in time to keep the latency time small. Both systems also contribute to the muon track measurement.

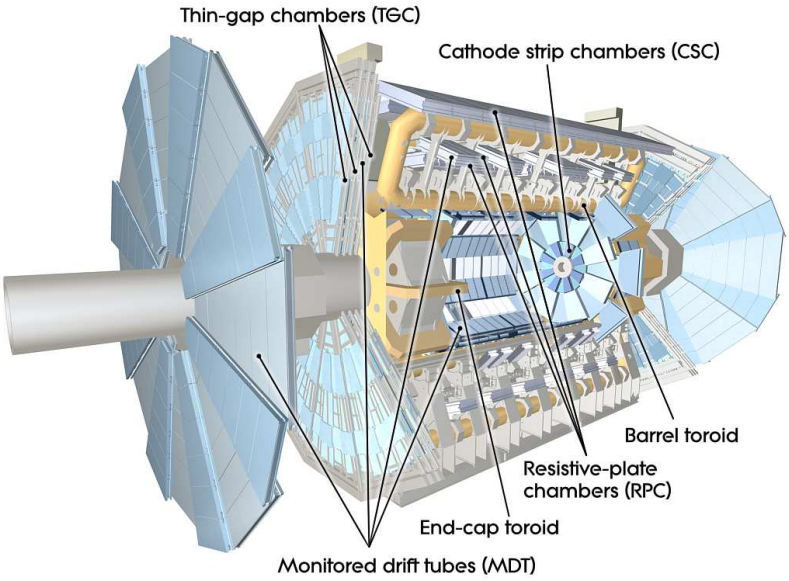

Figure 3.6: Overview of the ATLAS muon system [45].

The RPC chambers are located on both sides of the MDT middle layer in the barrel. The basic RPC unit is a narrow gas gap formed by two parallel resistive plates, separated by insulating spacers made of polycarbonate. The primary ionisation electrons are multiplied into avalanches by a high voltage field. The TGC are used as trigger detectors in the end-cap region ($1.5 < |\eta| < 2.7$). They are multi-wire proportional chambers providing a high spatial resolution and a good time resolution with a strongly quenching gas mixture. The RPC and TGC trigger chambers provide bunch crossing identification and measure the coordinate along the drift tubes of the MDT chambers.

The muon spectrometer provides stand-alone muon momentum measurement. A combination with measurements of the ID and the calorimeters improves the efficiency and resolution, especially for low p_{T} muons.

3.2.4 Trigger

To handle the high interaction rates at the LHC (up to 1 GHz at the design luminosity), an efficient trigger system is essential. To store interesting physics events the rate must be reduced to $\sim$ 400 Hz, leading to trigger only on New Physics and important Standard Model processes.

The ATLAS detector has a three-level trigger system. Each trigger level depends on decisions made by the previous stage and requires additional criteria, if necessary. The first part of the trigger chain is built by the Level-1 (L1) trigger which uses the information from the muon trigger chambers (RPC and TGC) as well as the reduced-granularity towers from calorimeters. The L1 trigger system is implemented in custom hardware processors and uses simple algorithms to make fast decisions. While the muon chambers select high p_{T} muons, the calorimeter objects searched for are high p_{T} electrons, photons, jets and also hadronically decaying τ leptons or large missing transverse energy and sum of transverse energy. The L1 trigger reduces the data rate to 75 kHz. If an event is selected, the data is transferred to the Level-2 (L2) trigger and regions of interest (RoI) are defined around the triggering objects.

The RoIs are used as seeds for the L2 trigger, which has full access to calorimeter information and lowers the event rate to 3.5 kHz. At this stage also Inner Detector tracks are incorporated into the trigger decision. In case of muons, the L2 measures the p_{T} more precisely and may increase the p_{T} threshold. It also applies isolation requirements to the objects. In case of electrons and τ leptons, the L2 requires a match of the calorimeter cluster with the Inner Detector track and also isolation. Photons do not have a track and hence less rejection power is gained here. In case of jets, the L2 sets the more precise p_{T} threshold.

The final trigger decision is carried out by the Event-Filter (EF). At this stage the standard offline reconstruction software is used to process the complete data from all detector systems. The events are fully reconstructed using up-to-date calibration and alignment constants and optimised thresholds. The events are finally written to mass storage devices at a rate of about 400 Hz.

The exact p_{T} thresholds (so called *trigger menu*) for each object depend on the luminosity. Combinations of different objects (multi-object triggers) are also possible. In addition, triggers can be prescaled that means that only 1 in N events passing the trigger is accepted. Details on triggers and the trigger menu used for collecting data in 2010 can be found in Ref.[105].

3.3 Luminosity detectors

A precise determination of the luminosity is needed for physics measurements. The luminosity is independently determined using several detectors and multiple algorithms, each having different acceptances, systematic uncertainties and sensitivity to backgrounds [106, 107]. In addition to the main detector, dedicated additional detectors are used to perform luminosity measurements. These are located at various points along the beam axis (z-direction) to provide information about the instantaneous and absolute luminosities received at ATLAS.

LUCID (LUminosity measurement using Cerenkov Integrating Detector) [45] detects inelastic proton-proton scattering on each side of the interaction point at a distance of 17 m. Coverage in the region $5.6 < |\eta| < 6.0$ is provided. Luminosity is monitored by counting the number of interactions per bunch in the Cherenkov counters.

The primary purpose of the Beam Conditions Monitor (BCM) is to monitor beam losses and provide fast feedback to the accelerator operations team. The BCM consists of two arms of diamond sensors located at z= ±18.4 m and at radius of 5.5 cm from the beam axis.

The ZDC (Zero Degree Calorimeters) [108, 45] detects forward neutrons and photons with $|\eta| > 8.3$ in both pp and heavy-ion collisions. The ZDC is located ±140 m from the interaction point, at the point where the straight section of the beam pipe splits back into two separate beam pipes. Eventually, each side of the ZDC will contain one electromagnetic module ($\sim$ 29 radiation lengths thick) and three hadronic modules (each $\sim$ 1.14 interaction lengths thick), but at the time of completing this monograph only the hadronic modules are installed.

The ALFA (Absolute Luminosity For Atlas) sub-detector [109] provides absolute luminosity measurements via elastic proton-proton scattering at small angles. The optical theorem connects the elastic scattering amplitude in forward direction with the total cross section, which can be used to determine the absolute luminosity. The ALFA detector consists of four Roman Pot stations, two on each side of the interaction point at ±240 m. One station houses two tracking detectors, each equipped with 1500 scintillating fibres.

3.4 Simulation of physics events

To understand the real data seen by the detector and to compare this with theoretical predictions, the simulation of particle interactions is necessary. The simulated data also enable to study the discovery potential of the detector and to understand signatures of interesting processes. Monte Carlo simulation and reconstruction of events are performed within ATHENA [110], the ATLAS offline software framework. The full event simulation is organised in steps described briefly below. More detailed description of the full ATLAS simulation infrastructure can be found in Ref. [111].

Event Generation This step is based on Monte Carlo (MC) techniques. Several generators, like PYTHIA [112] or HERWIG [113], are used to model particle interactions for physics analyses. The generation includes the simulation of the hard process, the initial and final state radiation, multiple interactions, beam remnants as well as hadronisation and decays. The τ decays are modelled with TAUOLA library [114, 115] which is taking into account the effects of the polarisation of the τ leptons. The effect of final state Quantum Electrodynamics (QED) radiation is simulated by PHOTOS [116]. The result of the event generation are the four-momenta of particles in

the final state, the so-called Monte Carlo generator level information. The signal and background Monte Carlo samples used for early data studies are generated with the default ATLAS MC10 tune [117].

Simulation The generated final state particles are subsequently passed through a detector simulation, to track the way of particles through the detector and simulate the interaction of particles with the detector material and the magnetic field. Their interaction with traversed material is simulated within the GEANT4 [118, 111] framework. Detailed information on the detector geometry and the magnetic field is used when simulating propagation of particles. At this step, the decay of long lived particles is handled. To enable a comparison with the detector output, the energy deposited in the sensitive regions of the detector is digitised into voltages and currents. Also detector noise is added as well as cross-talk effects. The output is the raw data format, and at this stage the simulation output matches the real data detector output format, except for the presence of truth information in the simulation, containing the generator level information about particles.

Pile-up At high luminosities multiple interaction at a single bunch crossing take place. Most of these collisions are elastic and inelastic scattering events (minimum bias) but the remnants of these processes are also recorded together with interesting interactions in the same bunch crossing (pile-up). The additional particles from pile-up events potentially cause difficulties in the reconstruction of the hard parton collision process. If the pile-up originates from the same bunch crossing as the main interaction, it is called in-time pile-up. In addition, there is also an out-of-time pile-up contribution, which means that the contribution is from an earlier bunch crossing. Other pile-up contributions are from the cavern background or from showers induced by particles from cosmic rays. Hence, an additional step simulating pile-up effects is performed in the physics event simulation.

Reconstruction In this step the digital signals are transformed into tracks and calorimeter clusters to form reconstructed objects like electrons, τ leptons or jets. The input from different detector components is also combined to reconstruct missing transverse energy. Each object is reconstructed by the use of a dedicated algorithm. In the next Section the particle reconstruction and identification algorithms for physics objects of interest are explained. This step is exactly the same for data and simulated events.

3.5 Particle reconstruction and identification

The particle reconstruction and identification is performed usually in two steps. First, information from basic detector units like calorimeter cells or pixels in the tracking system are gathered and evaluated. Then, identification algorithms make use of the condensed information to perform hypothesis tests and classify the object under investigation. Given a signature in the detector, the identification algorithms can only state a probability that this signature is caused by a certain particle type. In order to meet the needs of various physics analyses which may benefit from different identification efficiencies, a couple of working points for object identifications are supported. To avoid confusion between real physics objects and objects classified by an identification algorithm to be of a certain kind, the latter are referred to as *candidates*.

Electrons The reconstruction and identification of electrons [119, 120] starts with the information from the electromagnetic calorimeter. An algorithm searches for spatially grouped calorimeter cells with a significant energy deposition (cluster). To suppress photons, each cluster has to be matched to a charged particle track of the Inner Detector. The efficiency of the electron reconstruction is very high ($> 90\%$) and mainly limited by the energy loss and scattering in the material of the Inner Detector. However, at the LHC, backgrounds of multijets from QCD processes are large. Also rejection of background electrons, mainly from photon conversions and Dalitz decays is needed. Hence, several additional requirements are used to further suppress these backgrounds:

- Calorimeter information. Due to the fine granularity of the EM calorimeter, the lateral and longitudinal shower shape is used to separate electromagnetic from hadronic showers. The showers of QCD multijets are

more spread compared to electron showers of the same energy. Also the amount of energy deposited in the hadronic calorimeter, which should be low in the case of electrons, provides a good suppression of jets.

- The Inner Detector information. A minimum number of hits in the pixel and SCT detectors, presence of the transition radiation in the TRT detector and a transverse impact parameter (minimum distance of the extrapolated track to the beam axis) are used to identify electrons.

- Cluster-track match criteria. The rejection of jets can be significantly improved by ensuring the consistency between the EM calorimeter and the ID information. The extrapolation of an electron track into the electromagnetic calorimeter has to match with the barycentre of the corresponding shower. For jets this is usually not the case since additional charged particles and photons shift the shower position. The electron energy, E, measured in the EM calorimeter should match the momentum, p, measured in the ID. For jets, larger E/p values are expected since several tracks can belong to one jet and there is additional energy from neutral particles in the calorimeter.

The electron reconstruction and identification algorithm is designed to provide various levels of background rejection optimised for high identification efficiencies, over the full acceptance of the ID system, $|\eta| < 2.5$. Additionally up to $|\eta| < 4.9$ a dedicated algorithm can reconstruct forward electrons using calorimeter information only. The electron identification uses a cut-based selection. The cuts are optimised in bins of electron candidate E_{T} and η. There are three selections defined, with different levels of signal efficiency and purity: *loose*, *medium* and *tight*. Loose selection includes rough track-cluster matching, a cut on the hadronic leakage and on the shower shapes calculated in the second sampling of the EM calorimeter. In medium selection in addition to the loose cuts, tighter cuts on the track-cluster matching are applied and shower shape information calculated in the first sampling is used. Tight selection includes the same cuts as for the medium set and additionally require a hit in the B-layer of the pixel detector, TRT information and calorimeter isolation.

All trigger levels are used for triggering electrons. At the hardware-based L1 trigger, objects are selected only in the EM calorimeter. At the software-based L2 trigger, dedicated fast calorimeter and tracking algorithms are used. At the EF level, the electron reconstruction and identification, as described above, is applied and leads to highly efficient triggers.

In many analyses electrons are required to be isolated from the rest of the event. The first isolation variable is based on the total transverse momentum of charged particles in the Inner Detector in a cone ΔR centered around the electron candidate direction, $I_{PT}^{\Delta R}$, divided by the transverse momentum or transverse energy of the electron candidate. A second isolation variable is based on the total transverse energy measured in the calorimeter cells in a cone ΔR around the electron direction, $I_{ET}^{\Delta R}$, divided by the transverse energy of the electron candidate. In the reconstruction of both isolation variables, E_{T} of the electron candidate is subtracted.

Photons The reconstruction of photons [121] follows in its main aspects that of electrons. Both objects are treated similarly within an overall reconstruction algorithm. Although the definition of an electron object is rather straightforward, relying entirely on the presence of a track matching an electromagnetic cluster, that of a photon is a bit more involved, due to the fact that photons can be classified into two main categories: converted and unconverted. Photons reconstructed as converted are characterised by the presence of at least one track matching an electromagnetic cluster originating from a vertex inside the tracker volume, whereas unconverted photons do not have such a matched track. A dedicated energy calibration is applied to account for upstream energy losses, lateral leakage and longitudinal leakage, separately for converted and unconverted photon candidates.

Photon identification is based on the lateral and longitudinal energy profiles of the shower in the calorimeter. The photon candidate is required to deposit only a small fraction of its energy in the hadronic calorimeter. The transverse shower shape in the second layer of the electromagnetic calorimeter needs to be consistent with that expected for a single electromagnetic shower. Finally, the high granularity first calorimeter layer ($\Delta\eta = 0.0031$) is used to discriminate single photons from overlapping photon pairs from neutral meson decays produced in jet fragmentation, which are the main background source. Based on these criteria, a set of loose and tight identification

cuts, different for converted and unconverted photon candidates, is applied. The trigger chain for photons is similar to the one for electrons.

Muons The ATLAS muon identification and reconstruction algorithms take advantage of the multiple sub-detector technologies which provide complementary approaches and cover pseudorapidities up to 2.7 over a wide p_{T} range. The detector components involved in muon reconstruction are the muon spectrometer and the Inner Detector. However, muons also deposit some energy in calorimeters. The muon system allows the identification of muons with a p_{T} above 3 GeV. Very low momentum muons are difficult to reconstruct since they do not reach the spectrometer, lose too much energy in the calorimeter and/or do not leave a significant signal over the noise in the muon spectrometer.

ATLAS employs a variety of muon reconstruction algorithms [122]. They rely on the muon spectrometer for standalone muon reconstruction, but in addition they can use the Inner Detector and the calorimeters information. In majority of physics analyses so called *combined muons* are used. For their reconstruction, tracks and track segments found in the muon spectrometer are associated with the corresponding ID track to identify muons at their production vertex, imposing requirements on track quality and hit multiplicity in muon system. The combination improves the momentum resolution for muons below 100 GeV and suppresses the mis-identification of particles that escape the calorimeter and which are not muons. Two reconstruction chains are in use, the MUID [123] and the STACO [124]. The MUID algorithm globally fits all hits associated to muon tracks. The STACO algorithm determines transverse momentum of muons by a statistical combination of the Inner Detector and the muon spectrometer tracks. The performance of the two algorithms is very similar [125].

The muon triggers deploy the three level trigger system of ATLAS within the range of $|\eta| < 2.4$. At L1, muons are identified by coincidence signals from the RPC and TGC detectors. Muon candidates with a certain transverse momentum are taken as seeds for the high level triggers, L2 and EF. At the L2, the information of the MDTs is used in fast algorithms to reconstruct tracks, which are combined with tracks from the Inner Detector at the EF level.

The isolation variables for muons are defined in the same way as for electrons.

τ leptons Reconstruction and identification of τ leptons is described in details in Chapter 4.

Jets Quarks and gluons produced in the primary interaction or as initial or final state radiation evolve into collimated jets of hadronic particles. These jets appear in the detector as localised energy deposits (clusters) in the electromagnetic and hadronic calorimeters. Thus the first step of the jet reconstruction is the clustering of calorimeter cells including both the electromagnetic and hadronic systems. There are several jet finding algorithms available [126]. In ATLAS the default is the anti-k_{T} algorithm [127] using a distance parameter $R = 0.4$ or 0.6. Topological clusters [128] are used as an input. They are combined to form particle jets using the anti-k_{T} algorithm which is both infrared and collinear safe. The quantities $d_i = 1/p_{T,i}^2$ and $d_{i,j} = min(1/p_{T,i}^2, 1/p_{T,j}^2)\Delta R/R$ are first calculated for each cluster i and each cluster pair ij, where ΔR is the cone distance between the two clusters and R is a distance parameter which defines the radius of the jet. The minimum of this set of numbers is then identified; if it comes from a $d_{i,j}$, the corresponding clusters are merged, whereas if it comes from a d_i, the corresponding cluster is removed from the list of clusters and moved to the list of jets. These two steps are repeated until all clusters have been combined into jets. The net effect of this algorithm is to sequentially combine energy depositions around the highest-p_{T} clusters while ensuring that the distance between the resulting jets is always at least of order R. This procedure has a number of advantages when compared with other jet reconstruction algorithms. In particular, since the priority is given to high-p_{T} clusters, the algorithm is insensitive to collinear splitting, emission of soft partons, and pile-up.

The jets found by the algorithm are constructed from the raw signals of the calorimeter cells. As the ATLAS calorimeter is non-compensating for the energy lost in material before the calorimeters, this raw signal has to be calibrated. This is done by applying Monte Carlo based p_{T} and η dependent correction factors [129]. For the standard reconstruction of jets, currently two methods are used in ATLAS, a global cell weighting [130, 59] and

a cluster-level calibration method called local hadronic calibration [131]. In the global cell weighting calibration, weights are applied after the jet finding to the energies reconstructed in cells that form the jet constituents. The weights are functions of the cell energy density and the cell position. The dependence of the weights on the energy density is motivated by the observation that energy deposits with a low energy density are more likely to originate from the hadronic component of a shower. In the local hadronic calibration, topological clusters are classified by their shape, position and the structure of the energy deposit as hadronic or electromagnetic clusters. Weights similar to the weights applied in the global cell weighting calibration are applied to the energies of cells in hadronic clusters. A correction for energy not included in the cluster is applied. In this method, the calibrated clusters are used as the input to the jet reconstruction. At the jet level, both methods yield comparable results. After the calibration, additional corrections are applied at the jet level to correct for particles not reaching the calorimeter and for inefficiencies of the jet finding algorithm.

The L1 jet trigger is based on a sliding-window algorithm [132] that selects high energy depositions in the calorimeters. This information is passed to the L2 trigger based on a simplified version of a cone clustering algorithm, limited to a maximum of three iterations and performed on calorimeter clusters with full granularity. The EF uses the same reconstruction algorithms as the offline reconstruction, the only difference being the calorimeter calibration. Further details can be found in Ref. [59].

Missing transverse energy In a collider event the missing transverse energy is defined as the momentum imbalance in the plane transverse to the beam axis. The colliding protons do not have transverse momentum components and therefore the sum of the transverse momenta of all final state particles has to vanish as well. An imbalance may signal the presence of unseen particles, such as neutrinos or stable, weakly-interacting supersymmetric particles. The vector momentum imbalance in the transverse plane is obtained from the negative vector sum of the momenta of all particles detected in a pp collision and is denoted as missing transverse energy, $\vec{E}_T^{miss}$. The symbol $E_{\mathrm{T}}^{\mathrm{miss}}$ is used for its magnitude.

In its simple definition, the $E_{\mathrm{T}}^{\mathrm{miss}}$ is built by summation of calorimeter cell energies, addition of all muons and the estimated energy loss in the inactive material [133]. The calorimeter part is calculated from the energy deposits of calorimeter cells inside three-dimensional topological clusters [132], calibrated locally to the electromagnetic or hadronic scale depending on the energy deposit classification. The muon part takes into account the sum of the combined muon momenta from all isolated combined muons as well as the sum of all non-isolated muons reconstructed as tracks in the muon spectrometer. A muon is considered isolated if the distance ΔR to the nearest jet is at least 0.3. To avoid double counting due to the isolated muons, the sum of the energy of the calorimeter cells crossed by an isolated muon, is subtracted from the calorimeter term.

A more sophisticated method of the $E_{\mathrm{T}}^{\mathrm{miss}}$ calculation is called *refined calibration* [133, 134]. Since the calorimeter response depends on the particle type, the energy calibration is also different for different objects like, for example, electrons and jets. Thus, the calibration of all calorimeter cells which can be associated to a close-by reconstructed object, is replaced by the calibration specific for the type of the identified particle. The idea hereby is that these identified objects are calibrated with better accuracy than the hadronic energy deposits. The association follows a defined order: electrons, then photons, τ leptons, jets and finally muons. Energy deposits in cells which could not be associated are also included and here the global calibration weights are used. The resultant $E_{\mathrm{T}}^{\mathrm{miss}}$ of each object is then added together to form the refined calorimeter term and thus the refined final $E_{\mathrm{T}}^{\mathrm{miss}}$.

The $E_{\mathrm{T}}^{\mathrm{miss}}$ trigger requires that the magnitude of the vector sum of all transverse energies is larger than some thresholds. Only calorimeter information from the trigger towers is used at L1. At L2, results provided by L1 are refined by applying corrections taking into account muons reconstructed at L2. Contributions from the electromagnetic and hadronic calorimeters as well as from the muon spectrometers are recomputed with the full granularity of the detector at the EF. Only positive energy calorimeter cells above a certain threshold are considered to suppress electronic noise.

3.6 Data quality and preselection of events for early data analyses

After data are taken, several data quality flags are assigned, defining if the data are good enough to be used for physics analyses. Data quality flags are assigned for each sub-detector and for each reconstructed object in each detector region (e.g. barrel or end-cap) and for each luminosity block corresponding to several minutes of data taking. Information from the online and offline data quality monitoring is combined into a database containing LHC beam conditions, detector status and data flow information which can be used to create lists of runs and luminosity blocks usable for analyses (so called Good Runs List, GRL). Those lists are created for particular studies. This is because some analyses do not use the full detector, so even if some of the data for a muon analysis for instance are not collected correctly because of technical problems with the muon spectrometer, an analysis based only on the ID information can still use the data. The bad quality data events are removed from the analysis by applying the dedicated GRL list as the first selection on the data sample.

Following the basic data quality checks, further event cleaning is performed. Discharges in the hadronic calorimeter or coherent noise in the EM calorimeter can occasionally occur simultaneously with the proton-proton interaction. Cosmic rays or beam background can also lead to energy deposits, which are not part of the main collision. Those can lead to the high energy calorimeter deposits or leave high quality tracks in the detector and thus create incorrectly reconstructed jets, τ candidates and wrong $E_{\mathrm{T}}^{\mathrm{miss}}$ measurement [135]. To avoid such effects, cleaning requirements are applied on τ candidates and jets which do not overlap with electrons and muons. This cleaning is based on several jet properties, which are used to check quality of calorimeter energy deposits.

During data taking not functional Front End Boards and isolated not functional or high noise channels in the EM Calorimeter were observed. The inefficiencies are of 6% per electron during data taking in 2010. Using so called *object Quality Maps*, the two-dimensional histograms in η and ϕ, the information can be recovered of whether an electron is built from a cluster affected by detector problems, in which case it can be rejected [120]. This avoids large differences between data and Monte Carlo predictions which do not simulate the non-functioning areas.

Pile-up events can come from both the same bunch-crossing as well as from previous bunch-crossings. This leads to in-time and out-of-time pile-up, respectively. They are characterised by having more than one primary vertex. In early data analyses Monte Carlo pile-up samples are re-weighted such that their default vertex distributions match the data distribution.

Life can be very difficult for a little sub-atomic particle in a great big universe.

Terry Pratchett

4

Reconstruction and identification of τ leptons at ATLAS

As described in Chapter 2, the τ lepton has a short life time and thus cannot be detected directly. Instead it is identified through its decay products such as electrons, muons, pions, kaons and neutrinos. The τ lepton decays hadronically 65% of all cases, and the remaining fraction of decays are to lighter leptons. The leptonic decay modes cannot be distinguished from primary electrons or primary muons. Thus reconstruction of τ leptons in the ATLAS experiment is understood as a reconstruction of hadronic τ decay modes.

Reconstruction of τ leptons at hadron colliders remains a very difficult task in terms of distinguishing them from background processes dominated by QCD multijet production. However, τ_{had} decays possess certain properties that can be used to differentiate them from QCD jets, as shown in Figure 4.1. They decay in 72% of the cases with one charged particle (1-prong) and in 23% with three charged particles (3-prong). This leads to a low track multiplicity as compared to the QCD jets. The decay products are well collimated, forming a narrow hadronic shower in the calorimeters. The shape difference of the hadronic τ lepton decay and the QCD jet is due to the colour flow of these two objects. The τ lepton decays colour neutral via a W boson and thus its decay products form a narrow cone. Compared to this, the QCD jet, consisting of quarks and gluons, is not a colour neutral object. The colour field in such a jet can have enough energy to produce new quark-antiquark pairs, which fragment into colour-neutral hadrons. There is no energy limit in the colour field of a jet, which is why the jet shape is much broader compared to a hadronically decaying τ lepton.

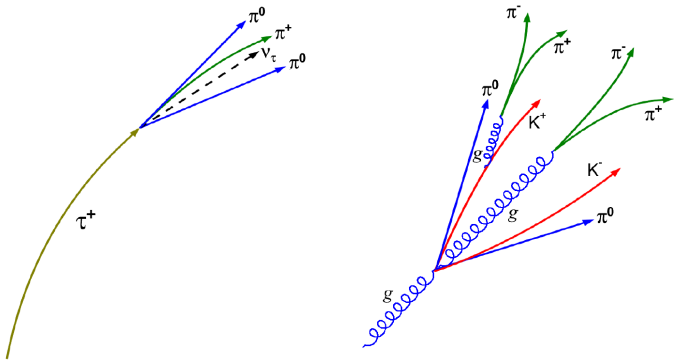

Figure 4.1: Illustration of (a) a hadronic τ decay and (b) a gluon-initiated QCD jet.

Also in τ_{had} decay, due to the presence of π^0's, a significant electromagnetic component, different than for the QCD jets, can be observed. Additionally, isolation from the rest of the event is visible both in the Inner Detector and the calorimeter. The visible invariant mass is smaller than the τ lepton mass, due to not detectable neutrino. The lifetime of the τ lepton in principle allows for the reconstruction of its decay vertex in the case of 3-prong decays. The flight path in the detector increases with the Lorentz boost of the τ lepton, and at the same time the angular separation of the decay products decreases. The resulting decay vertex can be resolved from the primary interaction vertex in the silicon tracker. These features are exploited in reconstruction and identification algorithms used in the ATLAS experiment in order to select efficiently τ_{had} decays.

4.1 Reconstruction of τ decays

The τ leptons reconstruction algorithm is based on information already provided by different sub-detectors, such as tracks reconstructed in the Inner Detector and energy deposits in the calorimeter. Reconstruction is done only for the visible part of the decay products (without neutrino), however, for specific studies the complete invariant mass of the $\tau\tau$ system may be reconstructed as described in Appendix A.

Historically, two different reconstruction algorithms, a track-based and a calorimeter-based, were developed in the ATLAS offline reconstruction software [59]. In the first data analysis they were run in a merged configuration.

- Calorimeter-based algorithm builds τ candidates from calorimeter jets reconstructed with the anti-k_{T} algorithm [127] (using a distance parameter $R = 0.4$) from topological clusters [128] with transverse energy above 10 GeV. The p_{T} of the τ candidate is further adjusted by applying multiplicative factors derived from Monte Carlo studies. Tracks within a cone size of $\Delta R < 0.2$ of the jet seed are associated to the τ candidate. The tracks are required to pass track quality criteria described in the next Section. The direction of the τ candidate is obtained from the η and ϕ of the seeding jet.

- Track-based algorithm builds τ candidates from a track with $p_{\text{T}} > 6$ GeV which is assumed to come from the charged pion and reproduces well the direction of the τ candidate (so called *leading track*). Then, other tracks around the seed track within a cone size of $\Delta R < 0.2$ are associated (so called *associated tracks*). It is also required that there are no tracks in the isolation ring $0.2 < \Delta R < 0.4$. Both the leading and associated tracks have to satisfy quality criteria as described in the next Section. The τ candidate energy is determined using the energy flow algorithm [59]. This method uses the measured track momentum to improve the overall measurement of the energy in the calorimeters, particularly for the low energy range. The direction of the τ candidate is calculated from tracks as p_{T}-weighted track barycentre.

τ candidates from the two algorithms are merged, providing they overlap within the cone of $\Delta R < 0.2$. Merged candidates are expected to be identified with higher purity, but in most first data analyses all calorimeter-based candidates are used in order to increase the yield. They include nearly all track-based candidates, as there are very few track-based candidates without a calorimeter-seed.

4.1.1 Track selection criteria for τ leptons reconstruction

Track selection should ensure high efficiency and quality of the reconstructed tracks over a broad dynamic momentum range, from 1 GeV to a few hundred GeV. Both the calorimeter-based and the track-based algorithms determine the charge of the τ candidates by summing up the charge of particle tracks reconstructed in the core region, $\Delta R < 0.2$ around the reconstructed direction of visible decay products. Therefore, the selection criteria for tracks of charged pions arising in τ_{had} decays are important factors in an efficient τ leptons identification. The incorrect charge assignment for τ candidates is dominated by combinatorial effects: 1-prong decays may migrate to 3-prong category due to photon conversions or the presence of additional tracks from the underlying event. A 3-prong decay might be reconstructed as a 1-prong decay due to inefficiencies in track reconstruction and selection. In the low-p_{T} range, the inefficiency is due to hadronic interactions in the Inner Detector material. In the high-p_{T}

Table 4.1: Track quality criteria for tracks of calorimeter-based and track-based τ candidates.

Track criteria		calorimeter-based candidate	track-based candidate leading track	track-based candidate associated track
p_T (GeV)	>	1	6	1
$\|\eta\|$	<	2.5	2.5	2.5
B layer hit	≥	1	no cut	1
Hits in pixel detector	≥	2	no cut	2
Hits in pixel and SCT detectors	≥	7	7	7
$\|d_0\|$ (mm)	<	1	2	1
$\|z_0\ sin\theta\|$ (mm)	<	1.5	10	1.5

range, the performance is degraded due to strong collimation of the multiple tracks from 3-prong decays. Also the contribution from the incorrect charge assignment of the individual tracks should not be neglected.

The quality criteria are applied on the number of hits in the pixel and SCT detectors, in the pixel detector and in the B-layer of the pixel detector as well as on the transverse, d_0, and longitudinal, z_0, impact parameters[1]. All quality criteria are listed in Table 4.1.

The τ candidates are classified as one or multi-prong depending on the number of tracks counted in the core region. For calorimeter-based candidates, tracks within the *isolation annulus*, $0.2 < \Delta R < 0.4$, where ΔR is a cone around the seed jet, are also counted for variable calculations, and are required to satisfy the same track quality criteria.

4.1.2 Energy calculation

Energy of τ candidates is calculated in two different ways, depending on their seed type. The basic energy of a τ candidate, reconstructed from calorimeter seed, is obtained as a sum over the energies of cells, within $\Delta R < 0.4$ of the seed jet axis, that form the topoclusters of the jet seed. This energy reconstructed at the electromagnetic (EM) energy scale is further calibrated by applying correction factors. For this purpose *response functions*, $R(p_T^{EM})$, are defined as $R(p_T^{EM}) = p_T^{EM}/p_T^{gen}$ where p_T^{EM} is the p_T of the τ candidate at the EM scale and p_T^{gen} is the true generated p_T of the candidate. Response functions are constructed using MC samples for different categories of τ candidates depending on the number of tracks and their $|\eta|$. 1-prong candidates are divided accordingly to EM energy fraction (f_{EM}), in an attempt to further classify these candidates based on the π^0 content. In order to derive response functions, τ candidates are binned in p_T^{gen} and the correction factor is constructed for each bin. In each bin the response is fitted to an asymmetric Gaussian and the mean of the fit gives the correction factor. Correction factors are associated for every p_T^{gen} bin to a value of p_T^{EM}. Obtained response function is used for calibrating reconstructed τ candidates to their final energy at the τ energy scale, p_T^{TES}. An example of the response function is shown in Figure 4.2 (a) for 1-prong τ candidates with $f_{EM} > 0.15$ in the barrel region. Markers show the correction factors and the solid line, the response function, being the result of a fit to these markers. The response function approaches unity for high values of p_T^{EM}. For low values of p_T^{EM}, the functional form of the response function diverges, so the minimum of the response function is used instead, indicated by the dashed line.

An example of the resolution obtained at the τ energy scale for 1-prong τ candidates in barrel region can be seen in Figure 4.2 (b). Resolution is defined as p_T^{TES}/p_T^{gen}. The fitted function is an asymmetric Gaussian.

Systematic uncertainty on the obtained p_T^{TES} is evaluated from six distinct sources: Monte Carlo event generator and underlying event model, hadronic shower model, amount of detector dead material, topological clustering noise thresholds, EM energy scale and, finally, non-closure. The non-closure accounts for deviations of kinematics of the calibrated τ candidate from the true kinematics. Individual contributions are added in quadrature. An ex-

[1]Impact parameter is a distance between the point of closest approach of a track and the interaction vertex. Transverse impact parameter is this distance in transverse plane (x,y) and longitudinal impact parameter is the z-coordinate of this point.

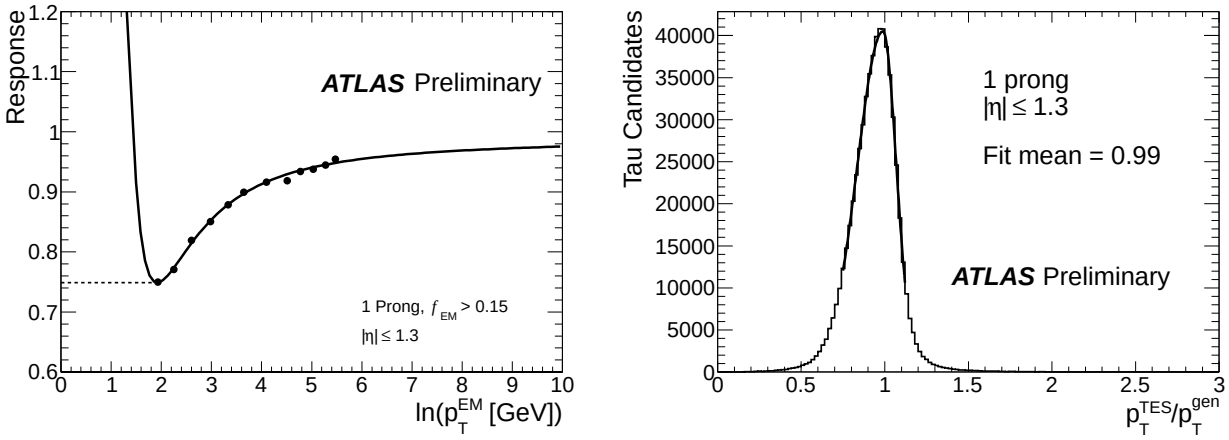

(a) (b)

Figure 4.2: Response functions for 1-prong τ candidates with $f_{\mathrm{EM}} > 0.15$ in the barrel region (a). Resolution for 1-prong τ candidates in the barrel region (b) [136].

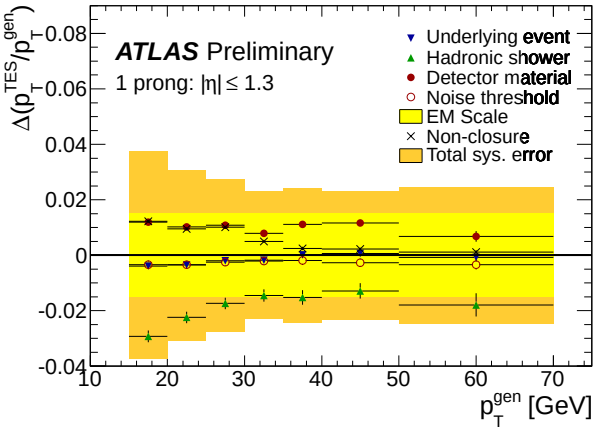

Figure 4.3: Final systematic uncertainty on the τ energy scale. Different markers represent various sources of uncertainty as indicated in the legend. The yellow band shows the combined uncertainty from all sources [136].

ample of the total systematic uncertainty on the τ energy calibration scale, along with contributions from different sources of systematic uncertainties are shown in Figure 4.3 for 1-prong τ candidates in the barrel region.

An energy flow algorithm is used for track-seeded τ candidates. This method divides the energy deposited in cells into following categories:

- *The pure electromagnetic energy*, E_T^{emcl}, seeded by an electromagnetic cluster isolated from the τ candidate tracks and with no substantial hadronic leakage. The energy is collected in a narrow window around the seed.
- *The charged electromagnetic energy*, E_T^{chrgEM}, seeded by the impact point of τ candidate tracks in each layer of the EM calorimeter. The energy is collected in a narrow window around seeds.
- *The charged hadronic energy*, $E_T^{chrgHAD}$, seeded by the (η, ϕ) of τ candidate tracks in each layer of the hadronic calorimeter. The energy is collected in a cone of $\Delta R = 0.2$ around seeds.

- *The neutral electromagnetic energy,* E_T^{neuEM} seeded by the (η, ϕ) of τ candidate tracks in presampler and two first layers of the EM calorimeter. The energy is collected from not yet used cells in a cone of $\Delta R = 0.2$ around seeds.

The energy deposits E_T^{chrgEM} and $E_T^{chrgHAD}$ are replaced by the track momenta (no hadronic neutrals) in order to define the τ energy scale. The contribution from neutral pions is included in E_T^{emcl} and E_T^{neuEM}. To account for overlapping of energy deposits of neutral and charged pions and energy leakage outside a narrow cone around the track, correction terms $\sum resE_T^{chrgEM}$ and $resE_T^{neuEM}$ are used. These terms are derived empirically from parametrisation of effects mentioned above, based on the Monte Carlo studies [137]. This leads to the following energy, E_T^{eflow}, definition:

$$E_T^{eflow} = E_T^{emcl} + E_T^{neuEM} + \sum p_T^{track} + \sum resE_T^{chrgEM} + resE_T^{neuEM}. \quad (4.1)$$

An advantage of the above approach for defining the energy scale is that it performs well for true hadronic decays of τ leptons but significantly underestimates the nominal energy of fake τ candidates from QCD jets. This effect comes from the fact that a cone of $\Delta R = 0.2$ is too narrow to efficiently collect the energy of a QCD jet (particularly with low transverse momentum) and also since a large fraction of the neutral hadronic component is omitted in the definition itself, as the energy deposit in the hadronic calorimeter does not contribute to the energy calculation. This method leads, however, to more pronounced non-Gaussian tails in the fractional energy response than the more conventional energy estimates from calorimetry only.

4.1.3 π^0 reconstruction

High granularity of the EM calorimeter in ATLAS allows for the identification of isolated sub-clusters from π^0 mesons inside the core region of the reconstructed τ candidates. It is done by the reconstruction of the topological sub-clusters from cells in a cone size of $\Delta R < 0.4$ around the direction of the leading track of the τ candidate. Only sub-clusters with a centre within $\Delta R < 0.2$ and with transverse energy above 1 GeV are considered. A cell subtraction procedure is applied to reduce the impact from energy deposits of nearby charged pions. Namely, before the clustering process, cells being closest to the impact point of the track ($\Delta R < 0.0375$) are removed. In addition, sub-clusters are accepted if their reconstructed energy in the first and presampler layers of the EM calorimeter exceeds 10% of their total energy. This methods finds 50% of the π^0 clusters in τ decays with one or two π^0 mesons, while approximately 65% of $\tau \to \pi\nu$ decays are reconstructed correctly without any π^0's [59]. Until now, the described method has been optimised with MC samples only for the track-based candidates.

4.1.4 τ lepton trigger

The L1 τ trigger is a hardware trigger based on EM and hadronic calorimeter information, using trigger towers of approximate size $\Delta\eta \times \Delta\phi = 0.1 \times 0.1$, with a coverage up to $|\eta| < 2.5$. At this level τ candidates are identified using three key features: the EM and hadronic energy in two-by-two collection of trigger towers and energy in the isolation region between two-by-two collection of trigger towers and the four-by-four collection surrounding it. Different thresholds to these quantities define various L1 τ triggers.

The L2 τ trigger is software-based. After refining the L1 position using the second sample layer in the EM calorimeter, its algorithm selects narrow jets by means of calorimeter lateral shape and transverse energy variables. Tracks are also reconstructed in regions passing the L1 trigger using the full detector granularity. The characteristic narrowness of tracks and calorimeter deposition and low track multiplicity of the τ_{had} decay are used to discriminate against background.

At the EF level, parts of the offline τ reconstruction algorithms are used on the seeds passing L2. Data from the whole detector can be accessed if necessary. This provides a wide range of more accurate identification variables. Rejection against dominant QCD multijet background by the High Level Triggers (L2 together with EF) is of the order of 10 or more, depending on the p_T range and tightness of the selection.

Different τ trigger signatures were used for collecting early data and for increasing instantaneous luminosities. Typically, the p_T threshold applied at EF was tightened with increasing luminosities. Additionally, different quality

requirements (loose, medium, tight) are available for each chain. The τ trigger and its performance in 2010 ATLAS data is fully documented in Ref. [138].

4.2 τ leptons identification

The reconstruction of τ candidates provides very little rejection against QCD multijets, electrons or muons. Their rejection comes from a separate identification step using variables calculated by the reconstruction algorithms. The identification is based on the combined information from the Inner Detector and the calorimeters. A traditional cut-based selection method as well as multivariate discrimination techniques are used. For early data only robust variables are used. These variables are expected to be well understood even with non-optimal detector calibration and limited knowledge of the detector performance.

4.2.1 Rejection of QCD jets

The variables used to discriminate against the QCD multijet background are described below. They are calculated for the calorimeter-based candidates.

Electromagnetic radius: Shower width weighted with the transverse energy in the EM calorimeter:

$$R_{\mathrm{EM}} = \frac{\sum_i^{\Delta R_i<0.4} E_{T,i}^{\mathrm{EM}} \Delta R_i}{\sum_i^{\Delta R_i<0.4} E_{T,i}^{\mathrm{EM}}},$$

where i runs over cells in the first three layers of the EM calorimeter associated to the τ candidate, ΔR_i is defined relative to the τ candidate jet seed axis and $E_{T,i}^{\mathrm{EM}}$ is the cell transverse energy. It is expected to be narrower for τ_{had} decays compared to QCD multijets.

Track radius: Tracks width weighted with the track p_{T}:

$$R_{\mathrm{track}} = \frac{\sum_i^{\Delta R_i<0.4} p_{T,i} \Delta R_i}{\sum_i^{\Delta R_i<0.4} p_{T,i}},$$

where i runs over all core and isolation tracks of the τ candidate, ΔR_i is defined relative to the τ candidate jet seed axis and $p_{T,i}$ is the track transverse momentum. Similar to the R_{EM} it tends to be smaller for τ_{had} decays than for QCD multijets.

Leading track momentum fraction:

$$f_{\mathrm{track}} = \frac{p_{T,1}^{\mathrm{track}}}{p_T},$$

where $p_{T,1}^{\mathrm{track}}$ is the transverse momentum of the leading core track of the τ candidate and p_T is the transverse momentum of the τ candidate. In case of τ_{had} decays, the leading track carries significant fraction of τ momentum.

Core energy fraction: Fraction of transverse energy in the core ($\Delta R < 0.1$) of the τ candidate:

$$f_{\mathrm{core}} = \frac{\sum_i^{\Delta R<0.1} E_{T,i}}{\sum_i^{\Delta R<0.4} E_{T,i}},$$

where i runs over all cells associated to the τ candidate within ΔR_i of the τ candidate jet seed axis. This variable measures the concentration of calorimeter energy deposits around the jet axis. For τ_{had} decays, energy tends to be more concentrated, resulting in a higher f_{core} compared to QCD multijets.

Electromagnetic fraction: Fraction of uncalibrated transverse energy of the τ candidate deposited in the EM calorimeter:

$$f_{\mathrm{EM}} = \frac{\sum_{i;\ i\in\mathrm{EM\ Calo}}^{\Delta R_i<0.4} E_{T,i}^{\mathrm{EMscale}}}{\sum_{j;\ j\in\mathrm{Calo}}^{\Delta R_i<0.4} E_{T,j}^{\mathrm{EMscale}}},$$

where $E_{T,i}$ ($E_{T,j}$) is the uncalibrated transverse energy deposited in cell i (j), and i runs over the cells in the first three layers of the EM calorimeter, while j runs over the cells in all layers of the calorimeter. For τ_{had} decays larger energy deposits in the EM calorimeter are expected due to the presence of neutral pions.

Cluster mass: Invariant mass computed from constituent clusters of the seed jet, m_{clusters}. This variable has larger values for QCD jets due to their higher multiplicity.

Track mass: Invariant mass of tracks in a cone of size $\Delta R = 0.4$, m_{tracks}. This variable has larger values for QCD jets due to their higher multiplicity.

Transverse flight path significance: The decay length significance of the secondary vertex for multi-track τ candidates in the transverse plane:

$$S_{\mathrm{T}}^{\mathrm{flight}} = \frac{L_{\mathrm{T}}^{\mathrm{flight}}}{\sigma(L_{\mathrm{T}}^{\mathrm{flight}})},$$

where $L_{\mathrm{T}}^{\mathrm{flight}}$ is the reconstructed signed decay length in the transverse plane and $\sigma(L_{\mathrm{T}}^{\mathrm{flight}})$ is its uncertainty. The tracks used for the secondary vertex fit are those associated to the τ candidate, but additional tracks with p_{T}> 6 GeV within $\Delta R < 0.2$ of the jet seed, and satisfying $|d_0| < 2.0$ mm, and $|z_0 \sin\theta| < 10$ mm, are also added to the vertex fit, even if they fail the B-layer and pixel detector criteria, and the tighter impact parameter criteria that are required for associated tracks.

Using those variables as an input, discriminants are designed to accept true τ candidates and reject fake τ candidates reconstructed from QCD multijet events. There are three different discriminants used for the early data-taking period: a cut based selection, projective likelihood identification, and identification with boosted decision trees.

The cut based τ identification uses cuts on only three uncorrelated variables: R_{EM}, R_{track} and f_{track}, binned for τ candidates that have one or multiple tracks. The cuts on R_{EM} and R_{track} are parametrised as a function of the p_{T} of the τ candidate, since the optimal cuts are strongly p_{T}-dependent due to the Lorentz collimation of the decay products in hadronic τ decays.

In the projective likelihood identification seven variables are used, three for 1-prong τ candidates (R_{EM}, R_{track}, m_{clusters}) and five for 3-prong τ candidates (R_{EM}, f_{track}, f_{EM}, m_{tracks}, number of vertices reconstructed in the event). The probability density functions (PDFs) used by this method are split into different categories, or bins, in order to maximise the discriminatory power. This categorisation is based on properties both of the τ candidate (p_T, seed, number of prongs) and of the event (number of reconstructed primary vertices). The PDFs are also produced for three separate p_T bins.

The identification of τ leptons with boosted decision trees algorithm (BDT) [139] uses all discriminating variables mentioned above. The BDT is trained separately on candidates with one track and with three tracks. Additionally, the BDT is binned by the number of reconstructed primary vertices (less than 3, and more than 2). The selections on the BDT score are made that yield roughly flat signal or flat background efficiency. The selections employ p_{T}-dependent cuts which compensate for the p_{T}-dependence of the BDT score.

4.2.2 Electron and muon vetos

In addition to the QCD multijets rejection, identification methods are also used to distinguish τ_{had} decays from electrons and muons. The cut-based electron veto provides a good separation between electrons and reconstructed τ candidates. Requirements are made on four variables:

$\boldsymbol{E_{\mathrm{max}}^{\mathrm{strip}}}$: The maximum energy deposited in the strip layer of the EM calorimeter, not associated with that of the leading track. This variable tends to be larger for τ_{had} decays due to presence of neutral pions and hadronic interactions in front and inside EM calorimeter.

$\boldsymbol{E_{\mathrm{EM}}/p^{\mathrm{Ltrk}}}$**:** The ratio between the energy deposited in the EM calorimeter, E_{EM}, and the momentum of the leading track, p^{Ltrk}. For electrons this variable is close to unity.

$\boldsymbol{E_{\mathrm{Had}}/p^{\mathrm{Ltrk}}}$**:** The ratio between the energy deposited in the first layer of the hadronic calorimeter, E_{Had}, and the leading track momentum. For electrons this ratio is smaller than for hadrons.

$\boldsymbol{N_{\mathrm{HT}}/N_{\mathrm{LT}}}$**:** The number of high threshold hits over the number of low threshold hits in the TRT. This ratio is higher for electrons than for pions as electrons are more likely to produce the transition radiation that leaves high threshold hits in the TRT.

One of the main characteristics of muons is the small amount of energy deposited in the calorimeters. The muon veto algorithm rejects events with total energy deposition in the electromagnetic and hadronic calorimeters (at the electromagnetic scale) below 5 GeV. Since the energy threshold for the calorimeter-seeded reconstruction of a τ candidate is 10 GeV (at the jet energy scale), this veto is fully efficient for these candidates.

4.3 τ reconstruction and identification performance in data

Prior to the start of data-taking, understanding of the expected performance of the τ reconstruction and identification relied on Monte Carlo simulations [59, 140]. More detailed understanding could only be achieved after the detector was in place and physics signals could be used for performance studies and for validation or tuning of the simulation.

In years 2008-2009 the ATLAS detector, already commissioned in its underground cavern, collected several hundred million cosmic ray events. Because cosmic ray muons interact with the detector mainly as minimum-ionising particles, most traverse all of the sub-detectors along their flight path. So, in addition to each sub-detector specific cosmic ray studies, these data samples provided the first opportunity to study the combined performance of different detector components and thus were used also for the test of the τ reconstruction and identification [9]. Since no τ leptons were expected in the cosmic ray data sample, the focus of this study was to exercise the algorithms designed to identify them, and to investigate how well the quantities used for the selection are modelled in the simulation. Good agreement between data and cosmic ray Monte Carlo for the properties of track- and calo-seeded τ candidates was found, in particular for quantities used in the identification algorithms.

The studies on the τ performance algorithms were continued with the first data coming from pp collisions. In December of 2009, shortly after the single-beam commissioning of the LHC, the ATLAS experiment recorded data from pp collisions at the centre-of-mass energy of 900 GeV. This data set was used to study τ identification variables [10]. These events were preselected using a minimum-bias trigger and dominated by soft interactions. While the number of actual τ leptons in this data sample was expected to be negligible, it still could be used to prepare for the commissioning of the τ reconstruction and identification algorithms at higher energies. The analysis was continued with the data from pp collisions at the centre-of-mass energy of 7 TeV [11, 12]. The following, more evolved, studies of the background rates for the τ identification are described below.

4.3.1 Estimation of QCD multijets background efficiency as a function of signal efficiency

Results presented in this Section are obtained with the signal derived from Monte Carlo samples with true hadronic τ decays ($W \to \tau\nu, Z \to \tau\tau$) and the background evaluated on data sample obtained from a selection of di-jet events collected by ATLAS in autumn 2010 [136]. As the signal, only reconstructed τ candidates coming from true τ hadronic decays and with $|\eta| < 2.5$ and $p_{\mathrm{T}} > 10$ GeV, are used. The reconstructed number of tracks is required to match the true number of prongs. Background di-jet events have to pass the L1 jet trigger and have at least two τ candidates, a leading one with $p_{\mathrm{T}} > 30$ GeV and a sub-leading one with $p_{\mathrm{T}} > 15$ GeV. $\Delta\phi$ between leading and

sub-leading candidates should be $\Delta\phi > 2.7$ rad. The leading candidate should be the one used by the L1 trigger and it is further ignored to avoid trigger bias. Only the sub-leading candidate is considered for identification and efficiency calculations. Using the reconstructed variables described in Section 4.2.1 as an input, discriminants for identification (Id) of τ candidates are designed to accept true hadronic decays of τ leptons and reject fake candidates reconstructed from QCD multijet events. Distributions of those variables for both signal and background are shown in Figures 4.4-4.6.

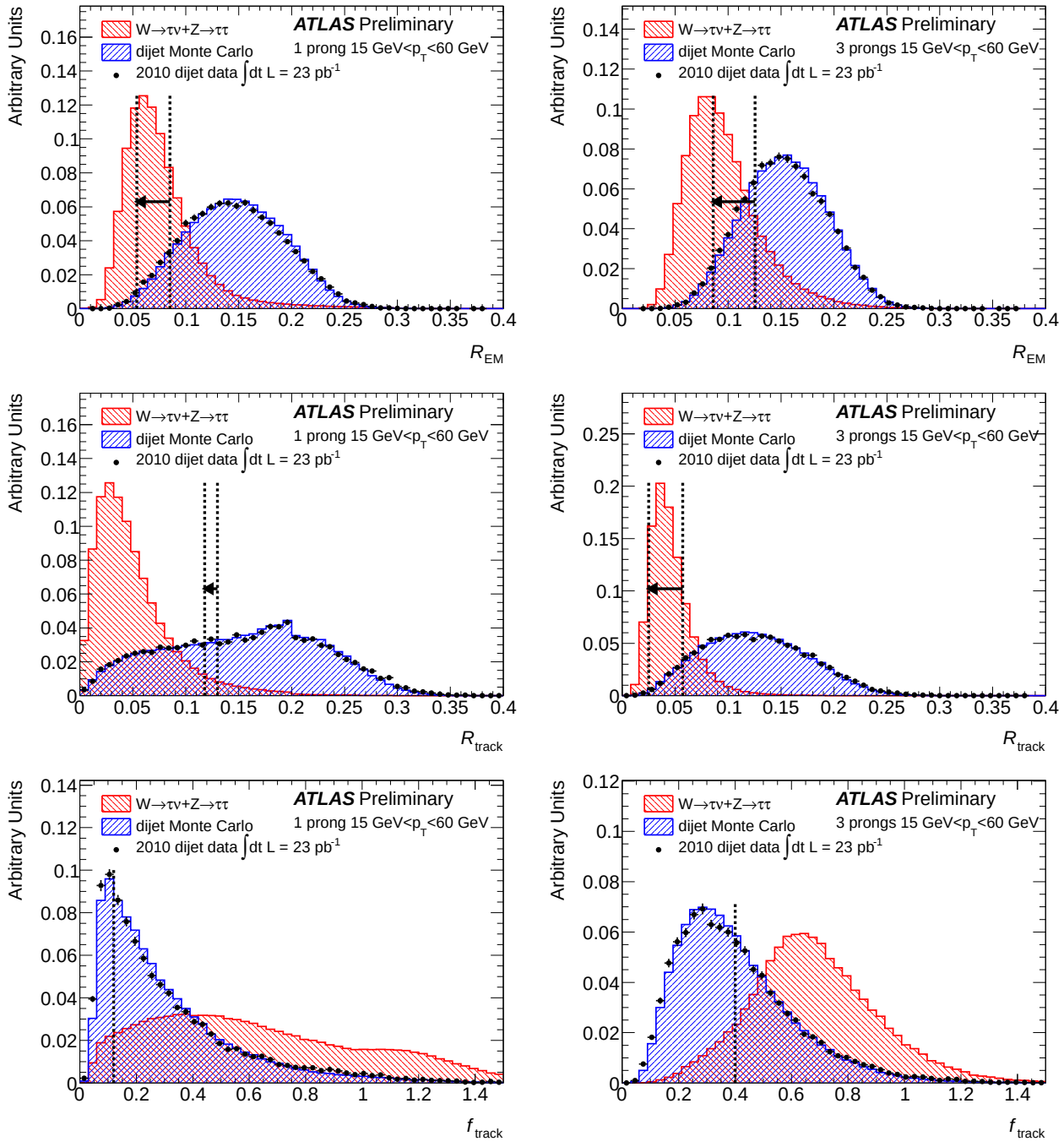

Figure 4.4: Distributions of R_{EM}, R_{track}, and f_{track}, for 1-prong (left) and 3-prong (right) τ candidates. The dashed lines indicate the cut boundaries for the cut-based identification. Since the cuts on R_{EM} and R_{track} are parametrised in p_{T}, the characteristic range of the cut values is shown for candidates with p_{T}= 20 GeV (60 GeV) by the right (left) dashed line [136].

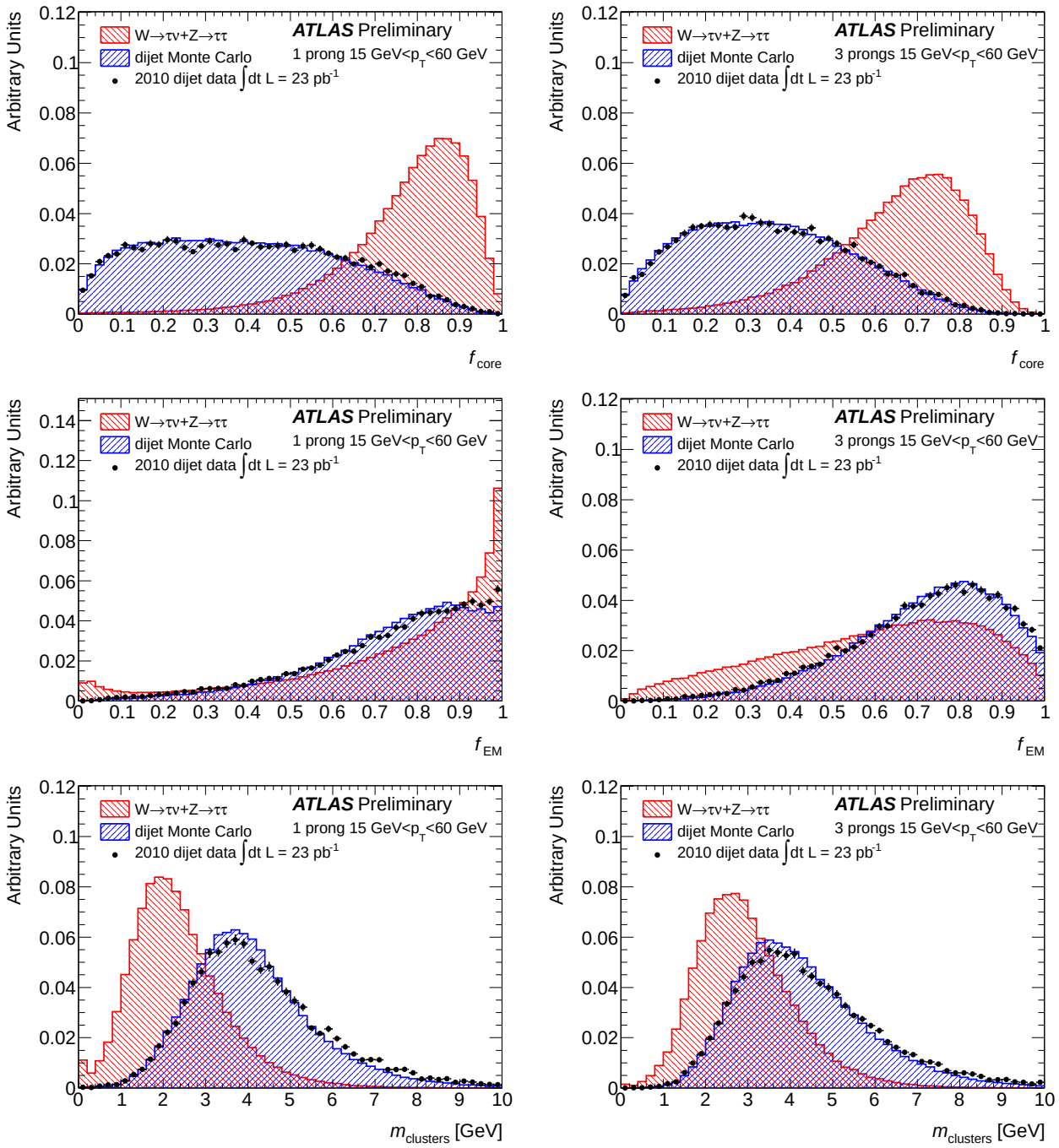

Figure 4.5: Distributions of f_{core}, f_{EM}, and m_{clusters}, for 1-prong (left) and 3-prong (right) τ candidates [136].

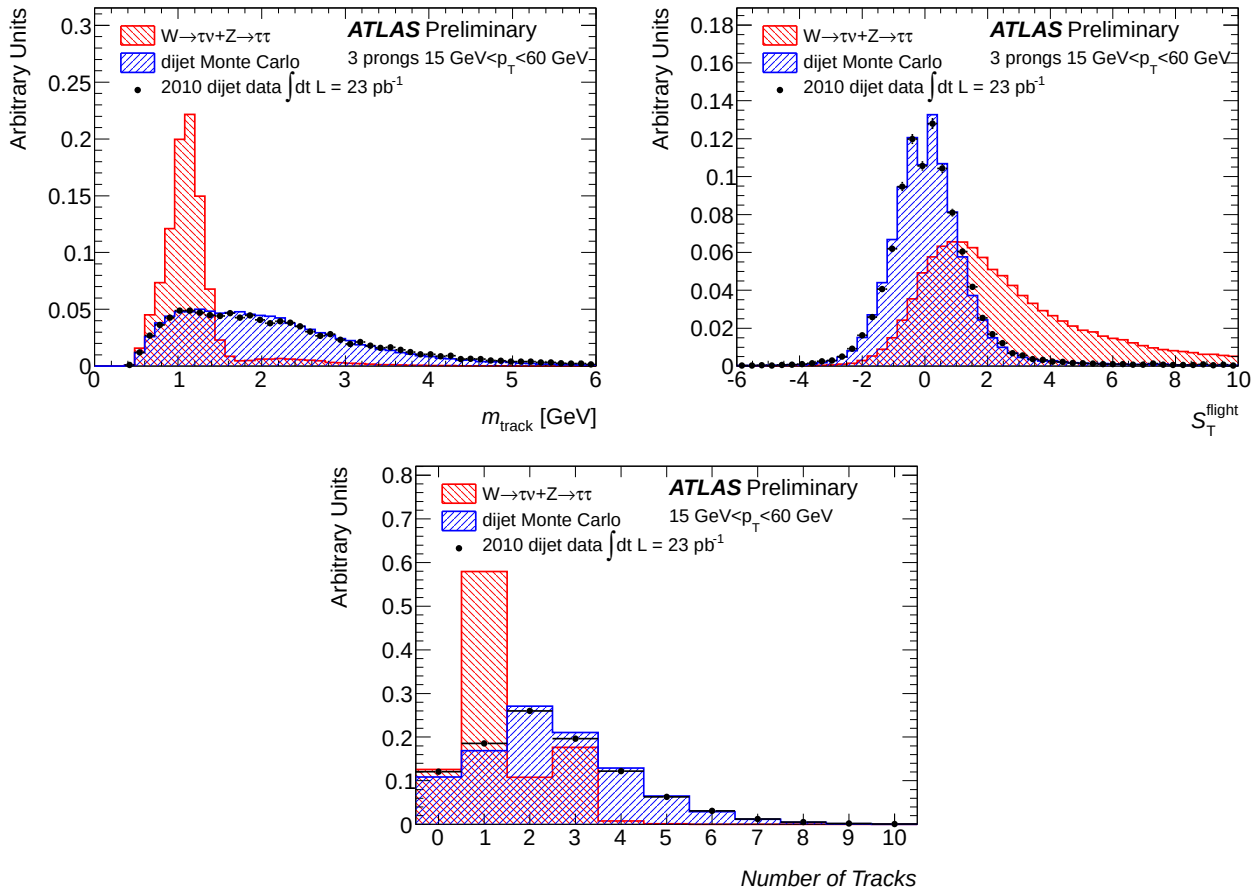

Figure 4.6: Top: Distributions of m_{tracks} (left) and $S_{\text{T}}^{\text{flight}}$ (right) for 3-prong τ candidates. Bottom: Distribution of the number of associated tracks to the τ candidates [136].

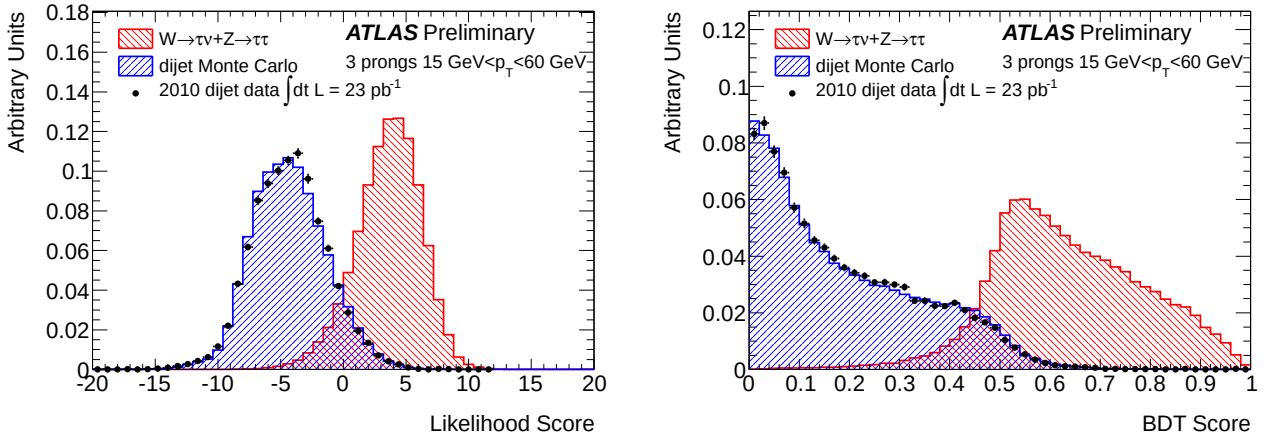

(a) (b)

Figure 4.7: The projective likelihood (a) and BDT (b) scores for 3-prong τ candidates [136].

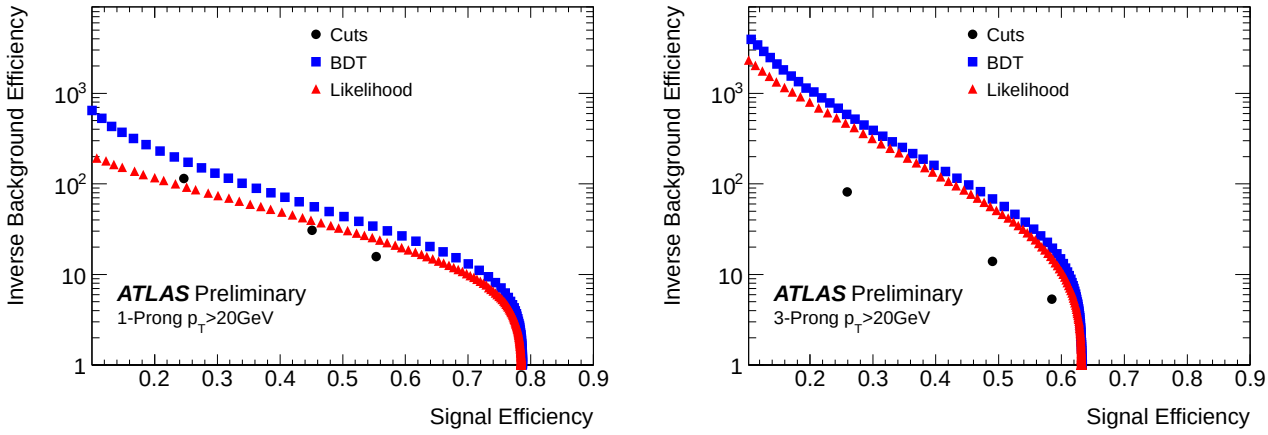

(a) (b)

Figure 4.8: Inverse background efficiency versus signal efficiency for all discriminants on 1-prong and 3-prong τ candidates with $p_{\mathrm{T}} > 20$ GeV [136].

As described in Section 4.2.1 three different discriminants are used: a cut-based selection, projective likelihood identification, and identification with BDT. An example of the projective likelihood and BDT scores for 3-prong τ candidates is shown in Figure 4.7.

The following definitions of the signal and background efficiencies are used.

Signal efficiency:

$$\varepsilon_{\mathrm{sig}}^{\text{1/3-prong}} = \frac{\left(\begin{array}{l}\text{\# of } \tau \text{ candidates with 1/3 reconstructed track(s), passing Id, and}\\ \text{truth-matched to a simulated 1/3-prong decay}\end{array}\right)}{(\text{\# of simulated } \tau_{\mathrm{had}} \text{ with 1/3 prong(s)})}$$

Background efficiency:

$$\varepsilon_{\mathrm{bkg}}^{\text{1/3-prong}} = \frac{(\text{\# of } \tau \text{ candidates with 1/3 reconstructed track(s), passing Id})}{(\text{\# of } \tau \text{ candidates with 1/3 reconstructed track(s)})}$$

The discriminants are optimised in p_{T}, η and one or 3-prong bins. Candidates with no reconstructed tracks fail the identification by definition. Multi-prong candidates use the same discriminant as for 3-prong candidates.

The τ_{had} signal and QCD multijet background efficiencies for each identification method are presented in Figure 4.8 for 1-prong and 3-prong candidates with $p_{\mathrm{T}} > 20$ GeV. The upper bound on the signal efficiency is limited by the tracking reconstruction efficiency and hence worse for 3-prong candidates.

The background efficiency depends on the p_{T} distribution of the τ candidates and the type of partons that initiated the jets. It can differ by as much as a factor of five, depending on whether the jet is quark or gluon initiated [141].

Physics analyses use the τ Id mainly in combination with an electron veto. Therefore, signal efficiencies and their systematic uncertainties are also evaluated in combination with the electron veto. Several combinations, called *working points*, of τ Id for 1-prong candidates, 3-prong candidates and electron veto are studied.

Expected signal efficiencies for the *looser* working point are in the range of 50 – 60% for the cut-based and likelihood-based identification methods and 40 – 50% for the BDT. For the *tighter* working point, the expected signal efficiencies are reduced to about 30% for the cut-based and about 40% for the likelihood-based identification methods and about 30% for the BDT. Figure 4.9 shows signal efficiencies for one exemplary working point corresponding to tighter selection, for each of the three discriminating methods. The systematic uncertainties on the τ Id efficiencies are evaluated using Monte Carlo samples with varied conditions in the event generation, detector

material, shower modelling, and reconstruction. Signal efficiencies obtained with those samples are presented by different labels in Figure 4.9. The yellow bands correspond to the final systematic uncertainty obtained by adding in quadrature the contributions from each source of systematic uncertainty.

For the looser working points, the estimated systematic uncertainty is in the range of (4-7)%, while for the tighter working points, the systematic uncertainty is near 10%. For candidates with $p_{\mathrm{T}}<$ 20 GeV, the systematic uncertainty is dominated by the shower modelling and the topological clustering noise threshold, while for higher p_{T} candidates, only the systematic contribution of the clustering threshold dominates.

First attempt to estimate the τ signal efficiency from data using the Standard Model process $W \rightarrow \tau\nu$ is described in Section 5.3.

4.3.2 Measurement of the τ mis-identification probability from QCD jets

The mis-identification of QCD jets as τ candidates is determined using different processes [141]. Events, where jets originate mainly ($\sim$ 90%) from quarks are obtained in the γ+jet selection. Events with a fraction of $\sim$ 65% of jets originating from quarks are selected in the Z($\rightarrow \ell\ell$)+jets analysis. Finally, events with a fraction of $\sim$ 50% of jets originating from quarks are selected in the di-jet/three-jet topology.

The di-jet/three-jet events

The data events considered have to pass one of jet triggers: L1 trigger with E_{T} threshold between 5 and 75 GeV for the early data-taking period and EF trigger with E_{T} threshold between 20 and 95 GeV for the later data-taking period. Events are required to have two jets with $|\eta| < 2.5$ and $p_{\mathrm{T}} > 15$ GeV, which are balanced in ϕ ($\Delta\phi \geq \pi - 0.3$ radians) and p_{T} ($|\Delta p_{\mathrm{T}}| \leq p_{\mathrm{T}}^{\mathrm{max}}/2$), where $p_{\mathrm{T}}^{\mathrm{max}}$ is the p_{T} of the leading jet. From these pairs of jets, one is chosen randomly as the tag jet and the other as as probe jet. Only the latter is used for the mis-identification measurement. In order to remove a very small fraction of events with real τ_{had} pairs, it is required in addition that the tag jet has at least four tracks associated with it. No further requirements are imposed on the probe jet. It is then required that a reconstructed τ candidate with at least one track and with $p_{\mathrm{T}} > 15$ GeV is within $\Delta R = 0.2$ of the probe jet.

The mis-identification probability, f_{Id}, is then calculated as a ratio between number of probe jets identified as τ candidates and number of probe jets reconstructed as τ candidates. Obtained f_{Id} is presented in Figure 4.10 for tighter working point of the cut-based identification algorithm as a function of τ candidate p_{T} for 1-prong and 3-prong τ candidates and for events with 1,2 or >2 reconstructed primary vertices.

The following sources of systematic uncertainties are included: the requirement on the exact level of p_{T} and ϕ balance of the tag and the probe jet and the requirement on the number of tracks in the tag jet. Thus each of these criteria is varied separately and the observed difference in the mis-identification probability is taken as a systematic uncertainty. In addition, the influence of the matching criterion of the probe jets to the reconstructed τ candidates, and the contamination of real τ leptons in the sample of probe jets was investigated and found to be negligible.

For the three-jet topology study, triplets of jets are selected, each of them satisfying $p_{\mathrm{T}}>$ 15 GeV and $|\eta| < 2.5$. These triplets are selected such that one of the jets is balanced in p_{T} and ϕ by the two other jets. From the latter, one is chosen randomly as a probe jet. The mis-identification probabilities are calculated in the same way as for the di-jet topology. Differences in the mis-identification probability compared to the di-jet topology of up to 40% are observed, due to the softer probe jet p_{T} spectrum and the denser environment in the three-jet events.

The γ+jet events

The mis-identification probability of τ candidates from hadronic jets can also be determined from topologies where a jet is balanced in p_{T} and ϕ by a photon. In order to select such events, EF photon triggers with E_{T} thresholds between 10 and 40 GeV including loose and tight photon identification are used. Exactly one isolated photon candidate is required in the event, with $p_{\mathrm{T}}>$ 15 GeV and within the pseudorapidity range of $|\eta| < 2.47$, excluding the transition region in the calorimeters. The jet in the event is selected requiring the same criteria for p_{T}, η and ϕ balance as for the di-jet topology. The results for the mis-identification probability obtained with these events

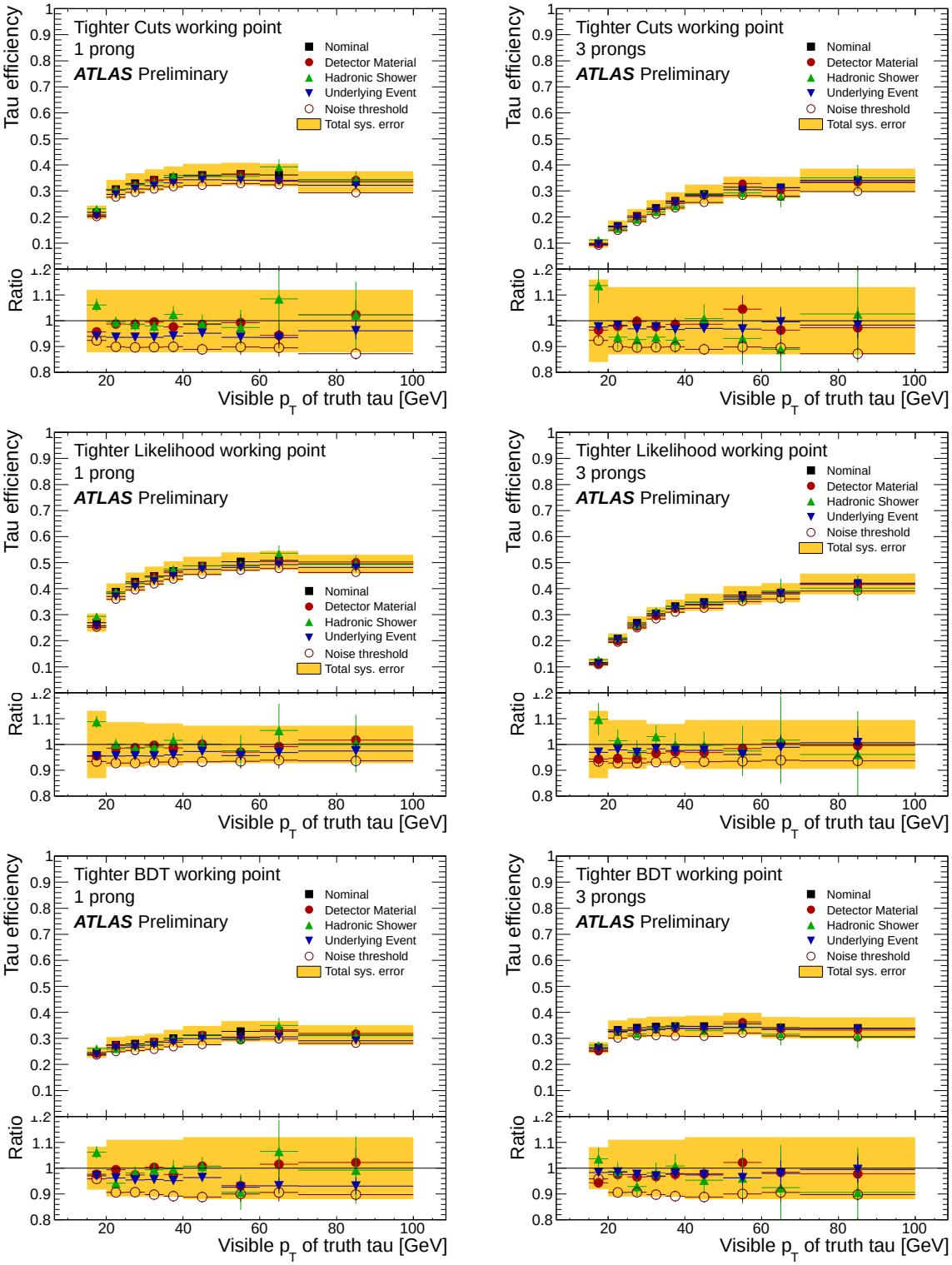

Figure 4.9: Signal efficiencies for the tighter working point as a function of p_{T} for 1-prong (left) and 3-prong candidates (right). Different labels correspond to signal efficiencies obtained for the different sources of systematic uncertainties. The ratio of the signal efficiency obtained from the modified event samples to that in the sample used in the analysis (nominal sample) is also presented. The first row shows the efficiency for the cuts; the second shows the likelihood; the third shows the BDT. The yellow band shows the total systematic uncertainty [136].

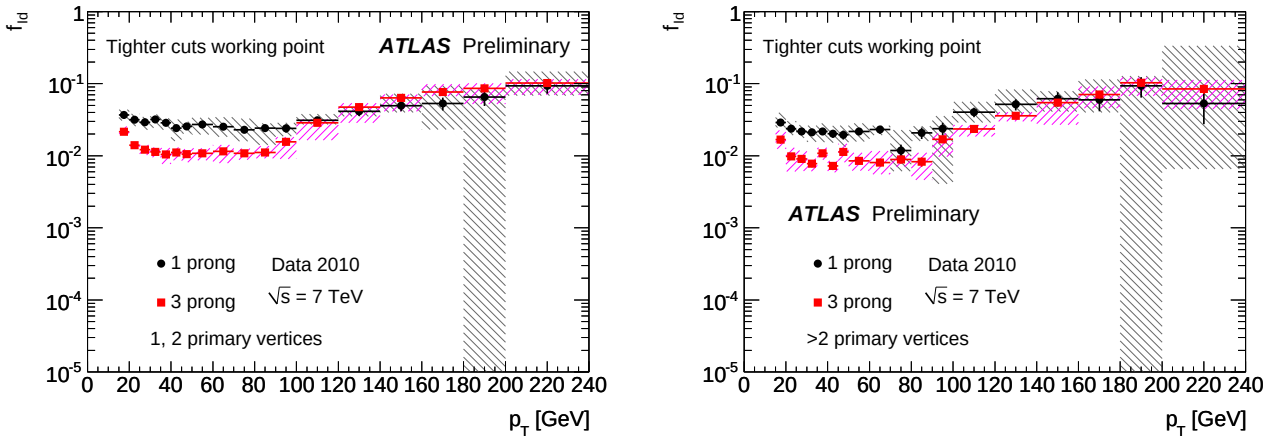

Figure 4.10: The mis-identification probability of QCD multijets from di-jet topologies as τ candidates shown as a function of τ candidate p_{T} for 1-prong and 3-prong τ candidates in events with one or two primary vertices (a) and more than two primary vertices (b) for the tighter working point of the cut-based identification algorithm. The statistical errors are represented by vertical bars; the shaded areas correspond to the total uncertainty. Large errors in some bins are due to the statistical fluctuations in samples used for estimation of systematic uncertainties [141].

are shown in Figure 4.11 for the tighter working point of the cut-based identification algorithm as a function of τ candidate p_{T} for 1-prong and 3-prong τ candidates and for events with 1,2 or >2 reconstructed primary vertices.

The same sources of systematic uncertainty as for the di-jet topology are considered with one exception: instead of considering requirement on the number of tracks in the tag jet, the effect of loosening the photon identification criteria by dropping the isolation requirement is considered. This increases the contamination of the selected event sample with di-jet events, thereby increasing the fraction of gluon-initiated probe jets and reducing the mis-identification probability by about 10%. This difference is included in the total systematic uncertainty.

The Z($\rightarrow \ell\ell$)+jets events

Finally, the mis-identification probability of τ candidates from QCD jets can be derived from the additional jets in Z($\rightarrow \ell\ell$)+jets events. Events are selected with one electron (muon) with an E_{T} (p_{T}) threshold of 15 GeV at EF trigger level. Electrons are required to have $E_{\mathrm{T}} > 20$ GeV and be inside $|\eta| < 2.47$, excluding the transition region in the calorimeters. Both electrons are required to pass medium electron identification. Muons are required to have $p_{\mathrm{T}} > 20$ GeV and be within $|\eta| < 2.5$. Additional quality criteria for each muon track reconstructed in the ID have to be satisfied [125]. Only events where the invariant mass of the tag leptons fall inside the Z mass window $71 < m_{\ell\ell} < 111$ GeV are selected.

The probability of QCD jets to be mis-identified as τ candidates is calculated from the additional τ candidates reconstructed in the event, satisfying $p_{\mathrm{T}} > 15$ GeV, $|\eta| < 2.5$ cuts and having one or three associated track. It is required in addition, that no electron or muon candidates are reconstructed within $\Delta R < 0.4$ around the τ candidate. The mis-identification probability is displayed in Figure 4.12 for the tighter working point of the cut-based identification algorithm as a function of τ candidate p_{T} for 1-prong and 3-prong τ candidates.

The sources of systematic uncertainties are the choice of the invariant mass window for the tag leptons which is varied, $80 < m_{\ell\ell} < 100$ GeV, reducing the expected background by roughly a factor of two, and the uncertainty on the energy scale of the electrons or muons, which is assumed to be 2%.

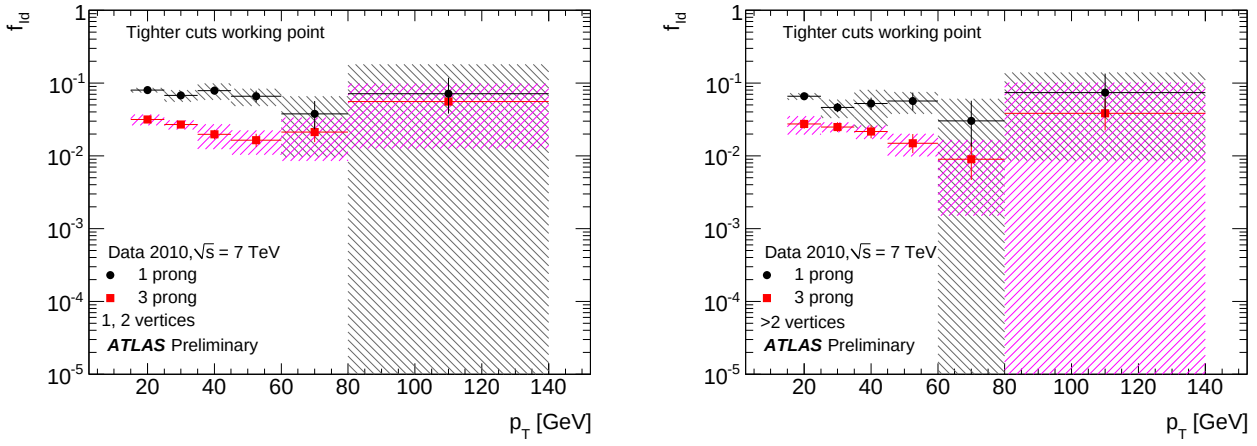

(a) (b)

Figure 4.11: The mis-identification probability of hadronic jets from γ+jet topologies as τ candidates. These are shown as a function of τ candidate p_{T} for 1-prong and 3-prong τ candidates in events with one or two primary vertices (a) and more than two primary vertices (b) for tighter working point of the cut-based identification algorithm. The statistical errors are represented by vertical bars; the shaded areas correspond to the total uncertainty. Large errors in some bins are due to the statistical fluctuations in samples used for estimation of systematic uncertainties [141].

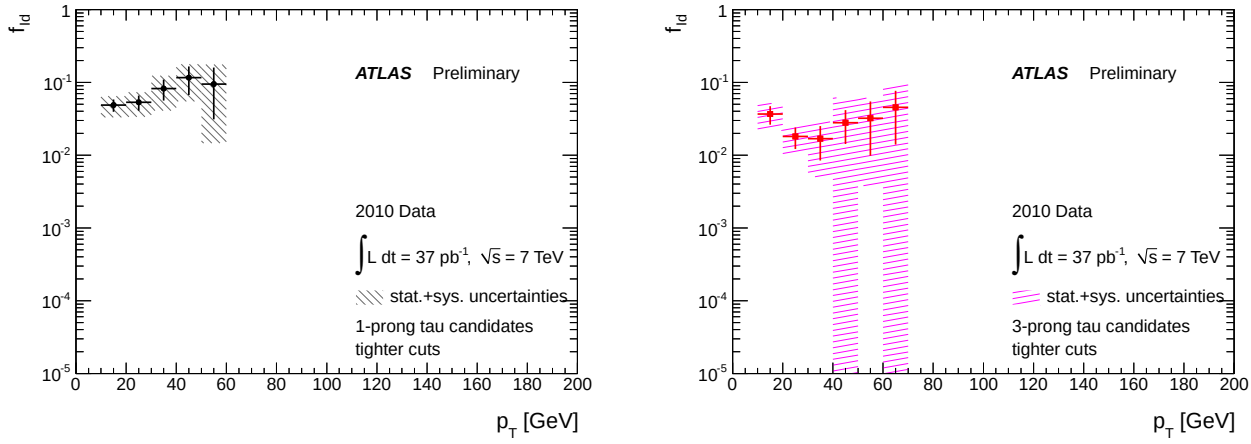

(a) (b)

Figure 4.12: The probability of hadronic jets from Z($\rightarrow \ell\ell$)+jets to be mis-identified as τ candidates as a function of τ candidate p_{T} for 1-prong (a) and 3-prong (b) τ candidates, for the tighter working point of the cut-based identification algorithm. The statistical errors are represented by vertical bars; the shaded areas correspond to the total uncertainty. Large errors in some bins are due to the statistical fluctuations in samples used for estimation of systematic uncertainties [141].

Summary of the measurements of the mis-identification from QCD jets

The mis-identification probabilities range from 10% to 0.1%, depending on the τ identification algorithm chosen, the number of prongs of the τ candidate, its p_{T}, the origin of the QCD jet being reconstructed as a τ candidate and the number of primary vertices found in the event. The differences in mis-identification probabilities found in the various topologies are attributed to the different fraction of quark-initiated jets (as opposed to gluon-initiated jets) in the topologies studied. When separating quark-initiated and gluon-initiated jets on truth-level, Monte Carlo studies indicate that good agreement of the mis-identification probabilities is observed across the three different samples studied.

4.3.3 Measurement of the mis-identification from electrons

The probability of an electron to be mis-identified as τ candidate is measured in a sample of $Z \rightarrow ee$ events. Events passing the electron EF trigger with a threshold of $E_T = 15$ GeV and medium identification criteria are selected. The electron candidate used by the trigger is required to have $p_{\mathrm{T}} > 30$ GeV and $|\eta| < 2.47$ (excluding the transition region in the calorimeters). In addition, the tag electron has to pass tight identification and has to be isolated from the rest of the event, $I_{PT}^{0.4} < 0.06$. As the probe, a reconstructed τ candidate with $p_{\mathrm{T}} > 15$ GeV and $|\eta| < 2.5$ is selected. It has to have exactly one track associated. The 3-prong τ candidates are not used due to the too high background level.

The invariant mass of the tag-and-probe pair is required to fall inside the Z mass window $80 < m_{ee} < 100$ GeV. In order to suppress remaining backgrounds, mainly from $W \rightarrow e\nu$ processes, $E_{\mathrm{T}}^{\mathrm{miss}} < 20$ GeV is required, where the simple definition of the missing transverse energy is used as described in Section 3.5.

The probe candidates, satisfying the criteria above, are then subjected to the τ identification algorithms and to the electron veto. The mis-identification probability, f_{Id}, is defined as a ratio of number of probe candidates passing electron veto and τ Id and number of probe candidates. The mis-identification probabilities for the tighter working point of the cut-based identification algorithm are shown in Figure 4.13 as a function of p_{T} and $|\eta|$ of the probe candidate. The mis-identification probability is of the order of 1% for probe candidates with $p_{\mathrm{T}} > 20$ GeV independent of the τ identification algorithm applied. The influence of pile-up on the mis-identification probability of electrons as τ candidates is negligible.

Sources of systematic uncertainties considered are the background estimation, the energy scale of the probe electron and the choice of the signal mass window. However, the result is dominated by the current statistical uncertainties that are as large as ±50%.

4.4 Summary

The ATLAS package for reconstruction and identification of hadronically decaying τ leptons has gone a long way from a simple calorimeter-based algorithm [142] to the sophisticated, robust and effective one, described in this Chapter. The algorithm, tuned primarily only on Monte Carlo samples, was successfully validated on cosmic ray data and then on the first proton-proton collisions and finally optimised using full data sample collected in 2010. It appeared as ready to be used in the first studies with τ leptons in final states. Obtained performance is comparable to the one reported by the CMS collaboration [143].

In this Chapter, the reconstruction, energy scale calibration and identification of hadronically decaying τ leptons are presented. Three alternative identification methods are optimised to discriminate τ leptons from QCD jets: a cut-based discriminant, discrimination with a projective likelihood, and discrimination with boosted decision trees. A cut-based discriminant is optimised to reject electrons mis-identified as τ leptons. The versions of the algorithms described are those defined for data analysis of 2010 data and first half of 2011. The τ signal efficiency and the τ energy scale calibration and their systematic uncertainties are estimated from Monte Carlo samples. The mis-identification rate of QCD jets as τ candidates is determined using data samples with di-jet/three-jet events, γ+jet and Z($\rightarrow \ell\ell$)+jets events. The probability of an electron to be mis-identified as τ candidate is measured in a sample of $Z \rightarrow ee$ events.

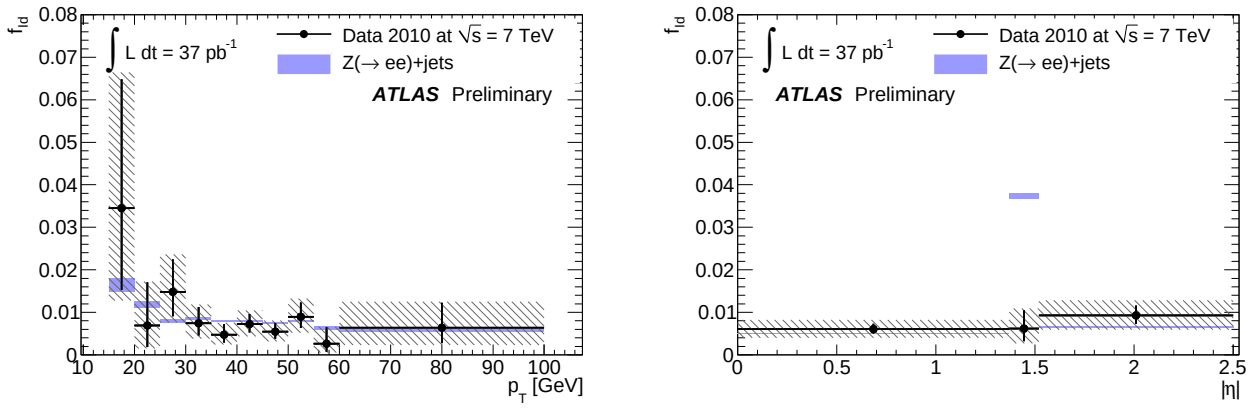

(a) (b)

Figure 4.13: The mis-identification probabilities as a function of τ candidate p_{T} (a) and $|\eta|$ (b) for the tighter working point of the cut-based identification algorithm. The dots are the data and the error bars represent the statistical uncertainty of the measurement with the shaded areas representing the total uncertainty. The squares represent the predictions from Monte Carlo, with the shaded areas representing the statistical uncertainty of the simulation [141].

Presented results are based on the first data collected by the ATLAS experiment and thus on small statistics. However it should be mentioned that since then, upon completion of this monograph, a lot of progress has been done. It concerns mainly performance of the τ reconstruction and identification [144] and determination of the τ energy scale and the associated systematic uncertainty [145]. In the latter case the first attempts to use $Z \rightarrow \tau\tau$ events for the in-situ measurement of the τ energy scale are presented.

As will be shown in the next Chapters, analyses with τ_{had} in final states suffer from background coming from mis-identification of electrons as τ candidates. In this Chapter only cut-based electron veto was described as used on the first data but presently also the BDT based electron veto exists giving a much better performance.

Polarisation in τ lepton decays can be measured through the kinematics of their decay products, especially in τ_{had} decays. The key element in those studies is reconstruction of neutral pions from τ_{had} decays. Their reconstruction can also improve τ identification by considering different decay modes separately. Even simple counting of neutral pions can help as decays without them will have an excellent energy resolution from the ID tracks. Good mass resolution is the only handle against dominant $Z \rightarrow \tau\tau$ background in $H \rightarrow \tau\tau$ searches. There is ongoing work on identification of π^0's within τ candidates using topoclusters from τ candidates jet seeds. Another developed method is similar to the one described in this Chapter but using parametrised hadronic shower profiles for subtracting the contribution from charged pions.

The remaining issue is also optimisation of τ reconstruction and identification for high p_{T}, when τ candidates form very narrow jets and reconstruction of 3-prong candidates starts to be challenging for the tracker. Such studies are crucial for searches for high mass resonances described in Section 2.5. Also, better fake τ candidates rejection is the key for improving the sensitivity for the $H \rightarrow \tau\tau$ searches. Finally, the τ reconstruction algorithm should be re-optimised to be less sensitive to pile-up which increased significantly in 2011 and 2012 data runs.

All above possible improvements are mentioned here only for completeness. Their detailed description and first results are out of the scope of this monograph.

Nothing is a waste of time if you use the experience wisely.

Auguste Rodin

5 Standard Model processes with τ leptons

In Chapter 2 the role of τ leptons in the search for New Physics phenomena at the LHC was discussed. Decays of Standard Model gauge bosons to τ leptons, $W \to \tau\nu$ and $Z \to \tau\tau$ are important background processes in such searches and their production cross sections need to be measured precisely. This is described in detail in Sections 5.1 and 5.2. Given a large cross section for these processes, they offer the first opportunity to study τ hadronic decays in the ATLAS experiment. The $W \to \tau\nu$ and the $Z \to \tau\tau$ decays are crucial to estimate τ lepton detection performance. An example application of the measured $W \to \tau\nu$ cross section to τ identification studies is presented in Section 5.3.

The data sample used in described analyses corresponds to a total integrated luminosity of (34 – 36) pb^{-1}, recorded with stable beam conditions and a fully operational ATLAS detector in 2010.

5.1 $Z \to \tau\tau$ cross section measurement

The $Z \to \tau\tau$ cross section measurement is performed using four different final states [16]. Two of them are the semileptonic modes, $\tau_\mu\tau_{\text{had}}$: $Z \to \tau_{\text{lep}}\tau_{\text{had}} \to \mu$ + hadrons + 3ν and $\tau_e\tau_{\text{had}}$: $Z \to \tau_{\text{lep}}\tau_{\text{had}} \to e$ + hadrons + 3ν with branching fractions (22.50 ± 0.09)% and (23.13 ± 0.09)%, respectively [46]. The remaining two final states are the leptonic modes, $\tau_e\tau_\mu$: $Z \to \tau_{\text{lep}}\tau_{\text{lep}} \to e\mu + 4\nu$ and $\tau_\mu\tau_\mu$: $Z \to \tau_{\text{lep}}\tau_{\text{lep}} \to \mu\mu + 4\nu$ with branching fractions (6.20 ± 0.02)% and (3.01 ± 0.01)%, respectively [46]. The semileptonic final state consists of an isolated lepton ℓ[1] and a τ candidate of opposite charge, as well as missing energy from the two τ decays. Those final states are advantageous as they provide an isolated lepton which can be triggered on. This feature makes them attractive for studies of the τ trigger and offline τ identification, as they can provide an unbiased sample of hadronic τ decays. Due to the large expected QCD multijet background contamination, the $Z \to \tau_{\text{had}}\tau_{\text{had}}$ and $Z \to \tau_{\text{lep}}\tau_{\text{lep}} \to 2e + 4\nu$ final states are not considered.

The $Z \to \tau\tau$ cross section has been measured previously in $p\bar{p}$ collisions at the Tevatron using the semileptonic τ decay modes [146, 147]. More recently the cross section was measured in pp collisions at the LHC by the CMS Collaboration, using both the semileptonic and leptonic modes [148].

As mentioned in Section 4.2, identification of τ_{had} decays is difficult and suffers from high fake rates, much higher than the fake rates from the identification of electrons or muons. Because of this, most of the backgrounds relevant for these final states involve a true lepton along with a QCD jet mis-identified as a τ candidate. The two leptonic modes are characterised by two isolated leptons of typically lower transverse momentum than those in $Z \to ee/\mu\mu$ decays. The $\tau_e\tau_\mu$ mode gives much cleaner signature as it does not suffer from τ mis-identification but

[1] The ℓ refers to either an electron or a muon in this monograph.

its yield is much lower. The $\tau_\mu\tau_\mu$ leptonic mode is overwhelmed by the $\gamma^*/Z \to \mu\mu$ production. A brief summary of the considered backgrounds is given below:

- **QCD multijet** - dominant background due to its large cross section. The lepton could be true (e.g. muons produced from heavy flavour decays) or fake, while the τ candidate is typically a mis-identified quark or gluon-initiated jet.

- **W + jets** - with a cross section about an order of magnitude higher than the signal, where the W decays leptonically while an associated mis-identified quark or gluon jet provides the fake τ candidate or second lepton, real or fake. The lepton and the jet in this process are biased towards having an opposite sign, similarly to the signal.

- $\boldsymbol{\gamma^*/Z \to ee, \mu\mu}$ - produces two oppositely charged leptons of the same flavour and is a dominant background in the $\tau_\mu\tau_\mu$ channel. The $\tau_e\tau_\mu$ channel is affected by this background if one of the leptons escapes detection and additional jets in the event contain hadrons that either decay leptonically or fake leptons. In the semileptonic final states this process can form a background if one of the leptons is mis-identified as a τ candidate, or if the γ^*/Z is produced in association with a jet mis-identified as a τ candidate and at the same time one of the leptons is not reconstructed.

- $\boldsymbol{t\bar{t}}$ - can contain a true τ lepton, or either jets or leptons that fake a τ_{had} as well as at least one real electron or muon. However, compared to other backgrounds the cross section for this process is small, making it less important.

Di-boson production has a much smaller cross section than the signal, and contributes to the background only in a very minor way. Possible contributions to the background from single-top and γ+jet production are found to be negligible.

5.1.1 Data and Monte Carlo samples

Events are selected using either single-muon or single-electron triggers. For the $\tau_\mu\tau_{\text{had}}$ and $\tau_\mu\tau_\mu$ final states, single-muon triggers requiring $p_{\text{T}} > (10 - 13)$ GeV, depending on the run period, are used. For the $\tau_e\tau_{\text{had}}$ and $\tau_e\tau_\mu$ final states, a single-electron trigger requiring $E_{\text{T}} > 15$ GeV is used. The efficiency for triggers is determined from data using a tag-and-probe method. The muon trigger efficiency is measured using $Z \to \mu\mu$ events and found to be close to 95% in the end-cap region, and around 80% in the barrel region. The electron trigger efficiency is measured using $W \to e\nu$ and $Z \to ee$ events and found to be $\sim$ 99% for offline electron candidates with $E_{\text{T}} > 20$ GeV and $\sim$ 96% for electron candidates with E_{T} between 16 and 20 GeV [105].

The inclusive W and γ^*/Z signal and background MC samples are generated with PYTHIA 6.421 [112] and are normalised to next-to-next-to-leading order (NNLO) cross sections [149, 150, 151]. For the $t\bar{t}$ sample the MC@NLO generator is used [152], while the di-boson samples are generated with HERWIG [113]. In all samples τ decays are modelled with TAUOLA [114]. All generators are interfaced to PHOTOS [116] to simulate the effect of final state QED radiation.

5.1.2 Selection of $Z \to \tau\tau$ candidates

Objects selection

Only events containing at least one primary vertex with three or more associated tracks, as well as fulfilling pre-selection requirements described in Section 3.6 are used in the analysis. As the next step following reconstructed objects are selected.

Combined muon candidates with $p_{\text{T}} > 15$ GeV for the $\tau_\mu\tau_{\text{had}}$ final states and $p_{\text{T}} > 10$ GeV for the $\tau_e\tau_\mu$ and $\tau_\mu\tau_\mu$ final states are used. Muon candidates are required to have $|\eta| < 2.4$ and a longitudinal impact parameter of less than 10 mm with respect to the primary vertex. In the final muon selection, combined muon tracks are also

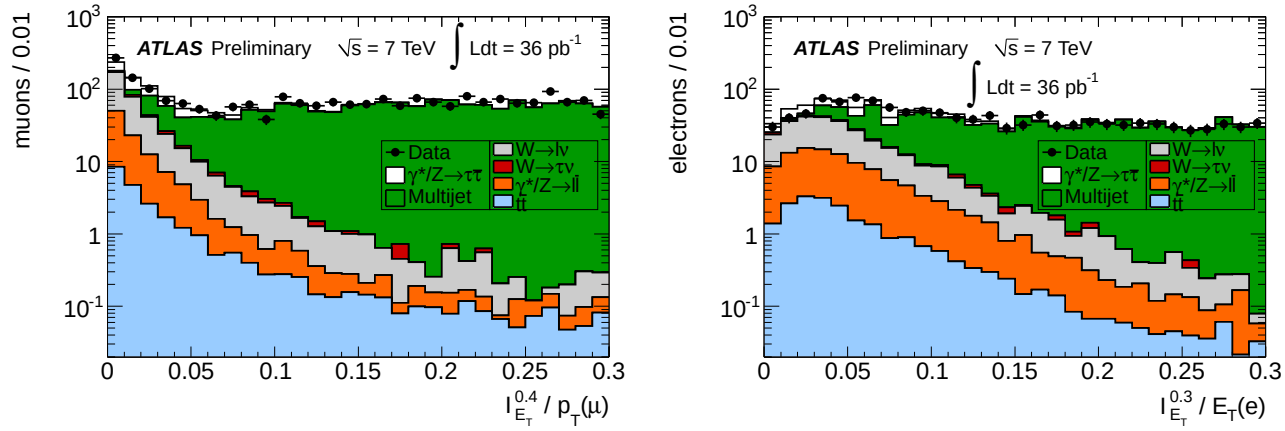

(a) (b)

Figure 5.1: Isolation (a) $I_{ET}^{0.4}/p_{\mathrm{T}}$ and (b) $I_{ET}^{0.3}/E_{\mathrm{T}}$ for muon and electron candidates, after selecting one τ candidate and one lepton with opposite signs in $\tau_\mu\tau_{\mathrm{had}}$ and $\tau_e\tau_{\mathrm{had}}$ final states. The QCD multijet background is estimated from data (see Section 5.1.3), other processes are estimated using MC [16].

required to pass several Inner Detector track quality criteria [125], resulting in an efficiency of ~ 92%, as measured in data using $Z \to \mu\mu$ events.

Electron candidates are selected if they have $E_{\mathrm{T}} > 16$ GeV and $|\eta| < 2.47$, excluding the transition region in the calorimeters. For the $\tau_e\tau_\mu$ final state, candidates are required to pass the medium identification, with an efficiency of ~ 89%. For the $\tau_e\tau_{\mathrm{had}}$ final state, electron candidates are required to pass the tight identification, with an efficiency of ~ 73%. Efficiencies are measured in data using $W \to e\nu$ and $Z \to ee$ events.

Jets used in this analysis are required to have a transverse momentum $p_{\mathrm{T}} > 20$ GeV and $|\eta| < 4.5$.

τ candidates are selected if they have $p_{\mathrm{T}} > 20$ GeV and $|\eta| < 2.47$, excluding the calorimeter transition region, and if they pass cut-based identification. Additionally, a dedicated selection to reject fake τ candidates from electrons is applied. This leads to an efficiency of ~ 40% (~ 30%) for 1-prong (3-prong) τ candidates as determined from the signal Monte Carlo sample. For fakes from QCD multijets the efficiency is ~ 6% (~ 2%) for 1-prong (3-prong) τ candidates, as measured in data using a di-jet selection. Details of these measurements are described in the previous Chapter.

For missing transverse energy the simple definition described in Section 3.5 is used. There is no direct requirement on $E_{\mathrm{T}}^{\mathrm{miss}}$ applied in this analysis but the quantity and its direction is used in several selection criteria described later.

Leptons from $Z \to \tau\tau$ decays are typically isolated from other particles, in contrast to electrons and muons from QCD multijet events coming mainly from heavy-flavours decays. Hence, isolation requirements (as defined in Section 3.5) are applied to both electron and muon candidates used in the four final states considered. A selection requiring $I_{PT}^{0.4}/p_{\mathrm{T}} < 0.06$ for the muon candidate and $I_{PT}^{0.4}/E_{\mathrm{T}} < 0.06$ for the electron candidate is used for all final states but the $\tau_\mu\tau_\mu$. Due to the presence of two muon candidates, the QCD multijet background is smaller in the latter one, and a looser isolation requirement, $I_{PT}^{0.4}/p_{\mathrm{T}} < 0.15$, increases the signal yield. In addition, for muon candidates, the requirement $I_{ET}^{0.4}/p_{\mathrm{T}} < 0.06$ is applied to all final states except the $\tau_\mu\tau_\mu$ final state where a looser selection, $I_{ET}^{0.4}/p_{\mathrm{T}} < 0.2$, is applied. For electron candidates, a selection requiring $I_{ET}^{0.3}/E_{\mathrm{T}} < 0.1$ is applied in both $\tau_e\tau_{\mathrm{had}}$ and $\tau_e\tau_\mu$ final states. The efficiencies for these isolation requirements are measured in data using $Z \to \mu\mu$ and $Z \to ee$ events and found to be (75−98)% for muons and (60−95)% for electrons, depending on the transverse momentum or energy respectively. Figure 5.1 shows the distribution of the $I_{ET}^{0.4}/p_{\mathrm{T}}$ variable for muon and $I_{ET}^{0.3}/E_{\mathrm{T}}$ variable for electron candidates.

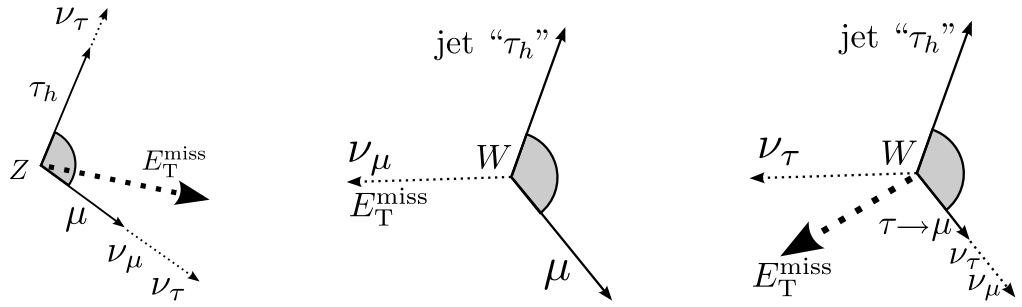

(a) $Z \to \tau\tau \to \mu\tau_{\mathrm{had}}$ (b) $W \to \mu\nu$ (c) $W \to \tau\nu \to \mu\nu\nu\nu$

Figure 5.2: Drawings of the transverse plane orientations of W and Z decay products and the $E_{\mathrm{T}}^{\mathrm{miss}}$. The shaded angles indicate the angle (less than π) between the lepton and the (fake) τ candidate. In (a), the Z is depicted to have nonzero p_{T}, which must be balanced on the left by some other activity omitted for clarity [14].

Event selection

Semileptonic final states For the $\tau_\mu\tau_{\mathrm{had}}$ ($\tau_e\tau_{\mathrm{had}}$) final state, at least one isolated muon (tight electron) candidate with $p_{\mathrm{T}} > 15$ GeV ($E_{\mathrm{T}} > 16$ GeV) and one τ candidate with $p_{\mathrm{T}} > 20$ GeV are required in the event. The QCD multijet background is largely suppressed by the τ identification and lepton isolation requirements. Any event with more than one muon or electron candidate is vetoed, which strongly suppresses background from $\gamma^*/Z \to \ell\ell$ + jets events. To increase background rejection, the selection criteria for the second lepton are relaxed: the ID track quality requirements are dropped for the muons, and the electrons need only to pass the medium selection and have $E_T > 15$ GeV.

After the selection described above, the largest background is W+jets production. It is suppressed by two additional selection criteria based on variables that exploit kinematic correlations between the lepton and the $E_{\mathrm{T}}^{\mathrm{miss}}$. Because the mass of the Z boson is much larger than the mass of the τ lepton, the τ leptons in $Z \to \tau\tau$ are boosted such that their decay products are collimated along the trajectory of the parent τ lepton. Ignoring underlying interactions in the event and mis-measurements of $E_{\mathrm{T}}^{\mathrm{miss}}$, the $E_{\mathrm{T}}^{\mathrm{miss}}$ is the vector sum of the p_{T} of the neutrinos, as shown in Figure 5.2(a). The majority of the produced Z bosons have low p_{T}, and therefore the τ leptons are produced back-to-back, but in the case when the Z has a significant nonzero boost in the transverse plane, the $E_{\mathrm{T}}^{\mathrm{miss}}$ vector falls in the angle between the decay products of the Z.

In contrast, in events from the $W \to \ell\nu$ + jets background, the neutrino, jet, and lepton all point in different directions, balancing p_{T} in the transverse plane, as shown in Figure 5.2(b). Ignoring underlying interactions in the event and mis-measurements of $E_{\mathrm{T}}^{\mathrm{miss}}$, the $E_{\mathrm{T}}^{\mathrm{miss}}$ vector should therefore point along the neutrino which is *not* in the angle between the fake τ candidate and the lepton. In $W \to \tau_{\mathrm{lep}}\nu$ events, shown in Figure 5.2(c), there are two additional neutrinos, but the $E_{\mathrm{T}}^{\mathrm{miss}}$ still tends to point outside of the angle between the fake τ candidate and the lepton. In this analysis this is explored by placing a requirement on:

$$\sum \cos\Delta\phi = \cos\left(\phi(\ell) - \phi(E_{\mathrm{T}}^{\mathrm{miss}})\right) + \cos\left(\phi(\tau_{\mathrm{had}}) - \phi(E_{\mathrm{T}}^{\mathrm{miss}})\right). \tag{5.1}$$

The variable $\sum \cos\Delta\phi$ is positive when the $E_{\mathrm{T}}^{\mathrm{miss}}$ vector points towards the direction bisecting the decay products and is negative when it points away. The distributions of $\sum \cos\Delta\phi$ are shown in Figure 5.3(a) and 5.3(b) for the $\tau_\mu\tau_{\mathrm{had}}$ and $\tau_e\tau_{\mathrm{had}}$ final states, respectively. The peak at zero for $Z \to \tau\tau$ corresponds to events where the decay products were back-to-back in the transverse plane. The W + jets backgrounds accumulate at negative $\sum \cos\Delta\phi$ whereas the $\gamma^*/Z \to \tau\tau$ distribution has an asymmetric tail extending into positive $\sum \cos\Delta\phi$ values, corresponding to events where the Z boson has higher p_{T}. Events are therefore selected by requiring $\sum \cos\Delta\phi > -0.15$. The $\sum \cos\Delta\phi$ variable, in addition to being a good discriminating variable against the W + jets background, is robust against mis-measurements of $E_{\mathrm{T}}^{\mathrm{miss}}$. It is also only a function of the direction of the $E_{\mathrm{T}}^{\mathrm{miss}}$, which is generally more accurately measured than its magnitude. The $E_{\mathrm{T}}^{\mathrm{miss}}$ direction is most susceptible to mis-measurement when the

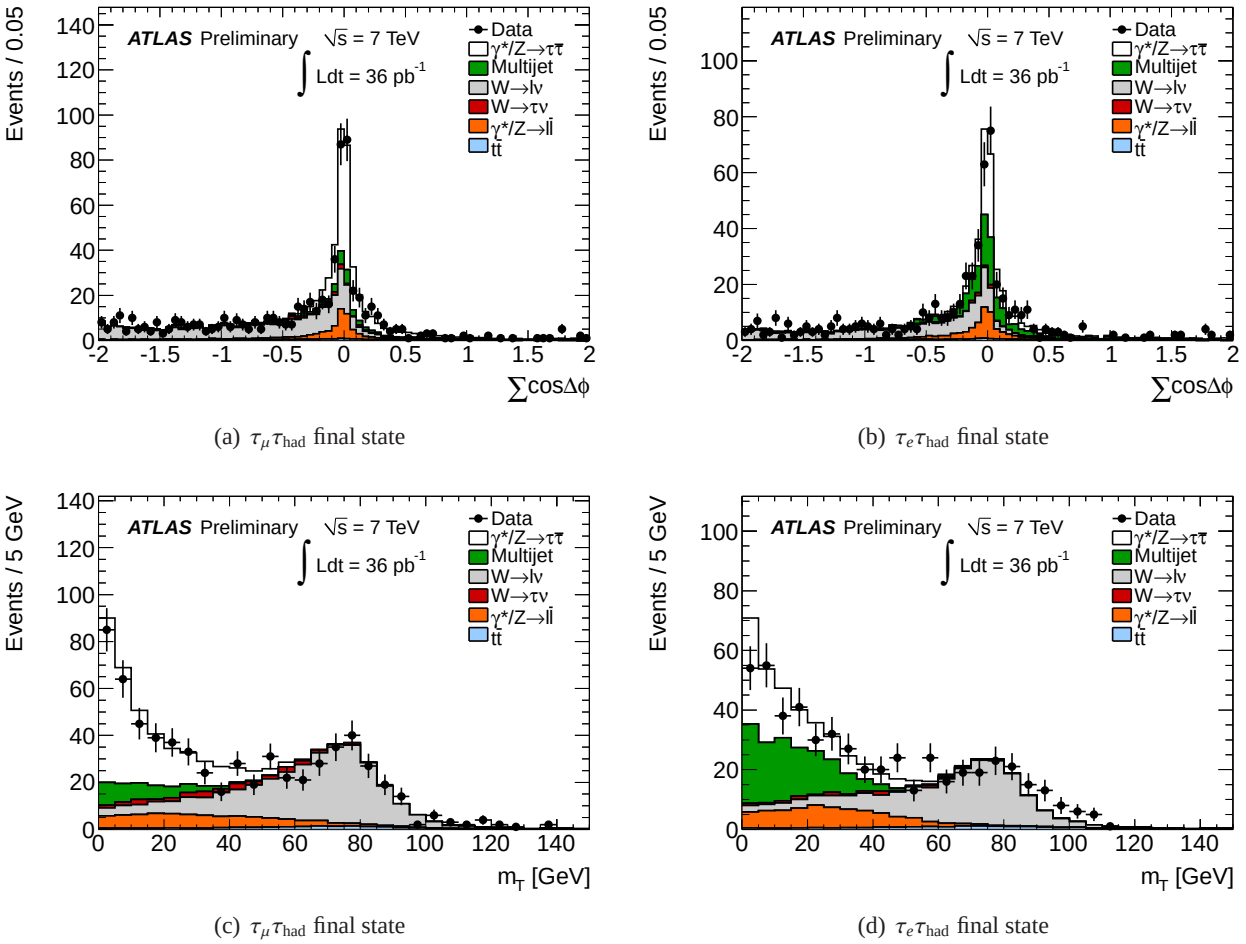

(a) $\tau_\mu\tau_{\text{had}}$ final state

(b) $\tau_e\tau_{\text{had}}$ final state

(c) $\tau_\mu\tau_{\text{had}}$ final state

(d) $\tau_e\tau_{\text{had}}$ final state

Figure 5.3: Distributions of $\sum \cos\Delta\phi$ for the (a) $\tau_\mu\tau_{\text{had}}$ and (b) $\tau_e\tau_{\text{had}}$ final states. Distributions of m_{T} for the $\tau_\mu\tau_{\text{had}}$ (c) and $\tau_e\tau_{\text{had}}$ (d) final states. Distributions are shown after the object selection and requirements of one electron or muon candidate and the charge of the τ candidate to be of opposite sign to that of the lepton. The QCD multijet background is estimated from data and other processes from Monte Carlo [14].

magnitude is small. Events with small $E_{\text{T}}^{\text{miss}}$ tend to have the decay products back-to-back, which is accepted by the $\sum \cos\Delta\phi$ cut regardless of the direction of the $E_{\text{T}}^{\text{miss}}$.

The second quantity used to suppress the W + jets background is the transverse mass:

$$m_{\text{T}} = \sqrt{2\, p_{\text{T}}(\ell) \cdot E_{\text{T}}^{\text{miss}} \cdot \left(1 - \cos\Delta\phi(\ell, E_{\text{T}}^{\text{miss}})\right)}\,. \tag{5.2}$$

Figures 5.3(c) and 5.3(d) show its distribution for the $\tau_\mu\tau_{\text{had}}$ and $\tau_e\tau_{\text{had}}$ final states. The $Z \to \tau\tau$ distribution piles up towards zero because when the $E_{\text{T}}^{\text{miss}}$ and the lepton align, $\cos\Delta\phi$ tends towards one and m_{T} tends towards zero. In $Z \to \tau_{\text{lep}}\,\tau_{\text{had}}$ events, the $E_{\text{T}}^{\text{miss}}$ usually aligns with the lepton because there are two neutrinos on the side of the leptonic decay. For $W \to \ell\nu$ events, m_{T} is maximal when the momentum vectors of the neutrino and lepton have zero z-components in the W rest frame, in which case m_{T} is a measure of the W mass. Only a loose cut on the transverse mass, $m_{\text{T}} < 50$ GeV, is required as many W + jets events are already rejected by the cut on $\sum \cos\Delta\phi$ variable.

Three additional selection criteria are required to select a clean sample of $Z \to \tau\tau$ events. The τ candidate and the isolated lepton are combined to reconstruct the invariant mass of the visible decay products of the two τ leptons, the visible mass, m_{vis}. Only events with $35 < m_{\text{vis}} < 75$ GeV are selected in order to include majority

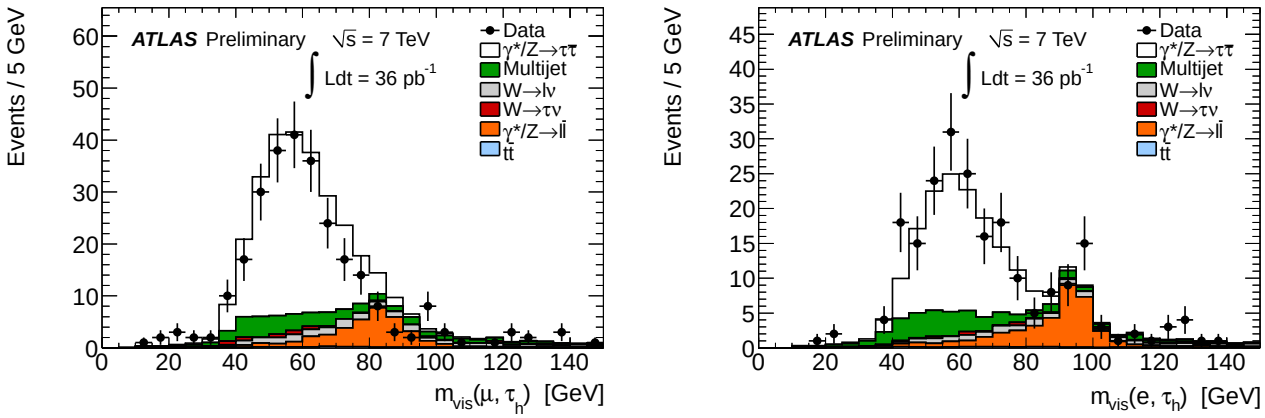

(a) $\tau_\mu\tau_{\text{had}}$ final state (b) $\tau_e\tau_{\text{had}}$ final state

Figure 5.4: Distributions of the visible mass, m_{vis}, for the (a) $\tau_\mu\tau_{\text{had}}$ and (b) $\tau_e\tau_{\text{had}}$ final states. Distributions are shown after the full event selections, except for the visible mass window [14].

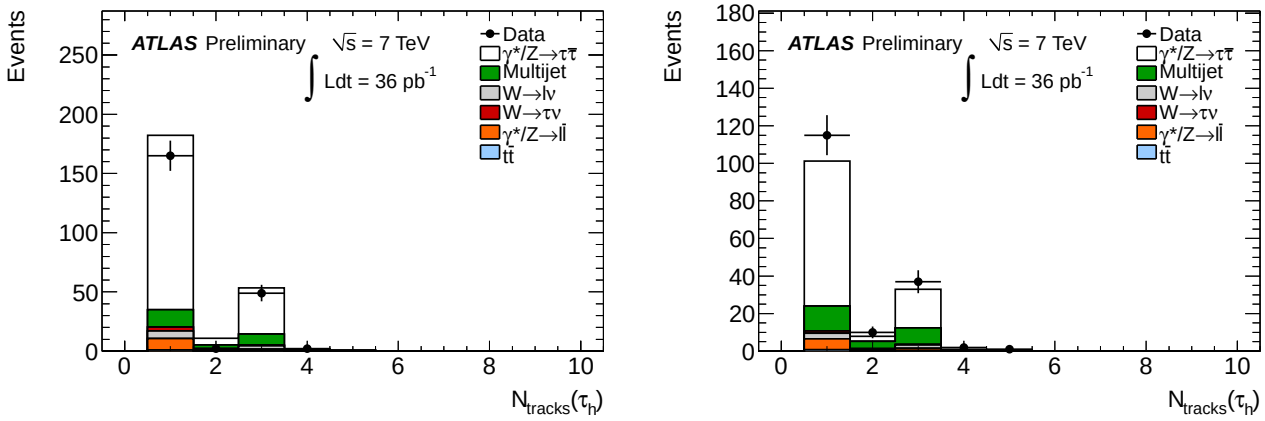

(a) $\tau_\mu\tau_{\text{had}}$ final state (b) $\tau_e\tau_{\text{had}}$ final state

Figure 5.5: The final τ candidate track distribution after all cuts in opposite signed bin, except the requirement on the number of tracks and on the magnitude of the τ candidate charge [14].

of the signal, while excluding $Z \to \ell\ell$ events. For $Z \to \mu\mu$ events, the peak of m_{vis} is at slightly lower values than for $Z \to ee$ events as muons mis-identified as τ candidates leave less energy in the calorimeter compared to mis-identified electrons, and the proportion of events where the τ candidate arises from a mis-identified jet, as opposed to a mis-identified lepton, is higher in $Z \to \mu\mu$ events.

The chosen τ candidate is required to have 1 or 3 associated tracks and unit charge. Additionally, the chosen τ candidate and the chosen lepton are required to have opposite charges as expected from $Z \to \tau\tau$ decays.

The distribution of the visible mass after the full selection except the visible mass window requirement is shown in Figure 5.4. The τ candidate track distribution after the full selection except the requirements on the number of associated tracks and on the magnitude of the τ candidate charge is shown in Figure 5.5.

Final state with electron and muon For $\tau_e\tau_\mu$ final state exactly one isolated medium electron candidate with $E_{\text{T}} > 16$ GeV and one isolated muon candidate with $p_{\text{T}} > 10$ GeV of opposite electric charge are required. Because signal events contain two leptons of different flavors, the contributions from $\gamma^*/Z \to ee$ and $\gamma^*/Z \to \mu\mu$ processes are small. The requirement $\sum \cos\Delta\phi > -0.15$ is applied as in the semileptonic final states, discriminating against $W \to \ell\nu$, and $t\bar{t}$ backgrounds. Figure 5.6 (a) shows the distribution of $\sum \cos\Delta\phi$ after the described selection

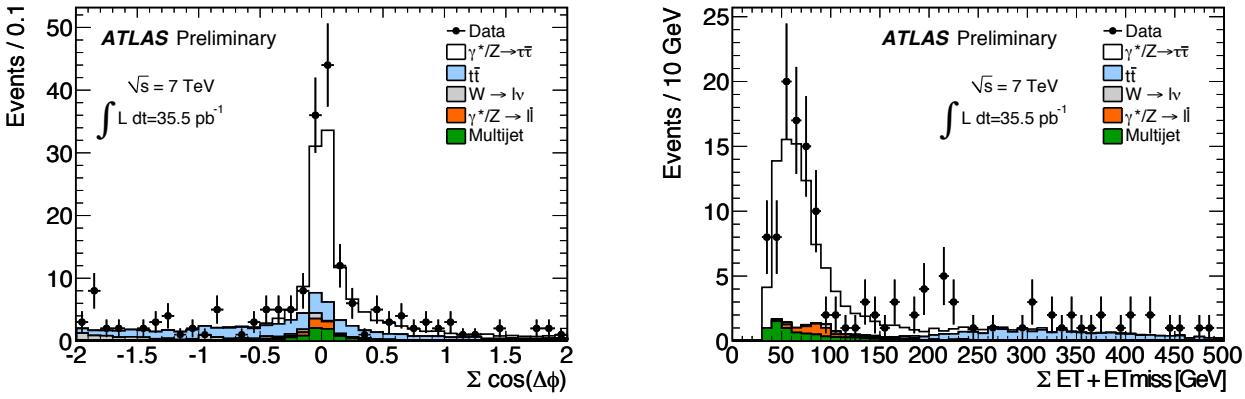

(a) (b)

Figure 5.6: Distributions of the (a) $\sum \cos\Delta\phi$ and (b) $\sum E_{\mathrm{T}} + E_{\mathrm{T}}^{\mathrm{miss}}$ after the isolation cuts for the $\tau_e\tau_\mu$ final state. The multijet background is estimated from data, other processes are estimated from Monte Carlo [14].

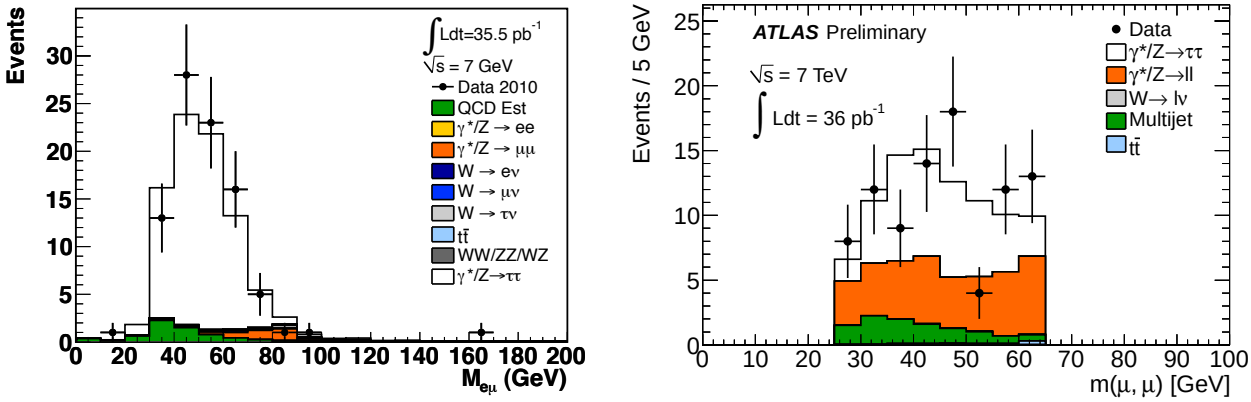

(a) $\tau_e\tau_\mu$ final state (b) $\tau_\mu\tau_\mu$ final state

Figure 5.7: Distributions of the visible mass for the (a) $\tau_e\tau_\mu$ and (b) $\tau_\mu\tau_\mu$ final states after the full event selection. For the $\tau_e\tau_\mu$ final state the visible mass window selection is not applied [14].

criteria. Further reduction of the $t\bar{t}$ background is based on the topology of $t\bar{t}$ events characterised by the presence of high-p_{T} jets and leptons, as well as large $E_{\mathrm{T}}^{\mathrm{miss}}$. The selection is made by requiring that events satisfy $\sum E_{\mathrm{T}} + E_{\mathrm{T}}^{\mathrm{miss}} < 150$ GeV cut, where $\sum E_{\mathrm{T}} + E_{\mathrm{T}}^{\mathrm{miss}}$ variable is defined as:

$$\sum E_{\mathrm{T}} + E_{\mathrm{T}}^{\mathrm{miss}} = E_{\mathrm{T}}(e) + p_{\mathrm{T}}(\mu) + \sum_{jets} p_{\mathrm{T}} + E_{\mathrm{T}}^{\mathrm{miss}}. \tag{5.3}$$

The distribution of $\sum E_{\mathrm{T}} + E_{\mathrm{T}}^{\mathrm{miss}}$ variable for data and Monte Carlo after the $\sum \cos\Delta\phi$ requirement is shown in Figure 5.6 (b).

Finally, the invariant mass of the two leptons is calculated. It is required to be within a wider range than in the semileptonic case, $25 < m_{e\mu} < 80$ GeV, as $\gamma^*/Z \to \ell\ell$ events are a small background in this final state. Figure 5.7(a) shows the distribution of the visible mass.

Two muons final state For $\tau_\mu\tau_\mu$ final state exactly two isolated muon candidates, one with $p_{\mathrm{T}} > 10$ GeV and one with $p_{\mathrm{T}} > 15$ GeV, are required. The muon candidates should have opposite charge. The signal region for this final state is defined by the invariant mass of the two muon candidates, $25 < m_{\mu\mu} < 65$ GeV.

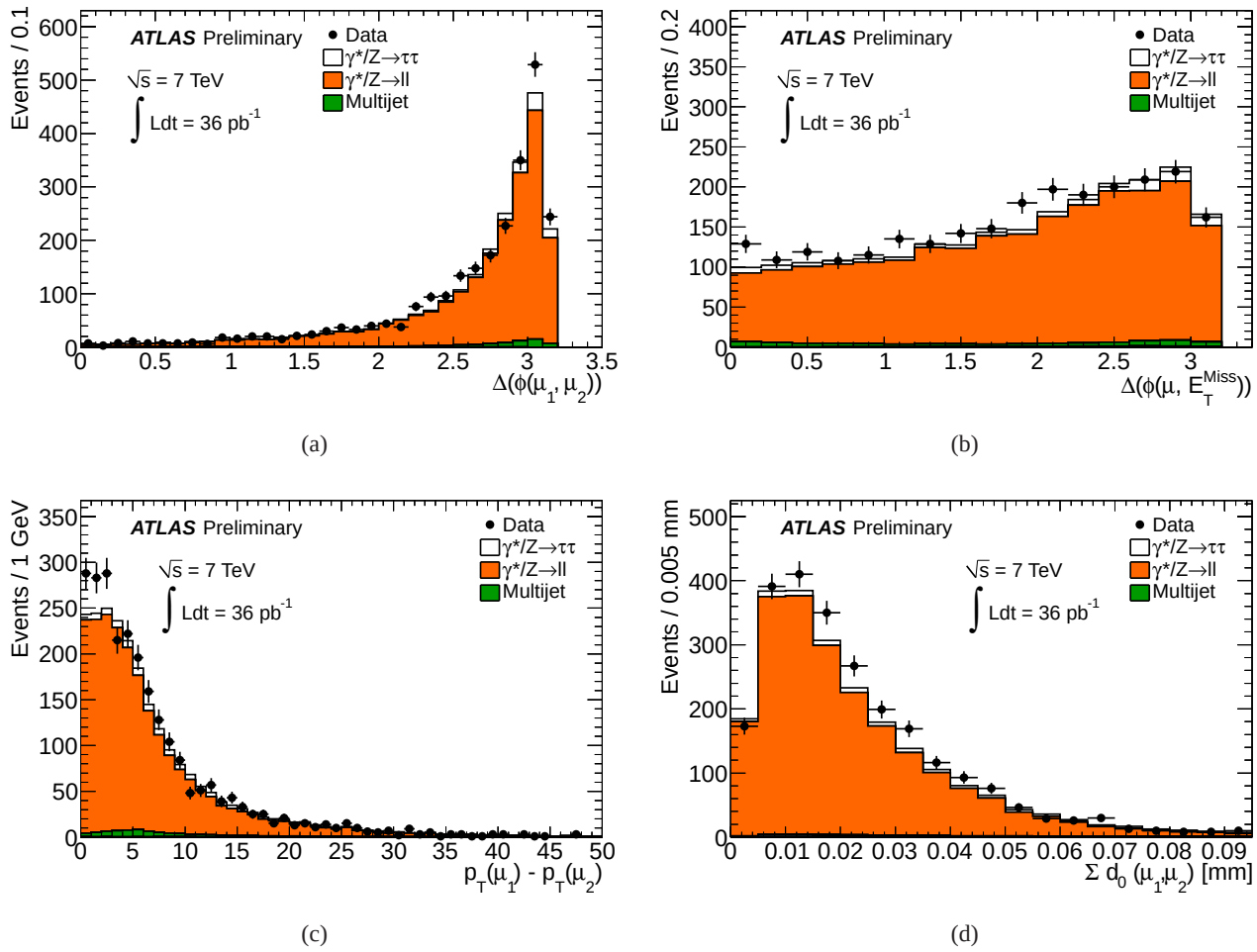

Figure 5.8: Distributions for the $\tau_\mu\tau_\mu$ final state for the signal and $\gamma^*/Z \to \ell\ell$ MC samples and data after the di-lepton, isolation and visible mass selections. The multijet QCD background is estimated from data. Other backgrounds are negligible on those plots. The observed differences are consistent with the assumed systematic uncertainties [14].

A boosted decision trees algorithm, BDT, is used to distinguish efficiently between signal and the main background. It is trained using MC samples, $Z \to \tau\tau$ as signal and $\gamma^*/Z \to \mu\mu$ as background after the selection described above. To maximise the available MC statistics for training and testing, no isolation requirements are applied to the muon candidates. The five variables are used for the BDT training: the differences in azimuthal angles between the two muon candidates ($\Delta\phi(\mu_1,\mu_2)$) and between the leading muon candidate and the $E_{\mathrm{T}}^{\mathrm{miss}}$ vector ($\Delta\phi(\mu_1, E_{\mathrm{T}}^{\mathrm{miss}})$), the difference in the p_{T} of the two muon candidates ($p_{\mathrm{T}}(\mu_1) - p_{\mathrm{T}}(\mu_2)$), the transverse momentum of the leading muon candidate ($p_{\mathrm{T}}(\mu_1)$), and the sum of the absolute transverse impact parameters of the two muon candidates ($\sum d_0(\mu_1,\mu_2) = |d_0(\mu_1)| + |d_0(\mu_2)|$), which has the highest discriminating power. Distributions of these variables, except $p_{\mathrm{T}}(\mu_1)$, for the events that are used for the BDT selection are shown in Figure 5.8. Differences between data and Monte Carlo are consistent with the estimated systematic uncertainties, and the agreement is the best in the regions most relevant for the signal and background separation.

In the analysis it is required that the BDT output is greater than 0.07, resulting in an efficiency of 0.38 ± 0.02. This cut is chosen as giving the best signal significance. The visible mass distribution after the full selection except the mass window requirement is shown in Figure 5.7(b).

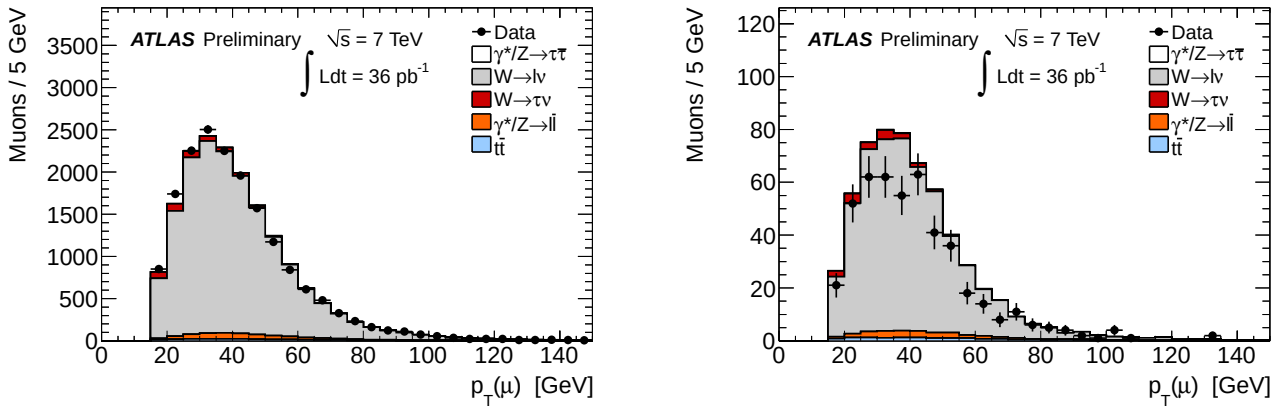

(a) no τ identification

(b) tight τ candidate

Figure 5.9: Muon p_{T} distributions in the W control region, with no (a) and tight (b) τ identification. Plots are for the $\tau_\mu\tau_{\mathrm{had}}$ final state. A similar effect is seen in the $\tau_e\tau_{\mathrm{had}}$ final state [14].

5.1.3 Background estimation

In order to estimate the final purity and significance of the selected signal events, the number of background events passing the selection has to be estimated. The estimated number of background events from electroweak processes ($W \to \ell\nu$, $W \to \tau\nu$, $Z \to \ell\ell$, di-boson production) and $t\bar{t}$ are taken from MC, providing that these backgrounds are small and the MC prediction agrees well with the observed data. To obtain such agreement, W boson MC samples are renormalised with a scale factor described below.

Rates of real and fake leptons produced in QCD multijet events, on the other hand, are not expected to be modelled well with MC. Thus estimated number of background events from QCD is data driven.

W+jets background

In the two di-leptonic final states, the $W \to \ell\nu$ and $W \to \tau\nu$ backgrounds are found to be small, and their contribution is obtained from simulations. In the two semileptonic final states, where these backgrounds are important, they are instead estimated from data by obtaining their normalisation from a W boson-enriched control region. A high-purity W sample is provided by requiring events to pass all selection criteria except those on m_{T} and $\sum \cos\Delta\phi$, rejecting the W background. The QCD multijet background contamination in this region is negligible. The MC estimate of the small $\gamma^*/Z \to \ell\ell$ and $t\bar{t}$ contribution is subtracted before calculating the normalisation factor.

As shown in Figure 5.9(a), the MC agrees with the data reasonably well before requiring the τ identification and overestimates the data after applying tight τ identification as shown in Figure 5.9(b). This is in agreement with results described in Section 4.3 where the τ fake rate from jets is overestimated by the MC. The W MC is therefore corrected by normalising it to the number of events observed in the data in the W control region. The obtained normalisation factor is 0.73 ± 0.06 (stat) for the $\tau_\mu\tau_{\mathrm{had}}$ final state and 0.63 ± 0.07 (stat) for the $\tau_e\tau_{\mathrm{had}}$ final state.

Since the differences between data and W MC are due to different τ fake rates in data and MC, a second method was also used, as a cross check, to normalise the W MC in the signal region. A scale factor for the τ fake rate measured in data with a dedicated fake rate study as described in Section 4.3 is estimated on $Z \to \ell\ell$+jet events, and applied as an event weight. The resulting estimated W background is in agreement with the W background estimate obtained using normalisation in the W control region.

$\gamma^*/Z \to \mu\mu$ background

The $\gamma^*/Z \to \mu\mu$ process is the most important electroweak background to the $\tau_\mu\tau_\mu$ final state. The normalisation of the Monte Carlo sample is checked after the di-muon selection, for events with invariant masses between 25 GeV

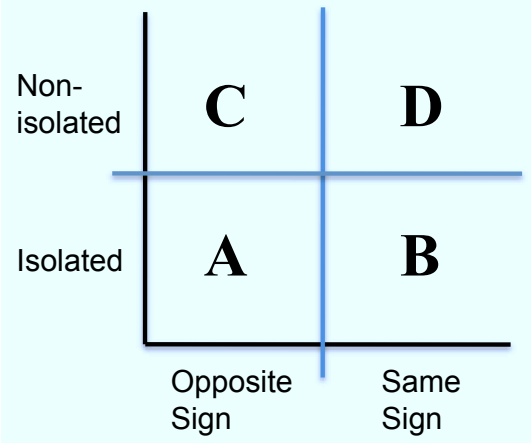

Figure 5.10: Schematic diagram of the control regions for the QCD multijet background estimation method.

and 65 GeV. In this region, the $\gamma^*/Z \rightarrow \mu\mu$ process is dominant and is expected to contribute to over 94% of the selected events. The expected backgrounds arising from other electroweak processes are subtracted and the QCD multijet contribution is estimated using a data-driven method described in the next Section. The number of $\gamma^*/Z \rightarrow \mu\mu$ events in the selected mass window is consistent between MC and data within the uncertainties of $\sim$ 8% (to be compared with a 7% difference in rate). Therefore no correction factor is applied to the $\gamma^*/Z \rightarrow \mu\mu$ MC prediction.

QCD multijets background

The QCD multijet background estimation is made using data-driven methods in all final states. In the $\tau_e\tau_\mu$ and semileptonic final states, the method takes advantage of the fact that the QCD multijet background is expected to be approximately the same regardless of whether the lepton and the τ candidate or second lepton have the same or the opposite sign. The following relation is used:

$$\frac{N^A_{\mathrm{QCD}}}{N^B_{\mathrm{QCD}}} = \frac{N^C_{\mathrm{QCD}}}{N^D_{\mathrm{QCD}}}, \tag{5.4}$$

where N^i_{QCD} is the number of QCD multijet events in four statistically independent regions, denoted by $i = \{A, B, C, D\}$ and defined as follows:

- A: signal region with the isolated lepton and the opposite sign requirement;
- B: control region with the isolated lepton and the same sign requirement;
- C: control region with the reversed lepton isolation requirement and the opposite sign requirement;
- D: control region with the opposite sign requirement and the isolation requirements reversed.

The four regions are illustrated schematically in Figure 5.10. This method uses the fact that the signal is composed of almost exclusively isolated leptons whose charges are opposite to the τ candidates or the second lepton charges, and therefore signal contributions can effectively be excluded in all control regions B, C and D.

The QCD multijet estimate is scaled from region B to region A, using Eq. 5.4:

$$N^A_{\mathrm{QCD}} = \frac{N^C_{\mathrm{QCD}}}{N^D_{\mathrm{QCD}}} N^B_{\mathrm{QCD}} = R_{OS/SS} N^B_{\mathrm{QCD}}. \tag{5.5}$$

The following values of $R_{OS/SS}$ are obtained:

Table 5.1: Estimated background events, expected number of signal events and number of events observed in data, N_{obs}, after the full selection, for each final state. The quoted uncertainties are statistical only [14].

	$\tau_\mu\tau_{\text{had}}$	$\tau_e\tau_{\text{had}}$	$\tau_e\tau_\mu$	$\tau_\mu\tau_\mu$
$\gamma^*/Z \to \ell\ell$	11.1 ± 0.5	6.9 ± 0.4	1.9 ± 0.1	36 ± 1
$W \to \ell\nu$	9.3 ± 0.7	4.8 ± 0.4	0.7 ± 0.2	0.2 ± 0.1
$W \to \tau\nu$	3.6 ± 0.8	1.5 ± 0.4	< 0.2	< 0.2
$t\bar{t}$	1.3 ± 0.1	1.02 ± 0.08	0.15 ± 0.03	0.8 ± 0.1
Di-boson	0.28 ± 0.02	0.18 ± 0.01	0.48 ± 0.03	0.13 ± 0.01
QCD multijet	24 ± 6	23 ± 6	6 ± 4	10 ± 2
Total background events	50 ± 6	37 ± 6	9 ± 4	47 ± 2
Expected signal events	186 ± 2	98 ± 1	73 ± 1	44 ± 1
Total expected events	235 ± 6	135 ± 6	82 ± 4	91 ± 3
N_{obs}	213	151	85	90

$1.07 \pm 0.04\,(\text{stat}) \pm 0.04\,(\text{syst})$ $\tau_\mu\tau_{\text{had}}$ final state
$1.07 \pm 0.07\,(\text{stat}) \pm 0.07\,(\text{syst})$ $\tau_e\tau_{\text{had}}$ final state
$1.55 \pm 0.04\,(\text{stat}) \pm 0.20\,(\text{syst})$ $\tau_e\tau_\mu$ final state.

Electroweak backgrounds in all three control regions are subtracted using MC simulations. For the same-sign control regions of the semileptonic final states, the W normalisation factor, calculated as described earlier, is applied. The QCD multijet background is estimated after the full selection in the two semileptonic final states, and after the di-lepton selection in the $\tau_e\tau_\mu$ final state, due to limited statistics. In this case the efficiency of the remaining selection criteria is obtained from the same-sign non-isolated control region.

This method assumes that the $R_{OS/SS}$ ratio is the same for non-isolated and isolated leptons. The measured variation of this ratio as a function of the isolation requirements is taken as a systematic uncertainty.

The QCD multijet background to the $\tau_\mu\tau_\mu$ final state is estimated in a control region defined after applying the full selection, but requiring the sub-leading muon candidate to fail the isolation selection criteria. A scaling factor is then calculated in a separate pair of control regions, obtained by requiring that the leading muon candidate fails the isolation selection and that the sub-leading muon candidate either fails or passes it. This scaling factor is further corrected for the correlation between the isolation variables for the two muon candidates. The QCD multijet background in the signal region is finally obtained from the number of events in the primary control region scaled by the corrected scaling factor.

Final background estimation

Table 5.1 shows the estimated number of background events per process for all final states. Also shown are the expected number of signal events, as well as the total number of events observed in data in each channel after the full selection.

5.1.4 Methodology for cross section calculation

The measurement of the cross section is done in each final state separately, and then the obtained values are combined. The calculation is performed using the formula:

$$\sigma(Z \to \tau\tau) \times \text{B} = \frac{N_{\text{obs}} - N_{\text{bkg}}}{A_Z \cdot C_Z \cdot \mathcal{L}}, \tag{5.6}$$

where

- B is the branching fraction for the considered final state;

- N_{obs} is the number of observed events in data;
- N_{bkg} is the number of estimated background events;
- $\mathcal{L}$ is the integrated luminosity for the final state of interest;
- C_Z is the correction factor that accounts for the efficiency of triggering, reconstructing and identifying the $Z \to \tau\tau$ events within the fiducial regions, defined as:
  - $\tau_\mu\tau_{\text{had}}$ final state: muon with $p_{\text{T}} > 15$ GeV and $|\eta| < 2.4$; τ candidate with $p_{\text{T}} > 20$ GeV and $|\eta| < 2.47$ (excluding transition region in the calorimeters); events with $\Sigma\cos\Delta\phi > -0.15$, $m_{\text{T}} < 50$ GeV and $35 < m_{\text{vis}} < 75$ GeV
  - $\tau_e\tau_{\text{had}}$ final state: electron with $E_{\text{T}} > 16$ GeV and $|\eta| < 2.47$ (excluding transition region in the calorimeters); τ candidate with $p_{\text{T}} > 20$ GeV and $|\eta| < 2.47$ (excluding transition region in the calorimeters); events with $\Sigma\cos\Delta\phi > -0.15$, $m_{\text{T}} < 50$ GeV and $35 < m_{\text{vis}} < 75$ GeV
  - $\tau_e\tau_\mu$ final state: electron with $E_{\text{T}} > 16$ GeV and $|\eta| < 2.47$ (excluding transition region in the calorimeters); muon with $p_{\text{T}} > 10$ GeV and $|\eta| < 2.4$; event with $\Sigma\cos\Delta\phi > -0.15$ and $25 < m_{\text{vis}} < 80$ GeV
  - $\tau_\mu\tau_\mu$ final state: leading muon with $p_{\text{T}} > 15$ GeV and $|\eta| < 2.4$; sub-leading muon with $p_{\text{T}} > 10$ GeV and $|\eta| < 2.4$; events with $25 < m_{\text{vis}} < 65$ GeV.

  The C_Z factor is determined as the ratio between the number of events passing the full selection after a complete detector simulation and the number of events in the fiducial region at the generator level. The four-momenta of electrons and muons are calculated including photons radiated within a cone of size $\Delta R < 0.1$. The four-momenta of τ candidates are defined by including photons radiated by both the τ leptons and their decay products within a cone of size $\Delta R < 0.4$. By construction C_Z accounts for migrations from outside of the acceptance. The correction by the C_Z factor provides the cross section within the fiducial region of each measurement
  $$\sigma^{\text{fid}}(Z \to \tau\tau) \times \text{B} = \frac{N_{\text{obs}} - N_{\text{bkg}}}{C_Z \cdot \mathcal{L}}, \tag{5.7}$$
  which is independent of the extrapolation procedure to the full phase space, and therefore is less affected by theoretical uncertainties in the modelling of the Z production;
- A_Z is the acceptance factor allowing the extrapolation of σ^{fid} to the total cross section, defined by Eq. 5.6. The A_Z factor is determined from Monte Carlo as the ratio of events at generator level whose $\tau\tau$ invariant mass, before final state radiation, lies within the mass window [66, 116] GeV, and the number of events at generator level that fall within the fiducial regions defined above. In this case the bare τ lepton decay products were dressed with photons radiated as described above for the C_Z factor. Dressing the τ lepton decay products allows to perform a partial QED final state radiation correction back to the Born level, that however excludes the radiation at wide angles. Using a dedicated sample, where the QED final state radiation was switched off, it was checked that the impact of the radiation at wide angles on the acceptance was -1.2% for the muon channel and -1.4% for the electron channel.
  The A_Z factor accounts for events that migrate from outside the invariant mass window into the fiducial region after applying selection criteria. The central values for A_Z and C_Z are determined using a PYTHIA Monte Carlo sample generated with the modified LO parton distribution functions MRSTLO* [153].

5.1.5 Systematic uncertainties

Several possible sources of systematic uncertainties on the A_Z and C_Z factors as well as on the background estimation are evaluated.

Systematic uncertainty on signal and background predictions

The efficiency of the lepton trigger, reconstruction, identification and isolation requirements are each measured separately in data, and the corresponding Monte Carlo efficiency for each step is corrected to agree with the measured values. These corrections are applied to all relevant Monte Carlo samples used for this study. Uncertainties on the corrections arise both from statistical and systematic uncertainties on the efficiency measurements. The largest contribution to the electron efficiency uncertainty comes from the identification efficiency for low-E_{T} electrons, where the statistical uncertainty on the measurement is very large. The total electron uncertainty is estimated to be between 5-9% relative to the efficiency, depending on the selection. For muons, the uncertainty is estimated to be 2-4% relative to the efficiency.

The uncertainties on the τ reconstruction and identification efficiencies are evaluated as described in Section 4.3. They are estimated to be around 10% relative to the efficiency for most cases, varying between 9% and 12% with the τ candidate p_{T}, number of tracks, and number of vertices in the event [154].

The probability for an electron or a QCD jet to be mis-identified as a hadronic τ is measured in data as described in Section 4.3. Correction factors are derived for the MC mis-identification probability for electrons, binned in η and applied to τ candidates matched in simulation to a generator-level electron. The uncertainty on the correction factor is taken as the systematic uncertainty. The QCD jet mis-identification probability is measured in $Z \to \ell\ell$+jet events. The difference with respect to the MC prediction for the same selection, added in quadrature with the statistical and systematic uncertainties of the measurement, is taken as the systematic uncertainty. These corrections are applied to τ candidates not matched to a generator-level electron.

The τ energy scale uncertainty is estimated as described in Section 4.1.2. The electron energy scale is determined from data by constraining the reconstructed di-electron invariant mass to the well-known $Z \to ee$ line shape. For the barrel region, the linearity and resolution are in addition controlled using $J/\psi \to ee$ events. The jet energy scale uncertainty is evaluated from simulations by comparing the nominal results to MC simulations using alternative detector configurations, alternative hadronic shower and physics models, and by comparing the relative response of jets across pseudo-rapidity between data and simulation [128]. Additionally, the calorimeter component of the $E_{\mathrm{T}}^{\mathrm{miss}}$ is sensitive to the energy scale, and this uncertainty is evaluated by propagating first the electron energy scale uncertainty into the $E_{\mathrm{T}}^{\mathrm{miss}}$ calculation and then shifting all topological clusters not associated to electrons according to their uncertainties [128].

The electron, τ and jet energy scale uncertainties, as well as the calorimeter component of the $E_{\mathrm{T}}^{\mathrm{miss}}$, are all correlated. Their effect is therefore evaluated by simultaneously shifting each up and down by one standard deviation; the jets are not considered in the semileptonic final states, while the τ candidates are not considered for the di-lepton final states. The muon energy scale, and the correlated effect on the $E_{\mathrm{T}}^{\mathrm{miss}}$, is also evaluated but found to be negligible in comparison with other uncertainties.

The uncertainty on the QCD multijet background estimation comes from three different sources. Electroweak and $t\bar{t}$ backgrounds are subtracted in the control regions and all sources of systematics on these backgrounds are taken into account. Each source of the systematic error is varied up and down by one standard deviation and the effect on the final QCD multijet background estimation is evaluated. The second set of systematic uncertainties is related to the assumption of the method used for the $\tau_e\tau_{\mathrm{had}}$, $\tau_\mu\tau_{\mathrm{had}}$ and $\tau_e\tau_\mu$ final state QCD multijet background estimations, namely that the ratio of opposite-sign to same-sign events in the signal region is independent of the lepton isolation. These systematic uncertainties are evaluated by studying the dependence of $R_{OS/SS}$ on the isolation criterion and, for the $\tau_e\tau_\mu$ channel, comparing the efficiencies of the subsequent selection criteria in the opposite- and same-sign regions. For the estimation of the QCD multijet background in the $\tau_\mu\tau_\mu$ final state, the uncertainties due to the correlation between the isolation of the two muon candidates are evaluated by propagating the systematic uncertainties from the subtracted backgrounds into the calculation of the correlation factor. The third uncertainty on the QCD multijet background estimation arises from the statistical uncertainty on the number of data events in the various control regions.

The uncertainty on the W+jets background estimation method is dominated by the statistical uncertainty on the calculation of the normalisation factor in the control region, as described in Section 5.1.3, and the energy scale uncertainty.

In the $\tau_\mu\tau_\mu$ final state, a smearing is applied to the transverse impact parameter of muons (d_0) with respect to the primary vertex to match the Monte Carlo resolution with the value observed in data. The muon d_0 distribution is compared between data and Monte Carlo using a sample of $Z \to \mu\mu$ events and is found to be well-described by a double Gaussian distribution. The 20% difference in width between data and simulation is used to define the smearing function which is applied to the d_0 of each simulated muon. The systematic uncertainty due to the smearing procedure is estimated by varying the widths and relative weights of the MC impact parameter distributions of the two muon candidates, within the estimated uncertainties on their measurement.

The uncertainty on the luminosity is taken to be 3.4%, as determined in [106, 107]. A number of other sources, such as the uncertainty due to the object quality requirements for τ candidates and jets, are also evaluated, but have a small contribution to the total uncertainty.

The MC is reweighted so that the distribution of the number of vertices matches that observed in data; the systematic uncertainty from the reweighting procedure amounts to a permille effect.

The lepton resolution and charge mis-identification are found to have only a sub-percent effect on C_Z and the background predictions.

Systematic uncertainties due to a few problematic calorimeter regions, affecting electron reconstruction, are also evaluated and found to have a very small effect.

The uncertainties on the theoretical cross sections by which the background Monte Carlo samples are scaled are also found to have only a very small impact on the corresponding background prediction, except for the $\tau_\mu\tau_\mu$ final state, which has a large electroweak background contamination.

Systematic uncertainty on the acceptance

The theoretical uncertainty on the geometric and kinematic acceptance factor A_Z is dominated by the limited knowledge of the proton Parton Distribution Functions (PDF) and the modelling of the Z boson production at the LHC. The uncertainty due to the choice of PDF set is evaluated by considering the maximal deviation between the acceptance obtained using the default sample and the values obtained by reweighting this sample to the CTEQ6.6 and HERAPDF1.0 [155] PDF sets. The uncertainties within the PDF set are determined by using the 44 PDF error eigenvectors available for the CTEQ6.6 NLO PDF set [156]. The variations are obtained by reweighting the default sample to the relevant CTEQ6.6 error eigenvector.

The uncertainties due to the modelling of W and Z production are estimated using MC@NLO interfaced with the HERWIG for parton showering, with the CTEQ6.6 PDF set and ATLAS MC10 tune and a lower bound on the invariant mass of 60 GeV. Since HERWIG, in association with external generators, does not handle τ polarisation correctly [157], the acceptance obtained from the MC@NLO sample is corrected, and the correction is of the order of 2% for the $\tau_e\tau_{\text{had}}$ and $\tau_\mu\tau_{\text{had}}$ channels, 8% for the $\tau_e\tau_\mu$ channel, and 3% for the $\tau_\mu\tau_\mu$ channel. The deviation with respect to the A_Z factor obtained using the default sample reweighted to the CTEQ6.6 PDF set central value and with an applied lower bound on the invariant mass of 60 GeV is taken as uncertainty.

In the default sample the QED radiation is modelled by PHOTOS which has an accuracy of better than 0.2%, and therefore has a negligible uncertainty compared to uncertainties due to PDFs. Summing in quadrature the various contributions, total theoretical uncertainties of 3% are assigned to A_Z for both the semileptonic and the $\tau_e\tau_\mu$ final states and of 4% for the $\tau_\mu\tau_\mu$ final state.

Summary of systematic uncertainties

The uncertainty on the experimental acceptance C_Z is due to the effect of the uncertainties described above on the signal MC, after correction factors are applied. For the total background estimation uncertainties, the correlations between the electroweak and $t\bar{t}$ background uncertainties and the QCD multijet background uncertainty, arising from the subtraction of the former in the control regions used for the latter, are taken into account. The largest uncertainty results from the τ identification and energy scale uncertainties for the $\tau_\mu\tau_{\text{had}}$ and $\tau_e\tau_{\text{had}}$ final states. Additionally, in the $\tau_e\tau_{\text{had}}$ final state, the uncertainty on the electron efficiency has a large contribution. This is also the dominant uncertainty in the $\tau_e\tau_\mu$ final state. In the $\tau_\mu\tau_\mu$ final state, the uncertainty due to the muon

Table 5.2: Relative statistical and systematic uncertainties in % on the total cross section measurement. The electron and muon efficiency terms include the lepton trigger, reconstruction, identification and isolation uncertainties, as described in the text. The last column indicates whether a given systematic uncertainty is treated as correlated (✓) or uncorrelated (X) among the relevant channels when combining the results. For the QCD multijet background estimation method, the uncertainties in the $\tau_\mu\tau_{\text{had}}$, $\tau_e\tau_{\text{had}}$ and $\tau_e\tau_\mu$ channels are treated as correlated while the $\tau_\mu\tau_\mu$ uncertainty is treated as uncorrelated, since a different estimation method is used, as described in Section 5.1.3 [14].

Systematic uncertainty	$\tau_\mu\tau_{\text{had}}$	$\tau_e\tau_{\text{had}}$	$\tau_e\tau_\mu$	$\tau_\mu\tau_\mu$	Correlation
Muon efficiency	3.8%	–	2.2%	8.6%	✓
Muon d_0 (shape and scale)	–	–	–	6.2%	X
Muon resolution and energy scale	0.2%	–	0.1%	1.0%	✓
Electron efficiency, resolution and charge mis-identification	–	9.6%	5.9%	–	✓
τ identification efficiency	8.6%	8.6%	–	–	✓
τ mis-identification	1.1%	0.7%	–	–	✓
Energy scale (e/τ/jets/$E_{\text{T}}^{\text{miss}}$)	10%	11%	1.7%	0.1%	✓
QCD multijet background estimate	0.8%	2%	1.0%	1.7%	(✓)
W normalisation factor	0.1%	0.2%	–	–	X
Object quality selection criteria	1.9%	1.9%	0.4%	0.4%	✓
Pile-up description in simulation	0.4%	0.4%	0.5%	0.1%	✓
Theoretical cross section	0.2%	0.1%	0.3%	4.3%	✓
A_Z systematics	3%	3%	3%	4%	✓
Total Systematic uncertainty	15%	17%	7.3%	14%	
Statistical uncertainty	9.8%	12%	13%	23%	X
Luminosity	3.4%	3.4%	3.4%	3.4%	✓

efficiency is the dominant source, with the muon d_0 contribution being important in the background estimate for that channel. The correlation between the uncertainty on C_Z and on $(N_{\text{obs}} - N_{\text{bkg}})$ is accounted for in obtaining the final uncertainties on the cross section measurements, which are summarised in Table 5.2.

5.1.6 Cross section measurement

To improve the accuracy of the cross section measurement the results for the various final states can be combined. The uncertainty of a combined cross section measurement is reduced by taking into account correlations of uncertainties between different final states.

A summary of the numbers of observed events in data and estimated signal events in data after subtraction of background contributions is given in Table 5.3. It shows also the acceptance factor A_Z, the correction factor C_Z, the branching fraction for each final state and the integrated luminosity.

From those numbers the individual cross sections are derived. They are calculated following Equation 5.6. The results are used as input numbers for the combined cross section and presented in Table 5.4. Both the fiducial cross sections and the total cross sections for an invariant mass window of [66, 116] GeV are shown.

The combination of the cross section measurements from the four final states is obtained by using the Best Linear Unbiased Estimate (BLUE) method [158, 159]. This technique is used for a combined estimate of individual estimates which may be correlated. The systematic uncertainties on the individual cross sections due to different sources are assumed to be either fully correlated or fully uncorrelated. This is summarised in Table 5.2 where the last column indicates whether a given source of systematic uncertainty has been treated as correlated or uncorrelated amongst the relevant channels when calculating the combined result. The total combined cross

Table 5.3: The components of the $Z \to \tau\tau$ cross section calculations for each final state. For $N_{\text{obs}} - N_{\text{bkg}}$ the first uncertainty is statistical and the second systematic. For all other values the total error is given [14].

	$\tau_\mu\tau_{\text{had}}$	$\tau_e\tau_{\text{had}}$	$\tau_e\tau_\mu$	$\tau_\mu\tau_\mu$
N_{obs}	213	151	85	90
$N_{\text{obs}} - N_{\text{bkg}}$	$164 \pm 16 \pm 4$	$114 \pm 14 \pm 3$	$76 \pm 10 \pm 1$	$43 \pm 10 \pm 3$
A_Z	0.117 ± 0.004	0.101 ± 0.003	0.114 ± 0.003	0.156 ± 0.006
C_Z	0.20 ± 0.03	0.12 ± 0.02	0.29 ± 0.02	0.27 ± 0.02
B	0.2250 ± 0.0009	0.2313 ± 0.0009	0.0620 ± 0.0002	0.0301 ± 0.0001
$\mathcal{L}$	35.5 ± 1.2 pb^{-1}	35.7 ± 1.2 pb^{-1}	35.5 ± 1.2 pb^{-1}	35.5 ± 1.2 pb^{-1}

Table 5.4: The production cross section times branching fraction for the $Z \to \tau\tau$ process in each final state. The fiducial cross sections measurements include also the branching fraction of the τ to its decay products. The first error is statistical, the second systematic and the third comes from the luminosity [14].

Final State	Fiducial cross section (pb)	Total cross section ([66, 116] GeV) (nb)
$\tau_\mu\tau_{\text{had}}$	$23 \pm 2 \pm 3 \pm 1$	$0.86 \pm 0.08 \pm 0.12 \pm 0.03$
$\tau_e\tau_{\text{had}}$	$27 \pm 3 \pm 5 \pm 1$	$1.14 \pm 0.14 \pm 0.20 \pm 0.04$
$\tau_e\tau_\mu$	$7.5 \pm 1.0 \pm 0.5 \pm 0.3$	$1.06 \pm 0.14 \pm 0.08 \pm 0.04$
$\tau_\mu\tau_\mu$	$4.5 \pm 1.1 \pm 0.6 \pm 0.2$	$0.96 \pm 0.22 \pm 0.12 \pm 0.03$

section of

$$\sigma(Z \to \tau\tau,\ 66 < m_{\text{inv}} < 116\ \text{GeV}) = 0.97 \pm 0.07\ (\text{stat}) \pm 0.06\ (\text{syst}) \pm 0.03\ (\text{lumi})\ \text{nb} \tag{5.8}$$

is obtained from the four final states, $\tau_\mu\tau_{\text{had}}$, $\tau_e\tau_{\text{had}}$, $\tau_e\tau_\mu$, and $\tau_\mu\tau_\mu$.

A comparison of the individual cross sections with the combined result is shown in Figure 5.11, along with the combined $Z \to \ell\ell$ cross section measured in the $Z \to \mu\mu$ and $Z \to ee$ final states by ATLAS [49]. The theoretical expectation of 0.96 ± 0.05 nb for an invariant mass window of [66, 116] GeV is also shown.

The obtained total production cross section for $Z \to \tau\tau$ can be also compared to results from other experiments. It agrees with the $Z \to \tau\tau$ cross section in four final states measured by the CMS collaboration [148], $1.00 \pm 0.05\ (\text{stat}) \pm 0.08\ (\text{syst}) \pm 0.04\ (\text{lumi})$ nb, in a mass window of [60, 120] GeV. A comparison is shown in Figure 5.12. This figure includes also the combined measurements of the $Z \to \mu\mu$ and $Z \to ee$ production cross sections by the ATLAS [160] and CMS [161] collaborations. The measured $Z \to \tau\tau$ cross section agrees well with other measurements and the theory prediction.

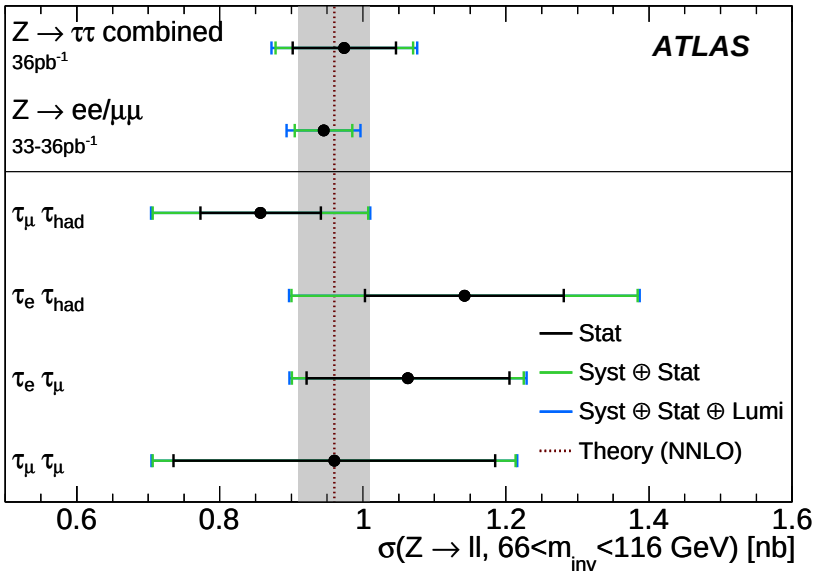

Figure 5.11: The individual cross section measurements by final state, and the combined result. The $Z \to \ell\ell$ combined cross section measured by ATLAS in the $Z \to \mu\mu$ and $Z \to ee$ final states is also shown for comparison. The grey band indicates the uncertainty on the NNLO cross section prediction [14].

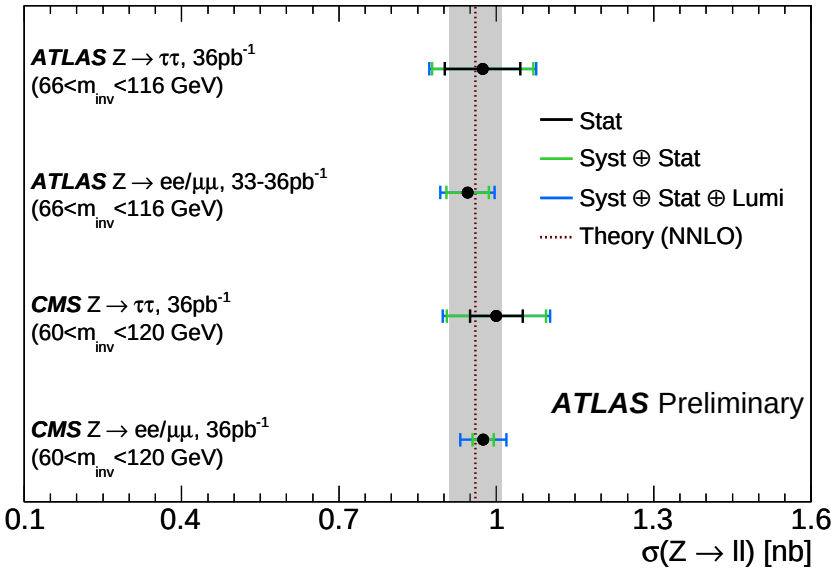

Figure 5.12: Comparison of the combined $Z \to \tau\tau$ cross section to the combined cross section measured by ATLAS and CMS in the $Z \to \mu\mu$ and $Z \to ee$ final states and to the combined measurement of the $Z \to \tau\tau$ cross section from the CMS collaboration. CMS measured the Z cross section in the mass range $60 < m_{\text{inv}} < 120$ GeV [14].

5.2 $W \to \tau\nu$ cross section measurement

Since purely leptonic τ decays cannot be easily distinguished from electrons and muons from $W \to e\nu$ and $W \to \mu\nu$ decays, the analysis presented in this section uses only hadronically decaying τ leptons [162]. The signature of this process is the presence of a τ candidate and missing transverse energy. $W \to \tau\nu$ decays are dominated by events with relatively low-p_{T} W bosons decaying into τ leptons with typical τ transverse momenta between 10 and 40 GeV. In addition, the distribution of the missing transverse energy, associated with the neutrinos from the W and τ_{had} decays, has a maximum around 20 GeV and a significant tail up to about 80 GeV.

Previous measurements at hadron colliders of W boson production with the subsequent decay $W \to \tau\nu$ based on $p\bar{p}$ collisions were reported by the UA1 collaboration [163] at the centre-of-mass energies of $\sqrt{s} = 546$ GeV and $\sqrt{s} = 630$ GeV and by the CDF and D0 collaborations [164, 165] at the centre-of-mass energy of $\sqrt{s} = 1.8$ TeV.

A brief summary of backgrounds important for this analysis is given below:

- **QCD multijet** - the dominant background source due to its large production cross section with events where one jet is incorrectly identified as τ candidate and a significant amount of mis-reconstructed $E_{\mathrm{T}}^{\mathrm{miss}}$.
- $\boldsymbol{W \to e\nu/\mu\nu}$ - processes contributing to the background if the lepton from the W boson decay is mis-identified as a single-prong τ candidate or if a fake τ candidate is reconstructed from a jet in the event. The $E_{\mathrm{T}}^{\mathrm{miss}}$ signature arises from a W decay neutrino or the mis-reconstruction of jets or of other objects in the event.
- $\boldsymbol{W \to \tau_{\mathrm{lep}}\nu \to e\nu/\mu\nu}$ - processes that are difficult to distinguish from primary electrons and muons therefore they contribute to the background similarly to $W \to e\nu$ and $W \to \mu\nu$.
- $\boldsymbol{Z \to \tau\tau}$ - the rate for this process is about ten times smaller than for the signal process. It contributes to the background if one of the τ leptons is identified as a τ candidate and second is lost.
- $\boldsymbol{Z \to ee/\mu\mu}$ - processes contributing if one of the decay electrons/muons is incorrectly reconstructed as τ candidate and the other one is lost, giving fake $E_{\mathrm{T}}^{\mathrm{miss}}$. These backgrounds are found to be negligible.
- $\boldsymbol{t\bar{t}}$ - process that has a much smaller cross section than the signal and contributes to the background if one of the W bosons produces a τ lepton in its decay and the other one decays into a pair of quarks, an electron, or a muon which are not reconstructed. Fully hadronic decays can also contribute to the fake τ identification. This background is found to be negligible.

5.2.1 Data and Monte Carlo samples

The data used are collected using combined τ and $E_{\mathrm{T}}^{\mathrm{miss}}$ triggers. In the earlier part of the 2010 data taking, corresponding to an integrated luminosity of 11 pb^{-1}, a loosely identified τ candidate with $p_{\mathrm{T}} > 12$ GeV (as reconstructed at the trigger level) in combination with $E_{\mathrm{T}}^{\mathrm{miss}} > 20$ GeV is required. In the second part of the period (24 pb^{-1}), a tighter τ identification and higher thresholds of 16 GeV and 22 GeV have to be used for p_{T} of τ candidate and $E_{\mathrm{T}}^{\mathrm{miss}}$, respectively, due to the increased luminosity. The signal efficiencies of these two triggers with respect to the offline selection as estimated from the simulation are (81.3±0.8)% and (62.7±0.7)%, respectively.

The MC samples used are the same as described in Section 5.1.1. The simulated events are re-weighted so that the distribution of the number of reconstructed primary vertices per bunch crossing matches that in the data.

5.2.2 Selection of $W \to \tau_{\mathrm{had}}\nu$ candidates

Events satisfying the trigger selection are required to have at least one reconstructed primary vertex formed by three or more tracks with $p_{\mathrm{T}} > 150$ MeV. Further preselection follows requirements described in Section 3.6.

Events are rejected if a jet or a τ candidate is reconstructed in the calorimeter transition regions to ensure a uniform $E_{\mathrm{T}}^{\mathrm{miss}}$ measurement.

In events where the $E_{\mathrm{T}}^{\mathrm{miss}}$ is found to be collinear with one of the jets (mainly QCD multijet events), the reconstructed $E_{\mathrm{T}}^{\mathrm{miss}}$ is likely to originate from an incomplete reconstruction of this jet. Therefore, a minimum separation $|\Delta\phi(\mathrm{jet}, E_{\mathrm{T}}^{\mathrm{miss}})| > 0.5$ rad is required for jets with $p_{\mathrm{T}} > 20$ GeV.

Objects selection

The following reconstructed objects are selected. τ candidates are selected if they have a transverse momentum 20 GeV $< p_{\mathrm{T}} <$ 60 GeV and $|\eta| < 2.47$ (excluding the calorimeter transition region). They are also required to pass tight identification criteria based on the BDT method. For τ candidates with transverse momenta above 20 GeV, the efficiency of the τ identification at the tight working point of the BDT identification is about 30% with a jet rejection factor of 100 for 1-prong τ candidates, while for 3-prong τ candidates it is about 35% with a rejection factor of 300 [154]. Additionally, a dedicated selection to reject fake τ candidates from electrons and muons is applied.

The missing transverse energy is obtained from the simple definition as described in Section 3.5. It is required to be above 30 GeV.

Event selection

In order to suppress electroweak backgrounds, electron and muon vetoes, additional to those provided by the τ identification algorithm, are applied. Events containing identified medium electrons or combined muons with $p_{\mathrm{T}} > 15$ GeV are rejected.

Only the highest-p_{T} identified τ candidate in the event is considered for further analysis. In order to reject more QCD multijet events, an additional cut to the $E_{\mathrm{T}}^{\mathrm{miss}} > 30$ GeV requirement is introduced. With a good approximation, the resolution of $E_{\mathrm{T}}^{\mathrm{miss}}$ components is proportional to $a \times \sqrt{\sum E_{\mathrm{T}}}$, where the scaling factor a depends on both the detector and reconstruction performance and $\sum E_{\mathrm{T}}$ is calculated from all calorimeter energy clusters. The factor a is about 0.5 $\sqrt{\mathrm{GeV}}$ for minimum bias events [133]. Thus the significance of $E_{\mathrm{T}}^{\mathrm{miss}}$, $S_{E_{\mathrm{T}}^{\mathrm{miss}}}$, is defined as:

$$S_{E_{\mathrm{T}}^{\mathrm{miss}}} = \frac{E_{\mathrm{T}}^{\mathrm{miss}}[\mathrm{GeV}]}{0.5\sqrt{\mathrm{GeV}}\sqrt{(\sum E_{\mathrm{T}}[\mathrm{GeV}])}}. \tag{5.9}$$

In order to remove events with large reconstructed $E_{\mathrm{T}}^{\mathrm{miss}}$ due to fluctuations in the energy measurement, events are rejected if $S_{E_{\mathrm{T}}^{\mathrm{miss}}} < 6$.

5.2.3 Background estimation

A good agreement between data and MC simulation in the W boson cross section measurement at ATLAS, where the W boson decays into an electron or muon is observed [160]. Therefore, the number of expected events from signal and electroweak background processes is obtained from simulation. An embedding technique is used as a cross-check of the results derived from MC. The muon in a high-purity sample of $W \to \mu\nu$ events is replaced by a simulated τ lepton. A good agreement between that sample and the corresponding MC sample is observed.

The data-driven method, similar to the one described in Section 5.1.3 is used to estimate the QCD multijet background contribution. It has been already used in the analysis which led to the first observation of $W \to \tau_{\mathrm{had}}\nu$ decays in ATLAS [166]. The method selects four independent data samples, three QCD multijet background-dominated regions (control regions) and one signal-dominated region (signal region). The samples are selected with criteria on $S_{E_{\mathrm{T}}^{\mathrm{miss}}}$ and on τ Id, which are assumed to be uncorrelated. An indirect correlation may arise anyhow due to the dependence of the τ Id rejection on the p_{T} of the τ candidate. This effect is taken into account when computing the systematic uncertainty. The following four regions are used in this analysis as shown in Figure 5.13:

- A: signal region with $S_{E_{\mathrm{T}}^{\mathrm{miss}}} > 6.0$ and τ candidates satisfying the τ Id described in Section 5.2.2;
- B: control region with $S_{E_{\mathrm{T}}^{\mathrm{miss}}} < 4.5$ and τ candidates satisfying the τ Id described in Section 5.2.2;

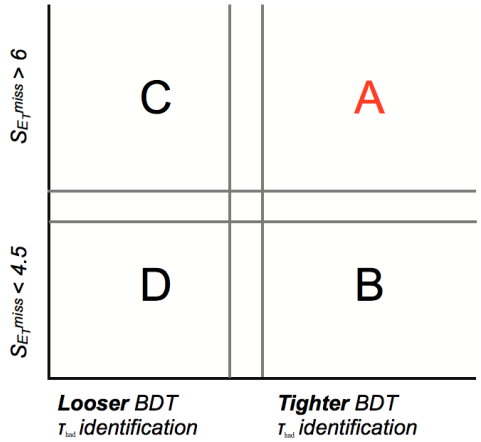

Figure 5.13: Schematic diagram of the four regions used for the QCD multijet background estimation, signal region A and the three control regions B,C and D.

Table 5.5: Estimated sample compositions in the signal region A and control regions B, C, and D [162].

	A	B	C	D
N^i (Data)	2335	4796	1577	27636
N^i_{sig}	1811 ± 25	683 ± 16	269 ± 8	93 ± 5
N^i_{EW}	284 ± 7	118 ± 4	388 ± 9	90 ± 4
N^i_{QCD}	127 ± 8	3953 ± 75	885±45	27444± 166

- C: control region with $S_{E_{\text{T}}^{\text{miss}}} > 6.0$ and τ candidates satisfying a looser τ Id but failing the signal region τ Id requirements;
- D: control region with $S_{E_{\text{T}}^{\text{miss}}} < 4.5$ and τ candidates satisfying a looser τ Id but failing the signal region τ Id requirements.

The looser τ Id region is defined with BDT score < 0.5 for 1-prong τ candidates and BDT score < 0.45 for multi-prong τ candidates.

Under the assumption that the shape of the $S_{E_{\text{T}}^{\text{miss}}}$ distribution for QCD multijet background is independent of the τ Id and the signal and electroweak background contribution in the three control regions is negligible, an estimate for the number of QCD multijet background events in the signal region A is provided by $N^{\text{A}}_{\text{QCD}} = N^{\text{B}}N^{\text{C}}/N^{\text{D}}$, where N^i, $i = \text{B}, \text{C}, \text{D}$, is the number of observed events in region i. The expected number of signal events in a given region is denoted as N^i_{sig}, and of the electroweak background events is denoted as N^i_{EW}. The statistical error on $N^{\text{A}}_{\text{QCD}}$ includes both the uncertainty on the estimation of this contamination, due to the MC statistics, and the statistical uncertainty of the data in the four regions. The resulting estimates of the sample compositions are summarised in Table 5.5.

A good quality of the description of the selected data by the background models can be seen in Figure 5.14, where data and the background estimates are shown. This Figure presents the distribution of $S_{E_{\text{T}}^{\text{miss}}}$ in regions A and B and the distribution of $E_{\text{T}}^{\text{miss}}$, the p_{T} spectrum of τ candidates, the number of tracks associated to the τ candidate, the distribution of $\Delta\phi(\tau, E_{\text{T}}^{\text{miss}})$ and the transverse mass, $m_{\text{T}} = \sqrt{2 \cdot p_{\text{T}}^{\tau} \cdot E_{\text{T}}^{\text{miss}} \cdot \left(1 - \cos\Delta\phi\left(\tau, E_{\text{T}}^{\text{miss}}\right)\right)}$, in the selected signal region A. In all the distributions a reasonable agreement is observed between the data and Monte Carlo prediction.

5.2.4 Method for cross section calculation

The calculation of the fiducial and the total cross sections follows equations 5.6 and 5.7 from Section 5.1.4. The fiducial region is defined by the following cuts: τ with 20 GeV $< p_{\mathrm{T}} <$ 60 GeV and $|\eta| < 2.5$ (excluding transition region in the calorimeters); events with $(\sum p^{\nu})_T > 30$ GeV and $|\Delta\phi(\tau, \sum p^{\nu})| > 0.5$ where $(\sum p^{\nu})_T$ is the transverse component of the sum of the simulated neutrino four-vectors. τ momentum is calculated from the sum of the four-vectors of the decay products from the simulated hadronic τ decay, except for the neutrinos. This momentum also includes photons radiated both from the τ lepton and from the decay products themselves, considering only photons within $\Delta R < 0.4$ with respect to the τ direction.

5.2.5 Systematic uncertainties

Summary of the systematic uncertainties is presented in Table 5.6.

The differences between the measured trigger responses of the two trigger components in data and Monte Carlo are used to determine the systematic uncertainty. A pure and unbiased sample enriched with $W \to \tau_{\mathrm{had}}\nu$ events is obtained in data by applying an independent τ ($E_{\mathrm{T}}^{\mathrm{miss}}$) trigger and some requirements on the event selection like the BDT τ Id. The corresponding τ ($E_{\mathrm{T}}^{\mathrm{miss}}$) trigger part is applied to this sample and the response of this trigger is compared to the response in MC. The observed differences are integrated over the offline p_{T} of τ candidates and $E_{\mathrm{T}}^{\mathrm{miss}}$ range used for the cross section measurement. The total systematic uncertainty after the combination of the different trigger parts is 6.1%.

The uncertainties on the τ reconstruction and identification efficiencies are evaluated as described in Section 4.3. The corresponding changes in the signal and EW background efficiencies due to those uncertainties are found to be 9.6% and 4.1%, respectively.

The rate of jets that are mis-identified as τ candidates is obtained from W$\to \ell\nu$+jets events by measuring the fraction of reconstructed τ candidates passing the τ identification. The difference of this mis-identification rate in MC compared to that in data is 30% and this is applied as a systematic uncertainty to the fraction of background events, where the lepton is not reconstructed and the τ candidate is mistaken by a jet. The overall uncertainty on the EW background is 7.2%.

The mis-identification probability of electrons as τ candidates is measured in data as described in Section 4.3. The systematic uncertainty is the difference between the fake rate in data and MC as a function of η, and it results in 4.5% relative uncertaintes for the EW background.

The signal and background acceptance depends on the energy scale of the clusters used in the computation of $E_{\mathrm{T}}^{\mathrm{miss}}$ and $S_{E_{\mathrm{T}}^{\mathrm{miss}}}$ and the energy scale of the calibrated τ candidates. The uncertainty due to cluster energy within the detector region $|\eta| < 3.2$ is at most 10% for p_{T} of 500 MeV and about 3% at high p_{T} [134]. In the forward region $|\eta| > 3.2$ it is estimated to be 10%. All clusters in the event are scaled corresponding to these uncertainties and $E_{\mathrm{T}}^{\mathrm{miss}}$ and $\sum E_{\mathrm{T}}$ are recalculated to determine the uncertainty. Simultaneously, the energy scale of τ candidates is varied according to its uncertainty [136]. As described in Section 4.1.2 this uncertainty depends on the number of tracks associated to the τ candidate, its p_{T} and the η region in which it was reconstructed, and ranges from 2.5% to 10%. Additionally, the sensitivity of the signal and background efficiency to the $E_{\mathrm{T}}^{\mathrm{miss}}$ resolution has been investigated [133]. Consequently, the yield of signal and EW background varies within 6.7% and 8.7%, respectively.

The uncertainty of the QCD multijet background estimation accounts for two different sources, the stability of the method of estimating the QCD multijet background events from data and the contamination of signal and EW background events in the control regions. The stability of the method and the small correlation of the two variables (τ Id and $S_{E_{\mathrm{T}}^{\mathrm{miss}}}$) used to define the control regions have been tested by varying the $S_{E_{\mathrm{T}}^{\mathrm{miss}}}$ threshold.

The systematic uncertainty due to the correction for signal and EW background contamination in the control regions was obtained by varying the fraction of these events in the regions within the combined systematic and statistical uncertainties on the MC predictions discussed above. The total uncertainty on the QCD background estimation is 3.4%.

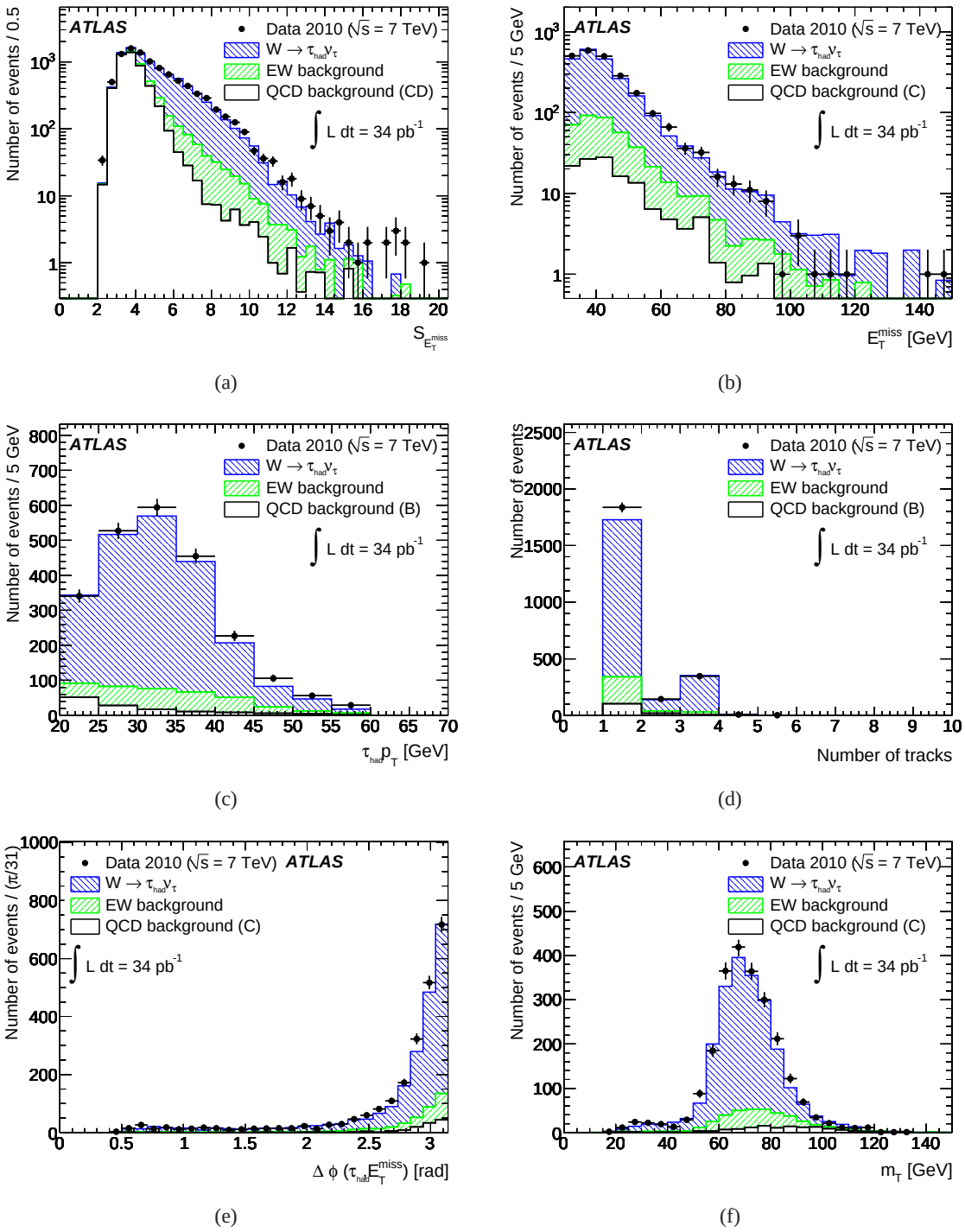

Figure 5.14: (a) Distribution of $S_{E_{\mathrm{T}}^{\mathrm{miss}}}$ in the combined region AB, extended over the full $S_{E_{\mathrm{T}}^{\mathrm{miss}}}$ range. The QCD background shape has been extracted from regions CD. (b) $E_{\mathrm{T}}^{\mathrm{miss}}$ in signal region A. The QCD multijet background shape has been extracted from control region C. (c) Transverse momentum and (d) number of tracks of τ candidates in signal region A. The QCD multijet background shape has been extracted from control region B. (e) Distribution of $\Delta\phi(\tau, E_{\mathrm{T}}^{\mathrm{miss}})$ and (f) transverse mass m_{T} in signal region A. The QCD multijet background shape has been extracted from control region C. The expectation from Monte Carlo signal and EW background in region A are also shown [162].

Table 5.6: Summary of systematic uncertainties for the $W \to \tau\nu$ cross section measurement. For the systematic uncertainty on the fiducial cross section measurement, correlations between the systematic uncertainties affecting C_W and N_{EW} are taken into account [162].

Systematic uncertainty on	C_W	N_{EW}	N_{QCD}	$\sigma^{\mathrm{fid}}_{W\to\tau_{\mathrm{had}}\nu}$
Trigger efficiency	6.1%	6.1%	-	7.0%
Energy scale	6.7%	8.7%	-	8.0%
τ Id efficiency	9.6%	4.1%	-	10.3%
Jet τ mis-identification	-	7.2%	-	1.1%
Electron τ mis-identification	-	4.5%	-	0.7%
Pile-up reweighting	1.4%	1.2%	-	1.6%
Electron reconstruction/identification	-	1.2%	-	0.2%
Muon reconstruction	-	0.3%	-	0.04%
Underlying event modelling	1.3%	1.1%	-	1.5%
Cross section	-	4.5%	-	0.7%
QCD estimation: Stability/correlation	-	-	2.7%	0.2%
QCD estimation: Sig./EW contamination	-	-	2.1%	0.1%
Monte Carlo statistics	1.4%	2.4%	6.0%	1.5%
Total systematic uncertainty	13.4%	15.2%	6.9%	15.1%

The procedure to include pile-up effects, the uncertainty on the lepton selection efficiency entering via the veto of electrons and muons and the influence of the underlying event modelling on $E_{\mathrm{T}}^{\mathrm{miss}}$ quantities is also evaluated and is found to have only small effects on the resulting cross section measurement.

The uncertainties on the cross sections used for the EW background are taken from ATLAS measurements, when available, or theoretical NNLO calculations, and lie between 3 and 9.7% [49, 167, 47, 168]. The uncertainty on the integrated luminosity is 3.4% [106, 107].

Systematic uncertainty on acceptance is estimated as in Section 5.1.5. The uncertainty resulting from the choice of the PDFs set is 1.9%. The difference in acceptance due to the modelling of W production is found to be smaller than 0.5%.

5.2.6 Cross section measurement

A summary of the numbers of observed events in data and estimated background contributions as well as the acceptance A_Z and the correction C_Z factors is given in Table 5.7. From those numbers the cross sections are derived. The measured fiducial cross section of the $W \to \tau_{\mathrm{had}}\nu$ is

$$\sigma^{\mathrm{fid}}_{W\to\tau_{\mathrm{had}}\nu} = 0.70 \pm 0.02\ (\mathrm{stat}) \pm 0.11\ (\mathrm{syst}) \pm 0.02\ (\mathrm{lumi})\ \mathrm{nb}, \tag{5.10}$$

and the total cross section is found to be

$$\sigma^{\mathrm{tot}}_{W\to\tau_{\mathrm{had}}\nu} = 7.2 \pm 0.2\ (\mathrm{stat}) \pm 1.1\ (\mathrm{syst}) \pm 0.2\ (\mathrm{lumi})\ \mathrm{nb}. \tag{5.11}$$

Alternative analyses are performed to confirm these results. For example, the BDT τ Id is replaced by the cut-based identification. Also, in order to study the influence of pile-up on the result, the signal selection is restricted to events with only one reconstructed primary vertex. In both cases consistent results are found.

Correcting the cross section for the hadronic τ decay branching ratio $BR(\tau \to \mathrm{hadrons}\ \nu) = 0.6479 \pm 0.0007$ [46] gives the following inclusive cross section $\sigma^{\mathrm{tot}}_{W\to\tau\nu}$:

$$\sigma^{\mathrm{tot}}_{W\to\tau\nu} = 11.1 \pm 0.3\ (\mathrm{stat}) \pm 1.7\ (\mathrm{syst}) \pm 0.4\ (\mathrm{lumi})\ \mathrm{nb}. \tag{5.12}$$

Table 5.7: Final numbers used in the cross section calculation. The errors include statistical and systematic uncertainties added in quadrature [162].

N_{obs}	2335
N_{QCD}	127 ± 9
N_{EW}	284 ± 43
A_W	0.0975 ± 0.0019
C_W	0.0799 ± 0.0107

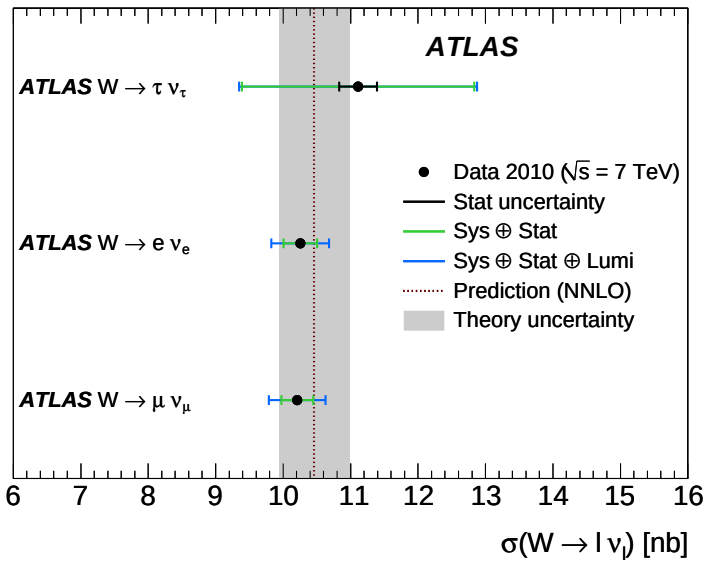

Figure 5.15: Cross sections for the different $W \to \ell\nu_\ell$ channels measured in ATLAS with 2010 data (points). Systematic, luminosity and statistical uncertainties are added in quadrature. The theoretical NNLO expectation is also shown (dashed line), together with its uncertainty (shaded area) [162].

The measured cross section is in good agreement with the theoretical NNLO cross section of 10.46±0.52 nb [49, 47, 168] and the ATLAS measurements of the $W \to e\nu$ and $W \to \mu\nu$ cross sections [160, 169]. The comparison of the cross section measurements for the different lepton final states and the theoretical expectation is shown in Figure 5.15.

5.3 Measurement of the τ identification efficiency using $W \to \tau\nu$ process

In both cross section measurements presented in previous sections the information about the τ identification efficiency was estimated in $Z \to \tau\tau$ MC samples as described in Section 4.3. In the following sections two complementary methods to measure the data-based τ identification efficiency using $W \to \tau_{\text{had}}\nu$ events are presented [170]. The first method uses a tag-and-probe technique, where events are tagged by selection imposed on the missing transverse energy of the event and the probe is the reconstructed τ candidate with no identification requirements applied. The track multiplicity spectrum of τ candidates is then fitted to templates in order to determine the τ signal contribution in data. The fitting is performed before and after applying a particular set of τ identification criteria, hence determining the identification efficiency.

The second method assumes that the $W \to \tau_{\text{had}}\nu$ production cross section is known. This and the fits using the background templates allow to extract the fraction of τ signal in selected $W \to \tau_{\text{had}}\nu$ events in data for given τ identification requirements. Obtained yield of τ candidates is compared to the Monte Carlo prediction in order to

derive the MC scale factor for the used τ identification method and working point.

Events used in this measurement have to pass the $E_{\mathrm{T}}^{\mathrm{miss}}$ trigger in order to apply a minimal bias on τ candidates. The $E_{\mathrm{T}}^{\mathrm{miss}}$ trigger threshold varied during data taking together with increasing luminosity and is required to be above $20 - 40$ GeV at the EF level. The tag-and-probe method does not depend on the luminosity thus the used data set contains many trigger items with or without prescales. In contrary, in the cross section normalisation method only un-prescaled triggers are used to accurately evaluate the acceptance.

The signal and background Monte Carlo samples are the same as for the $W \to \tau_{\mathrm{had}}\nu$ cross section measurement described in the previous Section. The only exception are samples used in the cross section normalisation method since the analysis requires the presence of jets depending on the trigger conditions. In this case the ALPGEN [171] $W+$ multi-jets samples interfaced with HERWIG and multi-parton interactions modelled by JIMMY [172] are used.

The existing backgrounds and the standard preselection of events are the same as for the $W \to \tau_{\mathrm{had}}\nu$ cross section measurement. In order to suppress $W \to \ell\nu$ and $Z \to \ell\ell$ backgrounds, events with electrons passing medium identification criteria and with $p_{\mathrm{T}} > 20$ GeV or combined muons with $p_{\mathrm{T}} > 15$ GeV are rejected.

5.3.1 Tag-and-probe method

The tag-and-probe method selects $W \to \tau_{\mathrm{had}}\nu$ events by requiring significant $E_{\mathrm{T}}^{\mathrm{miss}}$ on the tag side, and a reconstructed τ candidate on the probe side. For such τ candidates, the efficiency is determined if the events pass the τ identification criteria. This method suffers from the purity of the τ signal before identification and from the imperfect estimation of the QCD multijet background.

Similar event selection as this described for the $W \to \tau_{\mathrm{had}}\nu$ cross section measurement in Section 5.2.2 is applied. The $E_{\mathrm{T}}^{\mathrm{miss}}$ is required to be above 30 GeV and $S_{E_{\mathrm{T}}^{\mathrm{miss}}} \geq 6$. In addition the azimuthal separation between $E_{\mathrm{T}}^{\mathrm{miss}}$ and any jet with $p_{\mathrm{T}} > 20$ GeV is required to be $\Delta\phi(E_{\mathrm{T}}^{\mathrm{miss}}, \mathrm{jet}) \geq 0.7$ rad. This is to reject di-jet events where the energy of one of the jets is mis-measured and leads to large fake $E_{\mathrm{T}}^{\mathrm{miss}}$. The reconstructed probe τ candidates should have $p_{\mathrm{T}} > 20$ GeV and the leading track of the τ candidate is required to have $p_{\mathrm{T}} > 2.4$ GeV. If several candidates are present, the one leading to the transverse mass $m_{\mathrm{T}} = \sqrt{2p_{\mathrm{T}} \cdot E_{\mathrm{T}}^{\mathrm{miss}} \left(1 - \cos\Delta\phi(\tau, E_{\mathrm{T}}^{\mathrm{miss}})\right)}$ closest to 65 GeV (the most probable value from a true τ in a $W \to \tau_{\mathrm{had}}\nu$ event) is kept, while m_{T} itself must not be > 80 GeV. Also lepton vetoes provided by the τ identification algorithm are applied.

As already mentioned, the particle structure in QCD jets is more spread out than that in a τ candidate and a jet has higher track multiplicity. However, the association of tracks in the reconstructed τ candidate is restricted within $\Delta R < 0.2$ of the τ direction, as described in Section 4.1. Thus, the jets faking τ candidates can not get higher track multiplicity due to the limited cone size. To obtain better separation against QCD multijet events before τ identification, an anti-k_{T} style track counting method is introduced [127]. It takes into account the momentum correlation between tracks in the core of the reconstructed object ($\Delta R < 0.2$) and tracks around it ($0.2 < \Delta R < 0.4$). For real τ_{had} decays, tracks belonging to the τ_{had} decay are within the core and there is no correlation between these tracks and tracks in the outer region coming from pileup or the underlying event. For QCD jets, on the contrary, tracks from the jet are correlated over the full extent of the jet up to $\Delta R < 0.4$, but still uncorrelated to pile-up and underlying event tracks. This increases the average number of tracks associated to jet candidates while leaving the number of tracks associated to τ candidates almost unchanged.

The track multiplicity distribution is fitted in order to extract the signal contribution from data. The fit is done twice, before and after τ identification. In each fitting, the signal contribution in data is extracted. The ratio between values of the fits is the τ identification efficiency. The selection reduces background from $Z \to ll$ to a negligible level, and the small remaining $W \to \mu\nu$ background is absorbed, for simplicity, in the QCD multijet background modelling when an extra jet fakes a τ candidate and in the $W \to e\nu$ template when a real muon fakes a τ candidate. Thus, three contributions are considered: signal τ, electron and QCD multijet events. It results in six track multiplicity templates constructed. The QCD multijet background templates used in the fit come from the data (as described below), while the τ signal and electron contributions come from MC $W \to \tau\nu$ and $W \to e\nu$ samples. Since the electron fake rate is already measured in data as described in Section 4.3.3, the fraction of high

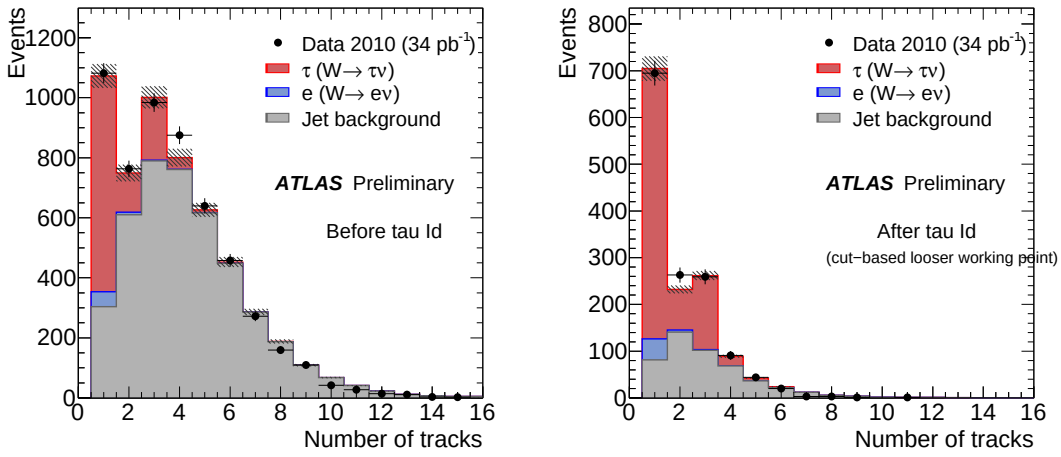

(a) (b)

Figure 5.16: Track multiplicity before (a) and after (b) cut-based τ Id looser working point. The hatching represents the systematic uncertainty. The normalisation of the different processes is determined through a fit to the track multiplicity spectrum [170].

p_{T} electrons is constrained in the fit using this result.

A QCD multijet enriched control region is defined by requiring $2 < S_{E_{\mathrm{T}}^{\mathrm{miss}}} \leq 4.5$. As obtained sample has a different p_{T} spectrum of the τ candidates as compared to the signal region, it is therefore reweighted by comparing p_{T} spectra in the control and signal regions for τ candidates with at least four tracks to avoid bias by the true signal. It has been checked that the track multiplicity spectrum is not strongly dependent on the chosen $S_{E_{\mathrm{T}}^{\mathrm{miss}}}$ range or on the p_{T} reweighting function. The slight differences observed are treated as systematic uncertainties.

Systematic uncertainties are estimated by comparing the τ identification efficiency obtained with nominal templates to the τ identification efficiency obtained with templates generated based on various systematic effects. The sources of systematic uncertainty considered are: $E_{\mathrm{T}}^{\mathrm{miss}}$ trigger, the modelling of the jet template (p_{T}-weighting and $E_{\mathrm{T}}^{\mathrm{miss}}$ significance cut), electron mis-identification probability, pile-up, shower model used in the simulation, the MC detector description and underlying event modelling. The total systematic uncertainty found is 3.7% for the cut-based τ Id looser working point.

Track multiplicity distributions are shown in Figure 5.16 before and after the cut-based τ identification looser working point. In all figures the different contributions are normalised to their respective number of events as measured from the track multiplicity fit. Data are well modelled and the (1,3)-track structure from real τ_{had} decays is visible.

The τ identification efficiency is evaluated for the different working points, as summarised in Table 5.8. Purities of 45–65% are obtained after identification when including all track multiplicities. They increase to 60–80% for candidates with $p_{\mathrm{T}} > 30$ GeV and one or three tracks. Although the signal purity is high enough after identification, the obtained statistical uncertainty on the efficiency determination is dominated by the background fluctuation before identification. A data/MC scale factor for the identification efficiency $\varepsilon_{\mathrm{data}}^{\mathrm{Id}}/\varepsilon_{\mathrm{MC}}^{\mathrm{Id}}$ is also reported. It can be seen that the measured efficiency in data is very close to the expected efficiency measured in MC (scale factors close to 1), and compatible within uncertainties.

5.3.2 Cross section normalisation method

In this method events passing the full selection in data are compared to the prediction in order to derive a scale factor for τ identification, assuming the $W \rightarrow \tau\nu$ production cross section is known and equal, via lepton universality, to the $W \rightarrow e\nu, \mu\nu$ cross sections measured by ATLAS [160].

Table 5.8: Total relative systematic uncertainty (Syst.), measured efficiency, and data/MC scale factor for different τ identification methods and working points. The first uncertainty is statistical, the second is systematic [170].

Method	Syst.	Efficiency	Scale factor
Cut-based looser	3.7%	$0.77 \pm 0.05 \pm 0.03$	$1.04 \pm 0.06 \pm 0.04$
Cut-based tighter	9.9%	$0.56 \pm 0.06 \pm 0.06$	$0.98 \pm 0.11 \pm 0.10$
Likelihood looser	5.0%	$0.82 \pm 0.07 \pm 0.04$	$1.02 \pm 0.09 \pm 0.05$
Likelihood tighter	5.7%	$0.60 \pm 0.06 \pm 0.03$	$0.95 \pm 0.09 \pm 0.05$
BDT looser	4.4%	$0.78 \pm 0.05 \pm 0.03$	$1.05 \pm 0.06 \pm 0.05$
BDT tighter	5.1%	$0.55 \pm 0.04 \pm 0.03$	$0.92 \pm 0.07 \pm 0.05$

The track multiplicity of τ candidates is fitted after the selection described below, using templates from MC samples for $W \to \tau\nu$ (only using truth-matched events) and electroweak backgrounds, and the QCD multijet background from data in order to extract the fraction of τ signal in data. While performing the fit to data, the normalisation of electroweak components is fixed to their measured cross sections [160] and the fraction of τ is the only free parameter. The statistical uncertainty on templates is taken into account by the fit and propagated to the fit uncertainty.

Each event is assigned to one of the three categories based on the $E_{\mathrm{T}}^{\mathrm{miss}}$ trigger and jet multiplicity (no extra jet with $p_{\mathrm{T}} > 20$ GeV, or 1 or 2 extra jets). Only unprescaled $E_{\mathrm{T}}^{\mathrm{miss}}$ triggers are used. Because of limited statistics in the high $E_{\mathrm{T}}^{\mathrm{miss}}$ trigger sample, all jet multiplicities are kept in one sample. $E_{\mathrm{T}}^{\mathrm{miss}}$ is required to be above 30 GeV or 40 GeV depending on the trigger used. $\Delta\phi(E_{\mathrm{T}}^{\mathrm{miss}}, \mathrm{jet}) \geq 0.5$ rad is required for events with extra jets to reject large fake $E_{\mathrm{T}}^{\mathrm{miss}}$ events. Additional rejection of fake $E_{\mathrm{T}}^{\mathrm{miss}}$ events is achieved with a requirement on the $E_{\mathrm{T}}^{\mathrm{miss}}$ significance partly based on tracks, defined as $S_{E_{\mathrm{T}}^{\mathrm{miss}}}^{\mathrm{vtx}} = E_{\mathrm{T}}^{\mathrm{miss}}/(1.0\ \sqrt{\mathrm{GeV}}\sqrt{\Sigma p_{\mathrm{T}}})$, where Σp_{T} is the scalar sum of p_{T} of tracks associated to the primary vertex. Σp_{T} is quite well modelled by MC and relatively robust against pile-up because of the primary vertex constraint. $S_{E_{\mathrm{T}}^{\mathrm{miss}}}^{\mathrm{vtx}}$ is therefore quite stable with varying instantaneous luminosity. $S_{E_{\mathrm{T}}^{\mathrm{miss}}}^{\mathrm{vtx}} > 6(7)$ is required for low $E_{\mathrm{T}}^{\mathrm{miss}}$ trigger sample with no (1 or 2) extra jets and $S_{E_{\mathrm{T}}^{\mathrm{miss}}}^{\mathrm{vtx}} > 8$ for the high $E_{\mathrm{T}}^{\mathrm{miss}}$ trigger sample. Selection of τ candidates is the same as for the tag-and-probe method. Depending on the trigger and jet multiplicity, different transverse mass windows are required: $60 < m_{\mathrm{T}} < 100$ GeV for low $E_{\mathrm{T}}^{\mathrm{miss}}$ trigger sample with no extra jet; $30 < m_{\mathrm{T}} < 90$ GeV when 1 or 2 extra jets are present; $30 < m_{\mathrm{T}} < 80$ GeV for the high $E_{\mathrm{T}}^{\mathrm{miss}}$ trigger sample.

The $E_{\mathrm{T}}^{\mathrm{miss}}$ trigger efficiency estimate, crucial for this analysis, is measured in data using a pure $W \to e\nu$ sample. It is further corrected by the ratio of the efficiencies of the $E_{\mathrm{T}}^{\mathrm{miss}}$ trigger in $W \to \tau\nu$ and $W \to e\nu$ MC samples. An obtained efficiency is applied as a weight to the $W \to \tau\nu$ MC sample instead of using the trigger simulation information directly.

The modelling of the jet multiplicity template is one of the crucial tasks in this study. The track multiplicity distributions are expected to be significantly different between high and low $S_{E_{\mathrm{T}}^{\mathrm{miss}}}^{\mathrm{vtx}}$ samples due to the $S_{E_{\mathrm{T}}^{\mathrm{miss}}}^{\mathrm{vtx}}$ variable definition. Thus, the $E_{\mathrm{T}}^{\mathrm{miss}}$ significance sidebands cannot be used here to obtain the track multiplicity template from jets, as it is done in the tag-and-probe method. Instead, the jet template is extracted from $W \to e\nu$+jets events, selected by requiring a single electron trigger, a single electron passing medium identification requirements, $E_{\mathrm{T}}^{\mathrm{miss}} > 30$ GeV, $S_{E_{\mathrm{T}}^{\mathrm{miss}}}^{\mathrm{vtx}} > 6$ as for the signal region, exactly one τ candidate not overlapping with the electron within $\Delta R < 0.2$ and $30 < m_{\mathrm{T}} < 90$ GeV. The track multiplicity thus obtained is well described by MC simulation, and used in the fit to represent jets.

Systematic uncertainties are estimated by comparing the fit result with nominal templates to the fit result with templates generated with varied conditions to account for various systematic effects. The considered sources of systematic uncertainty are: jet background modelling, uncertainty on the W production cross section measured by

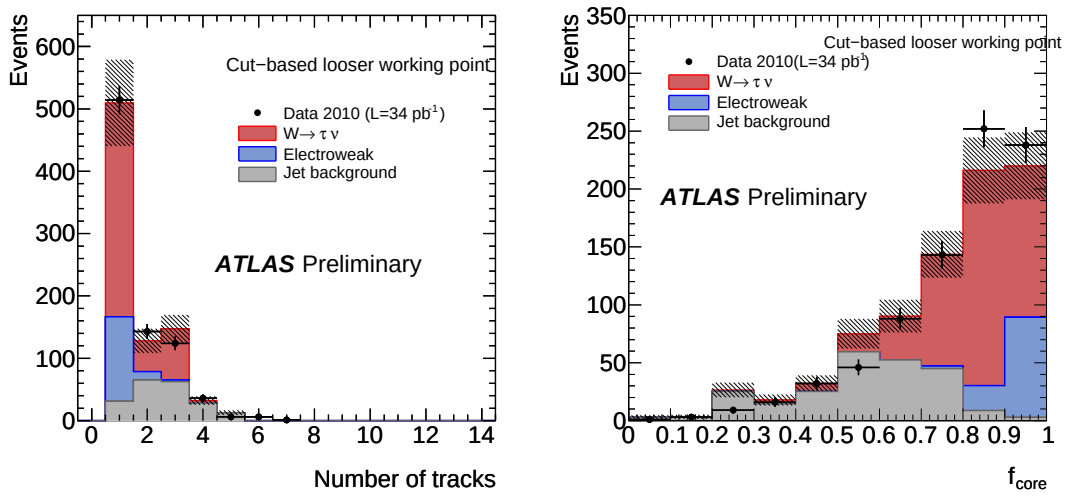

(a) (b)

Figure 5.17: Track multiplicity (a) and core energy fraction, f_{core} (b) distributions in the signal region after cut-based τ identification looser working point, summed over the three event categories. The hatching represents the systematic uncertainty [170].

ATLAS, trigger efficiency, lepton identification, electron mis-identification, τ, electron and jet energy scale, pile-up and underlying event. The total systematic uncertainty found for the cut-based τ identification looser working point is 12.9%. The dominant systematic effect is the τ energy scale.

The track multiplicity distribution (summed over the three event categories) is shown in Figure 5.17(a) after the looser-cuts τ identification is applied. The jet and τ contributions are normalised to the fractions as predicted by the fit. The model reproduces the data quite accurately and the (1,3)-track structure of real τ_{had} decays is clearly visible. Identification variables are also reasonably well described, as shown in Figure 5.17(b).

The data over MC τ identification efficiency scale factor is evaluated for different working points, as summarised in Table 5.9. They are all compatible with unity within uncertainties. Systematic uncertainties are significantly larger with the cross section method because it suffers from a large uncertainty on the τ energy scale.

Table 5.9: Data over MC τ identification efficiency scale factors measured with the cross section method for different τ identification methods and working points. The first uncertainty is statistical, the second is systematic [170].

Method	Scale factor
Cut-based looser	1.00 ± 0.05 ± 0.13
Cut-based tighter	0.96 ± 0.05 ± 0.14
Likelihood looser	1.02 ± 0.04 ± 0.16
Likelihood tighter	1.00 ± 0.07 ± 0.13
BDT looser	0.94 ± 0.07 ± 0.13
BDT tighter	0.89 ± 0.05 ± 0.10

5.4 Summary

This Chapter presents the first measurements of $Z \to \tau\tau$ and $W \to \tau\nu$ cross sections in the ATLAS experiment, the milestones for the physics with τ leptons in final states.

The $Z \to \tau\tau$ cross section is measured in four different final states defined by the decay modes of the τ leptons: muon-hadron, electron-hadron, electron-muon, and muon-muon. Cross sections are measured separately for each final state in fiducial regions of a high detector acceptance, as well as in the full phase space, over the mass region 66 - 116 GeV. The individual cross sections are combined and the product of the total Z production cross section and $Z \to \tau\tau$ branching fraction is measured to be 0.97 ± 0.07 (stat) ± 0.06 (syst) ± 0.03 (lumi) nb in agreement with NNLO calculations and other experimental results.

The cross section for the production of W bosons with subsequent decay $W \to \tau\nu$ is also measured in a region of high detector acceptance and then extrapolated to the full phase space. The product of the total W production cross section and the $W \to \tau\nu$ branching ratio is measured to be 11.1 ± 0.3 (stat) ± 1.7 (syst) ± 0.4 (lumi) nb. The measured cross section is also in good agreement with the theoretical NNLO cross section.

The first study to determine the hadronic τ decay identification efficiency with $W \to \tau\nu$ events is reported. Two approaches are used. In the tag-and-probe method, events are tagged by having significant missing transverse energy, while the probe is the hadronic τ decay candidate. The track multiplicity spectrum is fitted simultaneously before and after applying τ identification, hence determining the efficiency. The second technique assumes that the $W \to \tau\nu$ production cross section is known and compares expected yields to those measured in data. The results are consistent with Monte Carlo predictions and with each other.

All presented measurements were performed using data collected in 2010 only, but during completing the presented monograph more studies have been done with higher statistics data sets.

The $Z \to \tau\tau$ cross section was re-measured using the integrated luminosity of 1.34 – 1.55 fb^{-1} [173] for 2011 data sample. The statistical error on the cross section was decreased by a factor of three in respect to the result presented in this Chapter.

Also the τ identification efficiency measurement with $W \to \tau\nu$ events was repeated with 2011 data and the first measurement of this efficiency with $Z \to \tau\tau$ process was performed [144].

The $W \to \tau\nu$ decay was also used for the first measurement of τ polarisation at hadron colliders [174]. Similar analysis with $Z \to \tau\tau$ process is under preparation.

As mentioned in Section 2.2, a measurement of the cross section of top quark pair production with τ leptons in final state is of interest because it can open a window to physics beyond the Standard Model. The ATLAS collaboration published recently such studies [175] based on an integrated luminosity of 2.05 fb^{-1}. Events with an isolated electron or muon and a τ lepton decaying hadronically are used. No New Physics signs are found. The measured cross section is in good agreement with the Standard Model prediction.

Be careful what you wish for; you may get it.

Old proverb

6

Standard Model Higgs boson searches with τ final states

As mentioned in Section 2.3, the decay of the neutral Higgs bosons into a pair of τ leptons is a valuable channel for the SM Higgs boson searches at the LHC. This search is complementary to searches with other decays in the same mass range. Two analyses have been performed. The first one, fully leptonic, with both τ leptons decaying into leptons, and requiring the Higgs boson to be produced in association with jets. The second one, semi-leptonic, with one τ lepton decaying into lepton and second decaying hadronically. The first one is an independent search for the Standard Model Higgs boson [176] and the second is part of the search for the Minimal Supersymmetric Standard Model Higgs boson, done in conjunction with other search channels [177]. Both analyses are based on a data sample corresponding to an integrated luminosity of 1.06 fb^{-1} collected at the LHC in the first half of 2011.

6.1 $H \to \tau_{\text{lep}}\tau_{\text{lep}}$ + jets final state

The H $\to \tau_{\text{lep}}\tau_{\text{lep}} \to \ell\ell + 4\nu$ final state is characterised by a back-to-back configuration of the two τ leptons in the Higgs boson rest frame. The sensitivity of the search is enhanced by requiring that the Higgs boson is produced in association with jets. In this case, the Higgs boson is more boosted in the transverse plane. This enhances the transverse momenta of the Higgs decay products and, as a consequence, the $E_{\text{T}}^{\text{miss}}$ of the event due to the undetected neutrinos from the two τ decays. The presence of large $E_{\text{T}}^{\text{miss}}$ and a high p_{T} jet allows this topology of Higgs boson decays to be differentiated from background processes as shown by previous studies [58]. The signal contributions considered here include the dominant gluon fusion production process, vector boson fusion (VBF) and W/Z associated production. Three final states are considered, two same flavour (SF) ee, $\mu\mu$ final states and one different flavour (DF) eμ final state.

The following are the dominant background processes:

- **$\gamma^*/Z(\to ll)$+jets**: $\gamma^*/Z \to \tau\tau$ decays form a largely irreducible background as they have similar event kinematics as the signal. This background is particularly important for low Higgs boson masses where the signal falls on the tail of the Z mass peak in the $\tau\tau$ mass distribution. γ^*/Z production with electron or muon pairs in the final state also contribute.

- **$W(\to l\nu)$+jets**: this process contributes to the background due to the presence of a charged lepton and $E_{\text{T}}^{\text{miss}}$ in the final state and its large cross section. Hadronic jets accompanying the W boson can be mis-identified as an electron, or a semi-leptonic decay in the cascade can give a signature similar to the one of an isolated lepton.

- **Di-boson production**: can lead to final states with two or more charged leptons from the leptonic decays of the W and Z bosons.
- $t\bar{t}$: can lead to final states with two leptons and $E_{\mathrm{T}}^{\mathrm{miss}}$ in the final state.
- **Single-t production**: contributes if W decays leptonically and one of the leptons is either due to a mis-identified hadronic jet or, for Wt production, comes from the decay of the second W boson.
- **QCD multijets**: contributes with true (e.g. produced from heavy flavour decays) or fake leptons and has a large cross section.

Requiring, after all the other selection criteria, at least one high p_{T} jet, reduces the $\gamma^*/Z \to \ell\ell$ acceptance by a factor of 7 and the $Z \to \tau\tau$ acceptance by a factor of 2.5, while the signal acceptance is reduced only by 30%.

6.1.1 Data and Monte Carlo samples

Events in eμ and $\mu\mu$ final states are selected using a combined muon trigger of $p_{\mathrm{T}} > 18$ GeV. Events passing a stand-alone muon trigger in the barrel region with $p_{\mathrm{T}} > 40$ GeV are also accepted. For eμ final state also an electron trigger with $E_{\mathrm{T}} > 20$ GeV passing medium identification criteria is used. For di-electron final state, a di-lepton trigger requiring two electron trigger objects with $E_{\mathrm{T}} > 12$ GeV and passing medium electron identification criteria is applied. The trigger efficiencies are measured in data as a function of the offline lepton p_{T} with the tag-and-probe method in a data sample enriched in $Z \to \ell\ell$ events. The single electron trigger efficiencies are about 98% while for the single muon trigger the efficiencies are between 73% and 87% for the barrel and end-cap regions, respectively. The di-electron trigger efficiency is calculated to be 98%. Monte Carlo simulation is corrected to agree with data by applying the trigger scale factors parametrised as a function of η, ϕ and p_{T}.

The cross sections for Higgs boson production were calculated following the prescriptions of the LHC Higgs cross section working group [55]. In gluon fusion they were calculated using HIGLU [178] and ggh@nnlo [179] at the NNLO. For the vector-boson fusion, the NNLO calculation was performed with VBF@NNLO [180, 55]. The SM $gg \to H$ production via gluon fusion was simulated with MC@NLO and the vector-boson production with HERWIG . The production of W and γ^*/Z bosons in association with jets is simulated with the ALPGEN generator, apart from the $\gamma^*/Z \to \tau\tau$ and $W \to \tau\nu$ processes, that are simulated with PYTHIA. The $t\bar{t}$ and single-t (s-channel) processes are generated with MC@NLO, the single-t (t-channel, Wt) process is generated with AcerMC [181], and di-boson production processes are generated with HERWIG. For all MC@NLO samples parton showers and hadronisation are simulated with HERWIG and the activity of the underlying event with JIMMY. The programs TAUOLA and PHOTOS are used to model respectively the decay of τ leptons and additional photon radiation in decays produced in PYTHIA, MC@NLO and HERWIG.

Residual differences in the pile-up between data and Monte Carlo samples are corrected by re-weighting the Monte Carlo events to reproduce the pile-up distributions in data.

6.1.2 Objects and event selection

Only events containing at least one primary vertex with three or more associated tracks, as well as fulfilling preselection requirements described in Section 3.6 are used in the analysis. As the next step, the following reconstructed objects are chosen.

Electron candidates are selected if they have $E_{\mathrm{T}} > 15$ GeV and $|\eta| < 2.47$ (excluding the transition region in the calorimeters) and pass the tight identification requirements. In addition, they should have $E_{\mathrm{T}} > 22$ GeV if the event is triggered by the single electron trigger. Identified electron candidates are required to be isolated, $I_{ET}^{0.2}/E_{\mathrm{T}} < 0.08$ and $I_{PT}^{0.4}/p_{\mathrm{T}} < 0.06$. Electron transverse energy scale and resolution in Monte Carlo are made to agree with data by applying rescaling and smearing of the simulated electron transverse energy.

Combined muon candidates are required to have $p_{\mathrm{T}} > 10$ GeV and $|\eta| < 2.5$. If the event is triggered by the single muon trigger, the muon candidate is required to have $p_{\mathrm{T}} > 20$ GeV. Additionally, the difference between the z-position of the point of closest approach of the muon Inner Detector track to the beam-line and the z-coordinate

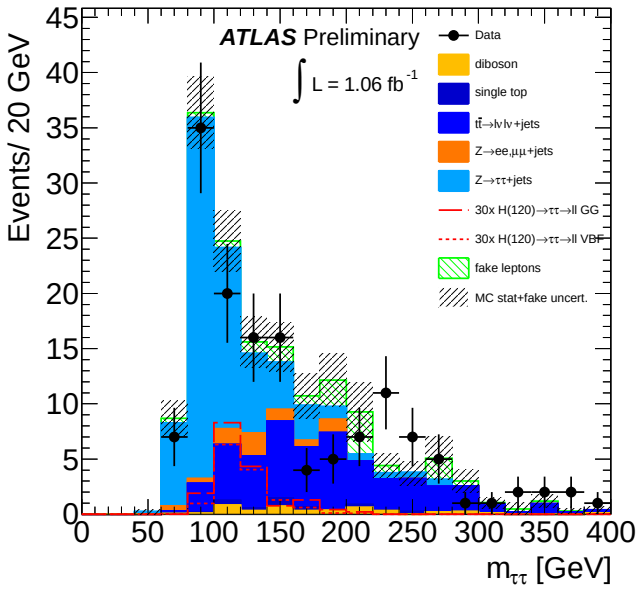

Figure 6.1: $m_{\tau\tau}$ invariant mass after all analysis cuts except the final cut on $m_{\tau\tau}$. The backgrounds with fake leptons and the $Z \to \tau\tau$ contribution are estimated from data. All other contributions are estimated using simulated event samples [176].

of the primary vertex is required to be less than 1 cm. This requirement reduces the contamination due to cosmic events and beam-induced backgrounds. Finally, Inner Detector hit requirements and muon quality criteria are applied in order to achieve a high-quality measurement of the muon momentum and reduce the mis-identification rate. Muon candidates are required to be isolated, $I_{ET}^{0.2}/E_{\mathrm{T}} < 0.04$ and $I_{PT}^{0.4}/p_{\mathrm{T}} < 0.06$. Muon transverse momentum resolution in Monte Carlo is made to agree with data by applying smearing of the simulated muon transverse momentum.

Jets are required to have $p_{\mathrm{T}} > 20$ GeV and $|\eta| < 4.5$. Missing transverse energy used in this analysis follows the simple definition as described in Section 3.5.

Objects reconstructed from the same localised response in the detector are removed, namely any selected electron within a distance $\Delta R < 0.2$ of a selected muon is removed from further consideration in the analysis. Similarly, any selected jet within $\Delta R < 0.2$ of a selected muon or electron is also removed.

Events are selected if they contain exactly two isolated leptons of opposite charge and of invariant mass $m_{\ell\ell} > 20$ GeV. Further, this requirement is tightened depending on the final state: $30 < m_{\ell\ell} < 75$ GeV for the SF final states and $30 < m_{\ell\ell} < 100$ GeV for the DF final state. The requirement is tighter in the SF final state in order to reject $\gamma^*/Z \to ee, \mu\mu$ backgrounds. As a next step, at least one jet with transverse momentum above 40 GeV and $E_{\mathrm{T}}^{\mathrm{miss}} > 30$ GeV for SF events and $E_{\mathrm{T}}^{\mathrm{miss}} > 20$ GeV for DF events is required.

The final invariant mass is reconstructed using the collinear approximation described in Appendix A. Events have to fulfil the following selection: $0.2 < x_1 < 0.8$ and $0.1 < x_2 < 0.6$, where $\mathrm{x}_{1,2}$ are momentum fractions carried away by visible τ decay products with momenta $p_{\mathrm{vis1,2}}$ and $p_{\mathrm{mis1,2}}$ are momenta carried by neutrinos:

$$x_{1,2} = \frac{p_{\mathrm{vis1,2}}}{(p_{\mathrm{vis1,2}} + p_{\mathrm{mis1,2}})} \,. \tag{6.1}$$

The requirement of an extra jet in the event improves the efficiency of these cuts. The next selection is $0.3 < \Delta\phi_{\ell\ell} < 2.5$ rad for SF events and $0.3 < \Delta\phi_{\ell\ell} < 2.8$ rad for DF events in order to reject $\gamma^*/Z \to \ell\ell$ and $t\bar{t}$ processes. A selected jet has to have $|\eta| > 0.5$ as jets produced in the $t\bar{t}$ decays tend to be more central than the ones produced in SM Higgs boson decays.

Table 6.1: Number of events after all selection criteria in data, expected background events and expected SM Higgs boson signal for a data sample corresponding to 1.063 fb^{-1}. The contribution of backgrounds with fake leptons and the $Z \to \tau\tau$ are estimated in a data-driven way. Errors are statistical only [176].

		ee + $\mu\mu$ + eμ
Observed data		46
$\gamma^*/Z \to \tau\tau$		25.4 ± 2.7
$\gamma^*/Z \to \ell\ell$		3.7 ± 1.2
$t\bar{t}$		13.2 ± 2.2
Single-t		1.2 ± 0.5
Di-boson		1.6 ± 0.6
Backgrounds with fake leptons		2.2 ± 0.9
Total Background expectation		47.4 ± 3.9
Expected signal events	$gg \to H$	VBF
m_H = 110 GeV	0.39 ± 0.06	0.35 ± 0.02
m_H = 115 GeV	0.39 ± 0.06	0.35 ± 0.02
m_H = 120 GeV	0.44 ± 0.05	0.38 ± 0.02
m_H = 130 GeV	0.40 ± 0.04	0.33 ± 0.01
m_H = 140 GeV	0.21 ± 0.02	0.19 ± 0.01

The invariant mass of the system formed by the two τ leptons and the leading jet, $m_{\tau\tau j}$, has to be above 225 GeV. The four-momentum of the two τ system is calculated in the collinear approximation (see Appendix A). This requirement reduces the background from $\gamma^*/Z \to ll$ processes [58]. Finally, only events with invariant mass of the two τ leptons system, $m_{\tau\tau}$, between 100 GeV and 150 GeV are considered. The acceptance of this selection is above (70-80)% for the SM Higgs signal in the Higgs mass range 110 GeV $\leq m_H \leq$ 140 GeV.

Figure 6.1 shows the $m_{\tau\tau}$ distribution of events passing the full selection described above except the final cut on $m_{\tau\tau}$. Table 6.1 shows the corresponding yields of events and MC expected number of events for 1.063 fb^{-1}. The expected numbers of signal and background events from simulations are normalised according to the theoretical cross section predictions described in the previous Section. Details on the estimated background events are given in the following Section.

6.1.3 Background estimation

The description of the dominant, largely irreducible $Z \to \tau\tau$ process in the simulation is confirmed by using the τ-embedding method: in a sample of selected $\gamma^*/Z \to \mu\mu$ data events, the muon tracks and associated calorimeter cells are removed and replaced by τ leptons from a simulated $Z \to \tau\tau$ decay.

The contribution of the $t\bar{t}$, single t, $Z \to \ell\ell$ and electroweak di-boson production backgrounds are estimated from simulation. Their MC description is confirmed by data by selecting control regions enriched in these background processes.

Backgrounds arising from the presence of fake leptons are derived from data in signal free control samples. The main sources of fake leptons are the QCD multijets, W+jets and semi-leptonic $t\bar{t}$ processes. Non-isolated leptons produced in heavy flavour meson decays, are included in this background.

The normalisation and the shape of the backgrounds with fake leptons are obtained from data with a template method [182] using a control region in which the lepton isolation criterion is reversed. The chosen template shape is the p_{T} distribution of the sub-leading lepton. After subtraction of the simulated backgrounds, the template shape of this background is obtained from a control sample, while the normalisation is obtained from a fit of the analysis data sample with the template shape. The uncertainty related to the estimation of backgrounds with fake leptons is

Table 6.2: Individual systematic uncertainties for SM Higgs signal and backgrounds. All numbers are relative errors expressed as percentages [176].

Relative Uncertainty (%)		
Uncertainty Source	Signal (m_H=120 GeV)	Background
	Object selection	
Lepton scale factors (%)	-2.7/+2.1	-4.2/+1.8
Lepton energy scale (%)	-0.3/+0.3	-0.8/+0.8
Lepton energy resolution (%)	-0.5/+0.2	-2.6/+0.3
Jet energy scale (%)	-7.8/+4.1	-9.8/+7.0
Jet energy resolution (%)	-2.0/+2.0	-2.5/+2.5
Jet reconstruction efficiency (%)	0.0	0.0
$E_{\mathrm{T}}^{\mathrm{miss}}$ reconstruction (%)	-5.3/+4.4	-2.7/+0.4
Pile-up (%)	-1.5/+1.5	-0.8/+0.8
Detector modelling (%)	-1.6/+1.6	-1.6/+1.6
	Process rate	
Fakes normalisation (%)	-	-1.9/+1.9
$Z \to \tau\tau$ embedding (%)	-	-0.5/+0.5
Cross section Z+jets (%)	-	-2.9/+2.9
Cross section $t\bar{t}$(%)	-	-4.8/+4.8
Cross section singleTop (%)	-	-0.2/+0.2
Cross section di-bosons (%)	-	-0.4/+0.4
Cross section $H(m_H$=120GeV) (%)	-10.8/+10.8	-
	Monte Carlo modelling	
Signal MC Generator (%)	-4.4/+4.4	-
PDF (%)	-4.8/+4.8	-3.0/+3.0
Luminosity (%)	-3.7/+3.7	-3.5/+3.5
MC statistics (%)	-6.5/+6.5	-8.0/+8.0

calculated from the uncertainty on the subtraction of other processes from MC simulation and from the difference in the p_{T} distribution shape between the control and the signal regions. The statistical contribution is the main component after all the selection cuts and it is around 50%, while the systematic uncertainty is up to 30% in the eμ channel.

6.1.4 Systematic uncertainties

The systematic uncertainties considered for the Higgs boson signal (m_H=120 GeV) and backgrounds are presented in Table 6.2. Uncertainty connected to the lepton scale factors takes into account correcting the MC samples for differences between MC and data. The muon momentum scale and resolution as well as electron energy resolution are smeared to match that is observed in data. The electron energy is corrected in data according to in-situ calibrations. The uncertainties associated to the re-scaling and smearing are taken into account. The uncertainty on the jet energy is determined from "up" and "down" variations corresponding to 1σ uncertainties obtained from data studies. The systematic uncertainty of the jet reconstruction efficiency accounts for the difference between data and MC in the reconstruction efficiency of calorimeter jets with respect to track jets, measured with a tag-and-probe method in QCD di-jet events. The efficiency depends on the jet p_{T} and the difference between data and MC has a negligible effect for jets with p_{T}>40 GeV. For estimating the $E_{\mathrm{T}}^{\mathrm{miss}}$ reconstruction uncertainty, the lepton and jet energy scale and resolution systematics are propagated to $E_{\mathrm{T}}^{\mathrm{miss}}$. Other uncertainties specific to the $E_{\mathrm{T}}^{\mathrm{miss}}$ reconstruction are also taken into account. Uncertainty connected to pile-up is introduced by reweighting of the MC events to match pile-up in data. Also a systematic uncertainty is assigned to the MC modelling of the detector

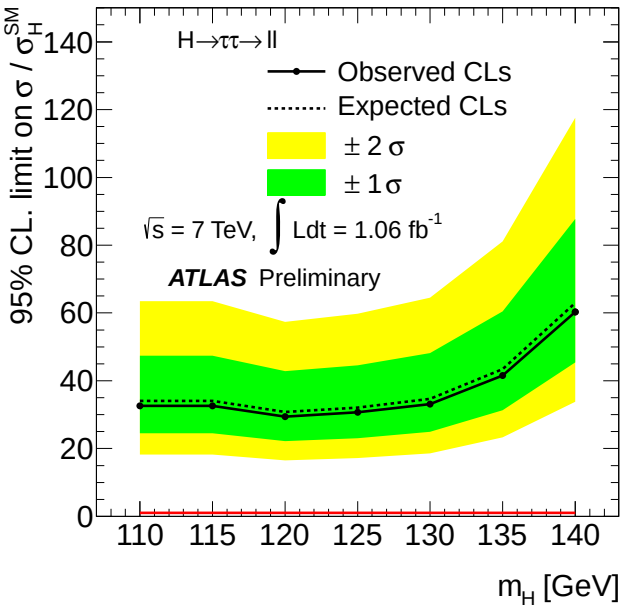

Figure 6.2: Expected and observed exclusion limits for neutral Higgs boson production in the SM as a function of m_H. The region above the solid limit curve is excluded at the 95% confidence level. The expected limit in confidence levels (CLs) are shown as the black dashed line. The green and yellow bands correspond to the 1σ and 2σ error bands on the expected limit, respectively. The red line represents the SM production rate [176].

acceptance. In particular, systematic effects on the treatment of the data with missing front-end boards for the LAr calorimeter are considered.

The uncertainties on the estimation of fake lepton background, described in previous Section, are considered. The τ-embedding sample is normalised to PYTHIA MC and the uncertainties on the MC prediction of $Z \to \tau\tau$ are taken into account. Additionally, the systematic uncertainty of the embedding method is obtained by comparing the central prediction, obtained from $Z \to \mu\mu$ events selected without any isolation requirement imposed on the muons, and an alternative sample, where a track-based isolation is required in the $Z \to \mu\mu$ selection.

An uncertainty of 4% is assumed in the inclusive cross section of the vector bosons production. In addition, relative uncertainty of 24% is applied to W/Z+1-jet uncertainty on the inclusive cross section. For the top quark pair production and single production of a top quark, the uncertainties are about 10% [183]. An uncertainty of 5% is assumed for all di-boson production processes. The uncertainties on the signal cross-sections depend on m_H and are in the range of (15 – 20)% for $gg \to H$ and (2.5 – 3)% for VBF production. The estimated uncertainty of 3.7% on the luminosity measurement [184] is applied to the normalisation of all MC samples.

In order to quantify the systematic uncertainty due to the choice of the signal MC generator, the default MC@NLO and HERWIG samples are compared with samples generated with POWHEG [185]. For the comparison, both generators are interfaced to HERWIG/JIMMY for hadronisation. A PDF uncertainty of 3% as an additional normalisation uncertainty on all the MC background samples, 7.8% on the Higgs boson gg fusion process and 2.3% on the Higgs boson VBF process are considered.

As can be seen from Table 6.2, the largest uncertainty is due to the jet energy scale.

6.1.5 Results

As shown in Table 6.1, no significant excess is observed in the data compared to the SM expectation.

The procedure to compute exclusion limits is based on the confidence levels method (CL_s) [186, 187]. The data is compared with two models: the null-signal hypothesis (background only) and the signal plus background

Table 6.3: Main correlated systematic uncertainties used in the analysis of $H \to \tau_{\text{lep}}\tau_{\text{had}}$ final state. These relative uncertainties (%) correspond to the overall effect on the per-event signal efficiency under the $\pm 1\sigma$ variation of the sources of systematic uncertainty [177].

$H \to \tau\tau$	τ_{lep} τ_{had}
Luminosity	± 3.7
Electron efficiency	± 3.5
Electron energy scale	$^{+1.3}_{-0.1}$
Muon efficiency	± 1.0
Jet/τ/$E_{\text{T}}^{\text{miss}}$ energy scale	$^{+19}_{-16}$

hypothesis applied to the profile-likelihood test statistics [188]. The asymptotic approximation is used rather than performing pseudo-experiments, because it is much less computational intensive.

Exclusion limits at the production of a SM Higgs boson are determined as a function of the Higgs boson mass. Only events in the mass region of 100 GeV $< m_{\tau\tau} <$ 150 GeV are considered in the limit setting procedure, that is based on counting events in the mass window. The Higgs boson exclusion is performed for the range 110 GeV $\leq m_H \leq$ 140 GeV.

A particular m_H is excluded if the signal hypothesis is rejected at the 95% confidence level (CL). The systematic uncertainties described in Section 6.1.4 are included as nuisance parameters. Correlation of the systematic uncertainties among processes are taken into account. The uncertainties on the luminosity, energy scale and acceptance are assumed to be correlated. Others, like the uncertainty on background process normalisation, are process specific and are considered to be uncorrelated.

Figure 6.2 shows the resulting exclusion limit for a SM Higgs boson production as a function of the Higgs boson mass. The limit is expressed relative to the cross section predicted by the SM. The expected and observed 95% confidence level limits are shown as dashed and solid lines, respectively. The green and yellow bands correspond to 1σ and 2σ error bands on the expected limit. Exclusion limits at the 95% confidence level of the order of 30 times the Standard Model rate are obtained.

6.2 $H \to \tau_{\text{lep}}\tau_{\text{had}}$ final state

Signal events in this final state are characterised by exactly one isolated lepton from leptonic τ decay and one τ candidate. The backgrounds considered, MC samples used and preselection of events are similar to the ones used for the H $\to \tau_{\text{lep}}\tau_{\text{lep}} \to \ell\ell + 4\nu$ final state.

The lepton transverse momentum has to be $p_{\text{T}} > 20$ GeV for muons and $p_{\text{T}} > 25$ GeV for electrons. The τ candidate has to have $p_{\text{T}} > 20$ GeV, one or three tracks and charge opposite to the one of the lepton. Missing transverse energy in the event should be larger than 20 GeV. Events with an additional lepton are removed to suppress the $\gamma^*/Z \to \ell\ell$ and $t\bar{t}$ background processes. Finally, to suppress the $W \to \ell\nu$ background process, the transverse mass of the lepton and missing energy system, $m_{\text{T}} = \sqrt{2\, p_{\text{T}}(\ell) \cdot E_{\text{T}}^{\text{miss}} \cdot \left(1 - \cos\Delta\phi(\ell, E_{\text{T}}^{\text{miss}})\right)}$, is required to be smaller than 30 GeV. The Missing Mass Calculator technique, described in Appendix A, is used to estimate the invariant mass of the pair of τ leptons.

The main background in this analysis is the same as for fully leptonic final state, the $\gamma^*/Z \to \tau\tau$ process. The invariant mass shape for this background is also estimated using the embedding technique. The QCD multijet and W+jets backgrounds are estimated from data using events with the same charges of τ candidate and lepton in the background-enhanced QCD and W+jets control regions. The difference between number of events with the same and opposite charges of τ candidate and lepton is added from simulation. The remaining backgrounds are estimated from simulation.

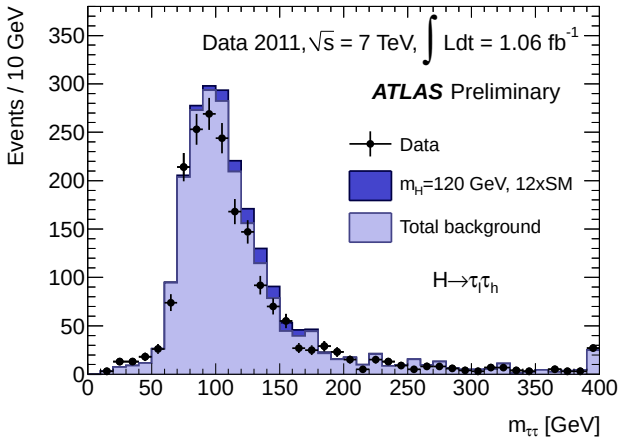

Figure 6.3: The invariant mass distributions for the candidate events selected, the total background and the signal expected in the $H \to \tau_{\text{lep}}\tau_{\text{had}}$ final state. Higgs boson mass hypothesis used to illustrate the signal and the multiplicative factor applied to its normalisation are indicated in the legend [177].

With such a selection, 1072 events is observed in data. The expected number of signal (m_H=120 GeV) is 8 with 1218 background events.These numbers are estimated in an interval containing about 90% of the signal around the most probable value of the invariant or transverse mass distributions of the pair of τ leptons. The distribution of the reconstructed invariant mass can be seen in Figure 6.3. The dominant contributions to the systematic uncertainty of the signal yield are summarised in Table 6.3.

The 95% CL limit on the cross section for individual final states and their combination are illustrated in Fig. 6.4(a), normalised to the Standard Model Higgs boson cross section, as a function of the Higgs boson mass. Exclusion limits obtained for the $H \to \tau_{\text{lep}}\tau_{\text{had}}$ final state at the 95% confidence level are of the order of 10 times the Standard Model rate. The combination of individual final states with the $\pm 1\sigma$ and $\pm 2\sigma$ variations of the background only expectation is illustrated in Fig. 6.4(b). As the $H \to \tau_{\text{lep}}\tau_{\text{had}}$ final state is significantly more sensitive than the $H \to \tau_{\text{lep}}\tau_{\text{lep}}$ final state, the combination differs only slightly from the $H \to \tau_{\text{lep}}\tau_{\text{had}}$ final state alone.

6.3 Summary

In this Chapter, the first search for a neutral Higgs boson produced according to the mechanism predicted by the SM and decaying into $\tau\tau$ channel in proton-proton collisions at the centre-of-mass energy of 7 TeV with the ATLAS experiment is presented. Both, the fully leptonic and the semi-leptonic final states are considered. No significant excess over the expected background is observed in the considered Higgs boson mass range of $100 < m_H < 140$ GeV. The observed (expected) upper limits on the cross section times the branching ratio of $H \to \tau\tau$ are between 6 (10) and 14 (30) times the Standard Model prediction. This search is complementary to searches with other decays in the same mass range.

A small statistics sample of the first data, corresponding to 1.06 fb^{-1} is used in the presented studies. The most recent results corresponding to the luminosity of 4.7 fb^{-1} [189] improve those limits to the observed (expected) limit between 2.9 (3.4) and 11.7 (8.2) in the mass range $100 < m_H < 150$ GeV. In this latter analysis, additionally, the $H \to \tau_{\text{had}}\tau_{\text{had}}$ final state is used in order to increase the signal yield. The studies of dataset collected in 2012 with the centre-of-mass energy of 8 TeV are ongoing.

For completeness of this Chapter, even though is out of the scope of this monograph, the recent Higgs search results should be mentioned [53]. The ATLAS experiment reports studies of the $H \to ZZ^* \to 4\ell$, $H \to \gamma\gamma$ and $H \to WW^* \to e\mu\, 2\nu$ channels with 5.8 – 5.9 fb^{-1} of pp collision data recorded during April to June 2012 at the

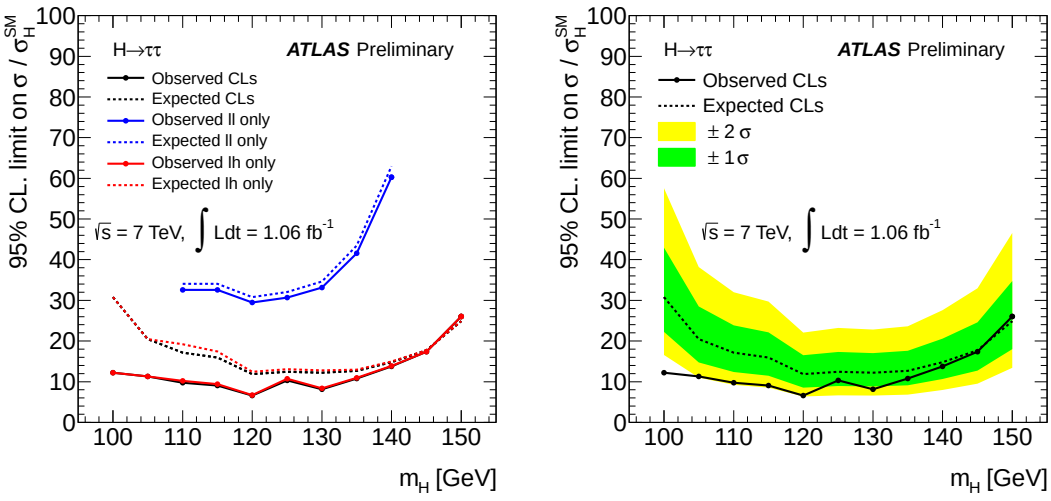

Figure 6.4: The observed and expected 95% CL upper limit on the SM Higgs boson production cross section divided by the Standard Model expectation as a function of m_H for the individual $H \to \tau_{\text{lep}}\tau_{\text{had}}$ (lh) and $H \to \tau_{\text{lep}}\tau_{\text{lep}}$ (ll) final states and their combination (a). The $H \to \tau\tau$ combined observed and expected 95% CL upper limits (b). The green and yellow bands reflect $\pm 1\sigma$ and $\pm 2\sigma$ variation respectively in the expected limit [177].

centre-of-mass energy of 8 TeV. These results are combined with results based on 2011 data (4.6 – 4.8 fb^{-1}). The Standard Model Higgs boson is excluded at 95% CL in the mass range 111 – 559 GeV, except for the narrow region 122 – 131 GeV. In this region, an excess of events with a significance of 5.9 σ is observed. Taking into account the entire mass range of the search, 110 – 600 GeV, the global significance of the excess is 5.1 σ. These results provide conclusive evidence for the discovery of a new particle with mass 126.0 ± 0.4(stat)±0.4 (syst) GeV. The CMS experiment reports similar results [54]. In this case also searches in $\tau\tau$ and bb channels are included, but no significant excess of events is found in those final states.

The decays to pairs of vector bosons identify the new particle as a neutral boson. The observation in the di-photon channel disfavours the spin-1 hypothesis. Although these results are compatible with the hypothesis that the new particle is the Standard Model Higgs boson, more data are needed to assess its nature in detail. The $H \to \tau\tau$ final state starts to be critical in this task as with it we can check if a new boson couples to fermions. τ leptons can probe the leptonic Higgs-Yukawa coupling which is not accessible from decays to a pair of photons or heavy bosons, WW/ZZ. The τ final state has also sensitivity both to SM and SUSY Higgs bosons. Its observation or exclusion can tell a lot about its nature and possible New Physics. Finally the $H \to \tau\tau$ final state can be used to study Higgs CP properties and in particular to study CP violation in the Higgs sector [190, 191].

There are two possible outcomes: if the result confirms the hypothesis, then you've made a measurement. If the result is contrary to the hypothesis, then you've made a discovery.

Enrico Fermi

Somewhere, something incredible is waiting to be known.

Carl Sagan

7

MSSM Higgs bosons searches with τ lepton final states

The coupling of the Higgs boson to the third generation down-type fermions is strongly enhanced for large regions of the MSSM parameter space. Hence, the final states with τ leptons are the most promising channels for MSSM Higgs boson searches at the LHC. In this Chapter the first studies in the ATLAS experiment on searches for neutral and charged Higgs bosons with τ lepton final states are presented. The data used in those searches were recorded with the ATLAS detector during the first half of 2011, corresponding to an integrated luminosity of (1.03-1.06) fb^{-1}.

7.1 Neutral MSSM Higgs bosons decaying to $\tau\tau$ pairs

A search for neutral MSSM Higgs bosons in the decay mode $H \to \tau\tau$ includes $e\mu 4\nu$ ($e\mu$), $e\tau_{\rm had}3\nu$ ($e\tau_{\rm had}$), $\mu\tau_{\rm had}3\nu$ ($\mu\tau_{\rm had}$),and $\tau_{\rm had}\tau_{\rm had}2\nu$ ($\tau_{\rm had}\tau_{\rm had}$) final states [177]. These decays have branching ratios of 6%($e\mu$), 23%($e\tau_{\rm had}$), 23%($\mu\tau_{\rm had}$), and 42%($\tau_{\rm had}\tau_{\rm had}$). The combination of $e\tau_{\rm had}$ and $\mu\tau_{\rm had}$ is referred to as $\ell\tau_{\rm had}$. Similar searches for neutral Higgs bosons have been performed at the Tevatron [67, 68] and the LHC [192, 193].

The production of W or Z bosons that subsequently decay into leptons constitutes the most important background for the $e\mu$ and $\ell\tau_{\rm had}$ final states. These processes include W+jets, γ^*/Z, $t\bar{t}$, single-top and electroweak di-boson production. $\gamma^*/Z \to \tau\tau$ events constitute an irreducible background for Higgs boson masses close to the Z boson mass. $\gamma^*/Z \to \ell\ell$ events contribute if one of the charged leptons or an accompanying jet is mis-identified. QCD multijet production provides a significant background contribution if there are real leptons from decays of heavy quarks or if jets are mis-identified as electrons, muons, or $\tau_{\rm had}$ decays. It is the dominant background in the $\tau_{\rm had}\tau_{\rm had}$ final state as it is more probable for a jet to be mis-identified as a hadronic τ decay than as a light lepton.

7.1.1 Data sample and Monte Carlo simulations

Events in $e\mu$ and $e\tau_{\rm had}$ final states are selected using a single-electron trigger with a $p_{\rm T}$ threshold of 20 GeV. Events in $\mu\tau_{\rm had}$ final state are selected with a single-muon trigger with a $p_{\rm T}$ threshold of 18 GeV. The same trigger can select $e\mu$ final state if the event is not triggered by an electron. The $\tau_{\rm had}\tau_{\rm had}$ events are selected by a hadronic τ decay trigger, which requests at least two τ candidates. The transverse energy thresholds used are 29 GeV on the leading τ candidate and 20 GeV on the sub-leading one. The total trigger efficiencies, with respect to the event selection described in the next Section, are 99%, 82% and $\sim$ 60% for electron, muon and the di-τ triggers respectively.

The cross section for Higgs boson production in the gluon fusion process are calculated using HIGLU [178] and ggh@nnlo [179]. For the b-quark associated production, a matching scheme [194] is used to combine the NLO

calculation for $gg \to b\bar{b}A/H/h$ in the four-flavor scheme [195, 196] and the NNLO calculation for $b\bar{b} \to A/H/h$ in the five-flavor scheme [197]. In both cases, the MSTW2008 set of parton distribution functions [48] has been used. The masses, couplings, and branching ratios of the Higgs bosons are computed with FeynHiggs [198].

The direct $gg \to A/H/h$ production is simulated with POWHEG [185], and the associated $b\bar{b}A/H/h$ production with SHERPA [199]. Both $gg \to A$ and $b\bar{b}A$ samples are generated at values of m_A in the range from 90 to 600 GeV. To obtain simulated samples for the decays of the H and h bosons, events with A boson decays with mass m_A closest to m_H and m_h respectively are scaled to the H/h production cross section. For any given m_A and $\tan\beta$, the masses m_H and m_h of the H and h bosons are calculated in the m_h^{max} MSSM benchmark scenario and A boson events with m_A closest to m_H and m_h, respectively, are combined with these samples with appropriately scaled cross sections to obtain a signal sample for $A/H/h$ production. The increase of the Higgs boson natural width with $\tan\beta$ is neglected as it is small compared with the experimental resolution of the mass definition used.

For processes of W, Z bosons, $t\bar{t}$ and single-top production the same Monte Carlo samples as described in Section 6.1.1 are used. The loop-induced process $gg \to WW$ is generated with gg2WW [200]. The generation of parton shower, hadronisation, the underlying event, the decays of τ leptons and the QED radiation follow description in Section 6.1.1.

The cross section for single gauge boson production is calculated at NNLO in QCD perturbation theory [150], for $t\bar{t}$ production at NLO+NLL [201, 202], and for single-top and di-boson production at NLO [152]. For the background processes the PDFs MSTW2008 ($W \to \ell$, $Z/\gamma^* \to \ell^+\ell^-$, single-top and di-boson) and CTEQ6.6 [156] ($t\bar{t}$) are used.

To match the pile-up observed in the data, events are reweighted so that the average number of interactions per bunch crossing agrees with the data.

7.1.2 Object and event selection

Events passing the trigger requirements are selected as collision events if they have a reconstructed vertex that is formed by three or more tracks and lies within 15 cm of the nominal interaction point along the beam axis.

Selection of electron and combined muon candidates follows the description in Section 6.1.2. τ candidates are required to have a transverse momentum $p_T > 20$ GeV, $|\eta| < 2.5$, 1 or 3 associated tracks and a charge of ± 1. The identification with BDT is required for the $\ell\tau_{\text{had}}$ final state and with a projective likelihood for the $\tau_{\text{had}}\tau_{\text{had}}$ final state. The efficiency of the likelihood (BDT) τ identification for τ candidates with $p_T > 20$ GeV is about 55% (60%) and the probability to mis-identify a jet as a τ lepton, as determined from a di-jet control sample, is about 5% (5%). The missing transverse energy is derived from the simple definition described in Section 3.5.

When candidates fulfilling the above criteria overlap with each other geometrically (within $\Delta R < 0.2$), only one of them is selected. The overlap is resolved by selecting muons, electrons and τ candidates in this order of priority.

The signature in the leptonic final state is one isolated electron, one isolated muon and $E_{\text{T}}^{\text{miss}}$ due to the undetected neutrinos from the two τ decays. The $t\bar{t}$, single-top and di-boson backgrounds are suppressed by the following requirements. The scalar sum of the transverse momentum of the electron, the transverse momentum of the muon and $E_{\text{T}}^{\text{miss}}$ must be smaller than 120 GeV, and the azimuthal opening angle between the electron and the muon must be larger than 2.0 rad.

The signatures of the semileptonic final state are an isolated electron or muon, a τ candidate, and $E_{\text{T}}^{\text{miss}}$ due to the undetected neutrinos from the two τ decays. Exactly one electron with $p_{\text{T}} > 25$ GeV or muon with $p_{\text{T}} > 20$ GeV and one oppositely-charged τ candidate with $p_T > 20$ GeV are required in the event. In order to suppress events from $\gamma^*/Z \to \ell\ell$ decays and from $t\bar{t}$ or single-top production only one reconstructed electron or muon candidate is allowed in the event. For the second lepton selection the less strict requirements are applied: the threshold for the transverse momentum of electron candidates is lowered to $p_{\text{T}} > 15$ GeV and a loose identification is used, for muon candidates the threshold for the transverse momentum is lowered to $p_{\text{T}} > 10$ GeV. Further rejection of $\gamma^*/Z \to \ell\ell$ events and QCD multijets is achieved by requiring $E_{\text{T}}^{\text{miss}} > 20$ GeV. Events with leptons from $W \to \ell\nu$ decays are suppressed by requiring the transverse mass, $m_{\text{T}} = \sqrt{2\, p_{\text{T}}(\ell) \cdot E_{\text{T}}^{\text{miss}} \cdot \left(1 - \cos\Delta\phi(\ell, E_{\text{T}}^{\text{miss}})\right)}$,

to be below 30 GeV.

The signature of the fully hadronic final state is characterised by two identified hadronic τ decays and $E_{\mathrm{T}}^{\mathrm{miss}}$ from the undetected neutrinos. Events with exactly two oppositely charged τ candidates that match the τ trigger objects inside a cone of radius $\Delta R = 0.2$ around the direction of the τ candidates are required. The τ candidates are also required to have $p_T > 45$ GeV for the highest-p_T candidate and $p_T > 30$ GeV for the second-highest-p_T candidate. These thresholds ensure that τ candidates are on the plateau of the trigger turn-on curve and help suppressing electroweak backgrounds. To further reject QCD jet processes and Z boson production a missing transverse energy of $E_{\mathrm{T}}^{\mathrm{miss}} > 25$ GeV is required. Finally, events are rejected if they contain an electron candidate with $p_{\mathrm{T}} > 15$ GeV or a muon candidate with $p_{\mathrm{T}} > 10$ GeV.

Corrections are applied to simulation to account for differences in the τ trigger efficiency between data and simulation. These are derived using control regions rich in $Z \to \tau\tau \to \mu$ + hadrons + 3ν events. Trigger and mis-identification scale factors for QCD multijets mis-identified as τ_{had} decays are measured from data using $W \to \mu\nu$+jets events [160] and are applied to Monte Carlo.

After the selection of signal candidates, different $\tau\tau$ mass reconstruction methods are used as described in Appendix A. The reconstructed mass is the best discriminating variable to distinguish between Z and neutral Higgs bosons. The effective mass, $m_{\mathrm{effective}}$, is used for the $e\mu$ final state, the Missing Mass Calculator (MMC) mass, $m_{\tau\tau}^{\mathrm{MMC}}$, for the $\ell\tau_{\mathrm{had}}$ final state and the visible mass, m_{vis}, for the $\tau_{\mathrm{had}}\tau_{\mathrm{had}}$ final state.

7.1.3 Background estimation

Data control samples are used to estimate or validate the most relevant background sources, QCD multijet production for all final states, and W+jets in the $\ell\tau_{\mathrm{had}}$ final state. The remaining backgrounds are estimated from Monte Carlo simulation.

The shapes of the mass distributions for the irreducible $Z \to \tau\tau$ background are determined from data with the embedding technique described in Section 6.1.3. For the $\tau_{\mathrm{had}}\tau_{\mathrm{had}}$ final state, the W+jets background is validated with an embedding technique as well. A sample of $W \to \mu\nu$ decays is selected based on Ref. [160] and the muon is replaced by a simulated hadronic τ decay.

Background estimation in the $e\mu$ final state The QCD multijet background estimation uses four independent samples selected with criteria on the isolation of the electron and muon and product of their charges as described in Section 5.1.3. The shape of the $m_{\mathrm{effective}}$ distribution in the signal region A is taken from control region C and the normalisation is derived by $n_A = r_{C/D} \times n_B$. Here, n_A and n_B denote the event yields in regions A and B and $r_{C/D}$ the ratio of the event yields in regions C and D after subtracting the contribution from non-QCD backgrounds estimated from simulation. This method relies on the assumption that the two variables used to define the four regions are uncorrelated and that the shape of the $m_{\mathrm{effective}}$ distribution does not depend on the isolation or product of the charges requirement. Obtained QCD multijet event yield in the signal region is estimated to be $n_A^{QCD} = 120 \pm 20$ (stat). The resulting $m_{\mathrm{effective}}$ distribution is shown in Fig. 7.1 (a).

Background estimation in the $\ell\tau_{had}$ final state For the background estimation in the signal region, apart from the $Z \to \tau\tau$ background, it is assumed that the shape of the MMC mass distribution is the same regardless of whether the lepton and the τ candidate have the same (SS) or the opposite (OS) charges. The OS backgrounds are therefore estimated from data as SS events and the difference between OS and SS is added from simulation separately. It is done for each bin in the MMC mass distribution, thus not only an estimation of the background normalisation but also of the MMC mass shape is obtained.

The ratio of OS and SS events for the QCD multijet background should be close to unity. It is checked with a data control sample that is dominated by low-E_{T} jets from QCD processes. The observed deviation of $r_{\mathrm{OS/SS}}^{\mathrm{QCD}}$ from unity is taken into account in the systematic uncertainties. For the W+jets background, a significant deviation of the ratio $r_{\mathrm{OS/SS}}^{W}$ from unity is expected and is estimated from a W+jets dominated control region selected by replacing the $m_T < 30$ GeV requirement in the nominal selection by $m_T > 50$ GeV. The contributions from $Z \to \tau\tau$ are

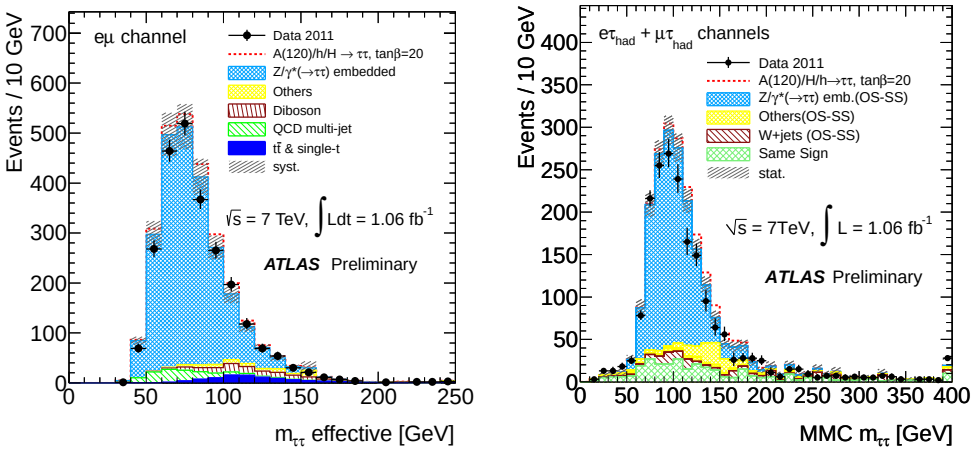

(a) (b)

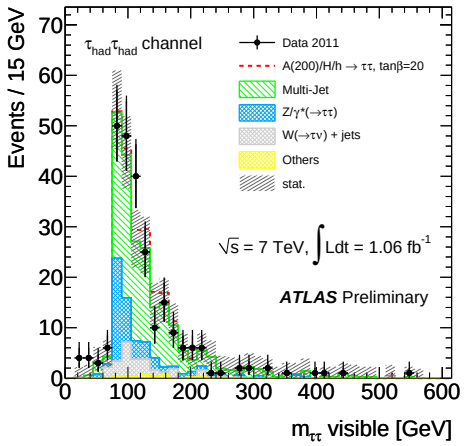

(c)

Figure 7.1: Effective mass distribution for the $e\mu$ (a), MMC mass distribution for the $\ell\tau_{\text{had}}$ (b) and visible mass distribution for the $\tau_{\text{had}}\tau_{\text{had}}$ (c) final states. The data are compared with the background expectation and an added hypothetical MSSM signal (m_A = 120 GeV, $tan\beta$ = 20 for (a) and (b), m_A = 200 GeV, $tan\beta$ = 20 for (c)). "OS-SS" denotes the difference between event yields with the opposite or the same charges of the lepton and the τ candidate [177].

taken from the embedded samples and remaining backgrounds from simulation. The total estimated background is $(2.10 \pm 0.05\ (\text{stat})) \times 10^3$. The resulting MMC mass distribution is shown in Fig. 7.1 (b).

Background estimation in the $\tau_{\text{had}}\tau_{\text{had}}$ final state The QCD multijet background is estimated by using a similar method as described for the $e\mu$ final state where the four control samples are defined by selection criteria on the product of the two τ candidates charges and the tightness of the τ identification criteria. For the latter, the nominal τ identification used in this analysis has been relaxed to the loose τ identification, corresponding to an 80% τ identification efficiency. The shape of the m_{vis} distribution is taken from sample C with τ candidates with the opposite charges and passing loose τ identification. It is scaled by the ratio of event yields in samples B and D with τ candidates with the same charges and passing nominal/loose τ identification. In all control samples the non-QCD background contributions are subtracted. The resulting estimate for the QCD multijet background in the signal sample is 157 ± 18 (stat) events. The electroweak backgrounds are the other sizable background components in this final state. They are estimated from simulation and validated with data using embedded samples. The resulting visible mass distribution is shown in Fig. 7.1 (c).

Table 7.1: Uncertainties on the number of selected events for those background contributions that are at least partially estimated from simulation and for a hypothetical signal (m_A = 120 GeV and $\tan\beta$ = 20 for the $e\mu$ and $\ell\tau_{\text{had}}$ final states and m_A = 200 GeV and $\tan\beta$ = 20 for the $\tau_{\text{had}}\tau_{\text{had}}$ final state). All numbers are given in %. When three numbers are given the first refers to the $e\mu$ final state, the second to the $\ell\tau_{\text{had}}$ final states and the third to the $\tau_{\text{had}}\tau_{\text{had}}$ final state. If an uncertainty is not relevant for a certain background, this is indicated by a "-". For the $e\mu$ final state, the uncertainty on the W+jets background is dominated by the statistical component and the systematic uncertainty is neglected; for the $\ell\tau_{\text{had}}$ final state the W+jets background is estimated from data [177].

	W+jets	Di-boson	$t\bar{t}$+ single-top	$\gamma^*/Z \to \ell\ell$	$\gamma^*/Z \to \tau\tau$	Signal
$\sigma_{inclusive}$	-/-/5	7	10	5/5/-	5	14/14/16
Acceptance	-/-/20	4/2/7	3/2/9	2/14/-	5/14/14	5/7/9
e efficiency	-/-/0.8	4/3.1/0.5	4/3.6/0.3	4/3.1/-	4/3.0/0.5	4/3.6/0.1
μ efficiency	-/-/0.3	2/1.2/0.4	2/1.1/0.0	2/1.3/-	2/1.8/0.4	2/1.0/0.1
τ efficiency and fake rate	-/-/21	-/9.1/15	-/9.1/13	-/48/-	-/9.1/15	-/9.1/15
Energy scales and resolution	$-/-/^{+34}_{-21}$	$2/^{+19}_{-9}/^{+26}_{-12}$	$6/^{+5}_{-4}$/12	$1/^{+39}_{-25}$/-	$1/11/^{+63}_{-23}$	$1/^{+30}_{-23}/^{+9}_{-8}$
Luminosity	-/-/3.7	3.7	3.7	3.7/3.7/-	3.7	3.7
Total uncertainty	$-/-/^{+45}_{-36}$	$10/^{+23}_{-16}/^{+32}_{-22}$	13/15/23	$8/^{+64}_{-56}$/-	$9/21/^{+67}_{-31}$	$16/^{+35}_{-30}/^{+26}_{-25}$

7.1.4 Systematic uncertainties

Systematic effects on the signal efficiency and the estimated number of background events can be grouped in the following categories: theoretical inclusive cross sections, acceptance, knowledge of detector performance (lepton identification and mis-identification efficiencies, trigger efficiencies, energy scales and resolution) and systematic uncertainties of the data-driven background estimation methods.

The uncertainties from different sources of various background processes which are partially or completely estimated from simulated events are summarised in Table 7.1.

Systematic uncertainties for simulated samples account for the following effects. The uncertainty on the theoretical inclusive cross section ($\sigma_{inclusive}$) for each individual signal and background process is obtained from variations of the renormalisation and factorisation scales and a variation of the strong coupling constant and the PDF sets within their uncertainties. The uncertainty on the acceptance is estimated by varying the renormalisation and factorisation scales, the matching parameters in ALPGEN and the choice of the PDF to MRST2001J [203] in the generation of simulated event samples.

The uncertainty on the trigger efficiencies (included in lepton efficiencies in Table 7.1) for electrons and muons is 1%. For the τ triggers this efficiency is determined from data in p_T bins for τ candidates and QCD multijets mis-identified as hadronic τ decays. The uncertainty for QCD multijets that are mis-identified as τ candidates is combined with the uncertainty of the offline mis-identification probability, resulting in a combined uncertainty of $\approx$ 10%. The uncertainties due to the limited knowledge of the detector performance are evaluated by varying the trigger, reconstruction and identification efficiencies for electrons, muons and τ candidates, and by varying the energy resolution and energy scale of electrons, muons, τ candidates, and energy deposits outside of these objects. These are propagated in a fully correlated way into the $E_{\text{T}}^{\text{miss}}$ scale and resolution. The difference in the impact of the energy scale and resolution uncertainty on the expected event yields in different final states is caused by requiring a hadronic τ decay(s). The luminosity uncertainty is 3.7% [106]. The uncertainties, apart from the ones related to the data-driven techniques, are treated as fully correlated between the three final states.

The systematic uncertainties from the data-driven estimate of the QCD background differ between final states. In the $e\mu$ final state it includes the systematic uncertainty on the subtracted non-QCD background and on the

Table 7.2: Observed numbers of events in data and total expected background contributions for the final states considered in this analysis, with their combined statistical and systematic uncertainties [177].

Final state	Data	Expected Background
$e\mu$	2472	$(2.6 \pm 0.2) \times 10^3$
$\ell\tau_{\text{had}}$	1913	$(2.1 \pm 0.4) \times 10^3$
$\tau_{\text{had}}\tau_{\text{had}}$	245	$233\ ^{+44}_{-28}$
Sum	4630	$(4.9 \pm 0.6) \times 10^3$

assumption of identical $m_{\text{effective}}$ shapes in the different control regions.

For the $\ell\tau_{\text{had}}$ final states, the most important uncertainties for the data-driven estimation of the QCD multijet and W+jets backgrounds are the statistical uncertainty on the number of SS events in the signal region and the uncertainty on the ratios between the OS and SS regions for QCD multijets and W+jets. An additional uncertainty of 10% is derived from the m_{T} dependence of this ratio for W+jets events.

For the $\tau_{\text{had}}\tau_{\text{had}}$ final state, the statistical uncertainty on the number of SS events in the signal region is the dominant uncertainty of the data-driven estimate of the QCD multijet contribution. The systematic uncertainties on the non-QCD background contributions in the control regions are propagated to the QCD multijet estimate. The systematic uncertainty is dominated by the energy scale and τ mis-identification efficiency uncertainty.

For the energy scale uncertainty, variations of the electron, muon, τ candidate, and $E_{\text{T}}^{\text{miss}}$ not only changes in normalisation but also in the shapes of the discriminating mass variables and therefore it was included as an additional uncertainty in the derivation of the Higgs boson exclusion limits in Section 7.1.5. In the channels where embedded data are used, systematic uncertainties are derived for the final decay products that are taken from simulation.

Systematic effects of the embedding method are estimated from variations of the embedding procedure. While in the analysis no isolation is required for the selected muons in order to avoid a bias on the embedded objects, the procedure is repeated on $Z \to \mu\mu$ data fulfilling standard isolation criteria for the $e\mu$ and the $\ell\tau_{\text{had}}$ channel. A second variation accounts for the energy deposition from the selected muons in the calorimeter, which is by default completely removed in a cone of radius $\Delta R < 0.1$ around the muon direction. The systematic uncertainties from these variations enter the limit calculation in the form of shape systematics. All other systematic uncertainties have no significant effect on the mass shape.

7.1.5 Results for the neutral MSSM Higgs bosons searches

Combining the estimated contribution from the various background processes and their uncertainties results in the final background estimate shown in Table 7.2. No significant excess of events over the Standard Model background expectation is observed in the data in any of the studied final states.

Exclusion limits at the 95% confidence level are set for MSSM Higgs boson $A/H/h$ production as a function of the parameters m_A and $\tan\beta$. The exclusion limits are derived with the profile likelihood method [188] based on the CL_{s} parameter from the analysis of the $m_{\text{effective}}$ distribution for the $e\mu$ final state, the $m_{\tau\tau}^{\text{MMC}}$ distribution for the $\ell\tau_{\text{had}}$ final state and the m_{vis} distribution for the $\tau_{\text{had}}\tau_{\text{had}}$ final state.

For the limit derivation, systematic uncertainties are separated into common, fully correlated (energy scale, acceptance, luminosity) and final state specific ones and are included as nuisance parameters. The $m_{\text{effective}}$, $m_{\tau\tau}^{\text{MMC}}$ and m_{vis} shape uncertainties due to the uncertainties in the energy scales of leptons, hadronic τ candidates and $E_{\text{T}}^{\text{miss}}$ for the backgrounds, obtained from simulation, are taken into account. Asymptotic formulae are used to find the median expected limit along with the $\pm1\sigma$ and $\pm2\sigma$ error bands. The combined limit and the contributions of the individual channels to the combination limits on the production of neutral MSSM Higgs bosons $A/H/h$ in the

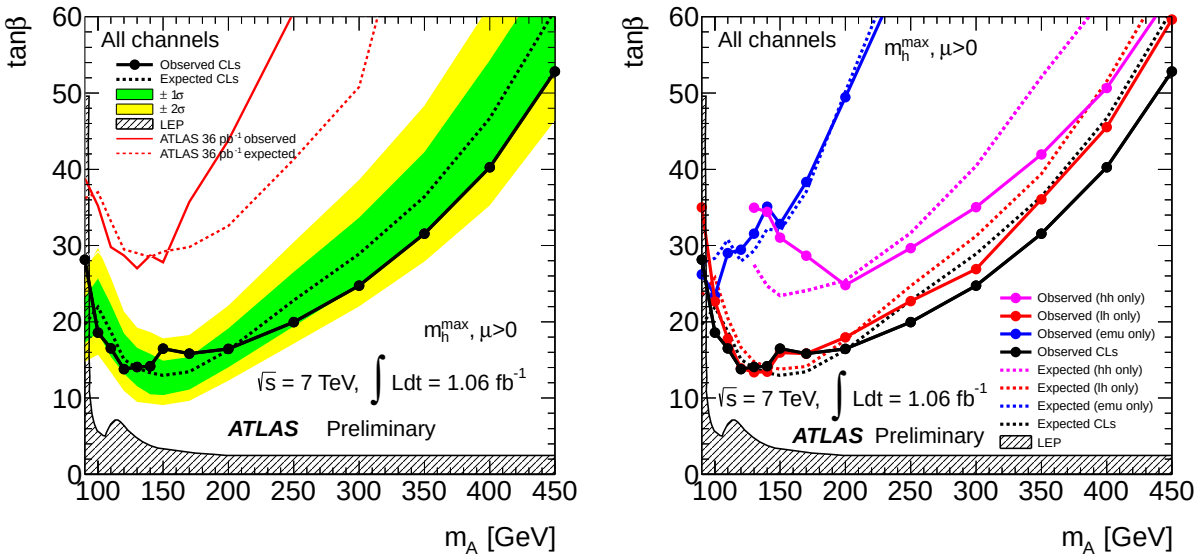

(a) (b)

Figure 7.2: Expected and observed exclusion limits in the $m_A - \tan\beta$ plane of the MSSM as derived from the combination of the analyses for the $e\mu$, $\ell\tau_{\text{had}}$ and $\tau_{\text{had}}\tau_{\text{had}}$ final states. The exclusion limits from analysing of 36 pb^{-1} of data and from LEP are also shown (a). The region above the drawn limit curve is excluded at the 95% confidence level. The dark grey (green) and light grey (yellow) bands correspond to the $\pm 1\sigma$ and $\pm 2\sigma$ error bands, respectively. The contribution of the individual channels to the combined limit (b) [177].

$\tan\beta - m_A$ plane, for the m_h^{max} scenario and Higgsino mass parameter $\mu > 0$ [65] are shown in Figure 7.2. These results exclude regions of parameters space beyond the existing limits from previous experiments at LEP [66] and the Tevatron [67, 68] and are similar to those recently obtained by the CMS Collaboration [192].

7.2 Search for charged Higgs bosons in $t\bar{t}$ decays

This section describes a search for charged Higgs bosons with masses in the range 90 – 160 GeV, using $t\bar{t}$ events with a leptonically or hadronically decaying τ lepton in the final state. Two final states, which are expected to give the highest sensitivity, are analysed:

- **τ_{had}+jets** [204]: $t\bar{t} \to b\bar{b}WH^+ \to b\bar{b}W(q\bar{q}')H^+(\tau_{\text{had}}\,\nu)$, i.e. both W and τ decay hadronically;
- **τ_{lep}+lepton/jets** [205]: $t\bar{t} \to b\bar{b}WH^+ \to b\bar{b}W(q\bar{q}'/\ell\nu)H^+(\tau_{\text{lep}}\,\nu)$, i.e. τ decays leptonically and W decays leptonically or hadronically, so called one or two leptons final state.

7.2.1 Data sample and Monte Carlo simulations

For the τ_{had}+jets final state, the combined τ and $E_{\text{T}}^{\text{miss}}$ trigger [206, 138], with a threshold of 29 GeV on the τ object and of 35 GeV on $E_{\text{T}}^{\text{miss}}$ is used for data selection. The one or two leptons final state analysis relies on events passing a single-lepton (electron or muon) trigger, with a p_{T} threshold at 20 GeV for the electron trigger and at 18 GeV for the muon trigger.

The Monte Carlo simulation of $t\bar{t}$, single-top, single vector boson and di-boson events is the same as described in Section 6.1.1. Overlap between $t\bar{t}$ and single-top final states is taken into account. A $t\bar{t}$ production cross section of 165 pb [207] obtained from the approximate NNLO calculations [202] is used (both for SM $t\bar{t}$ decays and decays via a charged Higgs boson). A top quark mass of 172.5 GeV is assumed and the PDFs is CTEQ66 [156]. The H^+

signal events are generated with PYTHIA using TAUOLA for τ lepton decays and PHOTOS for charged leptons radiating photons.

The Monte Carlo pile-up samples are reweighted in order to match vertex distribution in data. Only events with a reconstructed primary vertex with at least five associated tracks are considered.

7.2.2 The τ_{had}+jets final state

This study relies on the detection of τ+jets in $t\bar{t}$ events, where the hadronically decaying τ lepton comes from $H^+ \to \tau_{\text{had}}\,\nu$, while jets originate from hadronically decaying W boson. This topology has several advantages: the W boson can be fully reconstructed, the H^+ candidate can be reconstructed in the transverse plane, and the branching ratio of the W boson decay to quarks is larger than that to leptons. However, it needs to be distinguished from a large QCD multijet background. The background processes include the production of $t\bar{t}$, single-top, W+jets, γ^*/Z+jets, and QCD multijet events where there is either a true τ lepton, or another object mis-identified as a hadronically decaying τ.

Objects and events selection

Electron candidates are required to have $E_{\text{T}} > 20$ GeV and $|\eta| < 2.47$ (excluding the transition region in the calorimeters) and to be isolated $I_{ET}^{0.2} < 3.5$ GeV. Combined muon candidates are required to have $p_{\text{T}} > 10$ GeV and $|\eta| < 2.5$ and isolation $I_{ET}^{0.3}$ and $I_{PT}^{0.3} < 4$ GeV.

Jets are reconstructed with the anti-k_t algorithm with a size parameter of $R = 0.4$. They are required to have $p_{\text{T}} > 20$ GeV and $|\eta| < 2.5$. To identify jets initiated by b quarks, a combination of a discriminant based on an impact parameter in three dimensions and a secondary-vertex-tagger [208] with an identification efficiency of about 60% for b jets with $p_{\text{T}} > 20$ GeV in $t\bar{t}$ events is applied.

τ candidates are required to have $p_{\text{T}} > 20$ GeV, $|\eta| < 2.3$ and 1 or 3 associated tracks. They are identified using a likelihood identification method with an efficiency of about 30% for τ candidates with $p_{\text{T}} > 20$ GeV in $Z \to \tau\tau$ events. In some control regions, a loose τ identification is used corresponding to an efficiency of 60%. A dedicated algorithm is used to reject electrons.

The missing transverse energy is calculated using a refined calibration method described in Section 3.5.

When candidates, selected using the above criteria, overlap geometrically within $\Delta R < 0.2$, only one candidate in the following order of priority: muon, electron, τ, or jet, is kept.

An event is required to have a τ candidate and at least 4 jets with $p_{\text{T}} > 20$ GeV and $|\eta| < 2.5$. A τ candidate is asked to have $p_{\text{T}} > 35$ GeV and to be matched to the τ trigger object within $\Delta R < 0.1$. Events with a second identified τ candidate with $p_{\text{T}} > 20$ GeV or any identified electron ($E_{\text{T}} > 20$ GeV) or muon ($p_{\text{T}} > 10$ GeV) are vetoed. $E_{\text{T}}^{\text{miss}}$ is required to be larger than 40 GeV. Events with large reconstructed $E_{\text{T}}^{\text{miss}}$ due to the limited resolution of the energy measurement are rejected with a cut on the significance of $E_{\text{T}}^{\text{miss}}$(as defined in Section 5.2.2), $S_{E_{\text{T}}^{\text{miss}}} > 8$. At least one b-tagged jet is required. The qqb candidate, built from three jets with one of them b-tagged, with the highest sum of the constituents transverse momenta, must satisfy $m(qqb) \in [120, 240]$ GeV in order to be consistent with the top decay. For events passing the above selection cuts, the transverse mass of the τ candidate and $E_{\text{T}}^{\text{miss}}$, $m_{\text{T}} = \sqrt{2 p_{\text{T}} E_{\text{T}}^{\text{miss}} (1 - \cos\Delta\phi(\tau, E_{\text{T}}^{\text{miss}}))}$, is defined. This variable discriminates between $W \to \tau\nu$ background and the H^+ signal.

At the end of the selection cut flow, after applying data-driven methods as detailed in the next Section, 37 ± 7 background events are expected for $m_{\text{T}} > 40$ GeV. A potential signal yield depends on the charged Higgs boson mass and the branching ratio $t \to bH^+$. For example, 70 events are expected for $m_{H^+} = 130$ GeV and BR($t \to bH^+$)=0.1.

Background estimation

For backgrounds with intrinsic $E_{\text{T}}^{\text{miss}}$ from W decays the contribution from events in which electrons or jets are mis-identified as τ candidates is predicted using appropriate control samples while events with correctly identified τ

candidates are studied with the embedding method. Backgrounds due to QCD multijet events with $E_{\mathrm{T}}^{\mathrm{miss}}$ generated by detector effects are estimated using the shape of the $E_{\mathrm{T}}^{\mathrm{miss}}$ distribution in a suitable control region.

The background from events where electron is mis-identified as a τ candidate is measured with a tag-and-probe method on $\gamma^*/Z \to ee$ events (see Section 4.3.3). The result is compared to simulation and used to correct MC samples.

To study the probability for jets to be mis-identified as hadronically decaying τ leptons, a γ-jet control sample is used. The method is the same as described in Section 4.3.2 though based on a larger data set corresponding to 1.03 fb^{-1}. Jets in the control sample, similarly to the dominant $t\bar{t}$ background, originate predominantly from quarks. The main difference between $t\bar{t}$ and γ-jet events is the different fraction of b jets which is smaller in γ-jet events. However, the probability for a b jet to be mis-identified as a τ candidate is smaller than the corresponding probability for a light-quark jet. The average track multiplicity of b jets is higher, and variables which measure the mass of the τ candidate allow for a good discrimination. Hence, using the γ-jet mis-identification probability leads to a higher background estimate and is thus conservative. The denominator of the calculated mis-identification probability is the number of events with the reconstructed τ candidate with p_{T} greater than 20 GeV and $|\eta| < 2.3$, which passes an electron veto. The mis-identification probability is evaluated separately for the τ candidate with 1 or 3 associated tracks and measured as a function of its p_{T} and η. Further, it is applied to simulated $t\bar{t}$, single-top, and W+jets events. These events are required to pass the full event selection except for the τ identification. For these events, τ candidates, fulfilling the same requirements as in the denominator of the mis-identification probability measurement which do not overlap with a true τ lepton, are identified. Out of the remaining τ candidates, each one is considered to be potentially mis-identified as a τ candidate separately. The identified jet that corresponds to the τ candidate is removed from the event, affecting the number of reconstructed jets, the $E_{\mathrm{T}}^{\mathrm{miss}}$ significance of the event, and the number of b-tagged jets. If, after taking this into consideration, the event still passes the selection, then the event is counted as background event with a weight given by the mis-identification probability corresponding to the p_{T} and η of the τ candidate. The predicted number of events from the $t\bar{t}$ sample is 2.8 ± 1.0 (stat) $\pm$ 0.5 (syst). It is in agreement, within errors, with the MC prediction using truth information, 3.8 ± 0.6 (stat). All other backgrounds with jets mis-identified as τ candidates and with intrinsic $E_{\mathrm{T}}^{\mathrm{miss}}$ are at least two orders of magnitude smaller than $t\bar{t}$.

The QCD multijet background is estimated by fitting the $E_{\mathrm{T}}^{\mathrm{miss}}$ shape (and the $E_{\mathrm{T}}^{\mathrm{miss}}$ shape of other backgrounds) to data. For this purpose a control region is defined where the τ identification and b-tagging requirements are inverted. The τ candidates must pass a loose τ identification but fail the tight τ identification used in the baseline selection. In addition, the event is required not to contain any b-tagged jets and therefore also the requirement on the qqb mass is removed. Assuming that the shapes of $E_{\mathrm{T}}^{\mathrm{miss}}$ and m_{T} distributions are the same in the control sample and signal regions, the shape of the $E_{\mathrm{T}}^{\mathrm{miss}}$ distribution is used to model the $E_{\mathrm{T}}^{\mathrm{miss}}$ distribution for the QCD multijet background (after subtracting the background from other processes). The $E_{\mathrm{T}}^{\mathrm{miss}}$ distribution measured in data (for the baseline selection) is then fitted using two shapes: this QCD multijet model, and the sum of other processes (dominated by $t\bar{t}$, W+jets) for which the shape and the relative normalisation are taken from MC simulation. The free parameters in the fit are the overall normalisation (to the one in data) and the QCD multijet fraction. The QCD multijet fraction estimated with this method is (23 ± 10)%.

An embedding method is used for estimating the background from true τ candidates. The method consists of collecting a control sample of $t\bar{t}$, single-top, and W+jets events with a muon in data, and replacing the detector signature of this muon with that of a simulated τ lepton. The method has been validated in τ+jets events using early ATLAS data [182]. The contribution of backgrounds with the true τ to the final m_{T} distribution is estimated from this distribution for embedded events. The normalisation is taken from data in the region $0 - 40$ GeV of this distribution, where both the QCD background and the signal contamination for the expected range of sensitivity (BR($t \to bH^+ \approx 5\%$)) are low. Such a contamination is dealt with by subtracting the expected signal from the observed data before normalising the shape to the region $m_{\mathrm{T}} < 40$ GeV. In the range $40 < m_{\mathrm{T}} < 300$ GeV, there are 21 ± 5 background events with true τ candidates expected where the uncertainty is due to the limited number of events in the control sample and in the data in the region to which the shape is normalised to. In data, 26 events are observed after subtracting the background predicted by the mis-identification probability methods and the QCD

multijet estimate. Within statistical uncertainties, the background prediction and data agree well.

Systematic uncertainties

The main detector-related systematic uncertainties are mostly related to identification efficiencies and the energy/momentum resolution and scale of the physics objects described above. Uncertainties on trigger efficiency, luminosity, cross sections and acceptance are also taken into account.

The main systematic uncertainties on electron-τ candidates mis-identification include the systematic uncertainty due to the subtraction of QCD multijet and electroweak backgrounds and dependence on the tag selection. The total uncertainties on the scale factors (combining the statistical and systematic uncertainties of the measurement) are 24% in the barrel, 29% in the end-caps, and 100% in the transition region. Except for the end-cap region, they are dominated by statistical uncertainties. In total, the expected contribution of events with electrons mis-identified as τ candidates in the signal region is about 2 events which is about 5% of the expected background. Thus, reducing the current relatively large uncertainties would only lead to a minor improvement in the H^+ sensitivity.

The dominant systematic uncertainties on mis-identification of jets as τ candidates include contamination of the control sample with true τ_{had} from $Z \to \tau\tau$ and $W \to \tau\nu$ events, contamination of the control sample with QCD multijet events with a larger fraction of gluon-initiated jets than γ-jet events and contamination of the control sample by three-jet events. Also uncertainties connected to the assumption that the measurement of the mis-identification probability on the probe object is uncorrelated from the selection of the tag object is evaluated.

Additionally, the statistical uncertainty of the measurement of the mis-identification probability enters as uncertainty on any application of the mis-identification probability. The total systematic uncertainty is about $(15-24)$%, depending on p_{T} and η. The systematic uncertainties on the mis-identification probability are propagated into the background prediction for the baseline selection and enter the statistical evaluation as shape uncertainties.

The dominant systematic uncertainties on the QCD multijet background estimate are the uncertainties on the assumption that the $E_{\text{T}}^{\text{miss}}$ shape is identical in the signal and control regions and on the $t\bar{t}$ and W+jets shapes and relative normalisation from Monte Carlo (dominated by uncertainties on the $t\bar{t}$ cross section). The uncertainty on the QCD multijet fraction is dominated by the statistical uncertainty of the data set on which the fit is performed.

The systematic uncertainties on embedding method include the effect of additional QCD multijet background in the embedding and control sample selection, difference in the m_{T} shape as a consequence of loosening the selection with respect to the baseline selection, the impact of the incomplete treatment of the τ polarisation in embedded events and the impact on the m_{T} distribution due to the uncertainty on the τ energy scale. The statistical uncertainty of the estimate is 8% due to the limited size of the control sample, and additionally 20% due to the normalisation to data.

Results for the τ_{had}+jets final state

In Table 7.3 the final results on the backgrounds estimation are summarised. The obtained m_{T} distribution is shown in Fig. 7.3. The total systematic uncertainty on the background prediction is about 30% but can reach up to 70% for $m_{\text{T}} > 100$ GeV. For the signal, the total systematic uncertainty on the yield is about 40% with a small dependence on m_{H^+}.

The number of events with true τ candidates is estimated with the embedding method. The number of events with jets mis-identified as τ candidates and with intrinsic $E_{\text{T}}^{\text{miss}}$ is taken from γ+jets control samples and with electrons mis-identified as τ candidates from $\gamma^*/Z \to ee$ control samples. The QCD multijet contribution is estimated by taking its shape from a sideband region and fitting it to the data. The number of events with $m_{\text{T}} > 40$ GeV is given which allows for a better comparison of data and the expectation as the estimate from the embedding method is normalised to data in the range $m_{\text{T}} < 40$ GeV. A good agreement between the estimated background and the observed number of events is seen. Therefore, using data-driven background estimates, no statistically significant excess of events is observed in data.

Table 7.3: Expected number of background events from data-driven estimates after all selection cuts, and with an additional requirement of $m_T > 40$ GeV and number of events observed in data. Only statistical uncertainties are given [204].

	Events with/from					
	true τ jets	jet $\to \tau$ mis-id	$e \to \tau$ mis-id	QCD multijet	expected (sum)	data
$m_T > 40$ GeV	21 ± 5	2.4 ± 0.7	1.9 ± 0.2	12 ± 5	37 ± 7	43

Exclusion limits are set on the branching ratio for $t \to bH^+$, and in the $m_{H^+} - \tan\beta$ plane, by rejecting the signal hypothesis at the 95% confidence level applying the CL_s procedure. A profile likelihood ratio [188] is used with the m_T distribution as the discriminating variable. The statistical analysis is based on a binned likelihood function for the m_T distribution. Systematic uncertainties in shape and normalisation are incorporated via nuisance parameters. The final limits are based on the asymptotic distribution of the test statistic [188].

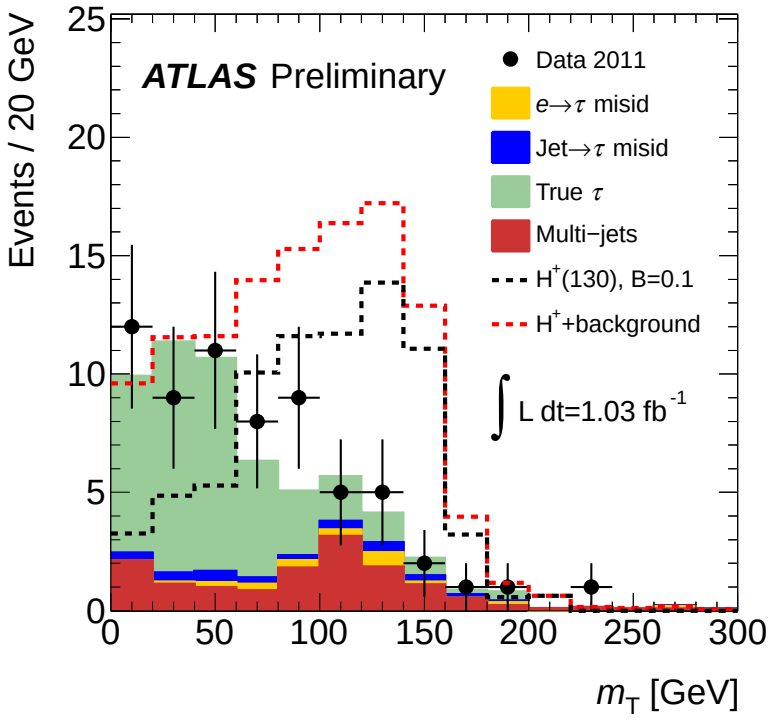

Figure 7.3: The m_T distribution after event selection. The observation in data, and the estimates from data-driven methods are compared. The distribution of the H^+ signal is given for a reference point in parameter space corresponding to BR($t \to bH^+$) = 10%, thus the SM-like $t\bar{t}$ background is reduced correspondingly [204].

The resulting exclusion limit is shown in Figure 7.4 in terms of BR($t \to H^+b$) × BR($H^+ \to \tau^+\nu$). Values of the product of branching ratios, BR($t \to bH^+$) × BR($H^+ \to \tau^+\nu$), larger than (0.03 – 0.10) have been excluded in the H^+ mass range (90 – 160) GeV. Figure 7.5 shows the upper limit in the context of the m_h^{max} scenario of the MSSM in the m_{H^+}-$\tan\beta$ plane. No exclusion limit is shown for charged Higgs boson masses close to 160 GeV as no reliable calculations for BR($t \to H^+b$) exist for $\tan\beta$ values in the range of interest. Interpreted in the context of the m_h^{max} scenario of the MSSM, values of $\tan\beta$ above (22 – 30) (depending on m_{H^+}) can be excluded in the mass range 90 GeV $< m_{H^\pm} <$ 140 GeV as shown in Figure 7.4. This result constitutes a significant improvement compared to existing limits provided by the Tevatron experiments [71] over the whole investigated mass range, but

in particular for charged Higgs boson masses close to the top quark mass.

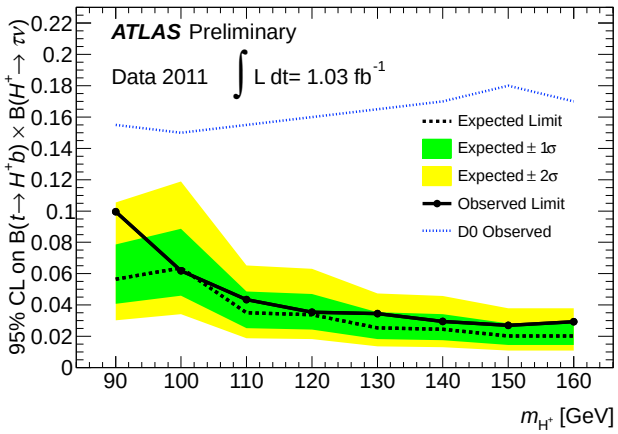

Figure 7.4: Expected and observed 95% CL exclusion limits for the charged Higgs boson production from top quark decays as a function of m_{H^+} in terms of BR($t \to H^+b$) $\times$ BR($H^+ \to \tau^+\nu$) [204]. For comparison, the best limit provided by the Tevatron experiments is shown [71].

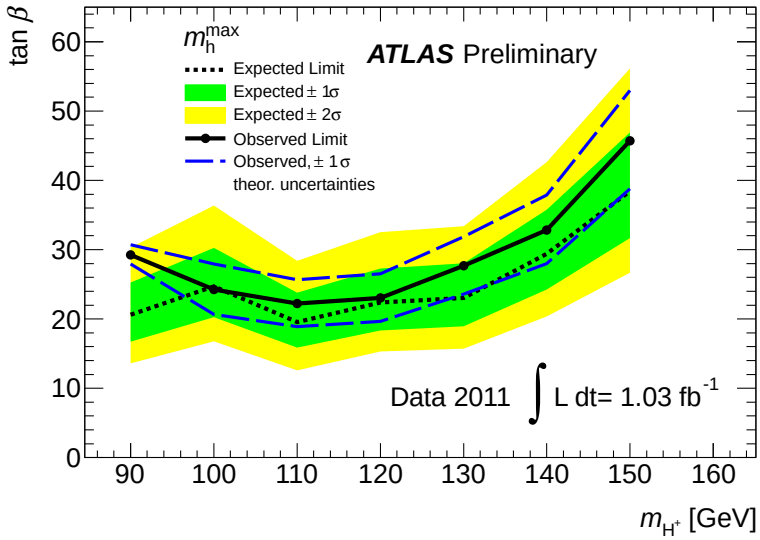

Figure 7.5: Limit for the charged Higgs boson production from top quark decays in the m_{H^+}-tanβ plane. Results are shown for the MSSM scenario $m_h^{\max}$ [204].

7.2.3 The one or two light leptons final state

This analysis is focused on the search for charged Higgs bosons in $t\bar{t}$ events with one or two electrons or muons in the final state. For the charged Higgs boson from $t \to bH^+$ process decaying only into $\tau\nu$, a small increase in the branching fraction for single-lepton and di-lepton decays of $t\bar{t}$ pairs occurs, as the τ decays leptonically more often than the W boson: $B(H^+ \to \tau_{\text{lep}} + \nu) \simeq 35\%$ while $B(W \to \ell + N\nu) \simeq 25\%$. In addition, the search strategies for charged Higgs bosons use variables discriminating between light leptons produced in τ_{lep} decays (from W or charged Higgs bosons) and light leptons arising directly from W boson decays. The background processes that enter the search for a charged Higgs boson in $t\bar{t}$ events with one or two leptons include the production of $t\bar{t} \to b\bar{b}WW$, single top, γ^*/Z+jets, W+jets and di-boson events, as well as QCD multijet events.

Object and event selection

Selection for electrons, muons, jets and $E_{\mathrm{T}}^{\mathrm{miss}}$ is the same as described in Section 7.2.2. The only difference is E_{T} selection for electrons ($E_{\mathrm{T}} > 15$ GeV) and p_{T} selection for muons ($p_{\mathrm{T}} > 15$ GeV).

In order to distinguish between leptons produced in τ_{lep} decays and leptons from direct decays of W bosons, the following discriminating variables are constructed. The first one is $\cos\theta_\ell^*$, a variable connected to the invariant mass of a b-quark and a light lepton coming from the same top quark, $m_{b\ell}$, defined as:

$$\cos\theta_\ell^* = \frac{2m_{b\ell}^2}{m_{\mathrm{top}}^2 - m_W^2} - 1 \simeq \frac{4\,p^b \cdot p^\ell}{m_{\mathrm{top}}^2 - m_W^2} - 1 \text{ with } p^b \cdot p^\ell = 2E_b E_\ell(1 - \cos\theta_{b\ell}) = 4E_b E_\ell \sin^2(\theta_{b\ell}/2), \tag{7.1}$$

where p^b and p^ℓ are the four-momenta of the b-quark and of the lepton ℓ (in any reference frame, since $\cos\theta_\ell^*$ contains an invariant product) and $\theta_{b\ell}$ is the angle between them. Note that both m_b^2 and m_ℓ^2 are neglected, hence $m_{b\ell}^2 \simeq 2\,p^b \cdot p^\ell$. If a top quark decay is mediated through H^+ and if the H^+ is heavier than the W boson, the b-quark usually has a smaller momentum than in the case of a W-mediated top quark decay. Also, a light lepton ℓ arising from a τ decay is likely to have a smaller momentum than a lepton coming directly from a real W boson. As a result, the presence of a charged Higgs boson in a leptonic top quark decay strongly reduces the invariant product $p^b \cdot p^\ell$, leading to $\cos\theta_\ell^*$ values mostly close to -1.

A second discriminating variable is the charged Higgs boson transverse mass [205], m_{T}^H, obtained by fulfilling the constraint $(p^{\mathrm{miss}} + p^\ell + p^b)^2 = m_{\mathrm{top}}^2$ on lepton+jets $t\bar{t}$ events, with more than one neutrino accounting for missing momentum and its transverse component $E_{\mathrm{T}}^{\mathrm{miss}}$:

$$(m_{\mathrm{T}}^H)^2 = \left(\sqrt{m_{\mathrm{top}}^2 + (p_{\mathrm{T}}^l + p_{\mathrm{T}}^b + p_{\mathrm{T}}^{\mathrm{miss}})^2} - p_{\mathrm{T}}^b\right)^2 - \left(p_{\mathrm{T}}^l + E_{\mathrm{T}}^{\mathrm{miss}}\right)^2. \tag{7.2}$$

By construction, m_{T}^H gives an event-by-event lower bound on the mass of the charged (W or Higgs) boson produced in the leptonic top quark decay.

In di-lepton $t\bar{t}$ events, the final state includes two leptons and missing energy, making its full reconstruction more complicated. In that case the generalised charged Higgs boson transverse mass, m_{T2}^H, is computed by the numerical maximisation of

$$m_{\mathrm{T2}}^H = \max_{\{constraints\}} [m_{\mathrm{T}}^H(p_{\mathrm{T}}^H)], \tag{7.3}$$

where

$$\left(m_{\mathrm{T}}^H(p_{\mathrm{T}}^H)\right)^2 = \left(\sqrt{m_{\mathrm{top}}^2 + (p_{\mathrm{T}}^H + p_{\mathrm{T}}^b)^2} - p_{\mathrm{T}}^b\right)^2 - \left(p_{\mathrm{T}}^H\right)^2 \tag{7.4}$$

and *constraints* stands for a set of constraints on masses of two top quarks, mass of W boson, $E_{\mathrm{T}}^{\mathrm{miss}}$and momenta of neutrinos. It leaves two free parameters over which the charged boson Higgs mass is maximised.

The transverse masses m_{T}^H and m_{T2}^H are larger than the true charged Higgs boson mass m_{H^+} and smaller than the top quark mass used in the constraints, m_{top}. Therefore, they can serve as discriminants between top quark decays mediated by a W or charged Higgs boson, based on their different masses.

Event selection for single-lepton events In order to select single-lepton $t\bar{t}$ events the following cuts are applied. Exactly one trigger-matched electron with $E_{\mathrm{T}} > 25$ GeV or muon with $p_{\mathrm{T}} > 20$ GeV is required. Only events with at least four jets with $p_{\mathrm{T}} > 20$ GeV and $|\eta| < 2.5$, including exactly two b-tagged jets are accepted. To select events with a large $E_{\mathrm{T}}^{\mathrm{miss}}$ while rejecting those in which the latter arises mostly from wrongly reconstructed leptons (i.e. where the azimuthal angle $\phi_{\ell,E_{\mathrm{T}}^{\mathrm{miss}}}$ between the lepton and $E_{\mathrm{T}}^{\mathrm{miss}}$ is small), it is required that:

$$\begin{aligned} &E_{\mathrm{T}}^{\mathrm{miss}} > 40 \text{ GeV} && \text{if } |\phi_{\ell,E_{\mathrm{T}}^{\mathrm{miss}}}| \geq \pi/6 \text{ rad}, \\ &E_{\mathrm{T}}^{\mathrm{miss}} \times |\sin(\phi_{\ell,E_{\mathrm{T}}^{\mathrm{miss}}})| > 20 \text{ GeV} && \text{if } |\phi_{\ell,E_{\mathrm{T}}^{\mathrm{miss}}}| < \pi/6 \text{ rad}. \end{aligned}$$

Table 7.4: Number of selected events for the simulated SM processes in the single-lepton channel (here, the fitted value of 165.1 pb is used for σ_{bbWW}) compared to that observed in data. The expected number of events for H^+ of mass 130 GeV is also given [205].

$t\bar{t}$ ($bbWW$)	Single top quark	W+jets	Z+jets	Di-boson	QCD	$\sum$ SM	Data	130 GeV H^+ $B(t \to bH^+) = 10\%$
3081	88	85	5.2	2.0	56	3317	3421	190

The iteration over all selected jets is performed and the combination of one b-jet and two light-quark jets (j) minimising:

$$\chi^2 = \frac{(m_{jjb} - m_{\text{top}})^2}{\sigma^2_{\text{top}}} + \frac{(m_{jj} - m_W)^2}{\sigma^2_W}, \tag{7.5}$$

is chosen in order to assign correctly jets and b-jets to the W and top decays. σ_{top} and σ_W are the assumed mass widths of the reconstructed top quark and W boson, as estimated from correctly-identified combinations in simulated $t\bar{t}$ events. The corresponding assignment efficiency is 74%. At this stage, events are removed if $\chi^2 > 5$. Events having a second electron with $E_{\text{T}} > 15$ GeV or muon with $p_{\text{T}} > 15$ GeV are also removed.

Table 7.4 shows the number of selected events of the SM processes and $t\bar{t}$ events with at least one decay $t \to bH^+$, assuming $m_{H^+} = 130$ GeV and a cross section of 38.7 pb. As expected, events surviving the selection cuts are mainly single-lepton $t\bar{t}$ events. The value of 165.1 pb is used for σ_{bbWW}, as obtained when setting the exclusion limit for that mass point, and $B(t \to bH^+) = 10\%$. It is obtained from the control region enriched in $t\bar{t} \to b\bar{b}WW$ events, defined by requiring $-0.2 < \cos\theta^*_\ell < 1$.

Figure 7.6 (a) shows the $\cos\theta^*_\ell$ distribution obtained by using the charged lepton and the associated b-jet. A signal enriched region with $t\bar{t} \to b\bar{b}H^+W$ and $t\bar{t} \to b\bar{b}H^+H^-$ events is selected by requiring $\cos\theta^*_\ell < -0.6$, as indicated by the arrow. Also, in order to enhance decays of charged (W or Higgs) bosons via τ_{lep}, the cut $m^W_{\text{T}} < 60$ GeV is applied. In a such defined signal region, the transverse mass m^H_{T} is used as a discriminating variable to search for charged Higgs bosons, as shown in Figure 7.6 (b). The data agree well with the SM expectations and neither an excess of events nor a significant deformation of the m^H_{T} distribution is observed.

Event selection for di-lepton events In order to select di-lepton $t\bar{t}$ events the following cuts are applied. Exactly two oppositely charged leptons, including at least one matched to the single-lepton trigger, electron with $E_{\text{T}} > 25$ GeV or muon with $p_{\text{T}} > 20$ GeV, are required. An event is selected if at least two jets with $p_{\text{T}} > 20$ GeV and $|\eta| < 2.5$, including exactly two b-tagged jets are present. For ee and $\mu\mu$ events, the di-lepton invariant mass $m_{\ell\ell}$ must be larger than 15 GeV and must satisfy $|m_{\ell\ell} - m_Z| > 10$ GeV (i.e. Z veto), together with $E^{\text{miss}}_{\text{T}} > 40$ GeV. For $e\mu$ events, the scalar sum of the transverse energies of the two leptons and all selected jets must satisfy $\sum E_{\text{T}} > 130$ GeV.

There is a four-fold ambiguity in assigning the two leptons and the two b-jets to their parents. In the first stage, the events which have a clearly incorrect pairing: $\cos\theta^*_\ell > 1$ for either of the two ℓ-b pairs are rejected. For events with $\cos\theta^*_\ell < 1$ for all pairings, the two ℓ-b pairs that minimise the sum of the distances $\Delta R(\ell, b)_{\text{pair 1}} + \Delta R(\ell, b)_{\text{pair 2}}$ in the η-ϕ plane are chosen. In simulated $t\bar{t}$ events, the assignment efficiency is 66%. The particles of the ℓ-b pair with the smallest $\cos\theta^*_\ell$ value are then assigned to the "H^+ side" and its partner pair to the "W side". In simulated events with a 130 GeV charged Higgs boson, this second assignment has an efficiency of 62%. The events for which the numerical computation of m^H_{T2} does not converge are discarded.

Table 7.5 shows number of events surviving the selection cuts. As expected, surviving background events are mainly $t\bar{t}$ events. The expected number of events for the Monte Carlo $t\bar{t}$ sample with at least one $t \to bH^+$ decay is also shown in the last column, assuming $m_{H^+} = 130$ GeV and a cross section of 35.3 pb. It corresponds to the fitted

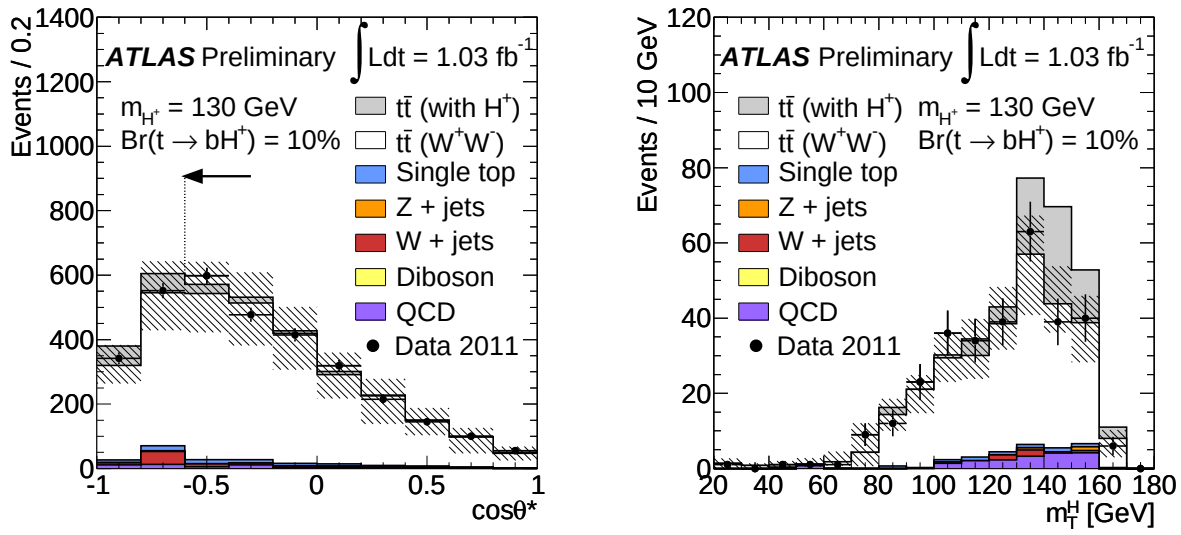

(a) (b)

Figure 7.6: Reconstruction of $\cos\theta_l^*$ (a) in the single-lepton events and of the transverse mass m_{T}^H (b) when $\cos\theta_l^* < -0.6$ and $m_{\mathrm{T}}^W < 60$ GeV. The fitted value of 165.1 pb is used for σ_{bbWW} and the hatched area shows the systematic uncertainties for the SM backgrounds. The grey histogram shows the predicted contribution of events with a 130 GeV charged Higgs boson, assuming $B(t \to bH^+) = 10\%$ and $B(H^+ \to \tau\nu) = 1$ [205].

Table 7.5: Number of selected MC events in the di-lepton analysis (here, a fitted value of 150.4 pb is used for σ_{bbWW}) compared to that observed in data and expected number of events for H^+ of mass 130 GeV [205].

$t\bar{t}$ ($bbWW$)	Single top quark	Z+jets	Di-boson	QCD and W+jets	$\sum$ SM	Data	130 GeV H^+ $B(t \to bH^+) = 10\%$
864	18	1.5	0.3	40	924	992	115

value of 150.4 pb for σ_{bbWW} (as obtained when setting the exclusion limit for that mass point) and $B(t \to bH^+) = 10\%$. Here, the control region enriched with $t\bar{t} \to b\bar{b}WW$ events is defined by requiring $-0.4 < \cos\theta_l^* < 1$. In this final state, a downward fluctuation of data in the control region yields fitted values of σ_{bbWW} slightly smaller than the SM prediction.

In Figure 7.7 (a) the $\cos\theta_l^*$ distribution on the "H^+ side" is shown. A signal region enriched with $t\bar{t} \to b\bar{b}H^+W$ and $t\bar{t} \to b\bar{b}H^+H^-$ events is selected by requiring $\cos\theta_l^* < -0.6$ on the "H^+ side", as indicated by the arrow. For the events found in this signal region, the generalised transverse mass m_{T2}^H is used as a discriminating variable to search for charged Higgs bosons, as shown in Figure 7.7 (b). Neither an excess of events nor a significant deformation of the m_{T2}^H distribution is observed.

Estimation of background with mis-identified leptons

The backgrounds with mis-identified leptons come from non-isolated leptons, arising from the semileptonic decay of heavy quarks, from the decay-in-flight of a $\pi^{\pm}$ or K-meson and, in the case of fake electron objects, from the

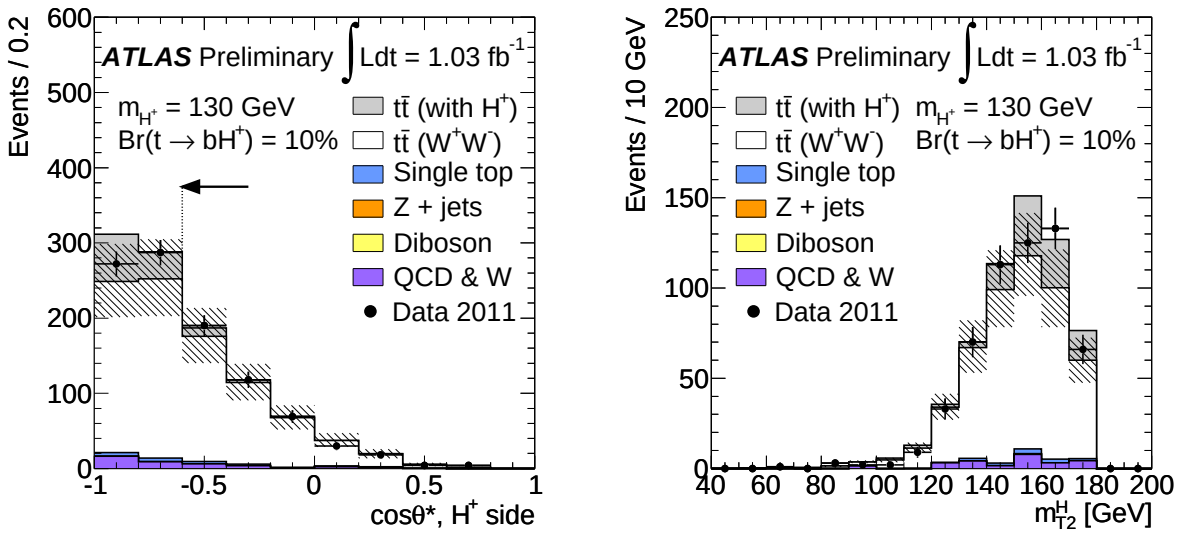

(a) (b)

Figure 7.7: Reconstruction of $\cos\theta_l^*$ on the "H^+ side" of the di-lepton events (a) and of the generalised transverse mass m_{T2}^H when $\cos\theta_l^* < -0.6$ (b). A fitted value of 150.4 pb is used for σ_{bbWW} and the striped area shows the systematic uncertainties for the SM backgrounds. The grey histogram shows the predicted contribution of events with a 130 GeV charged Higgs boson, assuming $B(t \to bH^+) = 10\%$ and $B(H^+ \to \tau\nu) = 1$ [205].

reconstruction of a π^0, photon conversion and shower fluctuations. All leptons coming from such mechanisms are referred to as *fake* leptons, as opposed to true isolated leptons (e.g. from the decay of W and Z bosons) which are referred to as *real* leptons. In the case of the single-lepton final state, fake leptons originate from QCD multijet events, in which a jet is mis-identified as a lepton. In the di-lepton final state, fake leptons can originate from QCD multijet events and $W(\to \ell\nu)$ + jets. The background due to fake leptons is estimated from data. For this purpose, the two data samples are defined, differing only in the lepton identification criteria. The first sample contains mostly events with real leptons and is referred to as the *tight* sample. The second one, obtained by loosening the lepton isolation requirements, contains mostly events with fake leptons and is referred to as the *loose* sample. In case of di-lepton channel, due to the presence of two leptons in the event, one of the leptons is required to pass the tight selection criteria, while the other lepton is required to pass the loose selection criteria in the loose sample, or the tight selection criteria in the tight sample.

The number of events containing fake lepton can be estimated from those tight and loose samples using the rates for a real or fake lepton to be identified as a tight lepton [205]. The measurement of these rates is derived using a tag-and-probe method in data $Z \to \ell\ell$ events with a di-lepton invariant mass in the range 86–96 GeV, where one lepton is required to fulfil the tight selection criteria. The rate at which the other lepton passes the same tight selection criteria defines a rate for a real lepton to pass the tight identification criteria. On the other hand, a control sample with fake leptons is selected by considering data events with exactly one lepton passing the loose criteria. To select events dominated by QCD processes, $E_{\mathrm{T}}^{\mathrm{miss}}$ is required to be between 5 and 20 GeV. After subtraction of other SM processes with true leptons, the rate at which a loose lepton passes tight selection criteria defines the fake rate for a fake lepton to pass the tight identification criteria. In the final parametrisation of the rates, any significant dependence on kinematical or topological observables such as the transverse momentum and pseudorapidity of the lepton, the jet multiplicity, the number of b-tagged jets, etc, are taken into account.

Systematic uncertainties

As for τ_{had}+jets final state, the main detector-related systematic uncertainties are due to identification efficiencies and the energy/momentum resolution and scale of the physics objects used in the analysis. Uncertainties on trigger efficiency, luminosity, cross sections and acceptance are also taken into account.

In the single-lepton channel, the W+jets background is not precisely predicted, especially after the b-tagging requirement. Hence, a factor 2 up and down normalisation uncertainty is assigned to the Monte Carlo W+jets background sample.

In the data-driven methods used to identify events with fake leptons, the main systematic uncertainties arise from the control region selection (the fake rates are calculated in a control region dominated by gluon-initiated events, but are later used in a data sample with a higher fraction of quark-initiated events) and from the Monte Carlo samples used for the subtraction of real leptons in the determination of the fake efficiencies, which are sensitive to the dominant detector-related systematic uncertainties.

Limits on the Branching Ratio of $t \to bH^+$

Assuming $B(H^+ \to \tau\nu) = 1$, upper limits are extracted on the branching ratio $B(t \to bH^+)$ as a function of the charged Higgs boson mass. As already mentioned, in the presence of a charged Higgs boson one can not rely on the predicted cross section for $t\bar{t}$ decaying into the $bbWW$ final state and it has to be estimated from data. Since the signal and the $t\bar{t}$ background are correlated, the event rate of the $t\bar{t} \to b\bar{b}WW$ background is derived from the measurement in the control region with $-0.2 < \cos\theta^*_\ell < 1$ in the single-lepton analysis or $-0.4 < \cos\theta^*_\ell < 1$ in the di-lepton analysis, while the signal region corresponds to $\cos\theta^*_\ell < -0.6$ (with the additional cut $m_{\text{T}}^W < 60$ GeV in the single-lepton case). Because $t\bar{t} \to b\bar{b}H^+W$ can be found in the control region[1], σ_{bbWW} is treated as a free parameter when the upper limits on the branching fraction $B(t \to bH^+)$ are derived.

A profile likelihood ratio is used with the m_{T}^H distribution for single lepton and m_{T2}^H distribution for di-lepton final state as the discriminating variables. The statistical analysis is based on a binned likelihood functions of those distributions. The limit itself is derived using the CL_{s} method.

Figure 7.8 shows the 95% confidence level upper limits on the branching fraction $B(t \to bH^+)$, obtained with the assumption that $B(H^+ \to \tau\nu) = 1$. In the single-lepton channel, the fitted values of $t\bar{t}$ cross section lie between 0.99 and 1.03 times the SM prediction, with uncertainties in the range (2–3)%. In the di-lepton channel, a downward fluctuation of data in the control region yields fitted values of $t\bar{t}$ cross section between 0.78 and 1.06 times the SM prediction, with uncertainties in the range (5–25)%. When a charged Higgs boson mass of 160 GeV is assumed, the b-jets coming from $t \to bH^+$ are usually so soft that they are not likely to survive the p_{T} cut at 20 GeV, leading to a significant loss of sensitivity for that mass point.

In the combined exclusion limit for both final states, the systematic uncertainties are assumed to be 100% correlated. Although the expected limit improves after the combination, the observed combined limit on $B(t \to bH^+)$ is actually found to be slightly worse when combining the two analyses than for the single-lepton channel only, see Figure 7.9 and Table 7.6. The compatibility with background is measured by p_0-values, which range between 26% and 50%. Hence, no indication of an H^+-like excess is found. Assuming $B(H^+ \to \tau\nu) = 1$, leads to the upper limits on the branching fraction $B(t \to bH^+)$ between 5.2% and 14.1% for charged Higgs boson masses in the range 90 GeV $< m_{H^+} <$ 160 GeV. This result constitutes an improvement compared to the limits provided by the Tevatron experiments. Except for the mass point at 160 GeV, obtained exclusion limits are also comparable to (or somewhat higher than) those presented by CMS [209] and by τ_{had}+jets analysis.

Finally, Figure 7.10 shows the upper limit in the m_{H^+}-$\tan\beta$ plane, in the context of the m_h^{max} scenario of the MSSM. No exclusion limit is shown for charged Higgs boson masses above 140 GeV since no reliable calculations of $B(t \to bH^+)$ exist for $\tan\beta$ values in the range of interest. Also, since the assumption $B(H^+ \to \tau\nu) = 1$ is not

[1] Also $t\bar{t} \to b\bar{b}H^+H^-$ events can contribute, but they are not considered in the following. Other searches for charged Higgs bosons, such as the one reported in Ref. [204], indeed suggest that top quarks decay into bH^+ in less than 10% of the cases, hence the contribution from $t\bar{t} \to b\bar{b}H^+H^-$ remains very small. By not considering these events, the estimation of the upper limit on $B(t \to bH^+)$ is somewhat conservative.

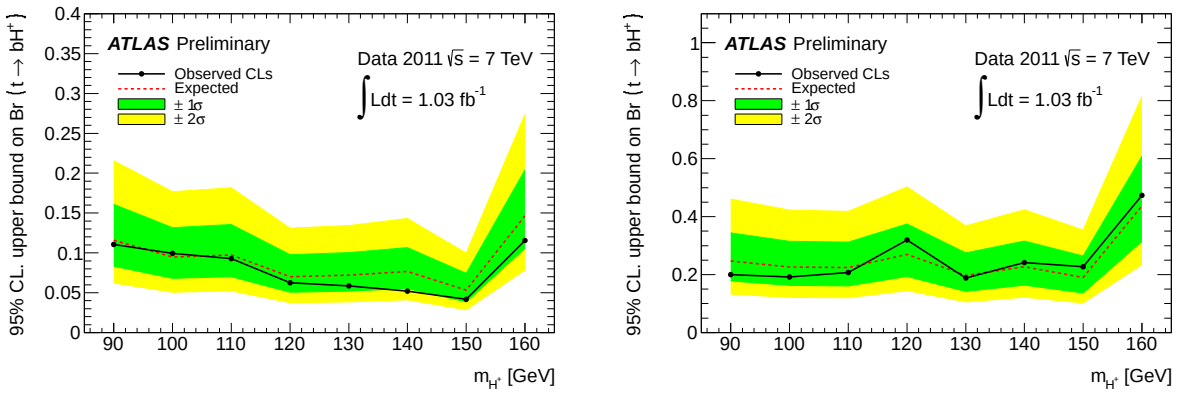

Figure 7.8: Upper limits on $B(t \to bH^+)$ in the single-lepton (a) and di-lepton (b) channels, as a function of the charged Higgs boson mass, obtained with the assumption that $B(H^+ \to \tau\nu) = 1$. All systematic uncertainties are included, as described in the text. Solid lines denote the observed 95% CL upper limits, while dashed lines represent the expected limits. The outer edges of the green and yellow shaded regions show the 1σ and 2σ error bands on the expected limits [205].

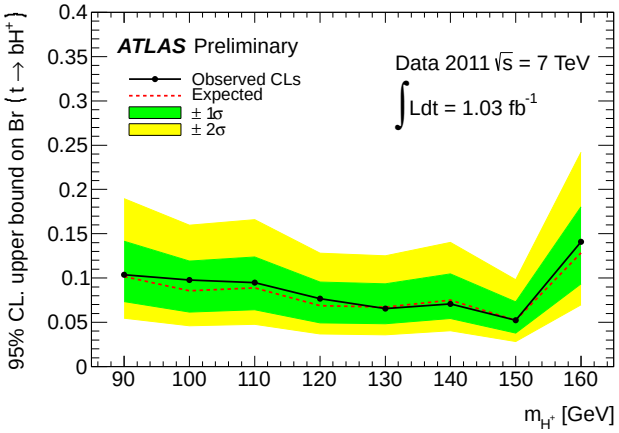

Figure 7.9: Upper limits on $B(t \to bH^+)$ for the combined single-lepton and di-lepton channels, as a function of the charged Higgs boson mass, obtained with the assumption that $B(H^+ \to \tau\nu) = 1$ [205].

fulfilled at low $\tan\beta$, no limits are derived in this region. In the context of the $m_h^{\max}$ scenario of the MSSM, values of $\tan\beta$ larger than (30–56) are excluded in the mass range $90 < m_{H^+} < 140$ GeV.

7.3 Summary

This Chapter presents the first searches for the MSSM Higgs bosons by the ATLAS experiment, based on the 1.03-1.06 fb^{-1} of proton-proton collision data at $\sqrt{s} = 7$ TeV. In all presented studies, observed number of events is consistent with the total number of background events.

A search for neutral Higgs bosons decaying to pairs of τ leptons is described. Four different di-τ decay final states are considered. Exclusion limits at the 95% confidence level are derived for A/H/h production in MSSM as a function of $\tan\beta$ and m_A, for the m_h^{max} scenario. These results exclude regions of parameters space beyond the existing limits from previous experiments and are similar to those recently obtained by the CMS Collaboration.

Table 7.6: Observed (expected) 95% CL upper limits on $B(t \to bH^+)$ in the single-lepton and di-lepton channels, and after their combination, as a function of the charged Higgs boson mass, obtained with the assumption that $B(H^+ \to \tau\nu) = 1$ [205].

m_{H^+} (GeV)	90	100	110	120	130	140	150	160
95% CL observed (expected) limit on $B(t \to bH^+)$ for the single-lepton channel	11.1% (11.6%)	9.9% (9.5%)	9.3% (9.7%)	6.3% (7.0%)	5.8% (7.2%)	5.2% (7.7%)	4.2% (5.3%)	11.6% (14.6%)
95% CL observed (expected) limit on $B(t \to bH^+)$ for the di-lepton channel	20.0% (24.7%)	19.2% (22.6%)	20.7% (22.4%)	32.0% (26.9%)	18.8% (19.8%)	24.2% (22.6%)	22.7% (19.0%)	47.3% (43.7%)
95% CL observed (expected) limit on $B(t \to bH^+)$ for the combined channels	10.4% (10.2%)	9.8% (8.5%)	9.5% (8.9%)	7.7% (6.9%)	6.6% (6.7%)	7.1% (7.5%)	5.2% (5.2%)	14.1% (12.9%)

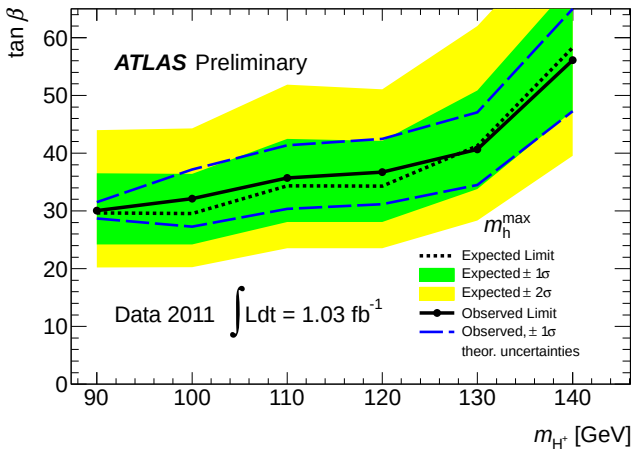

Figure 7.10: Limits for charged Higgs boson production from top quark decays in the m_{H^+}-tanβ plane, in the context of the m_h^{max} scenario of the MSSM, obtained with the assumption that $B(H^+ \to \tau\nu) = 1$. The 1σ band around the observed limit (blue dashed lines) is obtained by adjusting the theoretical uncertainties listed in the text and adding them linearly [205].

A search for charged Higgs bosons with masses in the range 90 – 160 GeV using $t\bar{t}$ events with a leptonically or hadronically decaying τ lepton in the final state is also described. Assuming $B(H^+ \to \tau\nu) = 1$, the upper limits on the branching fraction $B(t \to bH^+)$ between 5.2% and 14.1% for charged Higgs boson masses in the range $90 < m_{H^+} < 160$ GeV are set. In the context of the m_h^{max} scenario of the MSSM, values of tanβ larger than (30–56) are excluded in the mass range $90 < m_{H^+} < 140$ GeV Those results constitute an improvement compared to the limits provided by the Tevatron experiments.

The most recent results for the neutral MSSM Higgs searches in the ATLAS experiment corresponding to the luminosity of 4.7−4.8 fb^{-1} [210] tightened allowed phase space even more. The most recent results for the charged Higgs searches [211] are based on 4.6 fb^{-1} of proton-proton collision data at $\sqrt{s} = 7$ TeV. With respect to the early

results presented in this Chapter, the upper limits on the branching fraction $B(t \to bH^+)$, assuming $B(H^+ \to \tau\nu) = 1$, are narrowed to 1% and 7.5% for charged Higgs boson masses in the range $90 < m_{H^+} < 160$ GeV. Interpreted in the context of the m_h^{max} scenario of the MSSM, values of $\tan\beta$ larger than (14–28) can be excluded in the mass range $90 < m_{H^+} < 150$ GeV.

In light of the recent observation of a Higgs-like boson at the LHC, there is still a considerable part of the MSSM parameter space that is not excluded and is still compatible with the scenario that the recently discovered boson corresponds to the lightest CP-even MSSM Higgs boson.

The studies of the dataset collected in 2012 with the centre-of-mass energy of 8 TeV are ongoing.

This is also the place to summarize my thoughts about the changes that have occurred in elementary-particle physics in the past forty years. Most of the changes have been very good: we know a tremendous amount more about elementary particles; we have much more powerful and sensitive particle detectors; we have much higher energy accelerators and colliders; and our students are better trained. But some changes, I believe, are not so pleasant: we have lost the freedom to move quickly into new experiments; almost all experiments are large and complicated; usually experimenters have to work in very large collaborations; and it is no longer possible for a particle physicist to be a productive experimenter and at the same time be able to make calculations from first principles in much of modern particle theory. I do not see a way to reverse these unpleasant changes.

Martin L. Perl; Phys. perspect. 6 (2004) 401

8 Summary

This monograph summarises the first analyses of processes with τ leptons in the final state, performed with the data collected by the ATLAS detector at LHC with proton-proton collisions at the centre-of-mass energy of $\sqrt{s} = 7$ TeV in 2010 and first few months of 2011. However, there is a long history behind those results.

The LHC accelerator was originally conceived in 1980's and approved for construction by the CERN Council in late 1994. In 1992 the ATLAS collaboration wrote a Letter of Intent in which the building of a general purpose proton-proton detector for the LHC was proposed. Turning this ambitious scientific plans into reality proved to be an extremely complex and long task. Physicists of the ATLAS collaboration, working only with Monte Carlo simulations, were patiently waiting almost 20 years for real data to come. The last years before first collisions were particularly difficult because of multiple delays in the date of the LHC start, the race for the Higgs boson with the Tevatron and the infamous LHC accident in Autumn 2008.

Finally, in Autumn 2009, the LHC began operation and started probing completely new energy regimes. The ATLAS experiment started to successfully collect real data. The last three years were quite successful for the field of particle physics. Many known processes of the Standard Model were reproduced at the new, high centre-of-mass energies. The first results concerning New Physics processes were published in order to set new limits on discovery potential. In addition, there is already a hint for the Higgs boson discovery, as a new boson with mass of about (125-126) GeV was observed this Summer by both ATLAS and CMS collaborations.

With the first collision data, physics of τ leptons at hadron colliders entered a new era. After years of waiting, we finally could see the first τ leptons decaying in the ATLAS detector. This monograph documents these first observations.

As the first step, the ATLAS package for the reconstruction and identification of hadronically decaying τ leptons was tested and optimised with data. The mis-identification probabilities for QCD multijets and electrons to be reconstructed as τ candidates were measured with data using tag-and-probe methods. Also the first attempt to estimate the τ signal efficiency from $W \to \tau\nu$ process was performed. The package for τ reconstruction and identification was found to be robust and ready to be used in the first physics studies with τ leptons in final states.

With increasing statistics of data, the measurement of $W \to \tau\nu$ and $Z \to \tau\tau$ cross sections was possible. Although it was a rediscovery of well known processes, those measurements were done for the first time at the centre-of-mass energy of 7 TeV. Furthermore, as $W \to \tau\nu$ and $Z \to \tau\tau$ are important background processes to Higgs boson(s) and New Physics searches, their production cross sections needed to be measured precisely. Finally, they offered the first opportunity to study τ hadronic decays in detail. The measured cross sections agree well with theory predictions and measurements by other experiments.

The first analyses of Higgs boson(s) searches with τ leptons in final states presented in this monograph cover searches for both the SM and MSSM neutral Higgs boson(s) decaying into the $\tau\tau$ final state as well as MSSM

charged Higgs boson decays, $H^+ \to \tau\nu$. No significant excess over the expected background is observed in any of those studies. Nevertheless, even if performed on limited data statistics, they improved exclusion limits obtained previously by the Tevatron experiment and paved the path to future, full statistics studies.

It has to be stressed that the $H \to \tau\tau$ final state is particularly important for assessing properties of the new recently found boson, and for checking if this new particle is the Standard Model Higgs boson. With this final state we can check if the new boson couples to fermions and study its CP properties.

Presented studies represent only the very beginning of the ATLAS adventure with τ leptons. They open a way for high statistics and more sophisticated analyses as, for example, the measurement of τ polarisation in various production processes. Also, possible improvements in τ reconstruction and identification methods can give better background rejection in almost all described final states with τ_{had} decays. Those improvements can include for example development of the reconstruction of sub-structure of τ_{had} decays and also optimisation of the τ reconstruction and identification for high p_{T}.

All the great results obtained by the ATLAS collaboration and described in the presented monograph, as well as all the following, high statistics studies, show that not all changes in the high particle physics are so unpleasant as in pessimistic view of Marin Perl used as an opening quote above. The ATLAS collaboration, consisting of about 3000 physicists, is one of the largest collaborative efforts ever attempted in physics sciences. This community proved that people from different countries and culture can work in harmony, share knowledge, perform very complex analyses and in parallel enjoy their work a lot.

A

Appendix: $\tau^+\tau^-$ mass reconstruction techniques

An accurate mass reconstruction of a $\tau^+\tau^-$ system is challenging due to the presence of multiple neutrinos in the final state resulting in an $E_{\mathrm{T}}^{\mathrm{miss}}$ signature. Therefore, either partial reconstruction methods or approximations are used to obtain information about the invariant mass of the $\tau^+\tau^-$ resonance. Four of them are commonly used in the ATLAS experiment.

The simplest method is the so-called *visible mass*, m_{vis}, defined as the invariant mass of visible τ decay products. The visible mass provides no direct link to the invariant mass of the resonance as the contributions of the neutrino momenta are ignored.

The visible mass can be extended to the *effective mass*, $m_{\mathrm{effective}}$, by calculating the invariant mass of the visible τ decay products and the $E_{\mathrm{T}}^{\mathrm{miss}}$ according to

$$m_{\mathrm{effective}} = \sqrt{(p_{\tau^+} + p_{\tau^-} + p_{\mathrm{miss}})^2}, \tag{A.1}$$

where p_{τ^+} and p_{τ^-} denote the four-vectors of the electron, the muon from τ decay or τ candidates, and the missing momentum four-vector is defined as $p_{\mathrm{miss}} = (E_{\mathrm{T}}^{\mathrm{miss}}, E_{\mathrm{x}}^{\mathrm{miss}}, E_{\mathrm{y}}^{\mathrm{miss}}, 0)$. This definition extends the visible mass with information on the neutrino momenta. However, it provides an approximation, since the $E_{\mathrm{T}}^{\mathrm{miss}}$ measurement is sensitive only to the sum of all neutrino transverse momenta which contains large cancellations. Additionally, it is based on the assumption that $E_{\mathrm{T}}^{\mathrm{miss}}$ only accounts for neutrinos from the two τ_{had} decays. This hypothesis ignores possible contributions from detector effects and simultaneous proton-proton interactions.

The third technique, the *collinear approximation method* [212] makes use of the large boost of the τ leptons and assumes that the neutrinos are produced along the direction of the visible τ lepton decay products (i.e. $\phi_\nu \sim \phi_{\mathrm{vis}}$ and $\theta_\nu \sim \theta_{\mathrm{vis}}$). The second assumption is that $E_{\mathrm{T}}^{\mathrm{miss}}$ in the event is due only to undetected neutrinos of the τ decay. In this case, the total invisible momentum carried away by neutrinos of each τ decay can be estimated by solving two equations:

$$E_x^{\mathrm{miss}} = p_{\mathrm{miss}_1} \sin\theta_{\mathrm{vis}_1} \cos\phi_{\mathrm{vis}_1} + p_{\mathrm{miss}_2} \sin\theta_{\mathrm{vis}_2} \cos\phi_{\mathrm{vis}_2}, \tag{A.2}$$

$$E_y^{\mathrm{miss}} = p_{\mathrm{miss}_1} \sin\theta_{\mathrm{vis}_1} \sin\phi_{\mathrm{vis}_1} + p_{\mathrm{miss}_2} \sin\theta_{\mathrm{vis}_2} \sin\phi_{\mathrm{vis}_2}, \tag{A.3}$$

where E_x^{miss} and E_y^{miss} are the $x-$ and $y-$components of the $E_{\mathrm{T}}^{\mathrm{miss}}$ vector, p_{miss_1} and p_{miss_2} are the combined invisible momenta (there can be two neutrinos in a τ decay) of each τ decay, and $\theta_{\mathrm{vis}_{1,2}}$ and $\phi_{\mathrm{vis}_{1,2}}$ are the polar and azimuthal angles of the visible products of each τ decay. The invariant mass of the $\tau\tau$ system, $m_{\tau\tau}$, is derived as:

$$m_{\tau\tau} = \frac{m_{\mathrm{vis}}}{\sqrt{x_1 x_2}}\,, \tag{A.4}$$

where m_{vis} is the visible mass, and $x_{1,2}$ are momentum fractions carried away by visible τ decay products with momenta $p_{\text{vis1,2}}$

$$x_{1,2} = \frac{p_{\text{vis1,2}}}{(p_{\text{vis1,2}} + p_{\text{mis1,2}})} \,. \tag{A.5}$$

Despite offering a fully reconstructed invariant mass of the $\tau\tau$ pairs, the collinear approximation still have significant limitations. It can give a reasonable mass solution only for events where the $\tau\tau$ system is boosted and the visible τ decay products are not back-to-back in the plane transverse to the beam line. This method is also sensitive to the $E_{\text{T}}^{\text{miss}}$ resolution.

The last technique was introduced in Ref. [213] and is referred to as the *Missing Mass Calculator* (MMC). Conceptually, the MMC is a more sophisticated version of the collinear approximation method, not assuming a strict collinearity of the visible and invisible τ decay products. The only assumption is that there are no other neutrinos in the even except for those from the τ lepton decays. For each di-τ event, the MMC solves a system of four equations:

$$E_x^{\text{miss}} = p_{\text{miss}_1} \sin\theta_{\text{miss}_1} \cos\phi_{\text{miss}_1} + p_{\text{miss}_2} \sin\theta_{\text{miss}_2} \cos\phi_{\text{miss}_2}, \tag{A.6}$$

$$E_y^{\text{miss}} = p_{\text{miss}_1} \sin\theta_{\text{miss}_1} \sin\phi_{\text{miss}_1} + p_{\text{miss}_2} \sin\theta_{\text{miss}_2} \sin\phi_{\text{miss}_2}, \tag{A.7}$$

$$\begin{aligned} M_\tau^2 = {} & m_{\text{miss}_1}^2 + m_{\text{vis}_1}^2 + 2\sqrt{p_{\text{vis}_1}^2 + m_{\text{vis}_1}^2}\,\sqrt{p_{\text{miss}_1}^2 + m_{\text{miss}_1}^2}, \\ & -2p_{\text{vis}_1} p_{\text{miss}_1} \cos\Delta\theta_{\text{vm}_1}, \end{aligned} \tag{A.8}$$

$$\begin{aligned} M_\tau^2 = {} & m_{\text{miss}_2}^2 + m_{\text{vis}_2}^2 + 2\sqrt{p_{\text{vis}_2}^2 + m_{\text{vis}_2}^2}\,\sqrt{p_{\text{miss}_2}^2 + m_{\text{miss}_2}^2}, \\ & -2p_{\text{vis}_2} p_{\text{miss}_2} \cos\Delta\theta_{\text{vm}_2}, \end{aligned} \tag{A.9}$$

where E_x^{miss} and E_y^{miss} are the x- and y-components of the $E_{\text{T}}^{\text{miss}}$ vector, $p_{\text{vis}_{1,2}}$, $m_{\text{vis}_{1,2}}$, $\theta_{\text{vis}_{1,2}}$, $\phi_{\text{vis}_{1,2}}$ are the momentum, the invariant mass, the polar and the azimuthal angle of the visible τ decay products, and M_τ=1.777 GeV is the τ lepton mass. The other quantities are unknown, namely the combined momenta $p_{\text{miss}_{1,2}}$ of the neutrino (or neutrinos) for each of the two decaying τ leptons and the invariant mass of the neutrino(s) in the τ decay, $m_{\text{miss}_{1,2}}$. Finally, $\Delta\theta_{\text{vm}_{1,2}}$ is the angle between the vectors $p_{\text{miss}_{1,2}}$ and $p_{\text{vis}_{1,2}}$ for each of the two τ leptons, and it can be expressed in terms of other variables. The number of unknowns exceeds the number of constraints and thus the system is solved for a grid of points in the ($\Delta\phi_1$, $\Delta\phi_2$) parameter space, where $\Delta\phi_i$ is the difference between the azimuthal angles of the visible and invisible τ decay products. To determine the best estimate for the di-τ invariant mass in a given event, the $m_{\tau\tau}$ distribution from all scanned points in the grid are produced. At each scanned point, ΔR between the momentum vector of the visible τ decay products and the neutrino momentum vector is calculated and the obtained di-τ mass is weighted by a corresponding probability density function. The position of the maximum of the obtained $m_{\tau\tau}$ distribution is used as the final estimator $m_{\tau\tau}^{\text{MMC}}$for a given event. The MMC is becoming more and more popular in di-τ searches at ATLAS because of its superior performance.

Bibliography

[1] A. Kaczmarska, E. Richter-Was, and L. Janyst, *The track-based algorithm tau1p3p : integration with tauRec and performance for release 12.0.5*, ATL-COM-PHYS-2007-010, 2007.

[2] P. Bechtle and A. Kaczmarska et al., *Identification of hadronic tau decays with ATLAS detector*, ATL-PHYS-INT-2008-003, 2008.

[3] A. Kaczmarska, E. Richter-Was, M. Wolter, and L. Janyst, *Performance of the tau1p3p algorithm for hadronic tau decays identification with release 12.0.6*, ATL-PHYS-INT-2008-004, 2008.

[4] A. Christov and A. Kaczmarska et al., *Performance of the tau reconstruction and identification algorithm with release 14.2.10*, ATL-COM-PHYS-2008-196, 2008.

[5] K. Benslama and A. Kaczmarska et al., *Tau identification using the TauDiscriminant package*, ATL-COM-PHYS-2008-212, 2008.

[6] A. Christov and A. Kaczmarska et al., *Performance of the tau reconstruction and identification algorithm with release 14.2.20 and mc08 data*, ATL-COM-PHYS-2009-229, 2009.

[7] A. Christov and A. Kaczmarska et al., *Performance of the tau reconstruction algorithm with release 15.3.1.6 and mc08 data*, ATL-COM-PHYS-2010-744, 2010.

[8] S. Dhaliwal, A. Kaczmarska, W. Mader, and Y. Coadou, *Tau Reconstruction in ATLAS using Cosmic Ray Data*, ATL-COM-PHYS-2009-578, 2009.

[9] ATLAS Collaboration, *Studies of the performance of the ATLAS detector using cosmic-ray muons*, Eur. Phys. J. **C71** (2011) 1593.

[10] ATLAS Collaboration, *Commissioning of the ATLAS Tau-Lepton Reconstruction Using 900 GeV Minimum-Bias Data*, ATLAS-CONF-2010-012, 2010.

[11] ATLAS Collaboration, *Reconstruction of hadronic tau candidates in QCD events at ATLAS with 7 TeV proton-proton collisions*, ATLAS-CONF-2010-059, 2010.

[12] ATLAS Collaboration, *Tau Reconstruction and Identification Performance in ATLAS*, ATLAS-CONF-2010-086, 2010.

[13] A. Kaczmarska and E. Richter-Was, *$Z \to \tau\tau$ (e,τ_{had}) process for 100 pb^{-1} and ATLAS detector*, ATL-PHYS-INT-2009-019, 2009.

[14] P. Bechtle et al., *Benchmark Analysis for $Z \to \tau\tau \to$ lepton hadron with the First 100 pb^{-1}*, ATL-PHYS-INT-2010-075, 2010.

[15] ATLAS Collaboration, *Observation of $Z \to \tau_{\mathrm{had}}\tau_{\mathrm{lep}}$ Decays with the ATLAS detector*, ATLAS-CONF-2011-010 (2011) .

[16] ATLAS Collaboration, *Measurement of the $Z \to \tau\tau$ Cross Section with the ATLAS Detector*, Phys. Rev. **D84** (2011) 112006.

[17] M. Kobayashi and M. Maskawa, *CP-Violation in the Renormalizable Theory of Weak Interaction*, Prog. Theor. Phys. **49** (1973) 652.

[18] V. Valente (ed.), *ADONE : a milestone on the particle way*, Frascati Physics Series **8** (1997) .

[19] M. Perl et al., *Evidence for Anomalous Lepton Production in e+ e- Annihilation*, Phys. Rev. Lett. **35** (1975) 1489.

[20] G. Hanson SLAC-LBL Collaboration internal note (1978) .

[21] G. J. Feldman, *e+e- Annihilation*, Proceedings of the 19th International Conference on High Energy Physics, Tokyo, August 23-30, 1978 (Tokyo: Physical Society of Japan, 1979) (1978) 777.

[22] DELPHI Collaboration, *A precise measurement of the tau lifetime*, Eur. Phys. J. **C36** (2004) 283.

[23] Babar Collaboration, *Measurement of the tau lepton lifetime with BaBar*, Nucl. Phys. Proc. Suppl. **144** (2005) 105.

[24] Belle Collaboration, *Recent Belle results on the hadronic decays of tau lepton*, Nucl. Phys. Proc. Suppl. **198** (2010) 157.

[25] BES Collaboration, *Recent results from BESII*, Int. J. Mod. Phys. **A24** (2009) 279.

[26] CLEO Collaboration, *CLEO contributions to tau physics*, eConf **C0209101** (2002) TU15, arXiv:0210058 [hep-ex].

[27] KEDR Collaboration, *Tau mass measurement at KEDR*, Nucl. Phys. Proc. Suppl. **189** (2009) 21.

[28] T. Cole et al. in *Technical report*. Fermilab TM-1909, 1994.

[29] L. Evans and P. Bryant, *LHC Machine*, JINST **3** (2008) S08001.

[30] F. Englert and R. Brout, *Broken Symmetry and the Mass of Gauge Vector Mesons*, Phys. Rev. Lett. **13** (1964) 321.

[31] P. W. Higgs, *Broken Symmetries, massless particles and gauge fields*, Phys. Lett. **12** (1964) 132.

[32] P. W. Higgs, *Broken Symmetries and the Masses of Gauge Bosons*, Phys. Rev. Lett. **13** (1964) 508.

[33] G. Guralnik, C. Hagen, and T. Kibble, *Global Conservation Laws and Massless Particles*, Phys. Rev. Lett. **13** (1964) 585.

[34] P. W. Higgs, *Spontaneous Symmetry Breakdown without Massless Bosons*, Phys. Rev. Lett. **145** (1966) 1156.

[35] T. Kibble, *Symmetry Breaking in Non-Abelian Gauge Theories*, Phys. Rev. **155** (1967) 1554.

[36] H. Miyazawa, *Baryon Number Changing Currents*, Prog. Theor. Phys. **36 (6)** (1966) 1266.

[37] P. Ramond, *Dual Theory for Free Fermions*, Phys. Rev. **D3** (1971) 2415.

[38] Y. A. Gol'fand and E. P. Likhtman, *Extension of the Algebra of Poincare Group Generators and Violation of p Invariance*, JETP Lett. **13** (1971) 323. [Pisma Zh.Eksp.Teor.Fiz.13:452,1971].

[39] A. Neveu and J. H. Schwarz, *Factorizable dual model of pions*, Nucl. Phys. **B31** (1971) 86.

[40] A. Neveu and J. H. Schwarz, *Quark Model of Dual Pions*, Phys. Rev. **D4** (1971) 1109.

[41] J. Gervais and B. Sakita, *Field theory interpretation of supergauges in dual models*, Nucl. Phys. **B34** (1971) 632.

[42] D. V. Volkov and V. P. Akulov, *Is the Neutrino a Goldstone Particle?*, Phys. Lett. **B46** (1973) 109.

[43] J. Wess and B. Zumino, *A Lagrangian Model Invariant Under Supergauge Transformations*, Phys. Lett. **B49** (1974) 52.

[44] J. Wess and B. Zumino, *Supergauge Transformations in Four-Dimensions*, Nucl. Phys. **B70** (1974) 39.

[45] ATLAS Collaboration, *The ATLAS Experiment at the CERN Large Hadron Collider*, JINST **3** (2008) S08003.

[46] Particle Data Group Collaboration, K. Nakamura et al., *Review of particle physics*, J. Phys. **G37** (2010) 075021.

[47] C. Anastasiou, L. Dixon, K. Melnikov, and F. Petriello, *High-precision QCD at hadron colliders: electroweak gauge boson rapidity distributions at NNLO*, Phys. Rev. **D69** (2004) 094008.

[48] A. Martin, W. Stirling, R. Thorne, and G. Watt, *Parton Distributions for the LHC*, Eur. Phys. J. **C63** (2009) 189.

[49] ATLAS Collaboration, *Measurement of the $W \to l\nu$ and $Z/\gamma^* \to ll$ production cross sections in proton-proton collisions at $\sqrt{s} = 7$ TeV with the ATLAS detector*, JHEP **12** (2010) 060.

[50] ALEPH, DELPHI, L3, OPAL, SLD, CDF , D0 Collaborations, and the LEP Tevatron and SLD Electroweak Working Group Collaboration, *Precision Electroweak Measurements and Constraints on the Standard Model*, arXiv:1012.2367 [hep-ph].

[51] LEP Working Group for Higgs boson searches, *Search for the Standard Model Higgs boson at LEP*, Phys. Lett. **B565** (2003) 61.

[52] CDF and D0 Collaborations, *Combined CDF and D0 upper limits on Standard Model Higgs Boson production*, arXiv:1107.5518 [hep-ex].

[53] ATLAS Collaboration, *Observation of a new particle in the search for the Standard Model Higgs boson with the ATLAS detector*, Phys. Lett. B **716** (2012) 1.

[54] CMS Collaboration, *Observation of a new boson at a mass of 125 GeV with the CMS experiment at the LHC*, Phys. Lett. B **716** (2012) 30.

[55] LHC Higgs Cross Section Working Group, S. Dittmaier, C. Mariotti, G. Passarino, and R. Tanaka (Eds.), *Handbook of LHC Higgs cross sections*, CERN-2011-002, CERN, Geneva, 2011, All the numbers can be obtained at https://twiki.cern.ch/twiki/bin/view/LHCPhysics/CrossSections.

[56] D. L. Rainwater, D. Zeppenfeld, and K. Hagiwara, *Searching for $H \to \tau\tau$ in weak boson fusion at the LHC*, Phys. Rev. **D59** (1998) 014037.

[57] S. Asai et al., *Prospects for the Search for a Standard Model Higgs Boson in ATLAS using Vector Boson Fusion*, Eur. Phys. J. **C32S2** (2004) 19.

[58] B. Mellado, W. Quayle, and S. L. Wu, *Prospects for the observation of a Higgs boson with $H \to \tau^+\tau^- \to \ell^+\ell^- + E_{\mathrm{T}}^{\mathrm{miss}}$ associated with one jet at the LHC*, Phys. Lett. **B611** (2005) 60.

[59] ATLAS Collaboration, *Expected performance of the ATLAS experiment: detector, trigger and physics*, CERN-OPEN-2008-020, 2008.

[60] P. Fayet, *Supersymmetry and Weak, Electromagnetic and Strong Interactions*, Phys. Lett. **B64** (1976) 159.

[61] P. Fayet, *Spontaneously Broken Supersymmetric Theories of Weak, Electromagnetic and Strong Interactions*, Phys. Lett. **B69** (1977) 489.

[62] G. R. Farrar and P. Fayet, *Phenomenology of the Production, Decay, and Detection of New Hadronic States Associated with Supersymmetry*, Phys. Lett. **B76** (1978) 575.

[63] P. Fayet, *Relations Between the Masses of the Superpartners of Leptons and Quarks, the Goldstino Couplings and the Neutral Currents*, Phys. Lett. **B84** (1979) 416.

[64] S. Dimopoulos and H. Georgi, *Softly Broken Supersymmetry and SU(5)*, Nucl. Phys. **B193** (1981) 150.

[65] M. S. Carena, S. Heinemeyer, C. E. M. Wagner, and G. Weiglein, *Suggestions for Benchmark Scenarios for MSSM Higgs Boson Searches at Hadron Colliders*, Eur. Phys. J. **C26** (2002) 601.

[66] ALEPH Collaboration, DELPHI Collaboration, L3 Collaboration, OPAL Collaboration and LEP Working Group for Higgs Boson Searches, *Search for Neutral MSSM Higgs Bosons at LEP*, Eur. Phys. J. **C47** (2006) 547.

[67] CDF and D0 Collaborations and Tevatron New Physics Higgs Working Group (TEVNPHWG), *Combined CDF and D0 upper limits on MSSM Higgs boson production in tau-tau final states with up to 2.2 fb^{-1}*, `arXiv:1003.3363 [hep-ex]`.

[68] D0 Collaboration, *Search for neutral Higgs bosons decaying to tau pairs produced in association with b quarks in ppbar collisions at $\sqrt{s}$=1.96 TeV*, Phys. Rev. Lett. **107** (2011) 121801.

[69] LEP Higgs Working Group for Higgs boson searches Collaboration, *Search for charged Higgs bosons: Preliminary combined results using LEP data collected at energies up to 209 GeV*, `arXiv:0107031 [hep-ph]`.

[70] CDF Collaboration, *Search for charged Higgs bosons in decays of top quarks in p-pbar collisions at $\sqrt{s}$= 1.96 TeV*, Phys. Rev. Lett. **103** (2009) 101803.

[71] D0 Collaboration, *Search for charged Higgs bosons in top quark decays*, Phys. Lett. **B682** (2009) 278.

[72] M. Dine and W. Fischler, *A Phenomenological Model of Particle Physics Based on Supersymmetry*, Phys. Lett. **B 110** (1982) 227.

[73] L. Alvarez-Gaume, M. Claudson, and M. Wise, *Low-Energy Supersymmetry*, Nucl. Phys. **B 207** (1982) 96.

[74] C. R. Nappi and B. A. Ovrut, *Supersymmetric Extension of the SU(3) x SU(2) x U(1) Model*, Phys. Lett. **B 113** (1982) 175.

[75] M. Dine and A. E. Nelson, *Dynamical supersymmetry breaking at low-energies*, Phys. Rev. **D 48** (1993) 1277.

[76] M. Dine, A. E. Nelson, and Y. Shirman, *Low-energy dynamical supersymmetry breaking simplified*, Phys. Rev. **D 51** (1995) 1362.

[77] M. Dine, A. E. Nelson, Y. Nir, and Y. Shirman, *New tools for low-energy dynamical supersymmetry breaking*, Phys. Rev. **D 53** (1996) 2658.

[78] OPAL Collaboration, *Searches for gauge-mediated supersymmetry breaking topologies in e^+e^- collisions at LEP2*, Eur. Phys. J. **C 46** (2006) 307.

[79] ALEPH Collaboration, *Search for gauge mediated SUSY breaking topologies in ee collisions at centre-of-mass energies up to 209 GeV*, Eur. Phys. J. **C 25** (2002) 339.

[80] DELPHI Collaboration, *Search for supersymmetric particles in light gravitino scenarios and sleptons NLSP*, Eur. Phys. J. **C 27** (2003) 153.

[81] D0 Collaboration, *Search for squark production in events with jets, hadronically decaying tau leptons and missing transverse energy at* $\sqrt{s}$*=1.96 TeV*, Phys. Lett. **B 680** (2009) 24.

[82] CMS Collaboration, *Search for new physics with same-sign isolated dilepton events with jets and missing transverse energy at the LHC*, JHEP **1106** (2011) 077.

[83] CMS Collaboration, *Search for Physics Beyond the Standard Model Using Multilepton Signatures in pp Collisions at* $\sqrt{s}$*=7 TeV*, Phys. Lett. **B 704** (2011) 411.

[84] ATLAS Collaboration, *Search for Supersymmetry in Events with Large Missing Transverse Momentum, Jets, and at Least One Tau Lepton in 7 TeV Proton-Proton Collision Data with the ATLAS Detector*, ATLAS-CONF-2012-112, 2012.

[85] P. Langacker, *The Physics of Heavy* Z' *Gauge Bosons*, Rev.Mod.Phys. **81** (2009) 1199.

[86] J. L. Hewett and T. G. Rizzo, *Low-energy phenomenology of superstring-inspired* E_6 *models*, Phys. Reports **183** (1989) 193.

[87] M. Cvetic and S. Godfrey, *Discovery and identification of extra gauge bosons*, `arXiv:hep-ph/9504216 [hep-ph]`.

[88] A. Leike, *The Phenomenology of extra neutral gauge bosons*, Phys.Rept. **317** (1999) 143.

[89] T. G. Rizzo, Z' *phenomenology and the LHC*, `arXiv:hep-ph/0610104 [hep-ph]`. Published in Boulder, 2006, Colliders and Neutrinos (TASI 2006).

[90] R. Diener, S. Godfrey, and T. A. Martin, *Unravelling an Extra Neutral Gauge Boson at the LHC using Third Generation Fermions*, Phys.Rev. **D83** (2011) 115008.

[91] CDF Collaboration, *Search for new physics using high mass tau pairs from 1.96 TeV* $p\bar{p}$ *collisions*, Phys.Rev.Lett. **95** (2005) 131801.

[92] CMS Collaboration, *Search for New Ditau Resonances in pp Collisions at* $\sqrt{s}$ *= 7 TeV*, CMS-PAS-EXO-10-022, 2011.

[93] ALEPH, DELPHI, L3, OPAL and SLD Collaboration, *Precision electroweak measurements on the Z resonance*, Phys. Rept. **427** (2006) 257.

[94] ATLAS Collaboration, *A search for high mass resonances decaying to* $\tau^+\tau^-$ *in the ATLAS detector*, ATLAS-CONF-2012-067, 2012.

[95] G. Altarelli, B. Mele, and M. Ruiz-Altaba, *Searching for new heavy vector bosons in* $p\bar{p}$ *colliders*, Z. Phys. **C45** (1989) 109.

[96] CMS Collaboration, *The CMS experiment at the CERN LHC*, JINST **3** (2008) S08004.

[97] ALICE Collaboration, *The ALICE experiment at the CERN LHC*, JINST **3** (2008) S08002.

[98] LHCb Collaboration, *The LHCb Detector at the LHC*, JINST **3** (2008) S08005.

[99] LHCf Collaboration, *The LHCf detector at the CERN LHC*, JINST **3** (2008) S08006.

[100] TOTEM Collaboration, *The TOTEM experiment at the CERN Large Hadron Collider*, JINST **3** (2008) S08007.

[101] https://twiki.cern.ch/twiki/bin/view/AtlasPublic/LuminosityPublicResults#Annual_Charts_of_Luminosity.

[102] S. L. Glashow, *Partial-Symmetries of Weak Interactions*, Nucl. Phys. **22** (1961) 579.

[103] S. Weinberg, *A Model of Leptons*, Phys. Rev. Lett. **19** (1967) 1264.

[104] A. Salam, *Elementary Particle Theory*, p. 367 (Almqvist and Wiksell, Stockholm, 1968) .

[105] ATLAS Collaboration, *Performance of the ATLAS Trigger System in 2010*, `arXiv:1110.1530v2 [hep-ex]`.

[106] ATLAS Collaboration, *Luminosity Determination in pp Collision at sqrt(s)= 7 TeV Using the ATLAS Detector at the LHC*, Eur. Phys. J. **C71** (2011) 1630.

[107] ATLAS Collaboration, *Updated Luminosity Determination in pp Collisions at* $\sqrt{s} = 7$ *using the ATLAS Detector*, ATLAS-CONF-2011-011, 2011.

[108] ATLAS Collaboration, *Zero Degree Calorimeters for ATLAS (Letter of Intent)*, CERN-LHCC-2007-001, 2007.

[109] ATLAS Collaboration, *ATLAS Forward Detectors for Measurement of Elastic Scattering and Luminosity, Technical Design Report*, CERN-LHCC-2008-004, 2008.

[110] The ATLAS Computing group, *ATLAS Computing, Technical Design Report*, CERN-LHCC-2005-22, 2005.

[111] ATLAS Collaboration, *The ATLAS Simulation Infrastructure*, Eur. Phys. J. **C70** (2010) 823.

[112] T. Sjostrand, S. Mrenna, and P. Skands, *PYTHIA 6.4 physics and manual*, JHEP **05** (2006) 026.

[113] G. Corcella et al., *HERWIG 6.5*, JHEP **0101** (2001) 010.

[114] S. Jadach, Z. Was, R. Decker, and J. H. Kühn, *The τ decay library TAUOLA, version 2.4*, Comput. Phys. Commun. **76** (1993) 361.

[115] T. Pierzchala, E. Richter-Was, Z. Was, and M. Worek, *Spin effects in tau lepton pair production at LHC*, Acta Phys.Polon. **B32** (2001) 1277.

[116] P. Golonka and Z. Was, *PHOTOS Monte Carlo: A Precision tool for QED corrections in Z and W decays*, Eur. Phys. J. **C45** (2006) 97.

[117] ATLAS Collaboration, *Charged particle multiplicities in p p interactions at* $\sqrt{s} = 0.9$ *and 7 TeV in a diffractive limited phase-space measured with the ATLAS detector at the LHC and new PYTHIA6 tune*, ATLAS-CONF-2010-031, 2010.

[118] The GEANT4 Collaboration, S. Agostinelli et al., *GEANT4: A simulation toolkit*, Nucl. Instrum. Meth. A **506** (2003) 250.

[119] ATLAS Collaboration, *Expected electron performance in the ATLAS experiment*, ATLAS-PHYS-PUB-2011-006, 2011.

[120] ATLAS Collaboration, *Electron performance measurements with the ATLAS detector using the 2010 LHC proton-proton collision data*, Eur. Phys. J. **C72** (2012) 1909.

[121] ATLAS Collaboration, *Expected photon performance in the ATLAS experiment*, ATLAS-PHYS-PUB-2011-007, 2011.

[122] ATLAS Collaboration, *Determination of the muon reconstruction efficiency in ATLAS at the Z resonance in proton-proton collisions at* $\sqrt{s} = 7$ *TeV*, ATLAS-CONF-2011-008, 2011.

[123] T. Lagouri et al., *A muon identification and combined reconstruction procedure for the ATLAS detector at the LHC at CERN*, IEEE Trans. Nucl. Sci. **51** (2004) 3030.

[124] S. Hassani et al., *A Muon Identification and Combined Reconstruction Procedure for the ATLAS Detector at the LHC using the (MUONBOY, STACO, MuTag) Reconstruction Packages*, Nucl. Instrum. Meth. **A572** (2007) 77.

[125] ATLAS Collaboration, *Muon reconstruction efficiency in reprocessed 2010 LHC proton-proton collision data recorded with the ATLAS*, ATLAS-CONF-2011-063, 2011.

[126] G. P. Salam, *Towards Jetograpgy*, `arXiv:0906.1833v2 [hep-ph]`.

[127] M. Cacciari and G. P. Salam. Phys. Lett. B **641** (2006) 57; M. Cacciari, G. P. Salam and G. Soyez, http://fastjet.fr/.

[128] ATLAS Collaboration, *Measurement of inclusive jet and dijet cross sections in proton-proton collisions at 7 TeV centre-of-mass energy with the ATLAS detector*, Eur. Phys. J. **C71** (2011) 1512.

[129] ATLAS Collaboration, *Jet energy scale and its systematic uncertainty for jets produced in proton-proton collisions at* $\sqrt{s} = 7$ *TeV and measured with the ATLAS detector*, ATLAS-CONF-2010-056, 2010.

[130] C. Roda, I. Vivarelli, *Cell Based Jet Calibration*, CERN-ATL-PHYS-PUB-2005-019, 2005.

[131] ATLAS Collaboration, *Local hadronic calibration*, ATL-LARG-PUB-2009-001, 2009.

[132] W. Lampl et al., *Calorimeter Clustering Algorithms : Description and Performance*, ATL-LARG-PUB-2008-002, 2008.

[133] ATLAS Collaboration, *Performance of the Missing Transverse Energy Reconstruction and Calibration in Proton-Proton Collisions at a Center-of-Mass Energy of 7 TeV with the ATLAS Detector*, ATLAS-CONF-2010-057, 2010.

[134] ATLAS Collaboration, *Reconstruction and Calibration of Missing Transverse Energy and Performance in Z and W events in ATLAS Proton-Proton Collisions at 7 TeV*, ATLAS-CONF-2011-080, 2011.

[135] ATLAS Collaboration, *Data-Quality Requirements and Event Cleaning for Jets and Missing Transverse Energy Reconstruction with the ATLAS Detector in p-p Collisions at a Center-of-Mass Energy of* $\sqrt{s} = 7$ *TeV*, ATLAS-CONF-2010-038, 2010.

[136] ATLAS Collaboration, *Reconstruction, Energy Calibration, and Identification of Hadronically Decaying Tau Leptons in the ATLAS Experiment*, ATLAS-CONF-2011-077, 2011.

[137] D. Froidevaux, P. Nevski, and E. Richter-Was, *Energy flow studies with hadronic tau-decays using DC1 data samples*, ATL-COM-PHYS-2005-024, 2005.

[138] ATLAS Collaboration, *Performance of the ATLAS tau trigger in p-p collisions at* $\sqrt{s} = 7$ *TeV*, ATLAS-CONF-2010-090, 2010.

[139] A. Hoecker, P. Speckmayer, J. Stelzer, F. Tegenfeldt, and H. Voss, *TMVA, toolkit for multivariate data analysis with ROOT*, PoS ACAT:040,2007, CERN-2008-001, 2007.

[140] ATLAS Collaboration, *Cut based identification of hadronic tau decays*, ATL-PHYS-PUB-2010-001, 2010.

[141] ATLAS Collaboration, *Measurement of the Mis-identification Probability of τ Leptons from Hadronic Jets and from Electrons*, ATLAS-CONF-2011-113, 2011.

[142] M. Heldmann and D. Cavalli, *An improved tau-Identification for the ATLAS experiment*, ATL-PHYS-PUB-2006-008, 2006.

[143] CMS Collaboration, *Performance of tau-lepton reconstruction and identification in CMS*, J. Instrum.7 **P01001** (2012) .

[144] ATLAS Collaboration, *Performance of the Reconstruction and Identification of Hadronic Tau Decays with ATLAS*, ATLAS-CONF-2011-152, 2011.

[145] ATLAS Collaboration, *Performance of the Reconstruction and Identification of Hadronic Tau Decays with ATLAS*, ATLAS-CONF-2012-054, 2012.

[146] D0 Collaboration, *Measurement of sigma(p anti-p $\rightarrow$ Z + X) Br(Z $\rightarrow \tau^+\tau^-$) at $\sqrt{s}$ = 1.96 TeV*, Phys. Lett. **B670** (2009) 292.

[147] CDF Collaboration, *Measurement of sigma p anti-p $\rightarrow$ Z$\times$ Br (Z $\rightarrow$ 2tau) in p anti-p collisions at $\sqrt{s}$ = 1.96 TeV*, Phys. Rev. **D75** (2007) 092004.

[148] CMS Collaboration, *Measurement of the Inclusive Z Cross Section via Decays to Tau Pairs in pp Collisions at $\sqrt{s}$=7 TeV*, JHEP **08** (2011) 117.

[149] K. Melnikov, F. Petriello, *Electroweak gauge boson production at hadron colliders through O(α(s)^2)*, Phys. Rev. D **74**, 114017 (2006) .

[150] R. Gavin, Y. Li, F. Petriello et al., *FEWZ 2.0: A code for hadronic Z production at next-to-next-to- leading order*, arXiv:1011.3540 [hep-ph].

[151] S. Catani, L. Cieri, G. Ferrera, D. de Florian, and M. Grazzini, *Vector boson production at hadron colliders: a fully exclusive QCD calculation at NNLO*, Phys. Rev. Lett. **103** (2009) 082001.

[152] S. Frixione and B. Webber, *Matching NLO QCD computations and parton shower simulations*, JHEP **0206** (2002) 029.

[153] A. Sherstnev and R. S. Thorne, *Parton Distributions for LO Generators*, Eur. Phys. J. **C55** (2008) 553.

[154] ATLAS Collaboration, *Reconstruction, Energy Calibration, and Identification of Hadronically Decaying Tau Leptons in the ATLAS Experiment*, ATLAS-CONF-2011-077, 2011.

[155] H1 and ZEUS Collaboration, *Combined Measurement and QCD Analysis of the Inclusive e p Scattering Cross Sections at HERA*, JHEP **1001** (2010) 109.

[156] P. M. Nadolsky et al., *Implications of CTEQ global analysis for collider observables*, Phys. Rev. **D78** (2008) 013004.

[157] D. Grellscheid and P. Richardson, *Simulation of Tau Decays in the Herwig++ Event Generator*, arXiv:0710.1951v1 [hep-ph].

[158] L. Lyons, D. Gibaut, and P. Clifford, *How to combine correlated edtimates of a single physical quantity*, Nucl. Instrum. Meth. **A270** (1988) 110.

[159] A. Valassi, *Combining correlated measurements of several different physical quantities*, Nucl. Instrum. Meth. **A500** (2003) 391.

[160] ATLAS Collaboration, *A measurement of the total $W^{\pm}$ and Z/γ^{*} cross sections in the e and μ decay channels and of their ratios in pp collisions at $\sqrt{s}$ = 7 TeV with the ATLAS detector*, ATLAS-CONF-2011-041, 2011.

[161] CMS Collaboration, *Measurement of the W and Z inclusive production cross sections at $\sqrt{s}$=7 TeV with the CMS experiment at the LHC*, CMS-PAS-EWK-10-005.

[162] ATLAS Collaboration, *Measurement of the $W \to \tau\nu$ Cross Section in pp Collisions at $\sqrt{s}$ = 7 TeV with the ATLAS experiment*, Phys. Lett. **B706** (2012) 276.

[163] UA1 Collaboration, *Events with Large Missing Transverse Energy at the CERN Collider: II. Search for the Deacys of $W^{\pm}$ into Heavy Leptons and of Z^{0} into non-interacting Particles*, Phys. Lett. B **185** (1987) no. 1-2, 233.

[164] CDF Collaboration, *Measurement of the ratio sigma B($W \to \tau\nu$) / sigma B ($W \to e\nu$), in p anti-p collisions at $\sqrt{s}$ = 1.8 TeV* , Phys. Rev. Lett **68** (1992) no. 23, 3398.

[165] D0 Collaboration, *Measurement of the $W \to \tau\nu$ Production Cross Section in $p\bar{p}$ Collisions at $\sqrt{s}$ = 1.8 TeV*, Phys. Rev. Lett. **84** (2000) 5710.

[166] ATLAS Collaboration, *Observation of $W \to \tau\nu$ Decays with the ATLAS Experiment*, ATLAS-CONF-2010-097, 2010.

[167] ATLAS Collaboration, *A combined measurement of the top quark pair production cross-section using dilepton and single-lepton final states*, ATLAS-CONF-2011-040, 2011.

[168] A. D. Martin, W. J. Stirling, R. S. Thorne, and G. Watt, *Parton distributions for the LHC*, Eur. Phys. J. **C63** (2009) 189.

[169] ATLAS Collaboration, *Measurement of the inclusive $W^{\pm}$ and Z/γ cross sections in the electron and muon decay channels in pp collisions at $\sqrt{s}$ = 7 TeV with the ATLAS detector*, Phys. Rev. **D85** (2012) 072004.

[170] ATLAS Collaboration, *Measurement of Hadronic Tau Decay Identification Efficiency using $W \to \tau\nu$ events*, ATLAS-CONF-2011-093, 2011.

[171] M. L. Mangano, M. Moretti, F. Piccinini, R. Pittau, and A. D. Polosa, *ALPGEN, a generator for hard multiparton processes in hadronic collisions*, JHEP **07** (2003) 001.

[172] J. M. Butterworth, J. R. Forshaw and M. H. Seymour, *Multiparton Interactions in Photoproduction at HERA*, Z. Phys. **C72** (1996) 637.

[173] ATLAS Collaboration, *$Z \to \tau\tau$ cross section measurement in proton-proton collisions at 7 TeV with the ATLAS experiment*, ATLAS-CONF-2012-006, 2012.

[174] ATLAS Collaboration, *Measurement of tau polarization in $W \to \tau\nu$ decays with the ATLAS detector in pp collisions at $\sqrt{s}$ = 7 TeV*, Eur.Phys.J. **C72** (2012) 2062.

[175] ATLAS Collaboration, *Measurement of the top quark pair cross section with ATLAS in pp collisions at $\sqrt{s}$ = 7 TeV using final states with an electron or a muon and a hadronically decaying tau lepton*, `arXiv:1205.2067v1 [hep-ex]`.

[176] ATLAS Collaboration, *Search for the Standard Model Higgs boson in the decay mode $H \to \tau\tau \to l + 4$ neutrinos in Association with jets in Proton-Proton Collisions at $\sqrt{s}$ =7 TeV with the ATLAS detector*, ATLAS-CONF-2011-133, 2011.

[177] ATLAS Collaboration, *Search for neutral MSSM Higgs bosons decaying to $\tau^+\tau^-$ pairs in proton-proton collisions at $\sqrt{s}$ = 7 TeV with the ATLAS detector*, ATLAS-CONF-2011-132, 2011.

[178] M. Spira, *HIGLU: A Program for the Calculation of the Total Higgs Production Cross Section at Hadron Colliders via Gluon Fusion including QCD Corrections*, arXiv:9510347 [hep-ph].

[179] R. V. Harlander and W. B. Kilgore, *Next-to-next-to-leading order Higgs production at hadron colliders*, Phys. Rev. Lett. **88** (2002) 201801.

[180] P. Bolzoni, F. Maltoni, S.-O. Moch, and M. Zaro, *Higgs production via vector-boson fusion at NNLO in QCD*, Phys. Rev. Lett. **011801** (2010) 105.

[181] B. P. Kersevan and E. Richter-Was, *The Monte Carlo event generator AcerMC version 2.0 with interfaces to Pythia 6.2 and Herwig 6.5*, arXiv:0405247 [hep-ph].

[182] ATLAS Collaboration, *Data-driven estimation of the background to charged Higgs boson searches using hadronically-decaying tau final states in ATLAS*, ATLAS-CONF-2011-051, 2011.

[183] ATLAS Collaboration, *Measurement of the top quark pair production cross-section based on a statistical combination of measurements of dilepton and single-lepton final states at $\sqrt{s}$ =7 TeV with the ATLAS detector*, ATLAS-CONF-2011-108, 2011.

[184] ATLAS Collaboration, *Luminosity Determination in pp Collisions at $\sqrt{s}$ = 7 TeV Using the ATLAS Detector in 2011*, ATLAS-COM-CONF-2011-130, 2011.

[185] P. Nason, *A new method for combining NLO QCD with shower Monte Carlo algorithms*, JHEP **11546** (2004) 040.

[186] A. L. Read, *Presentation of search results: The CL(s) technique*, J. Phys. **G28** (2002) 2693.

[187] T. Junk, *Confidence Level Computation for Combining Searches with Small Statistics*, Nucl. Instrum. Meth. **A434** (1999) 435.

[188] G. Cowan, K. Cranmer, E. Gross and O. Vitells, *Asymptotic formulae for likelihood-based tests of new physics*, Eur. Phys. J. **C71** (2011) 1554.

[189] ATLAS Collaboration, *Search for the Standard Model Higgs boson in the $H \to \tau\tau$ decay mode in $\sqrt{s}$ = 7 TeV pp collisions with ATLAS*, arXiv:1206.5971 [hep-ex].

[190] Berge, S and Bernreuther, W, *Determining the CP parity of Higgs bosons at the LHC in the to 1-prong decay channels*, Phys. Lett. B **671** (2009) 470.

[191] Berge, S and Bernreuther, W and Ziethe J, *Determining the CP parity of Higgs bosons at the LHC in their tau decay channels*, Phys. Rev. Lett. **100** (2008) 171605.

[192] CMS Collaboration, *Search for Neutral Higgs Bosons Decaying to Tau Pairs in pp Collisions at $\sqrt{s}$ = 7 TeV* , CMS-PAS-HIG-11-009, 2011.

[193] ATLAS Collaboration, *Search for neutral MSSM Higgs bosons decaying to $\tau^+\tau^-$ pairs in proton-proton collisions at $\sqrt{s}$ = 7 TeV with the ATLAS detector*, Phys. Lett. B **705** (2011) 174.

[194] R. Harlander, M. Krämer and M. Schumacher, *Bottom-quark associated Higgs-boson production: reconciling the four- and five-flavour scheme approach* ,
CERN-PH-TH/2011-134 - FR-PHENO-2011-009 - TTK-11-17 - WUB/11-04
https://twiki.cern.ch/twiki/pub/LHCPhysics/MSSMNeutral/santandermatching-hks.pdf .

[195] S. Dittmaier, M. Kramer and M. Spira, *Higgs Radiation off Bottom Quarks at the Tevatron and the LHC*, Phys. Rev. **D70** (2004) 074010.

[196] S. Dawson, C. B. Jackson, L. Reina and D. Wackeroth, *Higgs Production in Association with Bottom Quarks at Hadron Colliders*, Mod. Phys. Lett. **A21** (2006) 89.

[197] R. Harlander and W. B. Kilgore, *Higgs boson production in bottom quark fusion at next-to-next-to-leading order*, Phys. Rev. **D68** (2003) 013001.

[198] M. Frank et al., *The Higgs Boson Masses and Mixings of the Complex MSSM in the Feynman-Diagrammatic Approach*, JHEP **0702** (2007) 047.

[199] T. Gleisberg et al., *Event generation with SHERPA 1.1*, JHEP **02** (2009) 007.

[200] T. Binoth, M. Ciccolini, N. Kauer, and M. Kramer, *Gluon-induced W-boson pair production at the LHC*, JHEP **12** (2006) 046.

[201] S. Moch and P. Uwer, *Heavy-quark pair production at two loops in QCD*, Nucl. Phys. Proc. Suppl. **183** (2008) 75.

[202] U. Langenfeld, S. Moch and P. Uwer, *New results for t bar t production at hadron colliders*, `arXiv:0907.2527 [hep-ph]`.

[203] A.D. Martin, R.G. Roberts, W.J. Stirling, R.S. Thorne, *MRST2001: partons and α_S from precise deep inelastic scattering and Tevatron jet data*, `arXiv:0110215v2 [hep-ph]`.

[204] ATLAS Collaboration, *Search for Charged Higgs Bosons in the τ+jets Final State in $t\bar{t}$ Decays with 1.03 fb^{-1} of pp Collision Data Recorded at $\sqrt{s}$ = 7 TeV with the ATLAS Experiment*, ATLAS-CONF-2011-138, 2011.

[205] ATLAS Collaboration, *Search for a charged Higgs boson decaying via $H^+ \to \tau_{\text{lep}} + \nu$ in ttbar events with one or two light leptons in the final state using 1.03 fb^{-1} of pp collision data recorded at $\sqrt{s}$ = 7 TeV with the ATLAS detector*, ATLAS-CONF-2011-151, 2011.

[206] D. Casadei et al., *The implementation of the ATLAS missing E_T triggers for the initial LHC operation*, ATL-DAQ-PUB-2011-001, 2011.

[207] ATLAS Collaboration, *Measurement of the top quark-pair production cross section with ATLAS in pp collisions at $\sqrt{s}$ = 7 TeV*, `arXiv:1012.1792 [hep-ex]`.

[208] ATLAS Collaboration, *Commissioning of the ATLAS high-performance b-tagging algorithms in the 7 TeV collision data*, ATLAS-CONF-2011-102, 2011.

[209] CMS Collaboration, *$H^+ \to \tau\nu$ in Top quark decays*, CMS-PAS-HIG-11-008, 2011.

[210] ATLAS Collaboration, *Search for neutral MSSM Higgs bosons in $\sqrt{s}$=7 TeV pp collisions with the ATLAS detector*, ATLAS-CONF-2012-094, 2012.

[211] ATLAS Collaboration, *Search for charged Higgs bosons decaying via $H^\pm \to \tau\nu$ in top quark pair events using pp collision data at $\sqrt{s}$ = 7 TeV with the ATLAS detector*, JHEP **1206** (2012) 039.

[212] M. S. R.K. Ellis, I. Hinchliffe and J. V. der Bij, *Higgs Decay to $\tau^+\tau^-$: A Possible Signature of Intermediate Mass Higgs Bosons at the SSC*, Nucl. Phys. **B297** (1988) 221.

[213] A. Elagin, P. Murat, A. Pranko, and A. Safonov, *A New Mass Reconstruction Technique for Resonances Decaying to di-tau*, `arXiv:1012.4686 [hep-ex]`.